The deglaciation of Kongsfjorden, Svalbard

—based on surface exposure dating of glacial erratics and Quaternary geological mapping of Blomstrandhalvøya

Oliver Rodney Grant

GEOV399 Thesis for Master degree in Earth Science

Quaternary geology and paleoclimate

June 2016

Department of Earth Science
University of Bergen

Department of Arctic Geology
University Centre in Svalbard

"I landed on the north side near an iceberg, where a small tract of rising ground was terminated by a perpendicular precipice of perhaps a thousand feet in height. This cliff was composed of a kind of bluish-grey marble, but, like all the rocks we had yet seen, was full of fissures in every direction. At a distance, it appeared like basaltic columns…"

W. Scoresby Jr, 1820

"…usually it occurs in the form of a more or less fuzzy crystalline, blue-grey marble with white or occasional red veins and aisles, and sometimes several wide secretions of coarse calcified lime; only in one place, on one of the isles, I met real crystals, and quite beautiful fossils…"

C. W. Blomstrand, 1864

"I circumnavigated the Island by boat, and found a number of deep-water inlets and bays bounded by variegated cliffs; and in many places where the marble had been smoothed and faced by Nature, a dazzling vista met my view."

E. Mansfield, 1911

"The splendid summer climate and pure air render it, in my opinion, an ideal place for a large class of invalids."

F. G. Gardner, 1912

Abstract

Surface exposure dating via ^{10}Be cosmogenic nuclide dating is used, alongside Quaternary geological mapping of landforms and sediments, to reconstruct the course of deglaciation following the Late Weichselian Glacial Maximum in Kongsfjorden, northwest Spitsbergen, Svalbard. Kongsfjorden hosted a fast-flowing paleo-Ice Stream at the Last Glacial Maximum, draining an ice dome over northwest Spitsbergen. One research aim is to resolve the nature of glacial retreat in the fjord, questioning whether it was a rapid collapse of the ice stream. A secondary objective is to couple the nature of retreat to the dynamic behaviour of the Svalbard-Barents Sea Ice Sheet during deglaciation.

Blomstrandhalvøya is a ca. 16 km^2 island close to the centre of Kongsfjorden, and can be considered a large roche moutonnée, overridden during repeated glacial advances toward the shelf-edge west of Kongsfjorden through the Quaternary. The island provides an ideal location to study landforms and sediments associated with the Late Weichselian glaciation and subsequent Holocene interglacial period. Detailed mapping reveals a periglacial dominated landscape development through the Holocene, with the north and east of the island affected by the Little Ice Age glacial advance and 20th Century surge activity of Blomstrandbreen.

Surface exposure dating of glacial erratics on Blomstrandhalvøya shows the initiation of retreat at ca. 15.6 ka, and continued lateral retreat through the Bølling-Allerød. A trimline-moraine complex observed on the southeast of the island yields a mid-Younger Dryas exposure age, and a number of samples produce similar ages below the trimline elevation, it is thus suggested that the trimline-moraine complex represents a Younger Dryas ice marginal position in the fjord. This is consistent with previous reconstructions in western Spitsbergen which show a suppressed marine limit through the Younger Dryas. The secondary field area, Ossian Sarsfjellet at the head of the fjord, reveals deglaciation ages within the Younger Dryas, thus suggesting a dynamic thinning of the remaining ice cap over central-eastern Spitsbergen.

Clusters of exposure ages, combined with published exposure and radiocarbon dates, allowed for an ice-surface reconstruction for the paleo-ice stream in Kongsfjorden, and subsequently used to illustrate the course of deglaciation in the fjord at six approximate time slices (16.6 ka, 15.6 ka, 14.5 ka, 12.7 ka, 0.02 ka, and present). The reconstructed nature of the deglaciation of Kongsfjorden significantly builds on previous work and conceptual models in the fjord and neighbouring areas in north/west Spitsbergen, highlighting the dynamic behaviour of the fjord glacier during retreat, and reflecting the upstream behaviour of the Svalbard-Barents Sea Ice Sheet following the Late Weichselian Glacial Maximum.

Acknowledgements

I am extremely grateful for the help and support I have received from innumerable people and organisations throughout this project, and give special mention here. My supervisors Dr Henriette Linge (UiB) and Dr Anne Hormes (GU, UNIS) have provided exceptional guidance and advice in every aspect of this project from field to paper, with continued enthusiasm and commitment to the project to which I am greatly indebted.

Thanks to the laboratory technicians in Bergen, particularly Lars Evje for his expert supervision in the cosmogenic nuclide laboratory. This project has been made possible by a number of extraordinary people who helped conduct fieldwork in the summer of 2014; Dr Ewa Lind (SU), Dr Maxime Debret (UdR), Dr Tommaso Piacentini and Marco Sciarra (Ud'A), Dr Claudio Berti (LU), and Buffy (GU) and the summer of 2015; Gauti Eliassen (UiO) provided expert company and inexorable humour in the field.

Fieldwork would have been impossible without the excellent logistics and support staff at the Sverdrup Norwegian Polar Research station in Ny-Ålesund; Christian Zoelly and Wojtek Moskal provided exceptional logistic support, while the staff at Kings Bay ensured an extremely comfortable and well-catered stay on both occasions. The logistics personnel at the UNIS provided field safety training for which I am hugely thankful. Thanks to Dr Jason Briner (UB) for providing dates for Irgens and Bratlie.

A debt of gratitude is owed to the staff at the SUERC led by Dr Derek Fabel, Maria Miguens-Rodriguez provided amazing guidance and facilitated my stay in the Cosmogenic Isotope Analysis Laboratory, and Dr Sheng Xu conducted the accelerated mass spectrometry analysis. Jacky and Jacqui Fordyce were exceptional hosts while at SUERC, ensuring I was well looked after and punctual despite the snow!

The staff at the Svalbard Science Forum guided me through the application process for the Arctic Field Grant which part-funded this project along with ICEBOUND. I would also like to thank Sille Myreng (NTNU) and Karoline Bælum (SSF) for their help while applying.

I would like to extend my thanks to friends in Bergen and the wider network from UiB and UNIS for welcoming and accommodating me over the past two years. Finally to my friends and family in the UK, for showing so much support, love, and faith in me, and encouraging me to pursue my dreams.

I am eternally grateful,

Oliver Grant

Bergen, 27 May 2016

Table of contents

1. Introduction

1.1 Research questions

This Master thesis aims to reconstruct the deglaciation of Kongsfjorden following the Late Weichselian Glacial Maximum, by addressing two research questions; (1) was the deglaciation of the fjord a collapse or a steady retreat?, and (2) what can the nature of glacial retreat in Kongsfjorden reveal about the wider deglaciation of the Svalbard-Barents Sea Ice Sheet?

To fulfil the research questions, two techniques are employed in this thesis, (1) cosmogenic surface exposure dating of erratic boulders and polished bedrock to obtain numerical ages for deglaciation for Blomstrandhalvøya and Ossian Sarsfjellet, and (2) detailed mapping of Quaternary landforms and sediments on Blomstrandhalvøya in the centre of the fjord.

The original working hypothesis questioned if Blomstrandhalvøya could be a dipstick for determining the thinning rate of the Kongsfjorden paleo-ice stream with the possibility to sample a vertical transect for exposure dating. The project is part of the wider ICEBOUND project, aiming to reconstruct ice sheet thickness from over Svalbard, to improve climate-ice sheet and uplift models (ICEBOUND 2010).

The present working hypothesis questions whether surface exposure dating from Blomstrandhalvøya and Ossian Sarsfjellet can be combined to reveal the timing of lateral and vertical glacial retreat, with Quaternary geological mapping elucidating glacial complexities and post-glacial landscape development. The results can then be compared within the framework of previous literature from within the fjord, and the wider context of the Svalbard-Barents Sea Ice Sheet.

1.2 Location of the study area

Kongsfjorden is located between 78.9° N to 79.1° N and 11.2° E to 11.4° E in northwest Spitsbergen (Figure 1.1), the largest island of the Svalbard archipelago located in the High Arctic 74° N to 81° N and 10° E to 35° E, with the Barents Sea to the east, the Fram Strait and Greenland Sea to the west, and the Arctic Ocean to the north. Approximately 60 % of the land area of Svalbard is glaciated (3.6×10^4 km^2) (Kohler *et al.* 2007), and five tidewater glaciers currently drain through Kongsfjorden, with the catchment also containing several cirque and valley glaciers (Figure 1.1c).

The SE–NW trending Kongsfjorden converges with the NE–SW trending Krossfjorden around Kapp Guissez, and open out to the west in the submarine Kongsfjordrenna cross-shelf trough (Figure 2.4, Figure 5.3), extending to the shelf-edge north of Prins Karls Forland (Ottesen *et al.* 2007; Ingólfsson & Landvik 2013). The primary field site of Blomstrandhalvøya is mapped in Figure 1.2.

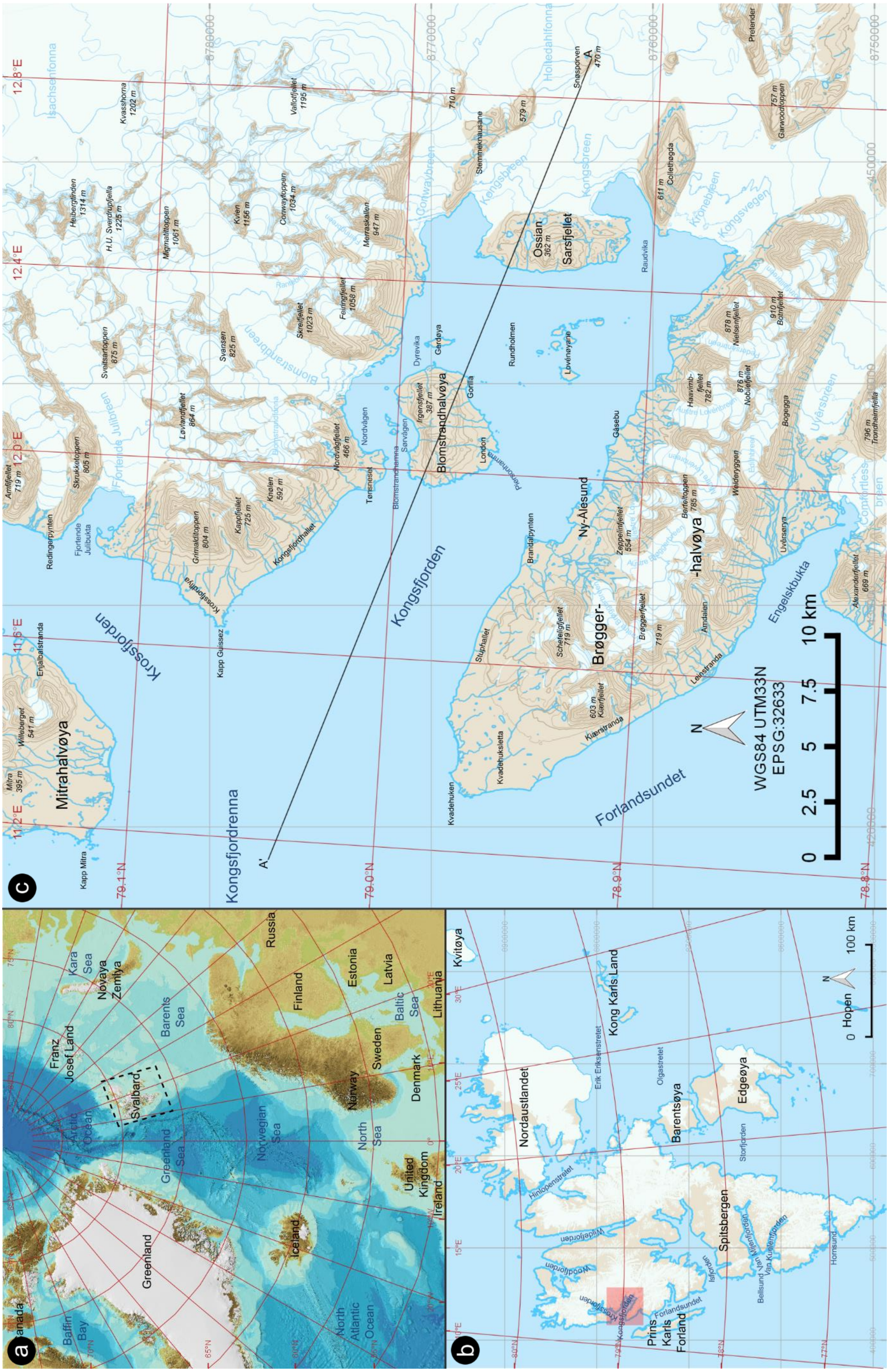
a
b
c
Greenland
Iceland
Svalbard
Norway
Sweden
Finland
Russia
Barents Sea
Norwegian Sea
Greenland Sea
North Sea
Nordaustlandet
Spitsbergen
Barentsøya
Edgeøya
Prins Karls Forland
Kong Karls Land
Kvitøya
Hopen
100 km
Mitrahalvøya
Krossfjorden
Kongsfjorden
Kongsfjordrenna
Blomstrandhalvøya
Ny-Ålesund
Brøgger-
-halvøya
Ossian Sarsfjellet
Forlandsundet
Engelskbukta
WGS84 UTM33N
EPSG:32633
0 2.5 5 7.5 10 km
A
A'

Figure 1.1: (a) Inset showing the location of Svalbard in relation to the North Atlantic region (background map data: (GEBCO 2014)), (b) inset showing the location of Kongsfjorden in relation to the Svalbard archipelago (background map data © Norwegian Polar Institute), and (c) location map of Kongsfjorden centred on Blomstrandhalvøya, with 50 m contours (background map data © Norwegian Polar Institute. Grey grid = UTM33N projection in metres, red grid = WGS84 projection in decimal degrees.

Figure 1.2: Localities on and around Blomstrandhalvøya, with 50 m contour intervals (map data © Norwegian Polar Institute). Grey grid = UTM33N projection in metres, red grid = WGS84 projection in decimal degrees.

1.3 Previous work on Blomstrandhalvøya and Kongsfjorden

Despite the close proximity of Blomstrandhalvøya to the settlement and research infrastructure of Ny-Ålesund (Figure 1.1), few publications exist documenting the Quaternary geology or glacial history specific to the area, however some key works are outlined below.

1.3.1 Regarding Quaternary geology

Vivian (1965) was among the earliest Quaternary geologists to publish from Blomstrandhalvøya, with an interest in dead-ice topography, he mapped and theorised the mass wastage events occurring on

the north of the island and linked them to melt-out of buried ice from Blomstrandbreen (see Figure 4.15). Contemporaneous to Vivian (1965), Herz and Andreas (1966a, 1966b) mapped the periglacial landforms in 1:10,000 scale on Irgensfjellet and the southeast of Blomstrandhalvøya (Figure 1.3), the authors also observed and monitored solifluction and cryoturbation processes. Paul and Evans (1974) observed the surge-type landform assemblage in the forefield of Blomstrandbreen, on the north of the island.

Bogen and Bønsnes (2003) and Krawczyk and Pettersson (2007) monitored fluvial activity in the Londonelva catchment on Blomstrandhalvøya (Figure 1.2), and estimated the denudation rate from dissolved solutes and transported sediments from automatic stations located at Jakobskjelda waterfall (Figure 1.2, Figure 4.9b). Lauritzen (2006) conducted a detailed study on the caves and karst system on Blomstrandhalvøya, identifying numerous active and relict karst and sea caves, as well as springs and dolines, and also dating of speleothems via Uranium-series dating. In July–August 2014, a team of geomorphologists led by Dr Tommaso Piacentini observed the Holocene rockfall activity on Blomstrandhalvøya and Ossian Sarsfjellet, producing some geomorphological maps of the area which are yet unpublished.

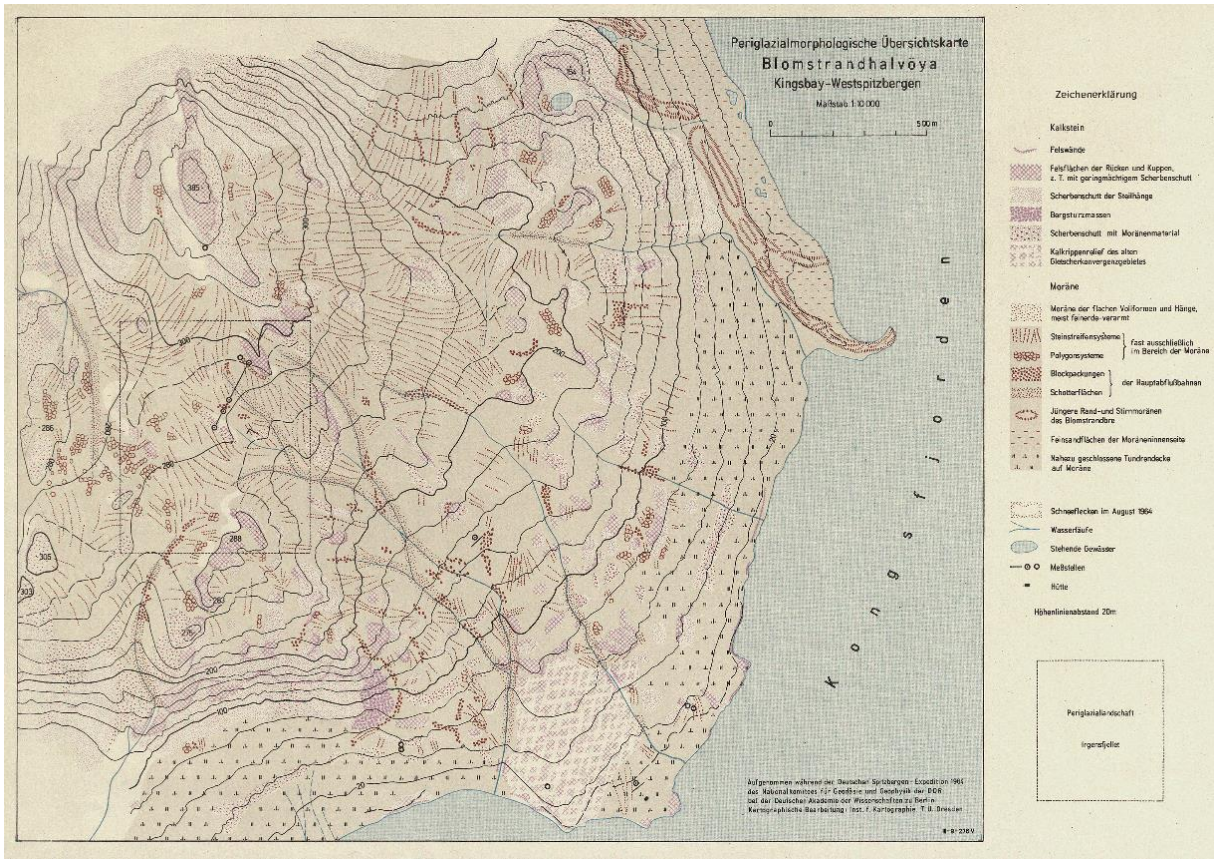

Figure 1.3: Map of the periglacial geomorphology of southeast Blomstrandhalvøya, detailing the abundance of cryoturbation features including stone stripes, polygon systems, block packs and gravel plains, as well as weathered bedrock, talus slopes and fluvial channels (Herz & Andreas 1966a).

1.3.2 Regarding glacial reconstructions

Lehman and Forman (1992) reconstructed the deglaciation of Kongsfjorden following the Late Weichselian Glacial Maximum, based on raised beaches and sediment stratigraphy, the authors proposed a two-step deglaciation with a stillstand or readvance in the Younger Dryas. Henriksen *et al.* (2014) used ^{10}Be cosmogenic surface exposure dating on erratic boulders from Kongsfjordhallet to reconstruct the deglaciation of the fjord, and identified the changing flow regime of the Kongsfjorden Ice Stream, as well as advances from local glaciers in the late Younger Dryas to Preboreal.

Liestøl (1988) and Streuff *et al.* (2015) focused on the late Holocene, Little Ice Age, and surge activity of glaciers in Kongsfjorden, with the latter analysing submarine landform assemblages from high resolution bathymetry data from the inner fjord (Streuff *et al.* 2015). Howe *et al.* (2003) and Maclachlan *et al.* (2010) combined swath bathymetry and seismic interpretation to study the submarine landforms and sediment thickness in the mid- to outer-fjord, Figure 1.4 provides a compilation of the swath bathymetry data from Kongsfjorden (Streuff 2013).

On Blomstrandhalvøya, Myers (2013) conducted a provenance study from erratic boulders, identifying a source area over central northwest Spitsbergen for boulders deposited during the Late Weichselian. In 2013, Dr Endre Før Gjermundsen sampled, and Dr Jason Briner dated, erratic boulders on the summits of Blomstrandhalvøya (Irgensfjellet, Bratliekollen, and Blomstrandsalen, see Figure 1.2) for ^{10}Be cosmogenic exposure dating, two of the exposure dates (68-BRATLIE and 69-IRGENS) are incorporated in this study.

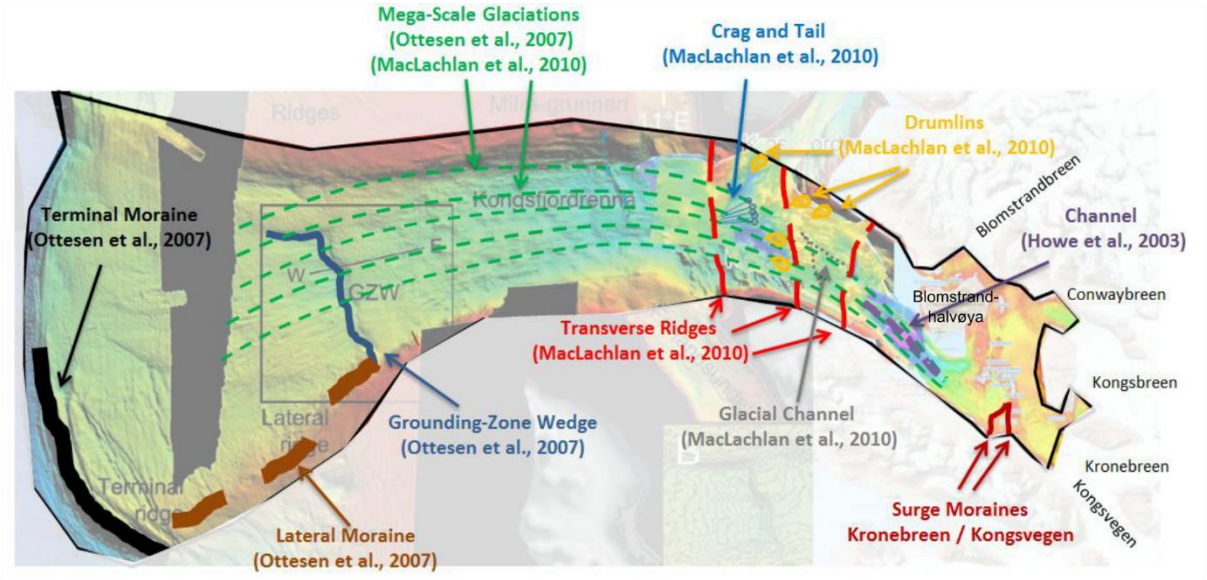

Figure 1.4: Compilation of the submarine landforms from Kongsfjorden and Kongsfjordrenna cross-shelf trough, from Howe *et al*. (2003), Ottesen *et al*. (2007), Maclachlan *et al*. (2010), and Streuff (2013), modified from Streuff (2013).

1.4 Cosmogenic nuclide dating in ice sheet reconstruction

Cosmogenic nuclides, such as ^{10}Be, allow for the direct dating of glacial landforms and deposits (Gosse & Phillips 2001), which is particularly beneficial in a High Arctic setting. Low biological productivity reduces the applicability of radiocarbon dating, and suitable material for luminescence dating is sparse (Alexanderson *et al.* 2014). Glacial erosion and transport generally produces freshly exposed rock surfaces as both boulders and bedrock, which are optimal for cosmogenic nuclide dating, as the initial exposure following ice retreat allows for the accumulation of cosmogenic nuclides (Ivy-Ochs & Briner 2014), the timing of which can be dated by measuring the ^{10}Be/^{9}Be ratio, calculating the ^{10}Be isotope concentration and dividing by a calculated production rate (Dunai & Lifton 2014).

The optimum sampling strategy for obtaining reliable exposure ages is to target boulders perched directly on bedrock (Dunai 2010; Alexanderson *et al.* 2014; Ivy-Ochs & Briner 2014), given the increased likelihood for nuclide inheritance in bedrock (producing too-old ages), and post-depositional movement of boulders on slopes and sediments (producing too-young ages) (Ivy-Ochs & Briner 2014). Sampling on vertical and lateral transects allow for the reconstruction of ice sheet thinning and retreat (Stone *et al.* 2003; Alexanderson *et al.* 2014; Ivy-Ochs & Briner 2014), and was used in northwest Spitsbergen to delimit the downwasting and geometry of the Late Weichselian ice sheet (Gjermundsen *et al.* 2013; Hormes *et al.* 2013; Landvik *et al.* 2013). No other available dating method can provide insights into paleoglacier dynamics in three dimensions as can cosmogenic nuclide exposure dating (Ivy-Ochs & Briner 2014).

The abundance of perched boulders at varying elevations on Blomstrandhalvøya and Ossian Sarsfjellet provide an ideal location for reconstructing the thinning and lateral retreat of the Kongsfjorden Ice Stream through ^{10}Be surface exposure dating. The long half-life of the ^{10}Be isotope (1.36 Ma (Nishiizumi *et al.* 2007)) and sufficiently high production rate make it a suitable target isotope for dating Late Glacial deposits despite its low abundance, given the recent advances in accelerated mass spectrometry for measuring atoms (Christl *et al.* 2014). The ^{10}Be/^{9}Be detection limit is as low as $<1 \times 10^{-15}$ (Maden *et al.* 2007; Xu *et al.* 2010; Matsubara *et al.* 2014). Thus the precision of the method and comparison to published data from the fjord should permit speculation as to the dynamic behaviour of the paleo-ice stream during retreat, and may be extrapolated to the nature of the Svalbard-Barents Sea deglaciation.

Detailed field mapping is a prerequisite for cosmogenic nuclide dating (Dunai 2010; Ivy-Ochs & Briner 2014), and is required to provide physiographic context to sampled boulders, necessary for later interpretation, as provenance, post-depositional movement, shielding and burial must be accounted for. The Quaternary geological mapping conducted for this study provides the geographic context for

the sampled boulders, and also provides an overview of land-forming processes related to glaciation and deglaciation, thus the exposure ages provide a chronological framework for outcome of mapping, while mapping provides a physiographic setting for exposure dating, and therefore both components are mutually beneficial.

2. Theoretical background and geological framework

2.1 Geological overview of site

2.1.1 Bedrock geology

Kongsfjorden is a ca. 27 km long, 4 to 5 km wide, and up to 400 m deep glacial fjord located on a tectonic boundary between the Northwestern Basement Province of Svalbard to the north-east, and the Tertiary fold-thrust belt to the southwest (Bergh *et al.* 2000; Svendsen *et al.* 2002). The medium to high-grade metamorphic marble of Blomstrandhalvøya belongs to the Middle Proterozoic Generalfjella Formation (A in Figure 2.1b) (Gee & Hjelle 1966; Hjelle 1979; Hjelle *et al.* 1999), which is part of the pre-Devonian (Caledonian) Hecla Hoek basement complex (Isachsen & Hoel 1913; Thiedig 1988; Buggisch *et al.* 1994).

The lower marbles consist of dolomite marbles with intercalations of graphitic quartz-calcite schist and quartzite (Kempe 1989), and the upper marbles are predominantly calcite and dolomite marbles (Niehoff 1989), also present are blue-grey calcareous to dolomitic schistose limestones (Thiedig 1988). Brecciated marbles occur frequently (Gjelsvik 1974), particularly to the west of the island where red iron oxide staining occurs in joints and calcite veins (Siggerud 1963; Kempe 1989; Niehoff 1989; Thiedig & Manby 1992; Piepjohn 1997), and reflect surface weathering below a pre-Devonian peneplain (Gjelsvik 1974; Thiedig & Manby 1992).

Red conglomerates of Lower Devonian age unconformably overly the marbles of the Generalfjella Formation, and are found in narrow grabens between thrust/reverse faults on Blomstrandhalvøya (Figure 2.1) (Gjelsvik 1974; Thiedig & Manby 1992). The general strike of faults on Blomstrandhalvøya is N–S deriving from Caledonian deformations, with phases of isoclinal folding and latter post-metamorphic crenulation (Thiedig & Manby 1992; Kempe *et al.* 1997). Compressive Late Devonian or Early Carboniferous Svalbardian Deformation preceded the karstification of Blomstrandhalvøya (Buggisch *et al.* 1994), and Tertiary orogeny further deformed the marbles (Siggerud 1963).

The north–south trending bands of marble on Ossian Sarsfjellet (Figure 2.1) are considered correlatives of the marble on Blomstrandhalvøya given the common reddish staining (Hjelle *et al.* 1999) and may represent tectonically repeated components of the Generalfjella Formation interlayering the mica schist, quartz phyllites, and albite-quartz phyllites of the Signehamna Formation (Orvin 1934; Siggerud 1963; Gee & Hjelle 1966).

2.1.2 Source area for erratics

A possible source area for the frequent occurrence of biotite-rich grey granite and granitic erratic boulders found on the field area is the Smeerenburgfjorden Complex (C in Figure 2.1b) (Ohta *et al.* 2002; Myhre *et al.* 2008; Myers 2013), with a band of post tectonic granites, granodiorites, aplite and pegmatite, running N–S from Lilliehöökbreen and outcropping at Stemmeknausane (Siggerud 1963; Gee & Hjelle 1966; Dallmann 2012), ca. 15 km east of Blomstrandhalvøya. Weakly foliated late tectonic grey granites are found closely associated with migmatites in northwest Spitsbergen (Hjelle 1979), the most likely source area for granitic erratics found on Blomstrandhalvøya and Ossian Sarsfjellet is east of Krossfjorden-Möllerfjorden, given that the other outcrops of grey granite and migmatite are northwest of Krossfjorden (Hjelle 1979).

Mica schist perched boulders are frequently found on Blomstrandhalvøya and Ossian Sarsfjellet, and likely derive locally from the Signehamna Formation found on Ossian Sarsfjellet (B in Figure 2.1) (Orvin 1934; Siggerud 1963; Gee & Hjelle 1966; Hjelle *et al.* 1999). Red conglomerate boulders of Devonian age are also observed on Blomstrandhalvøya, and may be products of local outcrops (Gjelsvik 1974; Thiedig & Manby 1992) or be further travelled from the Wood Bay Formation, found predominantly in northern Spitsbergen (D in Figure 2.1) (Friend & Moody-Stuart 1972).

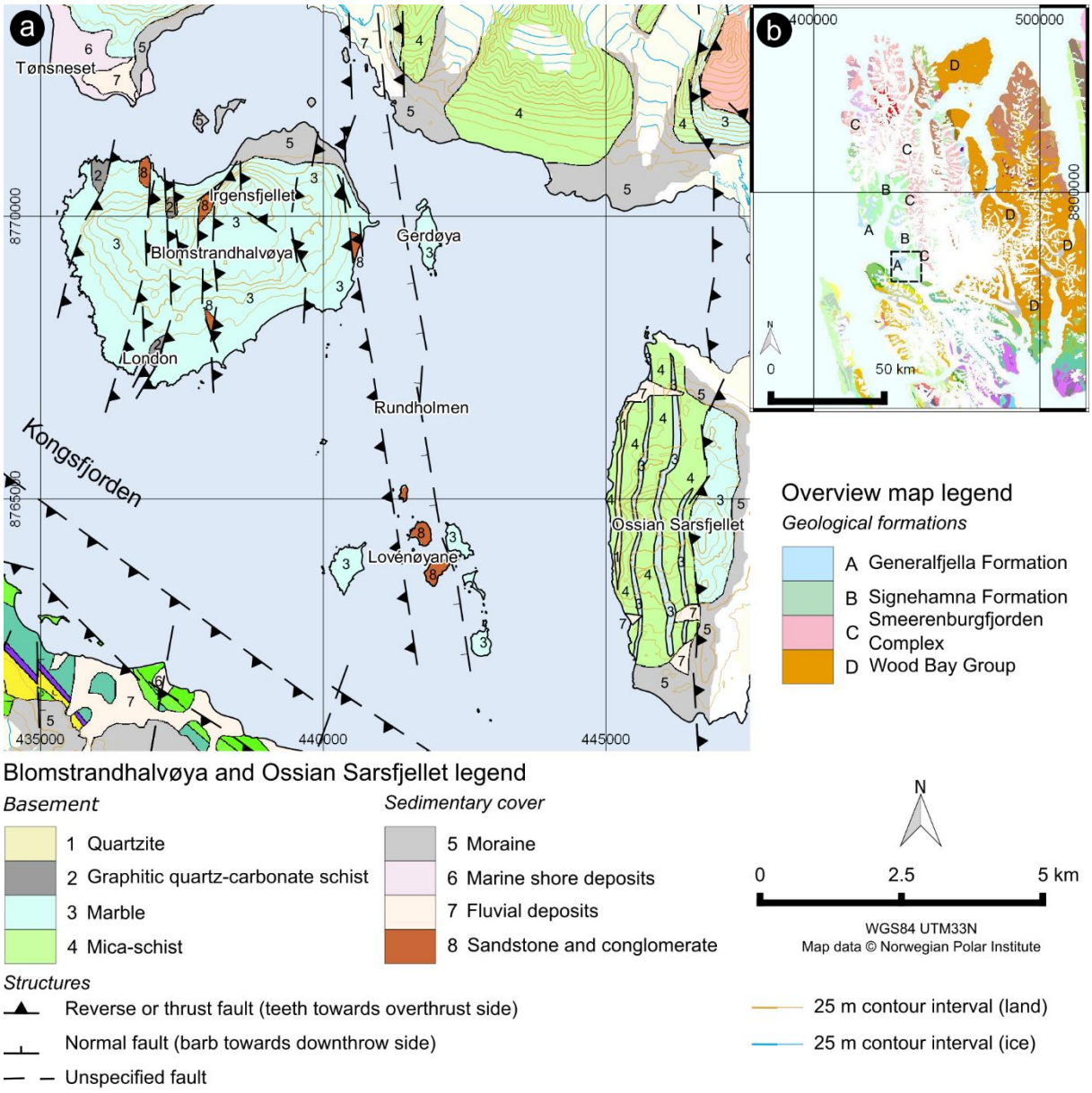

Figure 2.1: (a) Simplified geological map of inner-Kongsfjorden, with the main geological units, sedimentary cover, and tectonic structures displayed, modified from Hjelle *et al.* (1999). (b) inset map displaying the geological formations in northwest Spitsbergen, highlighting the key formations discussed in the text, modified from Web Map Service data (Norwegian Polar Institute 2016).

2.1.3 Commercial interests

The marble in Kongsfjorden was first recognised by William Scoresby Jr around 1818 (Scoresby 1820), and Christian Wilhelm Blomstrand described, in some detail, the marble and cave systems in Kongsfjorden following an expedition in 1861 (Blomstrand 1864), after whom Blomstrandbreen and Blomstrandhalvøya were named. The marble did not attract great commercial interest until the early 20th Century, when the Northern Exploration Company Limited of London (N.E.C.) staked a claim to Blomstrandhalvøya, or "Marble Island" as it was romanticised, following its rediscovery as a

commercial opportunity by Ernest Mansfield in 1906 (Figure 2.2a) (The Northern Exploration Company 1911). The N.E.C. began building in the summers of 1912 and 1913, with the construction of; a quay, footpaths, cabins, engineering sheds, and railroads, plus the installation of cranes and large steam powered channelling equipment centred around the new settlement of Ny-London (Figure 2.2b) (The Northern Exploration Company 1913). Marble samples were appraised by experts in the United Kingdom and abroad, with a positive consensus regarding their structural integrity and aesthetic qualities (Figure 2.2c), and valuations exceeding £250 billion (in present value) for the entire island (The Northern Exploration Company 1914).

Despite the glowing appraisals and enthusiasm of the N.E.C., virtually no marble was quarried from Blomstrandhalvøya, early commentators suggested that the permafrost conditions were maintaining the structural integrity of the brecciated marble, and so slabs crumbled on transport (Hagerup 1912; Hoel 1966). Experimental evidence performed by Siggerud (1963) however, shows no decrease in strength from marble samples exposed to fluctuating temperatures (-5 to +50°C), and no increase in weight when soaked in water, indicating that the Blomstrandhalvøya marbles have low porosity and are not susceptible to frost action (Siggerud 1963). It appears more likely that the heavily brecciated marbles on Blomstrandhalvøya were difficult to work into large slabs because of the N–S trending and intersecting schistosity and brittle fabrics caused the rock to crumble (Thiedig 1988).

It should also be considered that the N.E.C.'s activity on Blomstrandhalvøya was curtailed by the outbreak of WWI in 1914, combined with rising extraction costs and falling demand for marble in Europe, this led to financial hardship further compounded by the companies failed attempt to restart quarrying in 1919, hampered by plundered and sabotaged equipment (Barr *et al.* 2012). The signing of the Svalbard Treaty in 1920 led to the dissolution of the N.E.C., as their land claims were purchased by the Norwegian Government, Ny-London was subsequently dismantled, with recoverable materials used in the coal mines of Ny-Ålesund (Barr *et al.* 2012; Kruse 2014). The remnants of Ny-London are now regarded as cultural heritage, and a significant quantity of construction materials, quarrying machinery (Figure 2.2d), and test pits/boreholes are found in the southwest of Blomstrandhalvøya.

Figure 2.2: (a) Ernest Mansfield, "discoverer" of the Blomstrandhalvøya marbles and co-founder of the Northern Exploration Company Limited, standing with the original claim post on the island ca. 1906 (The Northern Exploration Company 1913), (b) the steam powered channelling equipment in operation, quarrying marble on Blomstrandhalvøya in 1912 (The Northern Exploration Company 1913), (c) the highest value marble variety, Nordern Lys No.1, valued at ca. £2500 per m^3 (present value) (The Northern Exploration Company 1914), and (d) some remnants of Ny-London, with the channelling machinery in the background (Photo: O. Grant).

2.1.4 Quaternary geology

Kongsfjorden is largely covered by Quaternary sediments, with glacial, littoral, marine and alluvial sediments interfingering at the coastal cliffs of Kongsfjordhallet on the northern shore of Kongsfjorden (Boulton 1979; Houmark-Nielsen & Funder 1999; Peterson 2008; Henriksen *et al.* 2014), where the oldest glacial sediments (>1 Ma) are found on Svalbard (Houmark-Nielsen & Funder 1999). Glacial, littoral, and marine sediments are also found in succession on the southern shore on Kongsfjorden, at Brandalpynten on the Brøggerhalvøya peninsula (Lehman & Forman 1992). Raised beaches and elevated shorelines are found in the vicinity of Kongsfjorden (Forman & Miller 1984; Forman *et al.* 1987; Miller *et al.* 1989; Forman 1990; Lehman & Forman 1992), with elevations up to 80 m at Kvadehuksletta, and dated up to ca. 290 ka (Forman & Miller 1984), raised marine features have been utilised to reconstruct the sea level and isostatic uplift history of the fjord, particularly since the Late Weichselian (Forman *et al.* 1987; Forman 1990; Lehman & Forman 1992).

Slope processes are observed within Kongsfjorden, with colluvial processes leading to talus slopes, protalus ramparts and talus-derived rock glaciers (Svendsen *et al.* 2002). Periglacial processes have also led to the extensive formation of patterned ground, solifluction lobes and mudboils (Herz & Andreas 1966a; Van Vliet-Lanoë 1988). Rockfalls have been a common occurrence through the Holocene (André 1997), most likely initiated by glacier debuttressing exposing formerly glaciated landscapes to an unstable state (Ballantyne 2002). Alluvial and glaciofluvial processes have developed large prograding delta systems distal to the tidewater glaciers in the fjord, with 4.5 x 10^6 m^3 sediment deposited in front of Kongsvegen between 1975 and 1983 (Svendsen *et al.* 2002). Dissolution of the Generalfjella Formation marble (Figure 2.1) and limestone in Kongsfjorden has led to karstification, with active and relict karst and sea-caves, bogaz forms, karst corridors, dolines and springs (Svendsen *et al.* 2002; Lauritzen 2006; Dallmann *et al.* 2015).

2.2 Geographic overview

2.2.1 Climatic setting of Kongsfjorden

The mean annual air temperature is between -4 to -5°C (Svendsen *et al.* 2002; Lauritzen 2006), ranging from a mean of +5°C in July, to -15°C in February (Svendsen *et al.* 2002). Mean annual precipitation is ca. 430 mm a^{-1}, with a range from 18 mm in June to 46 mm in September, and is approximately twice that measured at Longyearbyen (Killingtveit *et al.* 2003). Precipitation as snow is common between 8 to 10 months of the year (Table 4.2), with the greatest recorded mean depth generally occurring in April (Norwegian Meteorological Institute 2016). Kongsfjorden, at 79° N, is within the zone of continuous permafrost (Zhang *et al.* 1999; Humlum *et al.* 2003), aggrading to a depth of ca. 140 m recorded from a borehole close to Ny-Ålesund, and up to 400 m elsewhere in the fjord (Liestøl 1977).

The prevailing wind direction in Kongsfjorden is largely governed by topographic steering, with katabatic winds transporting cold dense air from the internal ice caps, flowing at 120° (east–southeast) from fjord head to mouth (Svendsen *et al.* 2002). The Polar Day occurs between 18th April and 23rd August in Kongsfjorden, during which period solar radiance is highly variable due to often persistent cloud and fog (Svendsen *et al.* 2002). The Polar Night occurs between 25th October and 17th February, the thickest sea ice is achieved in February but is typically slower growing and thinner (mean thickness ca. 0.7 m) than found in other high-Arctic settings (Gerland & Hall 2006).

2.2.2 Oceanographic setting of Kongsfjorden

Kongsfjorden is situated close to the northern maximum of the Western Spitsbergen Current, which transports a large amount of heat (35 to 70 TW) northwards from the Norwegian Sea in the form of warm saline Atlantic Water (Figure 2.3) (Svendsen *et al.* 2002). The strength of the West Spitsbergen Current has a significant bearing on the climatic conditions of Svalbard, and particularly western Spitsbergen (Hald *et al.* 2004), with the restricted growth of sea ice, atmospheric heat flux, and source of precipitation strongly tied to the strength of the North Atlantic Oscillation index (Svendsen *et al.* 2002). A large temperature and precipitation gradient exists across an east-west profile over Svalbard (Humlum 2002), owing to the warm (>3°C) and saline (>34.65 PSU) Atlantic Water to the west, and colder (-1.5 to 1.0°C) and fresher (34.3 to 34.8 PSU) Arctic and Polar Water to the east (Figure 2.3) (Cottier *et al.* 2005).

The oceanic circulation within the Kongsfjorden trough varies widely intra-annually, with the intrusion of Atlantic Water at intermediate depths in midsummer aided by northerly winds, while in winter, Arctic Water dominates (Cottier *et al.* 2005). The strong seasonality in the oceanography of Kongsfjorden is further amplified by seasonal melt of the tidewater glaciers in the fjord, leading to a strongly stratified water column and reduced surface currents (Svendsen *et al.* 2002) with a well-developed halocline in the inner-fjord (Elverhøi *et al.* 1983). Due to the strong summer brackish pycnocline, deep water circulation in the fjord acts almost independently of upper layer flow (Svendsen *et al.* 2002).

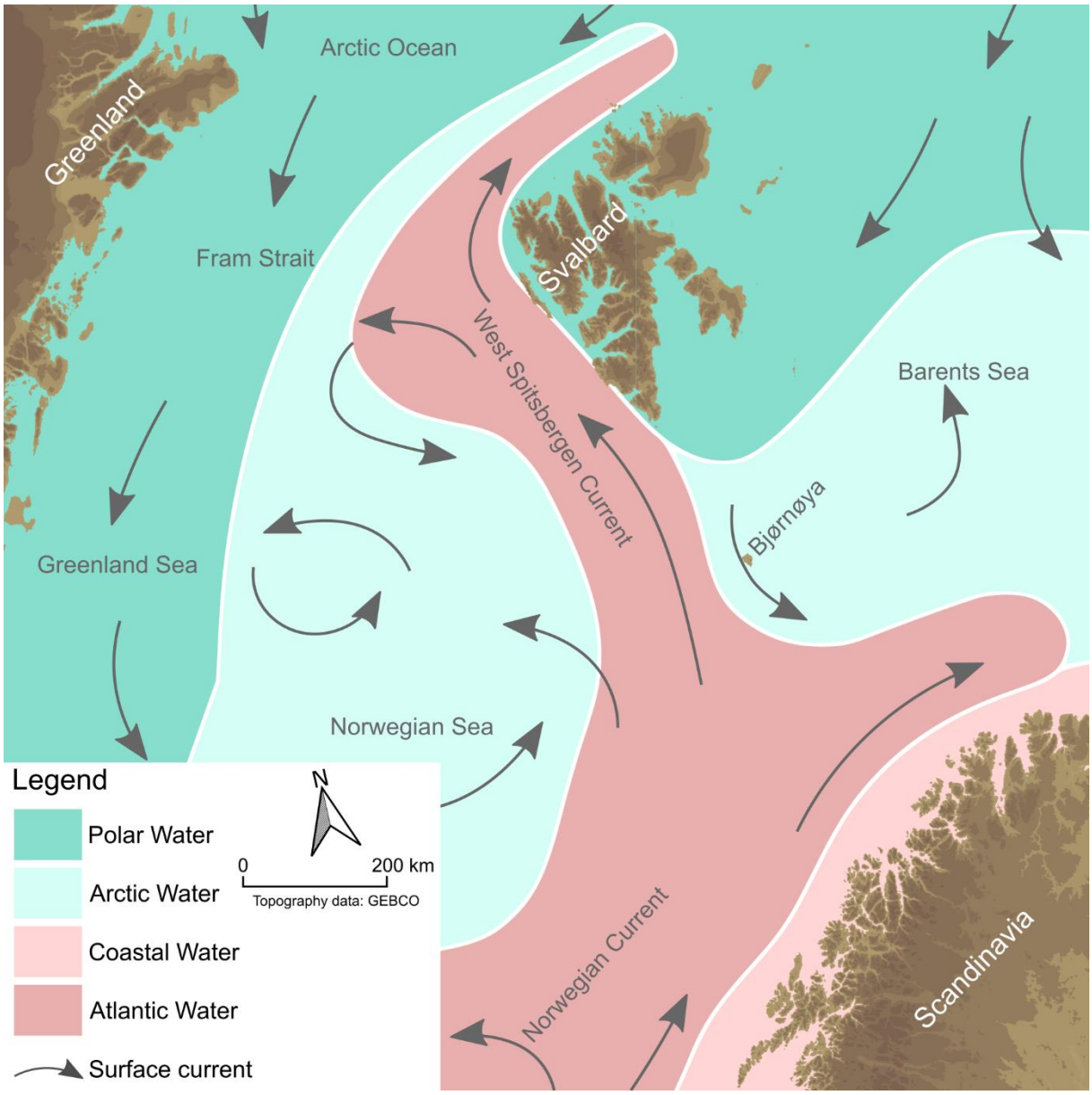

Figure 2.3: Surface water masses and surface currents in the vicinity of the Svalbard archipelago, modified from Hald *et al*. (2004) and Phillips *et al*. (Submitted for review).

2.3 Glacial history of the Svalbard-Barents Sea Ice Sheet

The western Svalbard slope consists of Late Pliocene and Quaternary sediments, with a series of trough-mouth fans and inter-fan areas overlying bedrock (Jessen *et al.* 2010), the sediments record the glacial inception of Svalbard from ca. 2.7 Ma (Mattingsdal *et al.* 2014), with first shelf-edge glaciation in the early- to mid-Pleistocene at ca. 1.5 Ma (Rebesco *et al.* 2014), and topographically focused ice streams became the dominant ice sheet mechanism for erosion and deposition with profound effect in last ca. 0.7 Ma (Patton *et al.* 2015).

At least four major glaciations have occurred in the Barents Sea region in the late Quaternary (last ca. 160 ka) (Patton *et al.* 2015). From the Late Saalian glaciation at Marine Isotope stage 6 (MIS 6) (Mangerud *et al.* 1998; Mangerud *et al.* 2001; Svendsen *et al.* 2004) there has been ice stream activity at MIS 5d at ca. 110 ka, MIS 4 at ca. 60 ka, and MIS 2 at ca. 20 cal ka (Mangerud *et al.* 1998).

The Late Weichselian glaciation of the Barents Sea began from ca. 32 ka (Andersen *et al.* 1996; Landvik *et al.* 1998; Siegert *et al.* 2002), and growth was rapid considering continental shelves were ice-free at the end of the Middle Weichselian (Mangerud *et al.* 1998). Warm Atlantic water was advected into the Norwegian Sea as far north as Spitsbergen (Figure 2.3) between 27 and 22.5 ka, providing a regional moisture source for rapid accumulation (Müller & Stein 2014). Competing theories exist for the build-up of the marine ice sheet, with thickening sea ice (Denton & Hughes 1981; Hughes 1987), versus ice accumulation on subaerially exposed islands caused by falling sea level (Kvasov 1978; Elverhøi *et al.* 1993; Howell *et al.* 2000).

The Late Weichselian Svalbard-Barents Sea Ice sheet was configured of two components, with the marine-based portion over the Barents Sea and convergent with the Fennoscandian Ice Sheet (Winsborrow *et al.* 2010), and local ice-domes over Svalbard (Mangerud *et al.* 1992). The growth and decay was out of phase, but the two components were contiguous during the Glacial Maximum (Mangerud *et al.* 1992). The maximum extent of the Svalbard-Barents Sea Ice Sheet during the Late Weichselian is reconstructed from isostatic uplift models, with the centre of uplift close to Kongsøya, eastern Svalbard (Figure 1.1b), indicating maximum ice thickness for a concentric single-dome ice sheet between 2000 to 3000 m (Lambeck 1996; Landvik *et al.* 1998; Forman *et al.* 2004), although Svendsen *et al.* (2004) suggest thinner ice with a maximum thickness of 1800 m.

A lack of terrestrial evidence was found to support an extensive glaciation of Svalbard in the Late Weichselian, given the preservation of delicate landforms such as raised beaches, subsequently the minimalist argument for restricted terrestrial ice caps and ice free areas during the last Glacial Maximum was advocated by a number of authors (Salvigsen 1977; Boulton 1979; Salvigsen 1979; Troitsky *et al.* 1979; Salvigsen & Nydal 1981; Boulton *et al.* 1982; Miller 1982; Salvigsen & Österholm 1982; Forman & Miller 1984; Forman 1989; Miller *et al.* 1989; Boulton 1990; Andersson *et al.* 1999; Houmark-Nielsen & Funder 1999; Andersson *et al.* 2000). However, the raised beaches around the Svalbard archipelago pointed to an extensive glaciation, and so the maximalist argument for shelf-edge glaciation with preservation beneath cold-based ice was maintained (Schytt *et al.* 1968; Grosswald 1980; Denton & Hughes 1981; Landvik *et al.* 1987; Mangerud *et al.* 1987; Mangerud *et al.* 1992; Svendsen *et al.* 1992; Landvik *et al.* 1998; Landvik *et al.* 2005; Ingólfsson & Landvik 2013).

The maximalist argument was corroborated by the identification of trough-mouth fans and streamlined mega-scale glacial features on the western Svalbard slope (Figure 2.4a) (Vorren *et al.* 1989; Ottesen *et al.* 2007). The general consensus now supports the maximalist argument for shelf-edge glaciation and an ice stream inter-ice stream configuration for the Late Weichselian Svalbard-Barents Sea Ice Sheet (Ingólfsson & Landvik 2013).

The configuration of the ice sheet over Svalbard has been reconstructed to show a complex multi-dome arrangement, via cosmogenic exposure dating (Hormes *et al.* 2011; Gjermundsen *et al.* 2013; Hormes *et al.* 2013; Landvik *et al.* 2013), and bathymetric profiling (Dowdeswell *et al.* 2010; Hogan *et al.* 2010), with fast-flowing ice streams bounded by slower moving cold-based or periodically active ice (Ottesen *et al.* 2007; Dowdeswell *et al.* 2008; Ottesen & Dowdeswell 2009; Landvik *et al.* 2013; Landvik *et al.* 2014). Cold-based ice during late Quaternary glaciations led to minimal erosion of the alpine topography in northwest Spitsbergen, channelising erosion in ice streams (Gjermundsen *et al.* 2015).

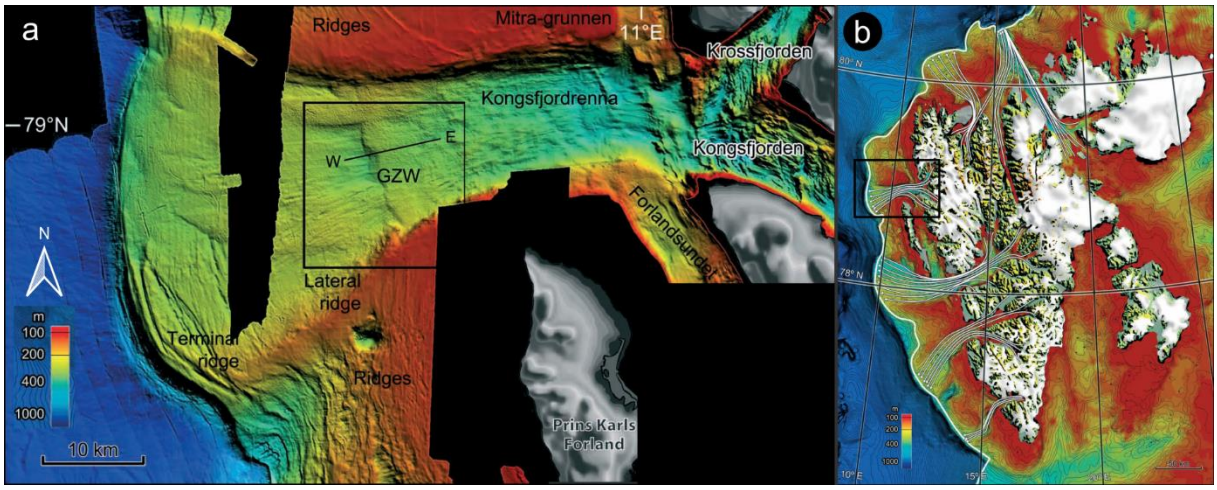

Figure 2.4: (a) Swath bathymetry from Kongsfjordrenna cross-shelf trough, with mega scale lineations, grounding zone wedges, lateral ridges and terminal moraine, (b) the location of the Kongsfjordrenna trough and paleo-ice flow direction, and the location of paleo-ice streams around Spitsbergen. Modified from Ottesen *et al.* (2007) and Ingólfsson and Landvik (2013).

2.4 Glacial history of Kongsfjorden

As an outlet for Svalbard-Barents Sea Ice Sheets, Kongsfjorden has been repeatedly glaciated in the Quaternary, with the stratigraphy and Kongsfjordhallet revealing an Early Pleistocene glaciation (>1 Ma), an Early Weichselian glaciation (ca. 91 ka), and a Late Weichselian glaciation (Houmark-Nielsen & Funder 1999).

2.4.1 Late Weichselian

The extent of the Late Weichselian glaciation in Kongsfjorden has been subject to debate, and used as evidence for the minimalist argument for Svalbard-Barents Sea glaciation. Forman (1989), Lehman and Forman (1992), and Houmark-Nielsen and Funder (1999) proposed that the Late Weichselian glaciation of Kongsfjorden was restricted to the trough, with the possibility of an ice tongue extending beyond the fjord mouth, thus leaving ice-free areas around coastal northwest Spitsbergen. Ice-free areas were consistent with the preserved raised beaches on Brøggerhalvøya and other areas in northwest Spitsbergen (Forman & Miller 1984). By contrast, Mangerud *et al.* (1992) argued that glaciomarine clay above till dated to ca. 15 cal ka BP from the continental shelf west of Spitsbergen proved shelf-edge glaciation.

It is now widely accepted that the Late Weichselian glacial advance reached the shelf break west of Kongsfjorden at ca. 24 cal ka BP (Landvik *et al.* 1998; Landvik *et al.* 2005; Jessen *et al.* 2010), and submarine morphology, including mega-scale glacial lineations, lateral moraines, and grounding zone wedges found in the Kongsfjordrenna Trough point to fast-flowing ice streaming through the Kongsfjorden-Krossfjorden system during the Late Weichselian (Figure 1.4, Figure 2.4a, and Figure 5.3) (Ottesen *et al.* 2005; Ottesen *et al.* 2007; Dowdeswell *et al.* 2008; Maclachlan *et al.* 2010; Ingólfsson & Landvik 2013; Dallmann *et al.* 2015). Retreat from the shelf-edge began at ca. 20.5 ka (Jessen *et al.* 2010) and reached the fjord mouth by ca. 16.3 ka (Landvik *et al.* 2005), by which time the Kongsfjorden Ice Stream had stabilised as a topographically bounded outlet glacier terminating close to the mouth of the fjord (Henriksen *et al.* 2014).

2.4.2 Younger Dryas

Traces of Younger Dryas ice marginal positions on Svalbard are sparse (Mangerud *et al.* 1992; Svendsen *et al.* 1996; Landvik *et al.* 1998; Patton *et al.* 2015), however, Lehman and Forman (1992) suggested that the suppressed marine limit between ca. 14.0 and 11.6 cal ka BP observed on Blomstrandhalvøya and inner Kongsfjorden (Figure 2.5) indicated a Younger Dryas stillstand or slight readvance in Kongsfjorden. Skirbekk *et al.* (2010) interpreted ice proximal conditions up to ca. 11.5 to 10.6 cal ka BP in a core from mid-Kongsfjorden, with an observed peak flux in dropstones at ca. 11.5 cal ka BP.

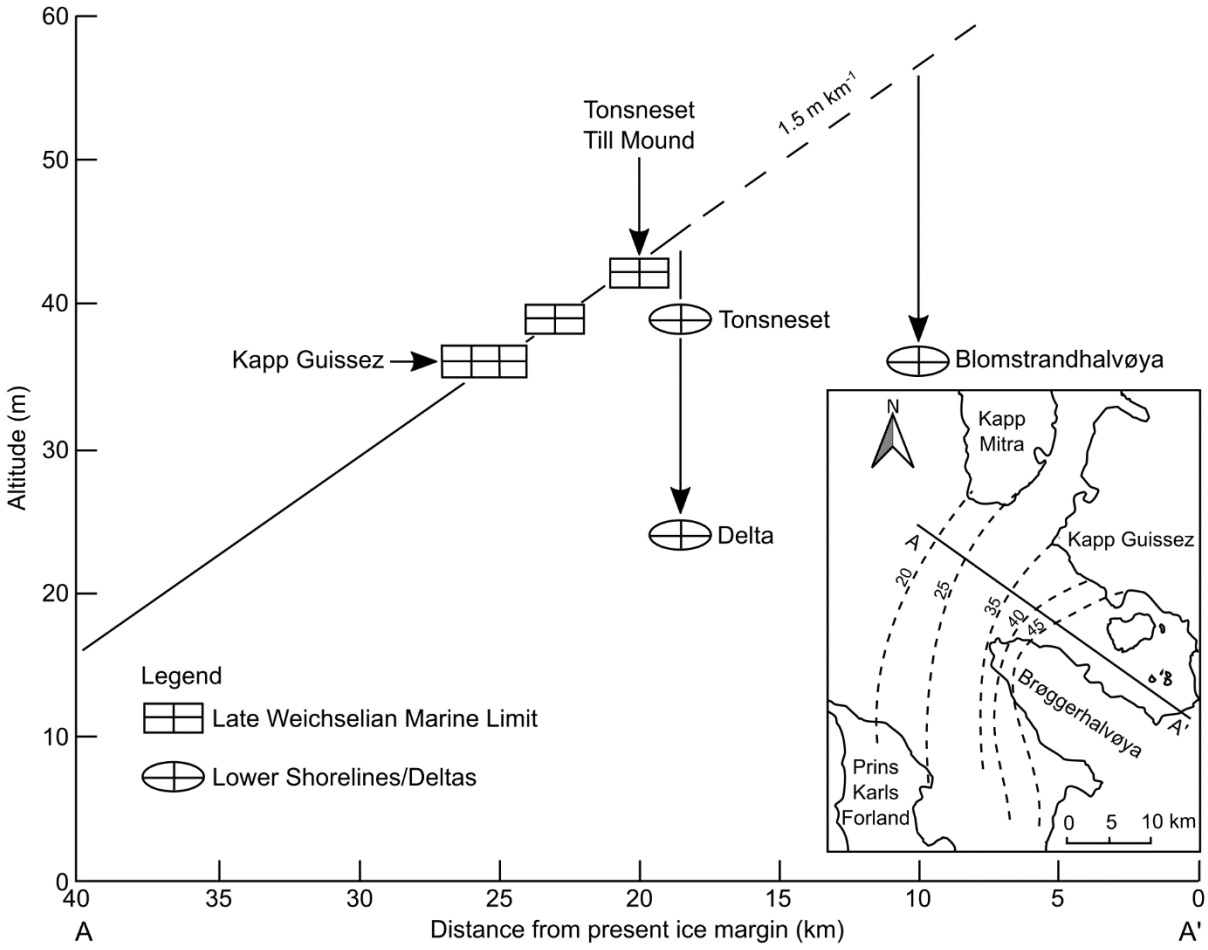

Figure 2.5: Late Weichselian Marine Limit along profile A'–A in Kongsfjorden, with regional isobases (m) presented in the inset map from Lehman and Forman (1987) and Forman (1990), modified from Lehman and Forman (1992).

2.4.3 Neoglacial and Little Ice Age

Evidence is emerging for a Neoglacial retreat centred on ca. 1.3 ka in western Spitsbergen (Reusche *et al.* 2014; Gislefoss 2015; Phillips *et al.* Submitted for review) suggesting an advance larger than the Little Ice Age (LIA) occurred during the mid- to late-Holocene (Dylan Rood, personal communication). As yet, no published data from Kongsfjorden suggests a pre-LIA advance, and so the Little Ice Age remains the maximum advance of glaciers in Kongsfjorden since the Younger Dryas (Streuff *et al.* 2015).

The fresh trimlines, ice cored moraines, and submerged end and retreat moraines demarcate the LIA in Kongsfjorden (Mellor 1957; Liestøl 1969), with tidewater glaciers extending up to 5 km beyond their present margins (Liestøl 1988; Streuff *et al.* 2015). Notably, Blomstrandbreen terminated on Blomstrandhalvøya, thus identifying it as a peninsula (halvøy) instead of an island (øy), which it became

in 1992 when the glacier receded (Svendsen *et al.* 2002), the historical name of Blomstrandhalvøya remains and is used throughout this study.

2.4.4 Late Holocene surge activity

All of the tidewater glaciers in Kongsfjorden have been identified as surge-type glaciers, with historically recorded surge activity (Liestøl 1969, 1988). Kronebreen and Kongsvegen surged in 1869 and 1948 respectively (Liestøl 1988; Streuff *et al.* 2015), Kongsbreen surged in 1897 (Streuff 2013), and Blomstrandbreen in 1966 (Sund & Eiken 2010), while the timing of the last surge of Conwaybreen is yet unknown (Farnsworth *et al.* 2016). The surges led to the formation of typical terrestrial and submarine landform assemblages (Evans & Rea 1999), including; crevasse-squeeze ridges, debris lobes (Streuff *et al.* 2015), flutes, and crevasse-fills (Paul & Evans 1974) within the LIA maximum position.

2.5 Types of fast-flowing glacier

Fast flowing glaciers are responsible for the majority of drainage of ice from present day (Truffer & Echelmeyer 2003) and paleo-ice sheets (MacAyeal 1993), including the Svalbard-Barents Sea Ice Sheet (Landvik *et al.* 2005). Ice streams, outlet glaciers, and (Greenlandic) isbræ are referred to in this study, and require clarity.

An ice stream is defined by Truffer and Echelmeyer (2003) as being shallow, with low driving stress (ca. 10 kPa), on a soft bed, and bounded by dynamically less active ice giving narrow lateral shear margins, an archetypal example would be the Whillans Ice Stream in west Antarctica. By contrast, outlet glaciers are steep with a high driving stress (>200 kPa), and are bounded by bedrock in deep troughs, giving lateral and vertical shear, an example of an outlet glacier and Greenlandic isbræ is the Jakobshavn Isbræ in western Greenland (Truffer & Echelmeyer 2003).

The Kongsfjorden paleo-ice stream would likely have shifted on the spectrum of fast flowing glacier types, from an ice stream at the Late Weichselian Glacial Maximum draining out through the Kongsfjordrenna cross-shelf trough (Figure 2.4a) (Ottesen *et al.* 2007; Batchelor & Dowdeswell 2014), to an outlet glacier during retreat, stabilised and bounded by the bedrock topography in Kongsfjorden (Henriksen *et al.* 2014).

3. Materials and methods

3.1 Quaternary geological mapping

3.1.1 Introduction to Quaternary geological mapping

The landforms and sediments produced and reworked by Quaternary glacial and interglacial periods on Blomstrandhalvøya provide a story of environmental development in Kongsfjorden. In order to extract the story from the landscape, it was necessary to map in detail the sediment cover and landforms observed, along with their cross-cutting relationships in order to ascertain relative chronology, with cosmogenic nuclide dating of glacial erratics providing numerical ages for deglaciation.

3.1.2 Mapping in the field

Prior to entering the field, Blomstrandhalvøya was divided into 22 A4 map-slips (Figure 3.1a), with 33 % overlap to the east and south of each map. Quantum GIS 2.4.0 and 2.10.1 (QGIS) was used to produce blank 1:7500 map-slips with 5 m contour intervals extracted from a 5 m resolution digital elevation model (Norwegian Polar Institute 2014), and accompanied by an orthorectified aerial photograph of the mapping site (Figure 3.1b) provided by the Norwegian Polar Institute.

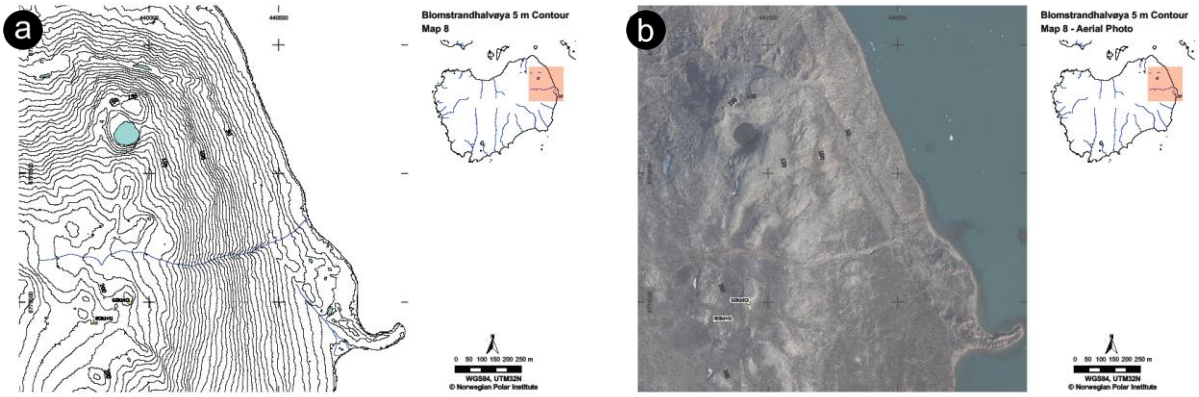

Figure 3.1: (a) Example of 1:7500 blank map-slip with 5 m contour interval with inset showing coverage on Blomstrandhalvøya, and (b) accompanying aerial photograph.

In the field, a handheld global positioning system (GPS) (Garmin Montana 600, Figure 3.2a) was used to aid precise positioning (± 3.65 m) of observed landforms and features, which were plotted onto blank map-slips with colour shading for sediment cover and symbology for landforms. A shovel was used to investigate the surface sediment and also to excavate sedimentary sections where possible,

which were cleaned with a trowel and logged with the aid of a metre rule (Figure 3.2b). Photographs, with scale where possible, were taken of observed landforms and sediments.

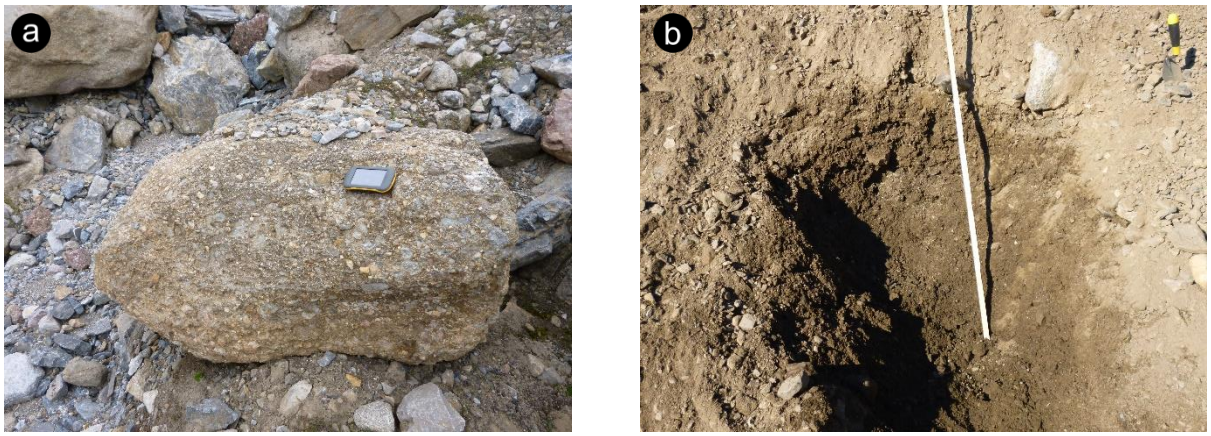

Figure 3.2: (a) Garmin Montana 600 GPS used in the field to aid precision of mapping, and (b) a section excavated with a shovel and cleaned with a trowel prior to logging and photographing.

3.1.3 Proofing and digitising

After returning from the field, each map-slip was inked-in on the accompanying aerial photograph, allowing for cross correlation of in-field observations and features on aerial photographs. The map-slips and inked-in aerial photographs were then scanned (Figure 3.3) and georeferenced with QGIS, and subsequently digitised by tracing boundaries of sediment cover, and plotting observed landforms with unique symbology using the legend from the Norwegian Geological Survey (2015) as a guide. Sediment logs were compiled and digitised with illustrating software (Inkscape 0.91), with drawing of logs and tracing of map boundaries aided by the use of a graphics tablet (Huion H610 PRO).

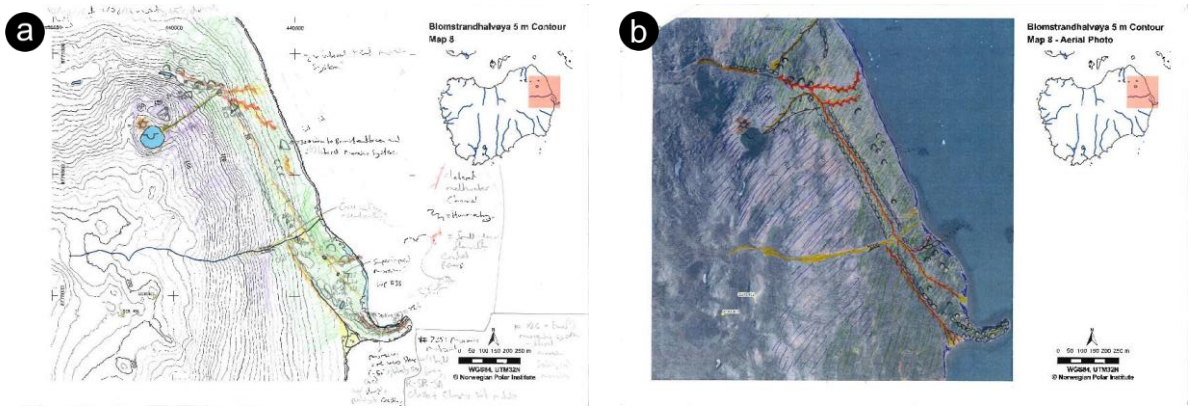

Figure 3.3: (a) Scanned map-slip coloured and symbolised in the field, and (b) accompanying inked-in aerial photograph, ready for digitising with GIS.

3.2 Cosmogenic nuclide dating

3.2.1 Introduction to cosmogenic nuclide exposure dating

Interactions between high-energy radiation, predominantly high-energy neutrons (Hunt *et al.* 2008), and atoms within the mineral lattice of exposed quartz, produces unstable nuclides such as ^{10}Be and ^{26}Al. Measuring the ratio of unstable to stable isotopes (e.g. ^{10}Be/^{9}Be) allows a calculation of unstable isotope concentration and thus the length of exposure (Lal 1991). The geologic ubiquity of quartz, it's tight crystal structure, and simple target chemistry of silicone and oxygen ensure a straightforward theoretical production via spallation of in-situ cosmogenic nuclides such as ^{10}Be from a cosmic source (Kohl & Nishiizumi 1992). Cosmic ray-induced spallation is the predominant nuclear reaction, and accounts for 96.4 % of the ^{10}Be isotope, with the remainder produced by muon capture (Dunai 2010).

^{10}Be has the longest half-life of known terrestrial in-situ cosmogenic nuclides (1.36 Ma (Nishiizumi *et al.* 2007)), but occurs in very low concentrations in the order of 1 x 10^6 atoms per gram of irradiated quartz (Von Blanckenburg *et al.* 1996). It is subsequently necessary to separate, concentrate, and purify quartz from a sample, and extract beryllium in a sequence of physical and chemical steps prior to AMS analysis to avoid various sources of contamination. At present there are no other methods available to directly date an exposed rock surface (Ivy-Ochs & Kober 2008), and cosmogenic nuclide dating is therefore highly suitable for reconstructing deglaciation events from erratic boulders and glacially polished bedrock (Ivy-Ochs & Briner 2014).

3.2.2 Field measurements and sampling

3.2.2.1 Sampling strategy

In order to obtain exposure ages which give the timing and extent of deglaciation, the sampling transects must have a lateral and vertical dimension. Two transects were sampled on Blomstrandhalvøya; BLOM samples were taken from the west of the island on a vertical transect leading to the summit, while GOR samples were obtained from the east and at various elevations. A third transect, SARS, was sampled on Ossian Sarsfjellet at the head of Kongsfjorden, providing lateral extent and a vertical profile.

Prior to sampling, suitable boulders were identified in the field, the criteria for selecting optimal boulders or bedrock is discussed by Gosse and Phillips (2001), and summarised as having; (1) experienced no prior exposure, (2) been continuously exposed in the same position, (3) not been covered, and (4) display minimal surficial weathering or erosion (Ivy-Ochs & Kober 2008). The sampled boulders were true erratics given the difference in lithology, as the bedrock is primarily marble and

mica schist (Figure 2.1a), boulders with non-local lithology, such as granite, were selected. Erratic boulders were sampled as their assumed travel distance infers adequate glacial erosion required to remove any previous exposure signal. Boulders perched on bedrock were desirable, as post-depositional movement and sediment cover is minimised.

Boulders exceeding 1 m^3 were preferentially chosen as their size increased the likelihood that the sample surface was above the surrounding topography during exposure, where snow shielding is reduced (Gosse & Phillips 2001). Surface weathering or erosion was identified through observation of the surface and surroundings of the boulder, pitted or flaking boulders were avoided, and lichen cover was used as an indicator of snow shielding, given the absence of lichen may represent deep or persistent snow cover or enhanced wind abrasion. A further pre-requisite for sampling was a large, preferably flat, sampling surface which allows for samples to be taken >30 cm from an edge, reducing the geometry controlled neutron leak and self-shielding effects (Gosse & Phillips 2001), and where possible, boulders were sampled in localities with minimal topographic shielding to reduce cosmic ray attenuation by surrounding obstacles.

Further, to quantify the degree of thinning of the ice-stream during deglaciation, it was necessary to identify boulders at varying elevations, and above the Late Weichselian Marine Limit, as sub-aqueous deposition would result in too-young exposure ages (Heyman *et al.* 2011) reflecting the timing of emergence rather than deglaciation. Bedrock samples were identified with a similar criteria as discussed above, however the amount of shielding was reduced by selecting quartz-rich bedrock samples in meteorologically exposed locations, where snow cover was assumed limited by wind-sweeping.

3.2.2.2 In-field measurements

Following the identification of a suitable boulder or bedrock outcrop, several measurements were obtained for documentation and later correction factors such as shielding and nuclide production rates. The elevation of boulders was acquired with a handheld Global Positioning System (GPS) (Garmin Montana 600, and Garmin GPSmap 60CSx) featuring a barometric altimeter (±3 m) which was calibrated daily to sea level, with readings subsequently checked against topographic maps. The GPS was used to log the Universal Transverse Mercator coordinates (±3.65 m) of sampled boulder or bedrock. Topographic shielding of the sample site was measured with a clinometer (Suunto ME-ST360 Tandem, Figure 3.4a) at 20° azimuth intervals, which were then interpolated to 10° intervals, the shielding factor for each sample was calculated with Eq. 1 (Dunne *et al.* 1999).

$$S_h = \frac{\sum_{i=1}^{n} 1 - \sin(\frac{\pi}{180} E_l)^{3.3}}{n}$$

Eq. 1

Where; S_h = sample shielding factor, n = number of azimuth recordings, and E_l = elevation measured with clinometer.

The physical dimensions (height, width, length) of the boulder were approximately measured with a metre-rule, and the degree of surface weathering estimated from observation of the rock surface relief and surroundings. Each boulder was photographed with scale from four cardinal directions to document the physiographic setting.

3.2.2.3 Sampling method

To retrieve samples of 1–2 kg from suitable boulders or bedrock, a hand operated petrol powered cut-off saw (Stihl TS410, Figure 3.4b) was used on most occasions to incise the surface to a depth of ca. 2.5 cm, given the loss of nuclide production caused by attenuation of cosmic-rays with depth. The cross-hatched incisions (Figure 3.4c) could then be exploited with a hammer and chisel to recover the slabs (Figure 3.4d). Where the cut-off saw was not used the entire sample was recovered with a hammer and chisel before being bagged and tagged. The cut-off stone saw is advantageous to using a hammer and chisel as any rock surface can be sampled rapidly (Gosse & Phillips 2001), and away from edges, thus reducing the sampling bias present when removing easy to obtain specimens by hand.

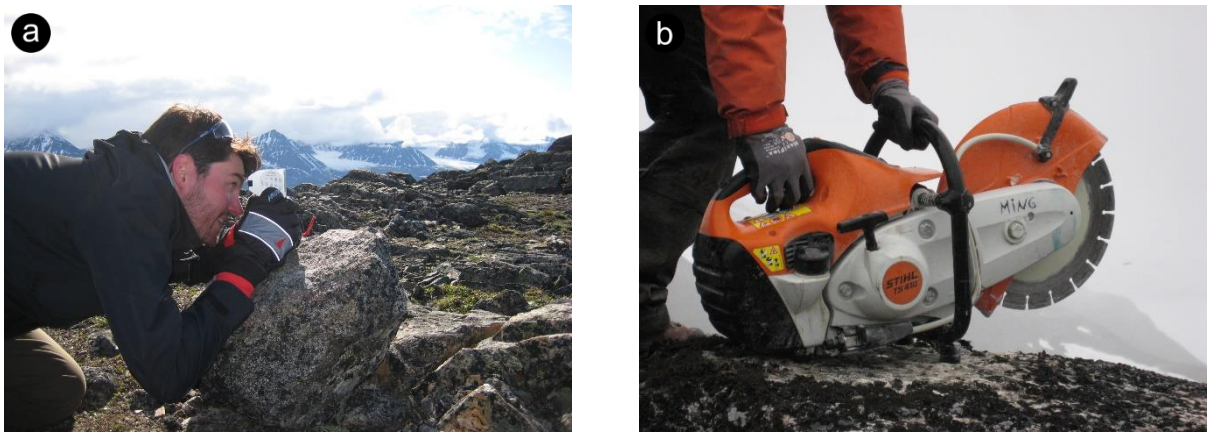

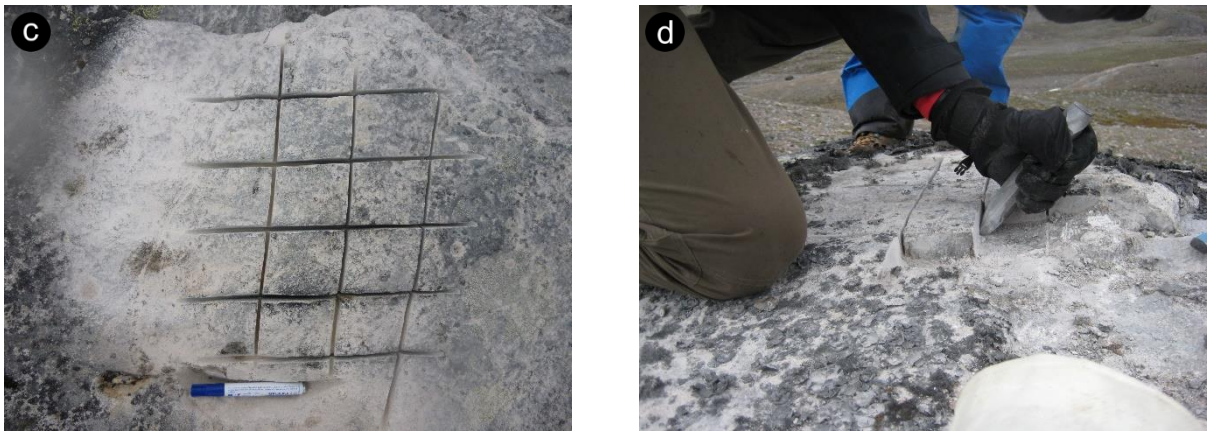

Figure 3.4: (a) Measuring topographic shielding of a boulder with a clinometer (Photo: H. Linge), (b) cut-off stone saw used to incise boulders/bedrock (Photo: H. Linge), (c) cross-hatched incision pattern on boulder surface with marker pen for scale (Photo: O. Grant) and (d) retrieving the slabs with a hammer and chisel (Photo: H. Linge).

3.2.3 Laboratory procedures

3.2.3.1 Sample documentation

The bulk rock samples collected in the field require numerous physical and chemical steps to separate and purify quartz, before extracting the beryllium and measuring the $^{10}Be/^{9}Be$ isotopic ratio with accelerated mass spectrometry (AMS). All laboratory procedures prior to precipitating beryllium hydroxide was carried out at the University of Bergen cosmogenic nuclide laboratory.

Between 1 and 1.5 kg was selected from each sample for processing, the first step was to obtain an average thickness of the sample required for a sample thickness correction factor, weighted thicknesses were achieved by measuring the thickness at 8 points on each clast (n), and weighting the average thickness by the surface area of the top surface, which was then summed for all clasts to give the weighted average thickness for the sample;

$$\overline{d} = \sum \frac{((\sum_{i=1}^{n} d_i)(\frac{A_i}{A_{tot}}))}{n}$$

Eq. 2

Where; $\overline{d}$ = Weighted average thickness for total sample, n = number of measurements per sample piece, i = index of summation, d_i = Individual thickness measurement for sample piece, A_i = Top surface area for sample piece, and A_{tot} = Top surface area for total sample.

Where the sample was highly fragmentary in nature, such as SARS1401, the average sample thickness was weighted by fraction mass (Eq. 3). The sample was divided, based on the A-axis length of each clast, into; large (>3 cm), medium (0.5–3 cm), and small (<0.5 cm) fractions. 5 fragments were taken from each fraction, and measured at 6 points to give the weighted average thickness;

$$\overline{d} = \frac{((\sum d_{il})(\frac{M_l}{M_{tot}})) + ((\sum d_{im})(\frac{M_m}{M_{tot}})) + ((\sum d_{is})(\frac{M_s}{M_{tot}}))}{n \times d_i}$$

Eq. 3

Where; d_{il} = Individual thickness measurements for large fragments, d_{im} = Individual thickness measurements for medium fragments, d_{is} = Individual thickness measurements for small fragments, M_l = Mass of large fragments, M_m = Mass of medium fragments, M_s = Mass of small fragments, M_{tot} = Mass of total sample, n = Number of fragments measured per fraction, and d_i = Number of individual measurements per fragment.

The top surface of each sample was surveyed with a hand lens to determine lithology and estimate the degree of weathering, as the majority of samples are granitic, the weathering estimate was based on surface roughness indicating grain by grain dissociation. Samples were then photographed with scale for documentation.

3.2.3.2 Separation, concentration and purification of quartz

Quartz grains inherently have multimineralic inclusions and imperfections in the crystal lattice, resulting in contamination by aluminium, iron, titanium, alkalis, and alkaline earth metals, which must be removed for successful chemical processing, and before measuring the $^{10}Be/^{9}Be$ ratio (Hunt *et al.* 2008). It is subsequently vital to separate and purify quartz from other minerals in the sample lithology prior to extracting beryllium, given that we do not yet know the ^{10}Be production rate in other common minerals (Dunai 2010), the separation and purification steps are displayed schematically in Figure 3.5.

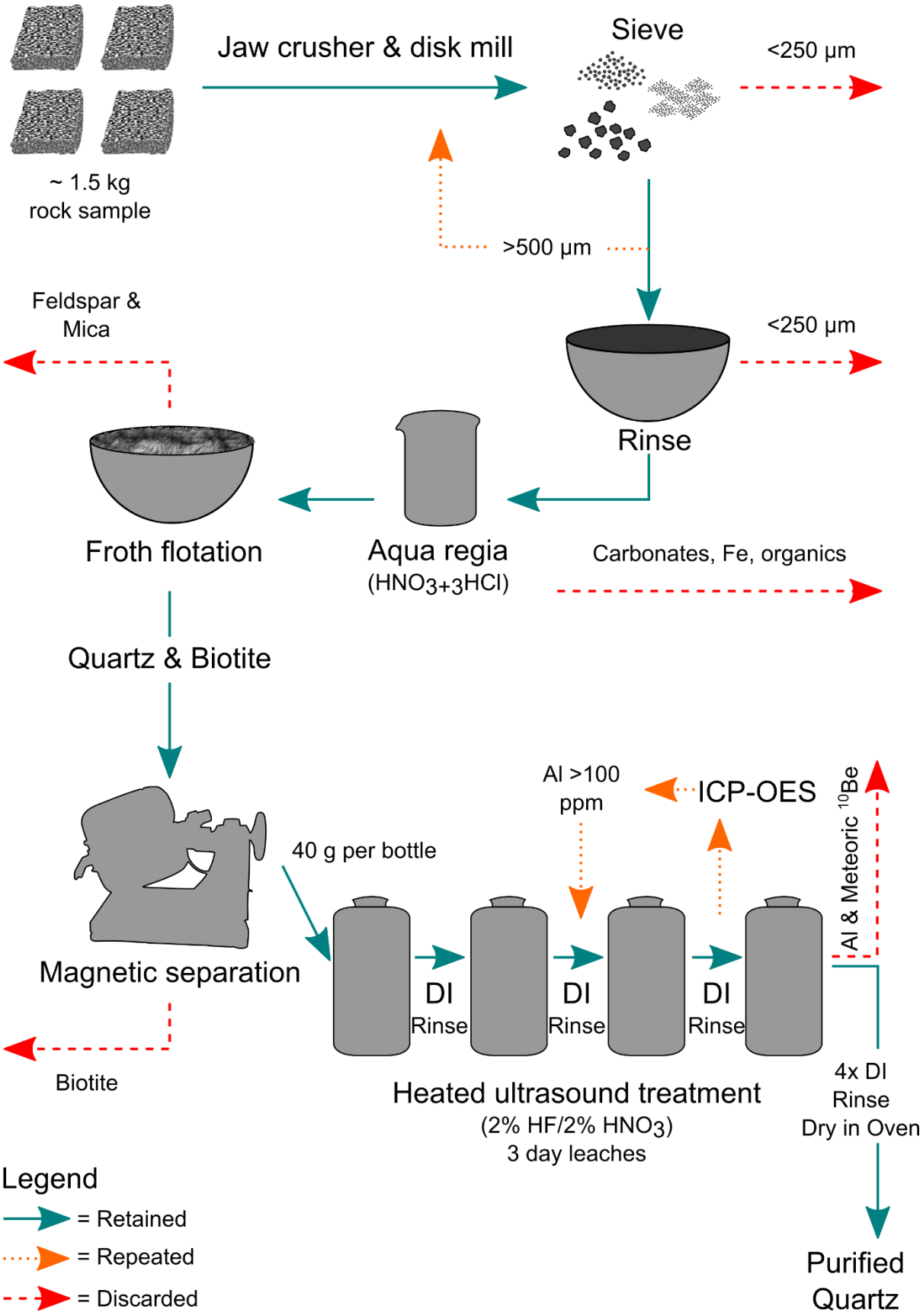

Figure 3.5: Procedures followed for separating and purifying quartz, modified from Bierman et al. (2002).

The first step was to crush each sample in a jaw crusher, reducing the sample to gravel sized clasts, those samples with an A-axis exceeding 5 cm were sliced with a stone saw before being fed to the jaw crusher. The sample was then sieved to three fractions, <250 µm was discarded, 250–500 µm was retained for later chemical processing, and >500 µm was further reduced via a disk mill and sieving to 250–500 µm, the target grain size for monomineralic particles and to improve yield, as finer fractions are more readily dissolved in subsequent chemical leaches (Kohl & Nishiizumi 1992). The total 250–500 µm fraction was then rinsed with tap water to remove any remaining finer particles prior to the chemical mineral separation procedures developed by Kohl and Nishiizumi (1992), Ivy Ochs (1996), and Child *et al.* (2000), which improve the yield of clean quartz by three orders of magnitude over heavy liquid separation, which also has high levels of cross-contamination, difficulty in removing feldspar and inability to remove meteoric ^{10}Be (Kohl & Nishiizumi 1992).

The first chemical step involved bathing the sample in a 25 % aqua regia solution (1:3 HNO:HCl) on a low heat setting overnight to remove any iron, organic material, and trace carbonates. 80 g of the sample was then etched with 1 % Hydrofluoric acid (HF) in a sealed plastic bottle on a heated roller for 1 hour, the solution was then decanted into a hazardous waste container, with the etched sample emptied into a stainless steel bowl for froth flotation (Purdue University Primelab 2007). The froth flotation process involved adding 4–5 drops of eucalyptus oil and a carbonated solution of acetic acid ($C_2H_4O_2$) and dodecylamine ($C_{12}H_{27}N$) giving laurylamine, into the sample. The sample was then agitated and froth poured off into a separate container for feldspar and mica (Herber 1969). Flotation was repeated until only heavier minerals remained, chiefly quartz and biotite, at which point the material was transferred to beakers and dried.

The sample was then ran through a Frantz Magnetic Separator at 0.8 A with an inclination of 10–15° and rear tilt of 20°. The magnetic separator attracts any ferrous trace metals, and the ferromagnetic and paramagnetic minerals, such as biotite, and repels diamagnetic quartz. Following magnetic separation and checking with a hand-lens, the sample was primarily quartz and so could be purified via heated ultrasound leaching.

For the leaching process, 40 g sample was added to a plastic bottle, which was then filled with a 2 % HF/2 % HNO_3 solution, the bottles were then sonicated in a heated ultrasonic bath for 99 minutes three times per day for three days, being hand shaken between each sonication. Between each third day, the HF/HNO_3 solution was decanted and the sample rinsed with deionised water, and fresh 2 % HF/2 % HNO_3 solution added. Following the third leach, an aliquot of 0.5 g was analysed with inductively coupled plasma optical emission spectrometry (ICP-OES) by Lars Evje to quantify the

concentration of aluminium and other trace metals including; calcium, chromium, iron, magnesium, and titanium, samples exceeding 100 ppm Al were further leached in the heated ultrasonic treatment.

Ultrasonic leaching was used to remove any remaining non-quartz aluminium bearing minerals, usually requiring 3 to 4 leaches to reduce Al to below 100 ppm (Bierman *et al.* 2002). The process also removes meteoric ^{10}Be (Figure 3.6), originating from the atmosphere. Meteoric ^{10}Be is absorbed into the outside of the mineral grains, and concentrations can be 3 orders of magnitude greater than in-situ produced ^{10}Be (Gosse & Phillips 2001), contamination by meteoric ^{10}Be would give spurious results, especially given that cleavage of quartz grains can also trap meteoric ^{10}Be (Ivy Ochs 1996). Ultrasound (>20 kHz) is necessary to agitate the sample for improved efficiency, however the method does present a source of uncertainty, as etching and heating may leach-out in-situ produced ^{10}Be (Kohl & Nishiizumi 1992).

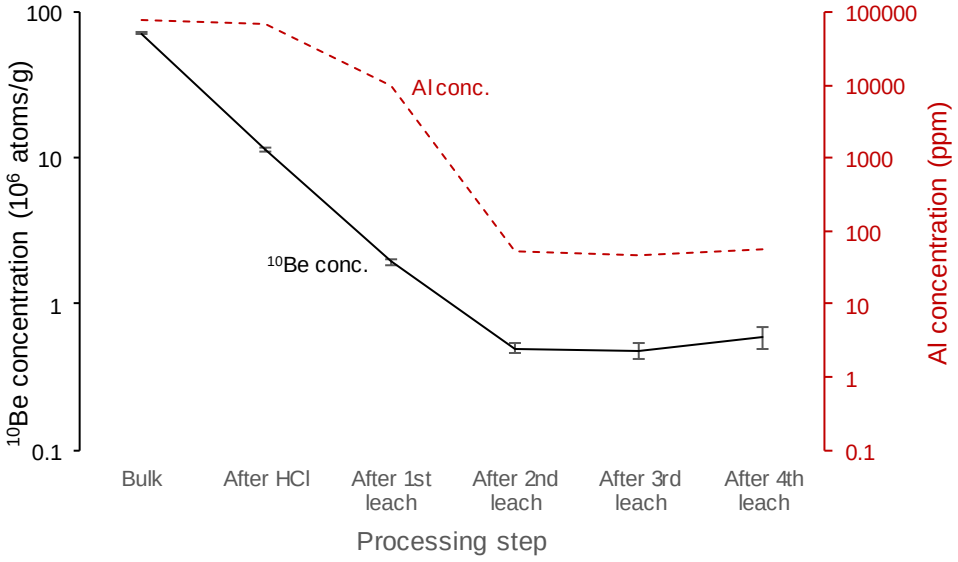

Figure 3.6: ^{10}Be concentration with uncertainties, and Al concentration from quartz after chemical steps including ultrasonic leaching, based on Nishiizumi et al. (1989) note the logarithmic axes.

The heated ultrasonic leaching treatment leaves purified quartz with low trace metal concentrations and presumably no meteoric ^{10}Be, which was then digested in 40 % HF for beryllium extraction which is outlined in Figure 3.7 and Figure 3.8.

3.2.3.3 Extracting the beryllium fraction

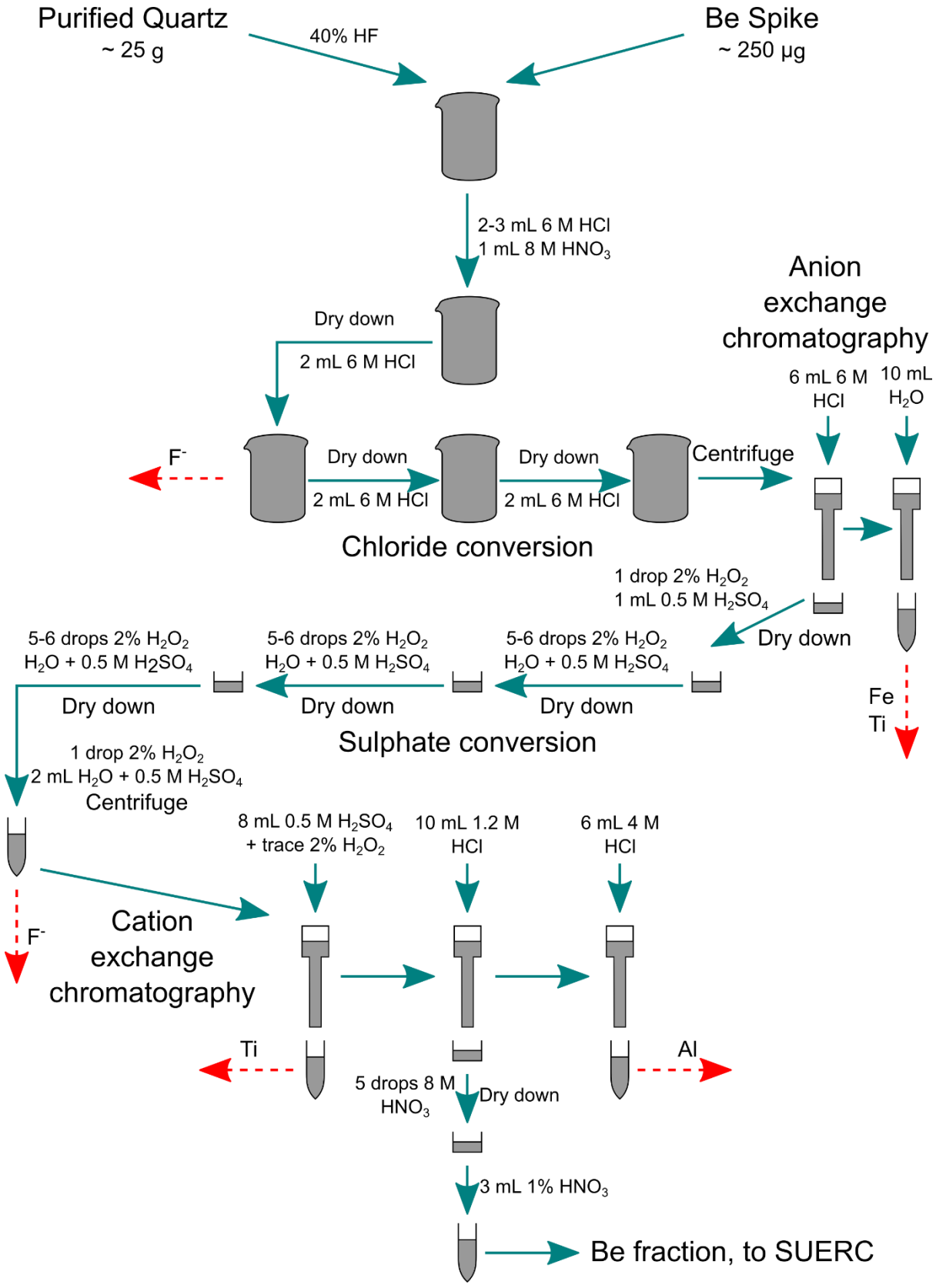

Figure 3.7: Procedures followed when extracting beryllium fraction from purified quartz, modified from Bierman et al. (2002).

The precise addition to the digested quartz of a beryllium spike, weighed to the fourth decimal with known ratio of $^{10}Be/^{9}Be$ (Scharlau 2453 batch: 14569501, $^{10}Be/^{9}Be$ ratio 4.02 x 10^{-15}), was necessary due to the unknown concentration of beryllium in the sample. Two possible sources of error arising at this step were presented by Ivy Ochs (1996); the beryllium spike introduces ^{10}Be, although carriers with very low $^{10}Be/^{9}Be$ ratios are used, and any accessory minerals still present during the digestion of purified quartz may dilute the ^{10}Be concentration, however this is only problematic for very young samples (Ivy Ochs 1996).

The HF solution was transferred to a Teflon beaker, 2–3 mL 6 M hydrochloric acid (HCl) and 1 mL 8 M nitric acid (HNO_3) was added, and the solution dried-down overnight in preparation for chloride conversion. The addition of 2 mL 6 M HCl and drying down was repeated three times to eliminate fluoride, and convert; Fe, Ti, Al, Be, alkalis, and other trace metals to chloride salts.

To prepare for anion exchange chromatography, the solution was centrifuged at 3000 rpm for 10 minutes. Anion columns were packed with Bio-Rad AG 1-X8 200–400 mesh resin, and then conditioned with the drainage of 10 mL 1.2 M HCl, followed by 10 mL 6 M HCl. A labelled “Al and Be fraction” 15 mL vial was placed under the column, and sample added to the column and drained, followed by 6 mL 6 M HCl. 1 drop of 2 % hydrogen peroxide (H_2O_2) was added to check for amber/gold colouration caused by Ti, the “Al and Be fraction” was then gently heated to near-dryness, while “Fe and Ti fraction” centrifuge tubes were placed under the column, and 10 mL deionised water was drained through the column.

The Al and Be fraction was converted from chloride to sulphate form, first the near-dry cakes were moistened with 5–6 drops of 2 % H_2O_2, followed by 2 mL deionised water containing trace 0.5 M H_2SO_4, reheated and dried down, which was repeated 3 times. The near-dry sample was then taken up with 2 mL deionised water containing trace 0.5 M H_2SO_4 and 1 drop of 2 % H_2O_2 was added and left to stand overnight. The sample was then transferred to a centrifuge tube and centrifuged at 3000 rpm for 10 minutes.

The cation columns were packed with Bio-Rad AG 50W-X8 200–400 mesh resin, which was stripped with 10 mL 4 M HCl, followed by 10 mL 1.2 M HCl and then conditioned with 10 mL 0.2 M H_2SO_4 with trace 2 % H_2O_2. A “Ti fraction” 15 mL centrifuge tube was placed below the column, and the sample was added and drained through the column, followed by 8 mL 0.5 M H_2SO_4 with trace of 2 % H_2O_2. A “Be fraction” 15 mL Teflon vial was then placed below the column, and 10 mL 1.2 M HCl was added to the column to elute the Be, with 5 drops of 8 M HNO_3 added to the vials before being gently heated to near-dryness. An “Al fraction” 11 mL centrifuge tube was placed below the column, and 6 mL 4 M HCl was drained through the column to elute Al.

The cation exchange chromatography step is necessary to remove Ti (Child *et al.* 2000), and to separately elute Be and Al. High cation concentrations in the Be fraction can cause lower ion source currents during AMS, resulting in large errors in exposure age (Ochs & Ivy-Ochs 1997). Hunt *et al.* (2008) suggest a source of uncertainty arising from the anion and cation exchange steps; channelling within the resin will decrease column efficiency if improperly packed, but would be detected by rapid drainage, trace elements within the resin may be eluted with the sample if overexposed to acid.

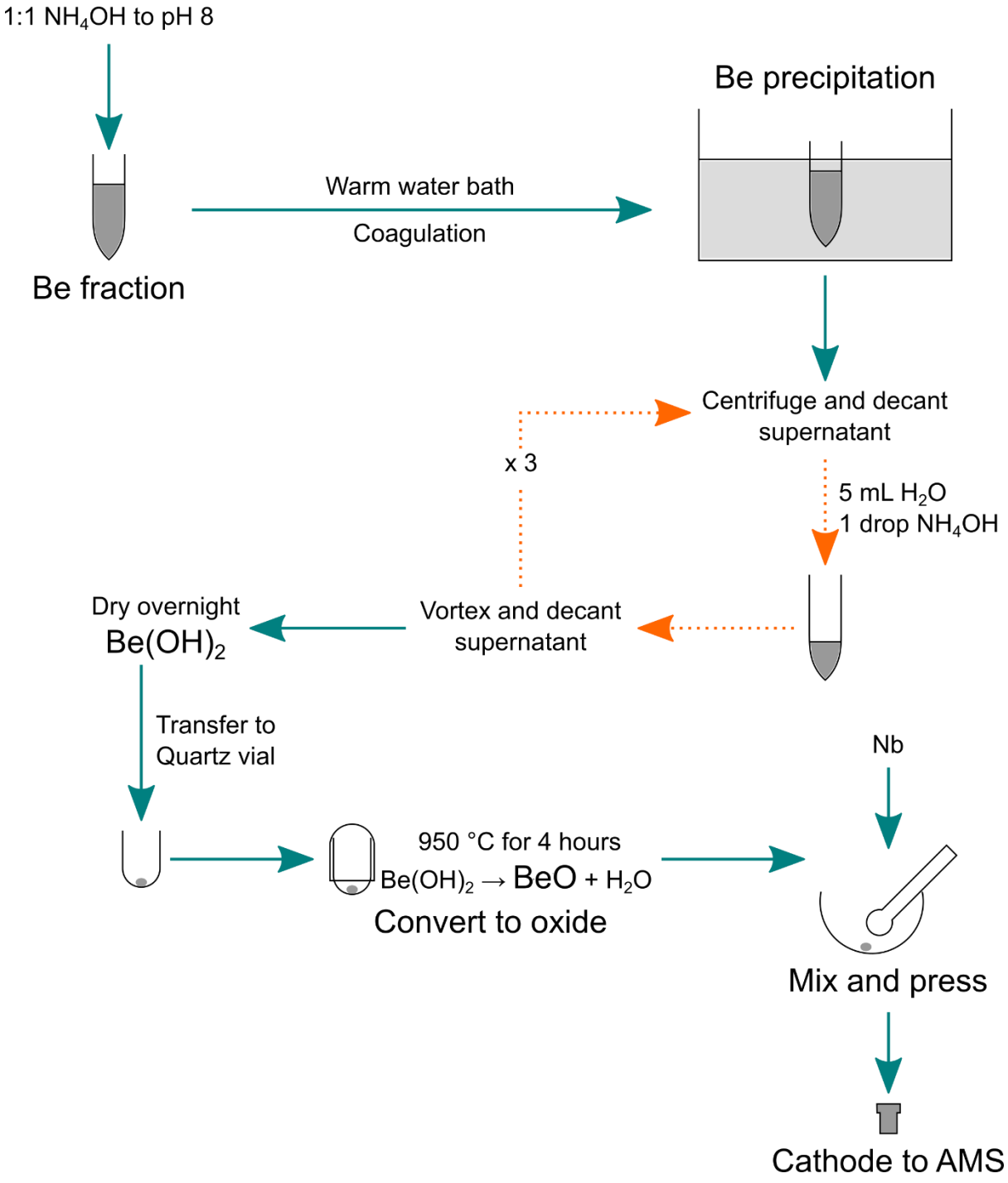

Figure 3.8: Procedures followed at SUERC to precipitate the beryllium fraction, oxidise and mix with niobium, prior to pressing into cathode for AMS.

The near-dry Be fraction was dissolved in 2 mL 1 % HNO_3 and transferred to a 15 mL centrifuge tube, at which point it was sealed and taken to the Cosmogenic Isotope laboratory at the Scottish Universities Environmental Research Centre (SUERC) in East Kilbride. The first step at SUERC was to precipitate the beryllium hydroxide ($Be(OH)_2$) by adding ammonium hydroxide (NH_4OH) to pH 8. The sample was left to coagulate in a warm water bath, then centrifuged at 3000 rpm for 10 minutes, with the supernatant disposed. 5 mL deionised water with 1 drop of NH_4OH was added, and the sample vortexed, then centrifuged at 3000 rpm for 10 minutes and supernatant decanted, this was repeated 3 times, and the remaining $Be(OH)_2$ was carefully dried overnight in the oven at 70°C.

The dry $Be(OH)_2$ was added to a pre-weighed (to the fourth decimal) quartz vial base, and the lid placed on, the sample was then oxidised in a 4 hour stepped furnace exceeding 950 °C to convert beryllium hydroxide to beryllium oxide ($Be(OH)_2 \rightarrow BeO + H_2O$), the most stable beryllium compound (Von Blanckenburg *et al.* 1996), and cooled overnight. The vial was again weighed to ascertain the mass of BeO, and the mass of niobium (Nb) needed for mixing and pressing (≥6 x mass of BeO). The BeO and Nb were then ground and mixed with a quartz pestle and mortar, then transferred to a copper AMS target cathode and hand pressed with a lever-press needle to pack the cathode.

At SUERC, Dr Sheng Xu measured the ^{10}Be to ^{9}Be isotopic ratio with a 5 MV NEC Pelletron accelerator mass spectrometer (Freeman *et al.* 2004; Xu *et al.* 2010) relative to the NIST SRM4325 standard with a reported isotope ratio of 3.06 x 10^{-11}, the resulting ratio measurements from the AMS were converted to the ^{10}Be concentration with Eq. 4 and Eq. 5, and uncertainty with Eq. 6 (Balco 2006):

$$N_{10} = \frac{1}{M_q}\frac{R_{10/9}M_C N_A}{A_{Be}} - n_{10,B}$$

Eq. 4

Where; N_{10} = ^{10}Be atoms per gram of quartz, M_q = mass of quartz sample (g), $R_{10/9}$ = isotope ratio without blank subtracted, M_C = mass of beryllium added as carrier (g), N_A = Avogadro's number (6.022 x 10^{23}), A_{Be} = molar weight of beryllium (9.012 g per mol^{-1}), and $n_{10,B}$ = number of atoms in process blank (Eq. 5).

$$n_{10,B} = \frac{R_{10/9B}M_{CB}N_A}{A_{Be}}$$

Eq. 5

Where; $n_{10,B}$ = number of atoms in process blank, $R_{10/9B}$ = isotope ratio measured in blank, and M_{CB} = mass of beryllium added as carrier to process blank.

$$\sigma N_{10} = \sqrt{(\frac{M_C N_A}{M_q A_{Be}} \sigma R_{10/9})^2 + (\frac{1}{M_q} \sigma n_{10,B})^2 + (\frac{R_{10/9} N_A}{M_q A_{Be}} \sigma M_C)^2}$$

Eq. 6

Where; σN_{10} = 1 standard error analytical uncertainty in ^{10}Be concentration in quartz.

The use of AMS is advantageous as counting atoms is much more efficient than counting decays for isotopes with a half-life as long as ^{10}Be (Bierman *et al.* 2002), sample decay counting would require decades or several kilograms of quartz, while conventional mass spectrometry cannot be tuned for the low isotopic ratios required for ^{10}Be/^{9}Be (Ivy Ochs 1996). The precision of AMS is approaching ±1 % for ^{10}Be/^{9}Be determination, and isobaric interference with boron (^{10}B) caused by its equal mass to ^{10}Be (Child *et al.* 2000) is no longer a big concern (Christl *et al.* 2014). It previously required several MV AMS systems to overcome ^{10}B isobaric interference, but is now possible in low energy (300 kV to 1 MV) AMS systems (Christl *et al.* 2014). The total precision of AMS is continually improving, the current ^{10}Be/^{9}Be detection limit is as low as <1 x 10^{-15} (Maden *et al.* 2007; Xu *et al.* 2010; Matsubara *et al.* 2014).

3.2.3.4 Data processing

The CRONUS-Earth calculator version 2.2 (CRONUS-Earth 2009) was used to calculate exposure ages from the concentration of ^{10}Be in the samples, the necessary inputs are listed in Table 3.1.

Table 3.1: Inputs required for exposure age calculation in the CRONUS-Earth calculator version 2.2, modified from Balco et al. (2008).

Field	Unit	Comments
Sample name	Text	BLOM14, GOR14, or SARS14 prefix depending on transect
Latitude	Decimal degrees (°)	Recorded with GPS
Longitude	Decimal degrees (°)	Recorded with GPS
Elevation	m	Recorded with GPS barometric altimeter
Sample thickness	cm	Calculated with Eq. 2 or Eq. 3
Sample density	g cm^{-3}	2.65 g cm^{-3} used (density of Quartz)
Shielding correction	Nondimensional between 0 and 1	Calculated with Eq. 1

Field	Unit	Comments
Erosion rate	cm a^{-1}	0 cm a^{-1} assumed
Nuclide concentration	atoms g^{1}	Calculated with Eq. 5
Uncertainties in nuclide concentration	atoms g^{1}	Calculated with Eq. 6

The spallogenic production rate of ^{10}Be in quartz was experimentally studied by Lal (1991) and found to be a function of altitude and latitude, with latitudes above 60° having higher production rates and low to zero reduction caused by the geo-magnetic dipole. Stone (2000) reformulated the scaling of the spallation production rate by casting it as a function of atmospheric pressure rather than altitude, as the cosmic ray flux increases with altitude given the reduced air pressure and atmospheric shielding effect (Stone 2000). The CRONUS-Earth calculator uses the spallation rate scaling from Lal (1991) and Stone (2000) based on the latitude and elevation inputs (Table 3.1).

The ^{10}Be production rate calibration model used in the calculation of exposure ages was the Baffin Bay/Arctic calibration data set scaled to the Lal/Stone model (Young *et al.* 2013), with a production rate of 3.96 ± 0.15 atoms g^{-1} a^{-1}, giving older and more precise exposure ages than the global production rate of 4.47 ± 0.40 atoms g^{-1} a^{-1} (Balco *et al.* 2008). The Arctic production rate of Young *et al.* (2013) was also selected due to its latitudinal similarity to Svalbard, and the timescale used in its calibration. The Young *et al.* (2013) model does not account for uplift or change in atmospheric pressure related to sea level and ice sheet interactions, as such time integrated changes (Stone 2000) will be within the uncertainty of the method and production rate calibration model (Young *et al.* 2013).

3.3 Calibrating radiocarbon dates

Where discussed in this study, radiocarbon dates have been calibrated to thousand calendar years before present (cal ka BP) from the published ^{14}C date and associated uncertainty (note: before present corresponds to AD 1950). The IntCal13 radiocarbon calibration curve is used (Reimer *et al.* 2013), and aided through the OxCal program online calibration calculator version 4.2 (OxCal 2015), and any marine reservoir effect is assumed to be included in the published ^{14}C date unless otherwise stated.

4. Results

4.1 Quaternary geological mapping

Within a restricted area of approximately 16 km^2, a wide variety of sediments and landforms are found on Blomstrandhalvøya, pertaining to different ages and paleoenvironments. Field observations, aerial photograph and digital terrain model analyses (Figure 4.1 to Figure 4.17) are drawn together in Figure D.1, Appendix D, a ca. 1:10,000 scale Quaternary geological map of Blomstrandhalvøya. The island can be subdivided into quarters; the northeast of the island bearing the freshest glacial deposits and landforms, the northwest has mostly exposed weathered bedrock and periglacial features, the southwest is dominated by marine and fluvial deposition and landforms, while the southeast is dominated by fluvial and slope processes. Blomstrandsalen is the ca. 2 km^2 saddle like depression in the centre of the island (Figure 1.2) (Isachsen 1912; Norwegian Polar Institute 2003), where periglacial processes reworking glacial deposits are observed.

4.1.1 Glacial features

The majority of surface sediments on Blomstrandhalvøya consist of unsorted diamictic material, with sub-angular to sub-rounded clasts of all sizes (Figure 4.1a). The drape of consolidated texturally heterogeneous diamictic material implies sub-glacial traction till (Evans *et al.* 2006), as glacier ice over-rode Blomstrandhalvøya pressure melting liberated basal debris and lodgement processes consolidated the till into packages up to 4 m thick (Figure 4.1b). Alternatively, the till drape could represent a sliding bed deposit, consistent with polished bedrock (Hindmarsh 1996) layered or stratified till (Figure 4.17 assuming all units are till) and interbeds related to high subglacial water pressure (Brown *et al.* 1987) or subglacial drainage (Eyles *et al.* 1982).

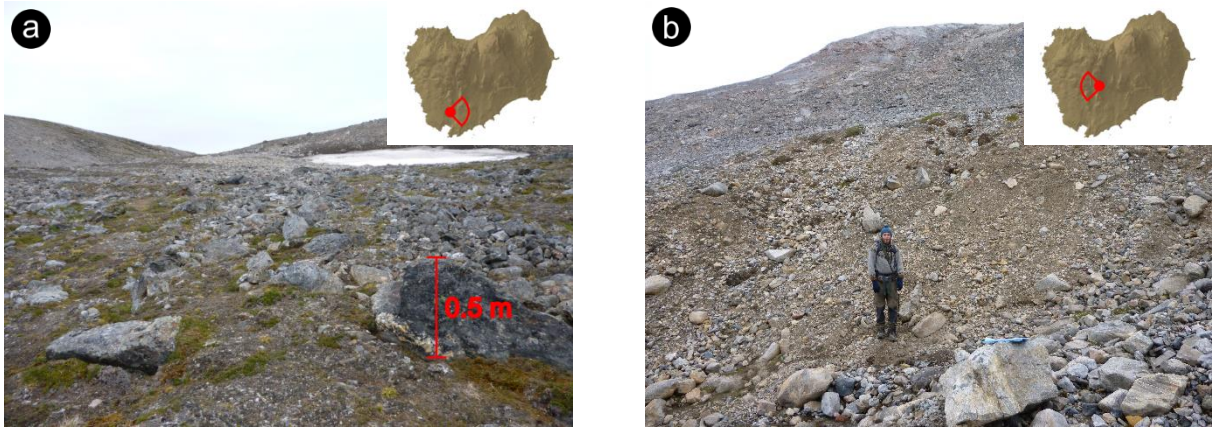

Figure 4.1: (a) Typical till drape found on Blomstrandhalvøya (Photo: O. Grant 33N 437400 8768300 facing east), and (b) natural exposure through till, logged in Figure 4.17, person for scale, (Photo: O. Grant 33N 437200 8768900 facing west).

A large number of erratic boulders, typically granite and mica schist (Myers 2013), are found on the island both within the surface sediments and perched on exposed bedrock, indicating glacial overriding of the site. The difference in deposition west to east on Blomstrandhalvøya may be indicative of ice stream dynamics, as basal debris was deposited as lodgement till on the east during advance, while the erratics, as englacial debris, (Alley *et al.* 1989) were deposited on the polished bedrock surfaces to the west during melt-out or retreat.

On the north east of Blomstrandhalvøya, a suite of ridges interpreted as end moraines and lateral moraines approximately 1 km in length are traceable along the slope (Figure 4.2c). The moraines consist of a clayey-silt matrix with rounded to sub-angular clasts and shell fragments (Figure 4.2a) indicating a marine origin of the sediments. Surface ponding and cracking indicate thawing of an ice core (Figure 4.2b) (Sletten *et al.* 2001). The outer lateral and end moraine are consistent with the maximum Little Ice Age extent of Blomstrandbreen (Liestøl 1988), and the moraines within represent 20th Century glacier front positions.

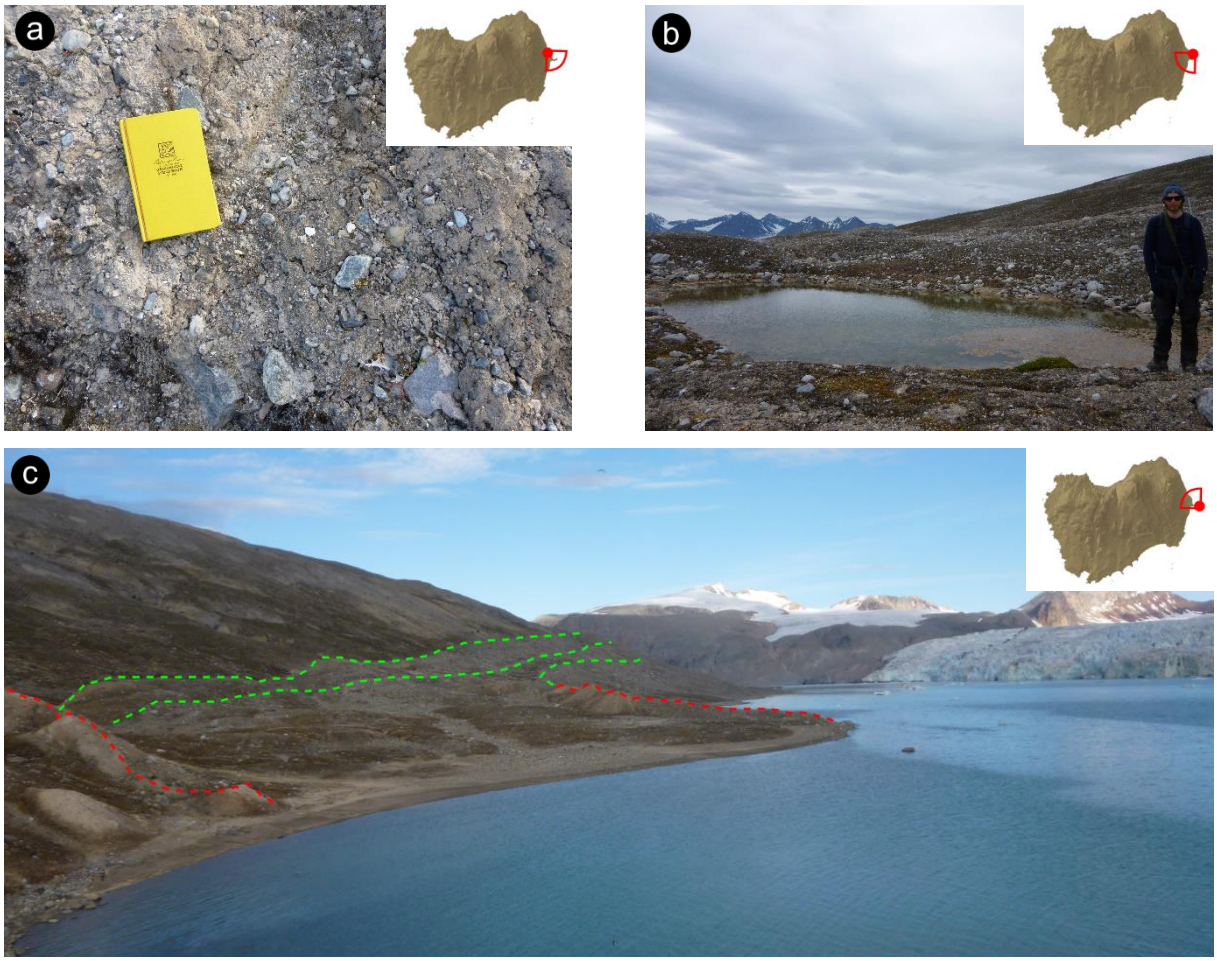

Figure 4.2: (a) Clay-silt matrix of the moraine ridges, including shell fragments and rounded to sub-angular clasts (Photo: O. Grant 33N 440900 8769900), (b) water ponding on top of moraine ridge (Photo: O. Grant 33N 440600 8770200 facing south west), and (c) suite of lateral (green stippled) and end (red stippled) moraines with Blomstrandbreen in the background (Photo: O. Grant 33N 440900 8769900 facing north west).

On the northeastern tip of Blomstrandhalvøya, several streamlined features oriented N–NE to S–SW are present, approximately 50 cm high, 1–2 m wide and up to 100 m long, and generally found with a boulder at the Blomstrandbreen-proximal end. The streamlined features are interpreted as flutes, and interpreted by Paul and Evans (1974) to represent infilling of subglacial tunnels by the extrusion of unfrozen pre-existing sediments, alternatively they were formed by the extension of the subpolar Blomstrandbreen ice tongue across the bay, altering the basal thermal regime (Sollid & Sørbel 1988). The flutes are often perpendicularly over-printed by smaller ridges up to 30 cm high which are interpreted as crevasse-fill ridges (Figure 4.3a), such a landform assemblage is ascribed to glacier surge activity (Christoffersen *et al.* 2005), and is found within the margins of the last known to surge from Blomstrandbreen in 1966 (Sund & Eiken 2010).

To the west of the fluted area, a series of arcuate steep and sharp-crested ridges up to 10 m high and 200 m long are found parallel to and 30 m behind the present beach (Figure 4.3b). The form of the ridge and it's sandy-silt matrix with oversized clasts indicate a moraine, and an ice front position which is therefore more recent than 1988 (Liestøl 1988), representing the last time Blomstrandhalvøya could be considered a peninsula, and may represent thrusting during ungrounding of Blomstrandbreen in Blomstrandhamna (Figure 1.1, Figure 1.2).

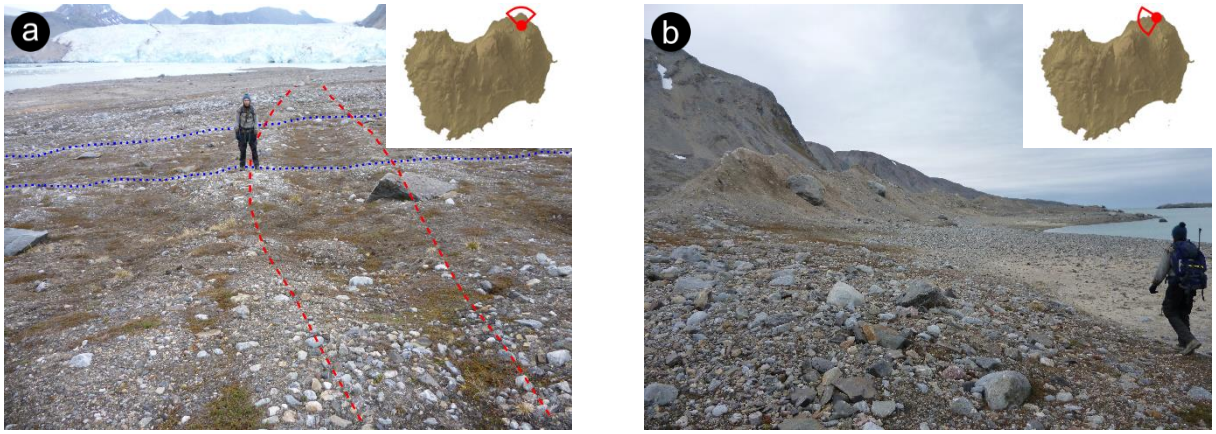

Figure 4.3: (a) Flutes (red stippled) with superimposed crevasse-fill ridges (blue dotted) on the northern tip of Blomstrandhalvøya (Photo: O. Grant 33N 439600 8771100 facing north), and (b) end moraines representing the most recent ice margin position on the island (Photo: O. Grant 33N 439300 8771500 facing west).

Further west, along the northern coastline of Blomstrandhalvøya and below the cliffs of Irgensfjellet, a prominent ca. 10 m high ridge consisting of a silty-sand matrix with rounded to sub-rounded clasts of all sizes sits on bedrock, and is accompanied by a series of subdued mounds and ridges of the same material which lead to the east (Figure 4.4). The prominent ridge aligns with the maximum Little Ice Age position of Blomstrandbreen and the smaller ridges and mounds aligning with recessional positions between the years 1861 and 1932 (Liestøl 1988).

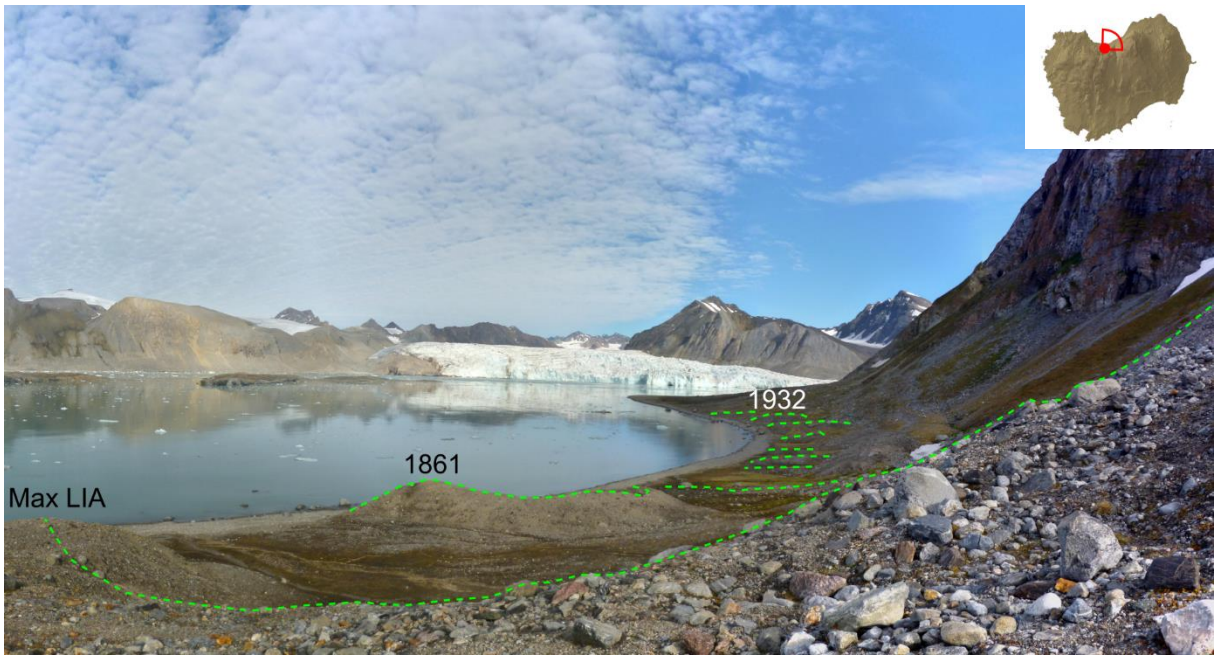

Figure 4.4: Maximum Little Ice Age moraine and recessional ridges and mounds (green stippled) with historic Blomstrandbreen Ice front positions mapped by Liestøl (1988), the distance between the Max LIA and 1932 moraine is approximately 700 m (Photo: O. Grant 33N 438100 8770600 facing northwest).

To the west of Blomstrandsalen, at ca. 325 m a.s.l., a 50 m long and 2–3 m high diamictic ridge trending north–south is found at the end of a faint ca. 100–150 m long break in slope trending east west (Figure 4.5). Both features are degraded, but their form may represent a lateral and end moraine pair, and could reflect an ice front position related to downwasting, however given the north–south strike of faults in bedrock, the end moraine may be till superimposed on a bedrock scarp, although no bedrock was reached during ca. 1 m deep excavation.

Figure 4.5: Degraded end moraine (stippled red line) found to the west of Blomstrandsalen, the slope to the left of the photograph shows a faint break in slope (green dotted line), person for scale (Photo: O. Grant 33N 437000 8769600 facing east).

Close to the centre of the Blomstrandsalen depression, a ca. 130 m long and 2–3 m high arcuate ridge is found, conspicuous in the low relief patterned ground surface (Figure 4.6a). The ridge is formed of a bimodal diamicton consisting of angular to sub-angular clasts and sand matrix (Figure 4.6c), and several boulders with erratic lithology, mostly mica schist and granite, are scattered on the crest and flanks of the feature. Excavation of the ridge failed to reach bedrock, although frost-weathered clasts of local lithology were observed. The ridge may represent an ablation-dominant medial moraine (Eyles & Rogerson 1978), an ice marginal position on Blomstrandsalen, or a subglacial divide as ice flows down separate gullies from Blomstrandsalen (Figure 4.6b).

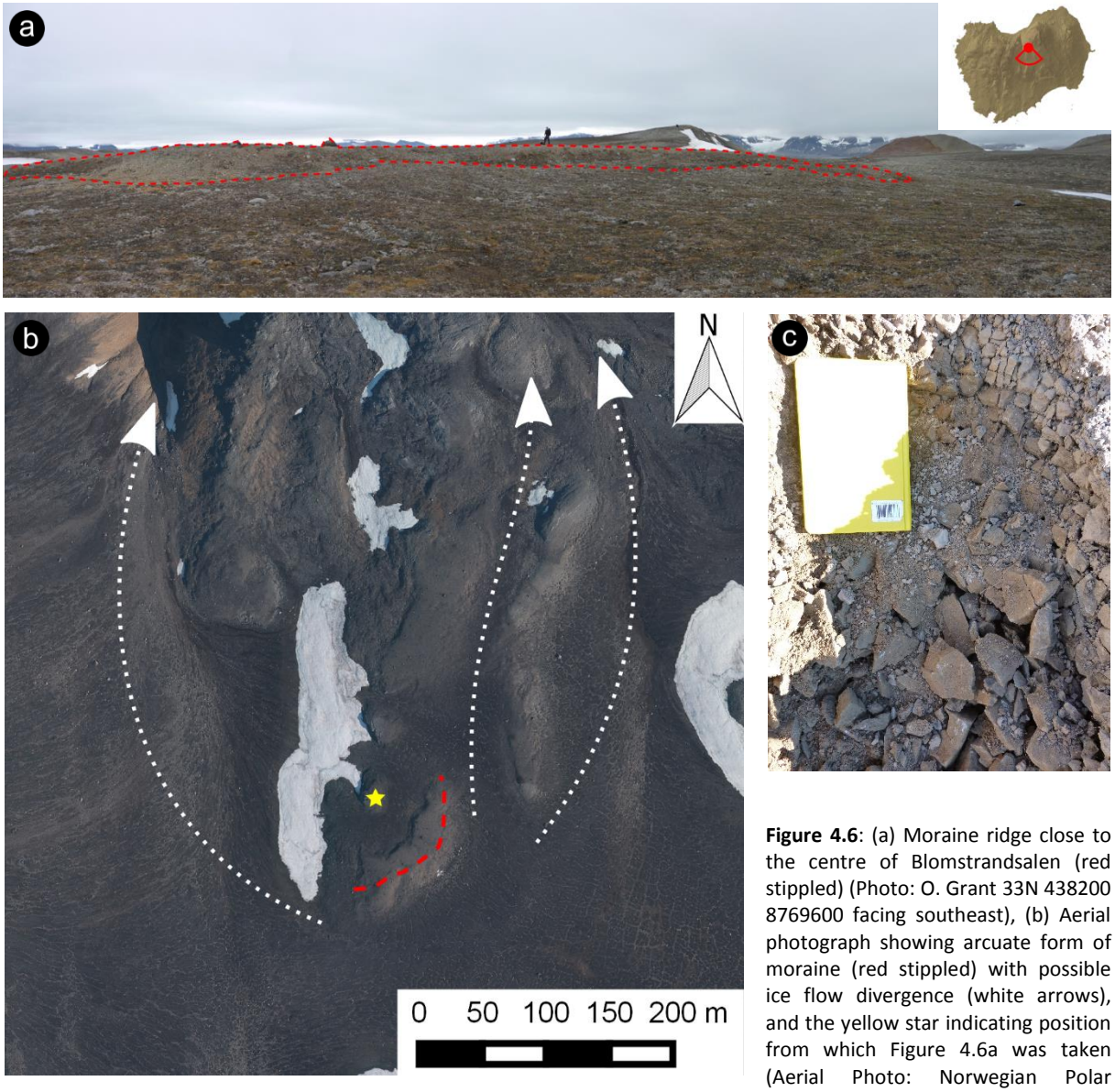

Figure 4.6: (a) Moraine ridge close to the centre of Blomstrandsalen (red stippled) (Photo: O. Grant 33N 438200 8769600 facing southeast), (b) Aerial photograph showing arcuate form of moraine (red stippled) with possible ice flow divergence (white arrows), and the yellow star indicating position from which Figure 4.6a was taken (Aerial Photo: Norwegian Polar Institute), and (c) diamictic sediments from excavated section of the moraine ridge, with frost weathered clasts (Photo: O. Grant).

On the south eastern slope of Blomstrandhalvøya, a trimline engraved in bedrock can be observed at ca. 120 m a.s.l., which continues to the east as a discontinuous degraded ridge composed of clay and silt-rich diamicton, giving a total length of the linear feature of ca. 1.5 km (Figure 4.7). The ridge is dissected by fluvial channels, and reworked by slope and solifluction processes, with numerous boulders moving downslope within the finer matrix. The combined trimline and degraded moraine feature may demarcate an ice-marginal position of the Kongsfjorden Ice Stream, during or post-dating the Late Glacial Maximum deglaciation.

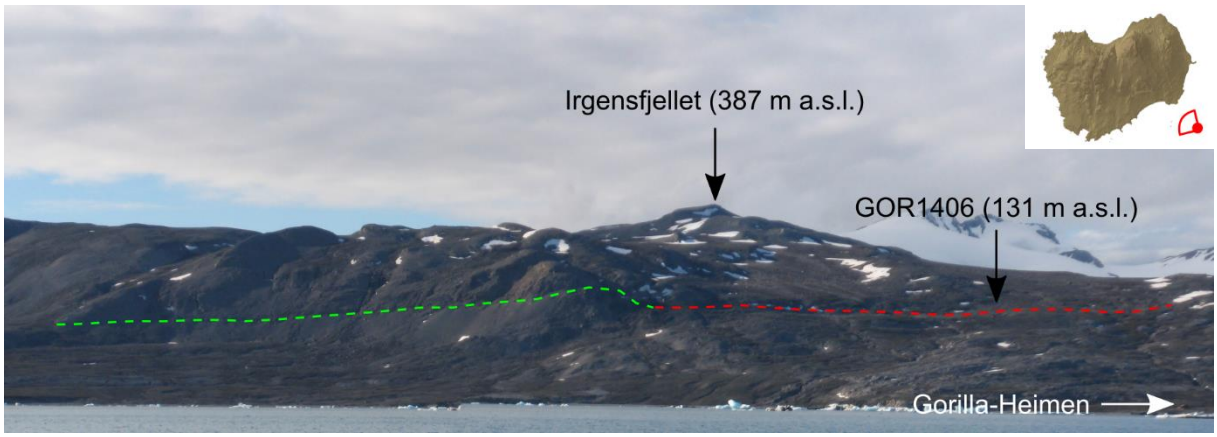

Figure 4.7: The trimline (green stippled line) and degraded moraine ridge (red stippled line) observed from close to Rundholmen in Kongsfjorden, with Irgensfjellet in the background and the location of sampled boulder GOR1406 indicated (Photo: H. Linge, facing northwest).

Sub-angular to rounded boulders of non-local lithology, typically granite, mica schist and Devonian conglomerate (Myers 2013), are abundant and scattered liberally on Blomstrandhalvøya, with a maximum observed diameter of ca. 3 m. On the east of the island, many boulders are partially buried by sediment (Figure 4.8a), by contrast in the west most boulders are perched directly on exposed bedrock or a thin drape of sediment (Figure 4.8b). Where marble bedrock is exposed, it is subject to physical (freeze-thaw) and chemical (carbonation) weathering, producing a pitted or rough microtopography with in-situ produced grus (Figure 4.8c) (Eppes & Griffing 2010), few polished surfaces are found, but where they exist they are heavily striated with fjord-parallel scours (Figure 4.8d).

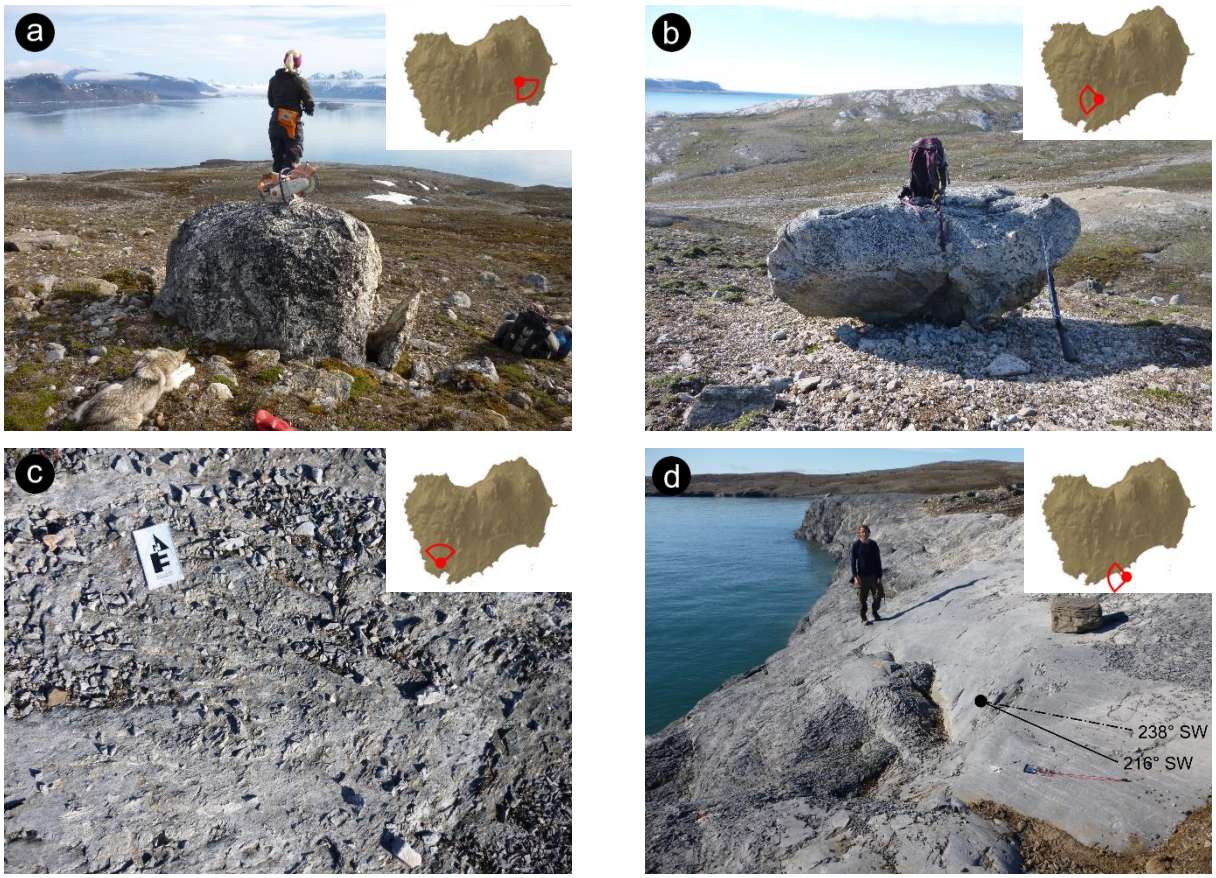

Figure 4.8: (a) Erratic boulder (GOR1406) partially buried by till (Photo: O. Grant 33N 439800 8769100 facing southeast), (b) erratic boulder (BLOM1407) perched on bedrock with thin sediment drape (Photo: O. Grant 33N 437400 8768200 facing west), (c) rough microtopography of chemically weathered marble bedrock and in-situ produced grus (Photo: O. Grant 33N 436200 8767200), and (d) polished bedrock enclave with two fjord-parallel dominant striae (stippled = relatively older) (Photo: O. Grant 33N 438100 8767100 facing west).

4.1.2 Fluvial and glaciofluvial features

Several converging, anastomosing, and diverging fluvial channels are observed on Blomstrandhalvøya, radially draining from the saturated sediments of the Blomstrandsalen plateau. Most channels were actively flowing during the field campaign in August 2015, however a number of channels were abandoned or appear active only ephemerally during the peak melt-season. The karst system on the island also influences the hydrology, with dolines, caves and springs (Lauritzen 2006) augmenting streamflow. Glacial activity on Blomstrandhalvøya has also impacted the pre-existing fluvial system, as well as producing glaciofluvial landforms.

Londonelva is an example of an actively flowing fluvial channel which can be observed immediately north of the settlement of Ny-London, and can be traced for ca. 2.2 km draining from the western summit (Bratliekollen 370 m a.s.l.) of the island, with a range in discharge of 18 L s^{-1} to 43 L s^{-1} and a nival flow regime between June and September (Bogen & Bønsnes 2003; Krawczyk & Pettersson 2007). The channel occupies a normal fault scarp extending north-south across the island (Thiedig & Manby

1992), forming a distinct U-shaped valley (Figure 4.9a) with tributary streams from small side-creeks, and braiding within the coarse diamictic channel sediments produces numerous abandoned channels. Londonelva flows over a waterfall (Jakobskjelda, Figure 4.9b) produced by an imbricated marble thrust-fault scarp (Thiedig & Manby 1992), before entering a braided confluence area and draining into Peirsonhamna (Figure 1.1, Figure 1.2) where a small alluvial fan of sorted sand and gravel is observed.

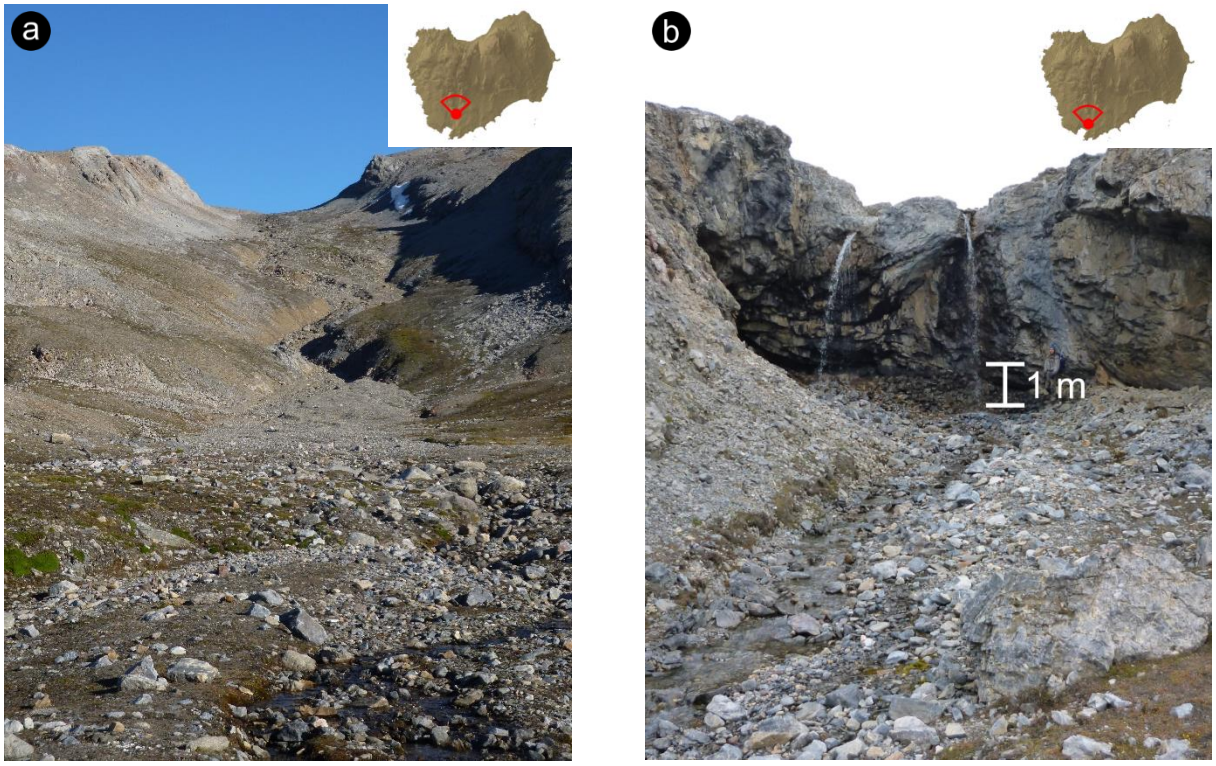

Figure 4.9: (a) The Londonelva channel, the distance to the U-shaped saddle is ca. 1.5 km (Photo: O. Grant 33N 437200 8768000 facing north), and (b) the Jakobskjelda waterfall with scale (Photo: O. Grant 33N 437100 8767800 facing north).

A karstic system has developed in the marble bedrock on Blomstrandhalvøya (Lauritzen 2006), comprising of active and relict caves, dolines, and bogaz-forms whereby faults have been widened into corridors (Ginés *et al.* 2009). The karst system affects the hydrology on the island, an example is the Irgenstjerna doline lake in the northeast of the island (Figure 1.2), the lake occupies a circular depression ca. 250 m in diameter at 140 m a.s.l., the water depth is below ca. 2 m, and very little sediment is visible at the base of the lake (Figure 4.10a) indicating recharge primarily through snowmelt, especially given the raised position of the lake providing a small catchment of ca. 0.07 km^2. There is no active outflow from the lake, however there does appear to be subterranean drainage, supplying a spring approximately 100 m downslope to the north (Lauritzen 2006).

The karst-corridor ca. 1 km north of Ny-London contains a series of collapsed depressions which are connected by a relict drainage channel (Figure 4.10b), while the coarse and angular material within the

depressions is often sorted into polygons or stone stripes implying periglacial reworking of frost-shattered debris.

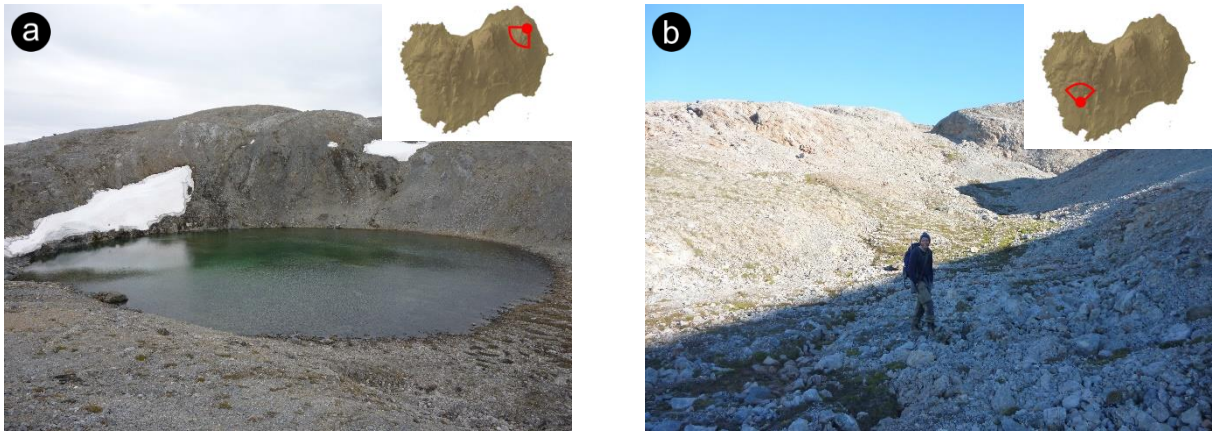

Figure 4.10: (a) Irgenstjerna doline lake at 140 m a.s.l. (Photo: O. Grant 33N 440000 8770700 facing southwest), and (b) bogaz-form located 1 km north of Ny-London, with relict fluvial channel (Photo: O. Grant 33N 436900 8768200 facing north).

The lateral moraines on the northeast of Blomstrandhalvøya (Figure 4.2c) have associated channels which run the length of the moraine ridge (Figure 4.11a), and are interpreted as glaciofluvial drainage channels. The channels appear as nested inset sequences (Benn & Evans 2010) and thus may delimit the retreat of the frozen margins (Dyke 1993) of Blomstrandbreen. The lateral moraine ridges have also re-routed a pre-existing fluvial channel which drained west–east from Blomstrandsalen, the north–south direction producing an alluvial fan immediately outside the Little Ice Age margin (Liestøl 1988) on the east of the island.

To the north of Blomstrandhalvøya, a 130 m long, <1 m high, and 2 m wide sinuous ridge of faintly stratified sand and sub-rounded gravel was observed at ca. 25 m a.s.l. (Figure 4.11b). The feature is interpreted as an esker, likely a sub-glacial tunnel fill given the broad crest (Warren & Ashley 1994), and thus reflects sub-glacial meltwater drainage, the flow direction appears east to west toward the paleo-calving front of Blomstrandbreen, however the ridge is heavily dissected by fluvial channels.

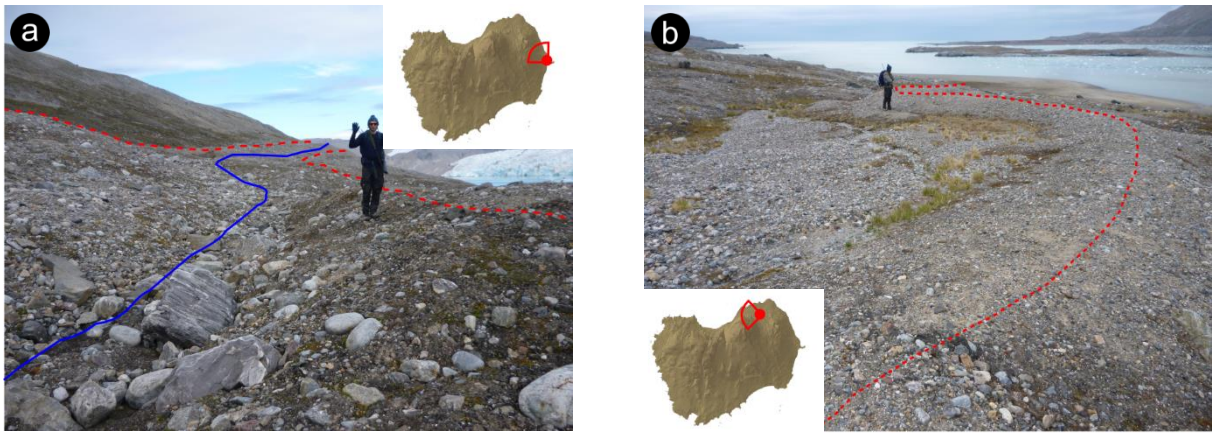

Figure 4.11: (a) A meltwater channel (blue solid line) nested between two lateral moraine crests (red stippled line) on the east of the island (Photo: O. Grant 33N 440700 8770100 facing northwest), and (b) meandering esker (red stippled line) formed of stratified sand and gravel found on the north of the island (Photo: O. Grant 33N 439000 8771100 facing west).

4.1.3 Marine, littoral and shore features

Relative sea level rise outstripped isostatic unloading during the deglaciation of Svalbard, leading to raised sequences of marine landforms and deposition as isostatic uplift overtook eustasy. On Blomstrandhalvøya the highest Late Weichselian marine limit is recognised at 36 m a.s.l. (Figure 2.5 and Figure 4.26) (Lehman & Forman 1992). On the southeast corner of the island, a flight of beach strandlines can be observed on a gentle 3.5° slope up to ca. 27 m a.s.l. (Figure 4.12a), indicating time-transgressive sea level regression of the Island following deglaciation, which would have occurred within 2 ka (Figure 4.26) (Forman *et al.* 1987).

The strandlines are formed in deposits of rounded to sub-rounded gravel and cobble which is sorted and generally lacking fines (Figure 4.12b), such material is found around the southern coastline of the island and close to Øvretjørna lake at 38 m a.s.l. (Figure 1.2). Further along the southern shore of the island, erosional terraces are found at varying elevations, and are filled with sorted gravel often including shell fragments, the highest scarp was found at 37 m a.s.l. (Figure 4.12c), while other distinct terraces occur at 30, 28 (Figure 4.12d), and 17 m a.s.l..

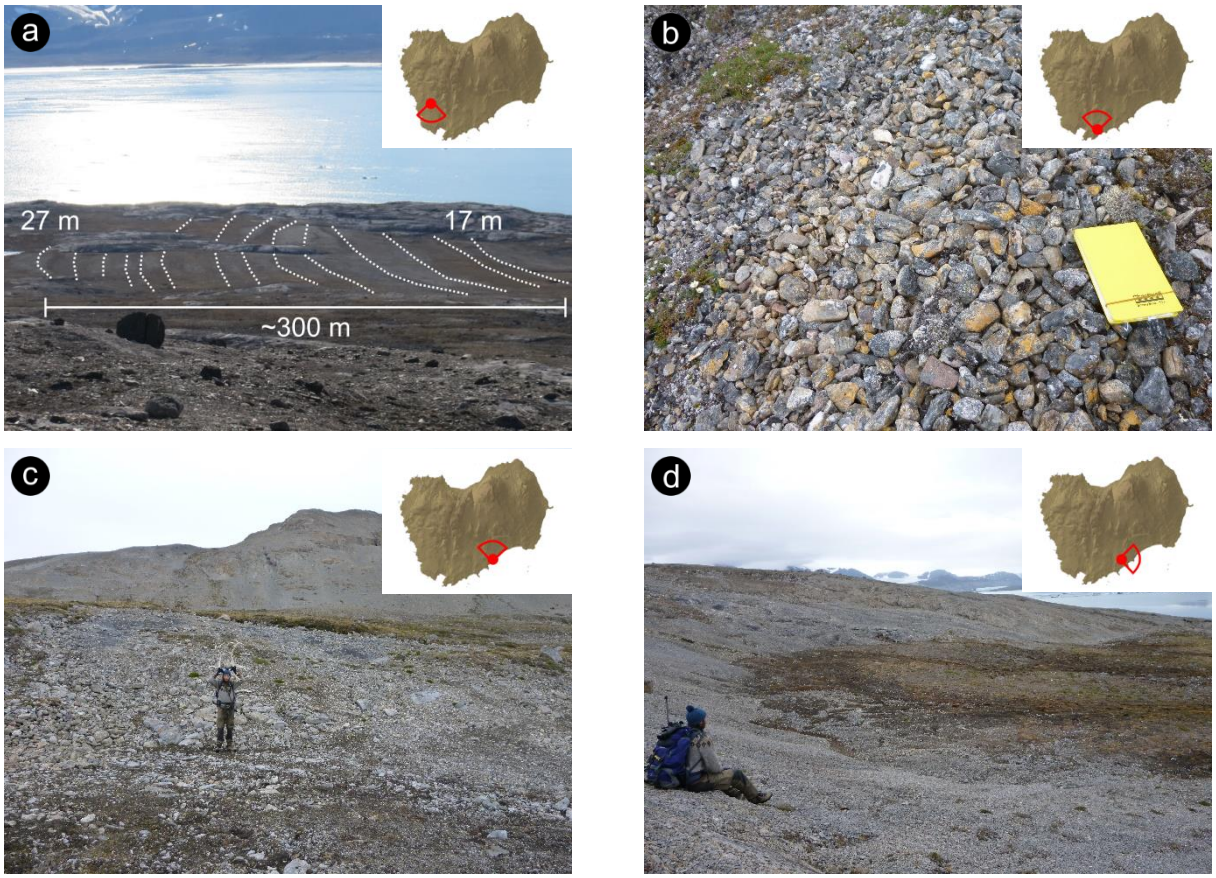

Figure 4.12: (a) Flight of raised beach strandlines (white dotted line) observed in the southeast of the island between 17 and 27 m a.s.l. (Photo: G. Eliassen 33N 436200 8768300 facing south), (b) typical sorted rounded to sub-rounded gravel and cobbles of marine or littoral origin observed on the south of the Island (Photo: O. Grant 33N 437300 8767300, A5 notebook for scale), (c) the highest marine erosional scarp observed at 37 m a.s.l. (Photo: O. Grant 33N 438900 8768300 facing north), and (d) a distinct marine terrace at 28 m a.s.l. with embayment (Photo: O. Grant 33N 438500 8768000 facing east).

4.1.4 Periglacial features

The sediments on Blomstrandsalen are supersaturated during the summer season when the active layer is thawed, cryoturbation has produced expansive areas of patterned ground on the low gradient plateau (Goldthwait 1976; Van Vliet-Lanoë 1988). Networks of asymmetric low-centred cells with a ca. 2 m diameter, coarse outer boundary of angular to sub-rounded erratic cobbles and boulders up to 30 cm high, and a fine silty-sand centre occur frequently (Figure 4.13a). The presence of frost susceptible fines can be explained by autochthonous weathering of carbonate bedrock (Etzelmüller & Sollid 1991), or heterogeneous till of allochthonous origin (Ballantyne & Matthews 1982), although till is not a prerequisite for formation given that sorted circles of frost-shattered debris were observed directly on bedrock (Figure 4.13b), made possible by the annual freeze-thaw cycle despite the thin (<20 cm) sediment cover (Goldthwait 1976).

Slope gradients between 3° and 6° produce sorted ellipses, while slopes between 4° and 11° produce stone stripes due to mass movement of supersaturated sediment induced by gravity (Goldthwait 1976), and such forms are common on the gentler slopes of Blomstrandhalvøya (Figure 4.13c), where stone stripes occur perpendicular to contours.

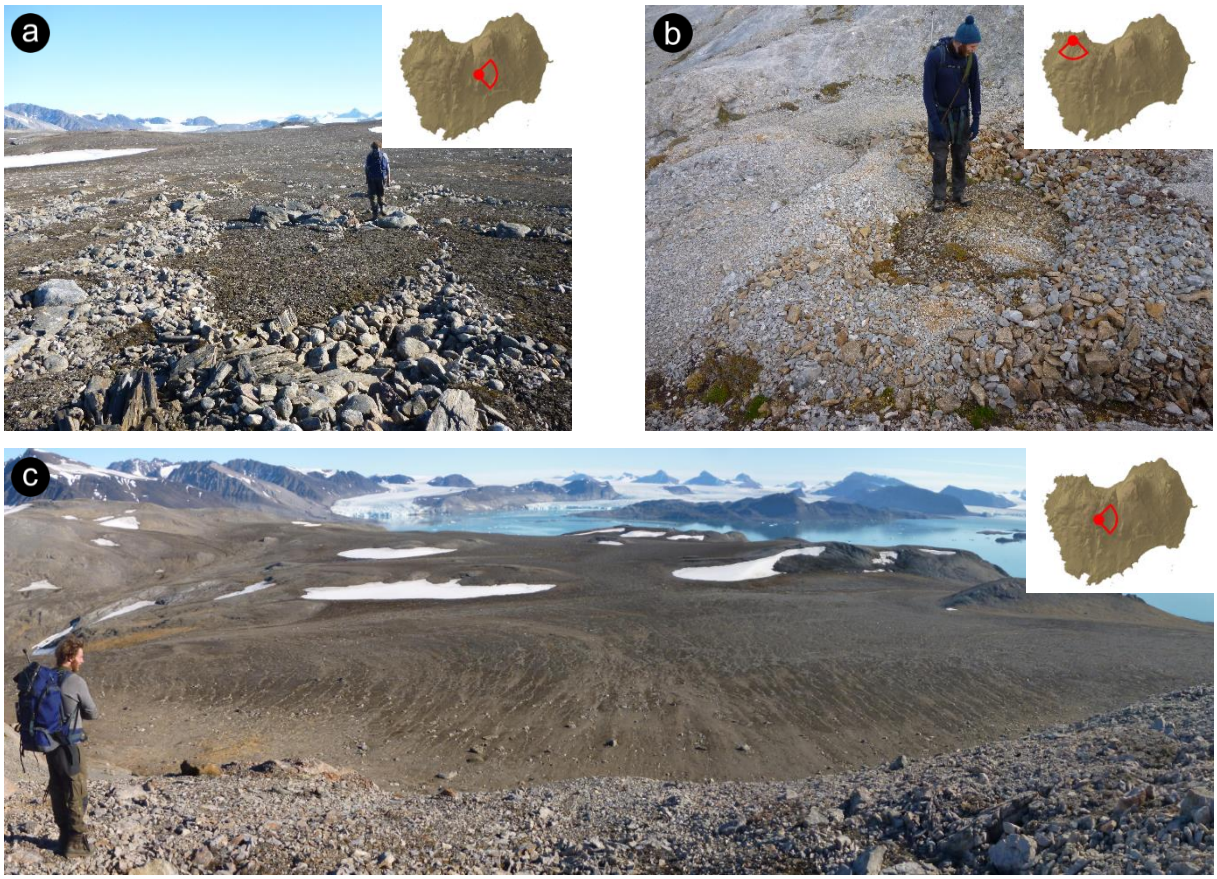

Figure 4.13: (a) Net of low-centred sorted circles on Blomstrandsalen, with coarse blocky boundary and fines-rich centre (Photo: O. Grant 33N 438200 8769200 facing east), (b) sorted circle formed from frost-weathered debris directly on bedrock (Photo: O. Grant 33N 436100 8770900), and (c) a view across the array of patterned ground on Blomstrandsalen, including sorted circles, ellipses, stone stripes, and frost boils (Photo: O. Grant 33N 437300 8769300 facing east).

Similar cryogenic processes may also explain the abundance of hummocky solifluction lobes on the slopes of Blomstrandhalvøya, where the drainage and frost susceptibility of sediments controls the differential heave (Van Vliet-Lanoë 1988), more frost susceptible underlying sediments burst through surface sediments to produce mudboils which can then move downslope as mass wastage (Herz & Andreas 1966b; Van Vliet-Lanoë 1995).

On the north of Blomstrandhalvøya, a break in slope is observed at ca. 60 m a.s.l., protruding up to 30 m from the rock wall, and extending for ca. 300 m along the slope (Figure 4.14a). The feature is composed primarily of coarse angular talus (Figure 4.14b), and has a gradient exceeding 45°, with depressions on the top (Figure 4.14c), and meltwater draining from the foot. The feature is identified

as a talus-derived rock glacier (Humlum 1982a; Humlum 1982b), and is briefly mentioned in literature (Svendsen *et al.* 2002). The feature occurs below a graphitic quartz-carbonate schist outcrop (Figure 2.1a) (Hjelle *et al.* 1999), indicating a lithological control on the sediment supply and subsequent formation of the rock glacier, implying a complex interaction between physiographic and climatic parameters controlling rock glacier evolution (Humlum 1998; Frauenfelder *et al.* 2003).

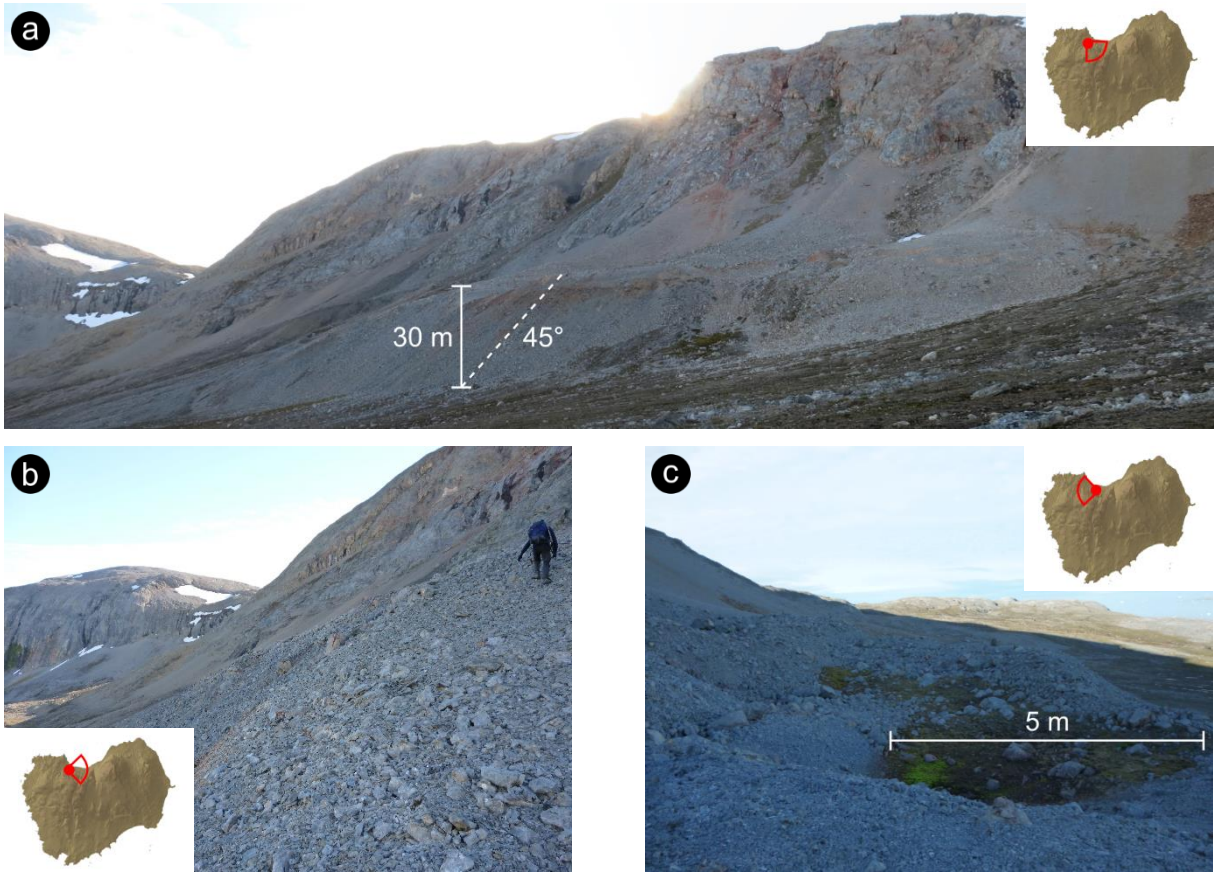

Figure 4.14: (a) The rock glacier on the northern slope of Blomstrandhalvøya, up to 30 m high and with a gradient around the angle of repose (Photo: G. Eliassen 33N 437000 8770300 facing southeast), (b) the angular talus forming the steep face of the rock-glacier (Photo: O. Grant 33N 437100 8770400 facing east), and (c) the ridge-and-furrow topography (Humlum 2000) on the surface of the rock glacier, some depressions were ponded (Photo: O. Grant 33N 437300 8770400 facing west).

On the north-eastern slopes of the island, hummocky terrain was encountered, with irregular topography and mass wastage of saturated diamictic material. Such slumping is likely related to melt-out of buried dead-ice from Blomstrandbreen (Figure 4.15), which was observed up to ca. 100 m a.s.l. (Vivian 1965). On the eastern slope of Blomstrandhalvøya, a fresh looking slide was observed ca. 40 m a.s.l., occurring in saturated clay-rich diamicton (Figure 4.16), and may be related to active layer thawing and supersaturation of sediment, exacerbated by snowmelt and karst spring activity. The ca. 20 m^2 feature is identified as a thaw slump, with characteristic headwall scarp and debris tongue (Kokelj *et al.* 2015), occurring on a moderate to strong slope inclined at 16°, and may be indicative of permafrost degradation on the island.

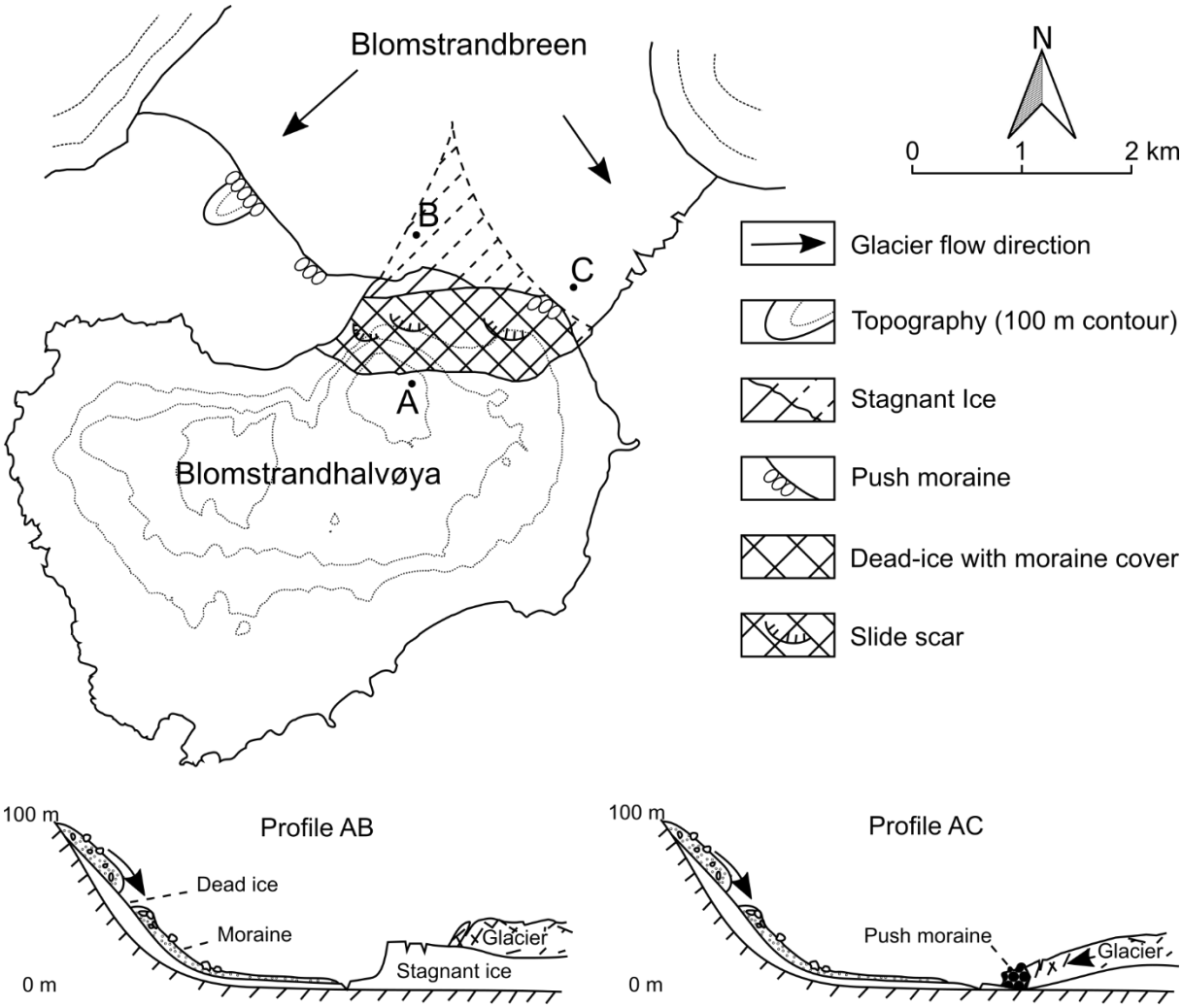

Figure 4.15: Dead-ice topography on the northern slope of Blomstrandhalvøya from melt-out of buried ice, with the 1963–64 Blomstrandbreen ice front position mapped. Profiles show stagnant ice being overridden by an active glacier reflecting the recorded surge of 1966 (Sund & Eiken 2010), producing the push moraines observed on the northern tip of the island (Figure 4.3b), modified from Vivian (1965).

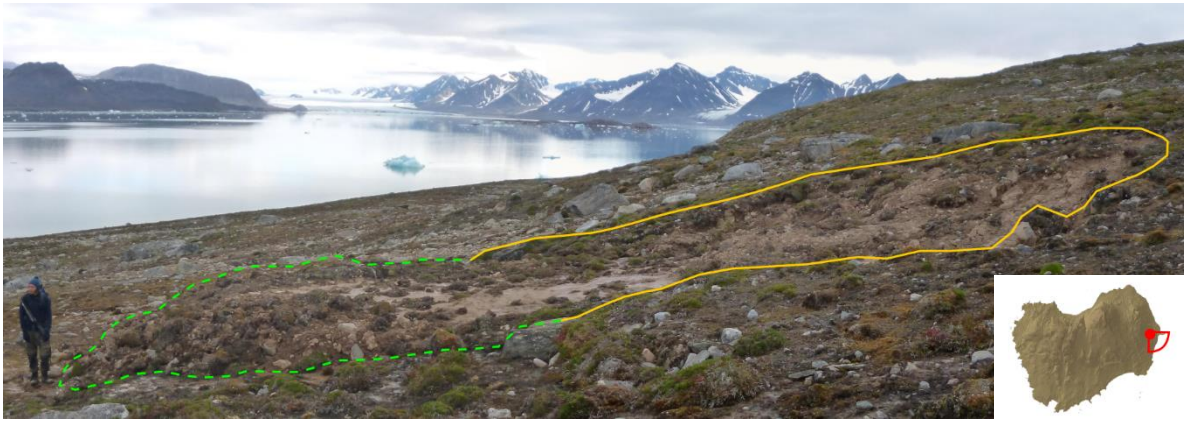

Figure 4.16: Thaw slump observed in saturated clay-rich diamicton on the eastern slope of Blomstrandhalvøya, with headwall scarp (solid yellow line) and debris tongue (green stippled) (Photo: O. Grant 33N 440400 8769900 facing southeast).

4.1.5 Sediment stratigraphy

A natural sediment section was observed in the upper reach of the Londonelva catchment at ca. 189 m a.s.l., as the stream has incised into the underlying sediments (Figure 4.17). Due to the steepness of the section and compaction of the diamicton, the section was examined through several windows which were excavated and cleaned with a shovel and trowel, a metre rule was used to aid logging, which was combined into a composite log. The section contains three units which were subsequently subdivided based on visible horizons and changes in clast size and roundness.

Unit C is a ca. 2.9 m thick matrix supported coarse to medium sandy diamicton with sub-angular to sub-rounded clasts of non-local lithology. The lower sub-unit C3 has an upward-coarsening matrix and a high occurrence of angular to sub-angular gravel sized clasts, and has a sharp upper contact with C2. The gradational boundary between C2 and C1 is marked by a lag of sub-angular to sub-rounded cobbles, the size of the clasts decreases upwards in C1. Unit C is interpreted as a till.

Unit B is a clast supported sub-angular to sub-rounded gravel horizon of ca. 25 cm, and has no oversized clasts, the unit also has a gradational lower and sharp upper boundary. Unit B is interpreted as fluvial gravel. The upper ca. 1.7 m represents unit A, consisting of angular to sub-angular clasts of local origin, namely marble and conglomerates, in a medium to coarse sandy matrix. Unit A is subdivided into four sub-units; A4 consists of gravel sized clasts with a sharp upper boundary to A3, which has a slightly fining-upward matrix and a sharp upper boundary to A2, consisting of cobble to boulder sized angular and sub-angular clasts with some erratic lithologies, grading into A1 which contains angular and sub-angular gravels in a matrix of medium sand with some silt fraction. Unit A is interpreted as colluvium.

The sedimentary package in the Londonelva channel may therefore represent deposition of basal till by glacial over-riding (Unit C), which was subsequently incised and sorted by a meltwater stream (Unit B), later filled-in by colluvium from the adjacent valley-side (unit A), and thus re-exposed by the present incision of the Londonelva stream. An alternative interpretation of the sediment package in the Londonelva catchment could be that Unit A and Unit C are both till, with Unit A representing a re-advance over the Late Weichselian till (Unit C), separated by a period of melt and retreat producing the sorted gravels in Unit B.

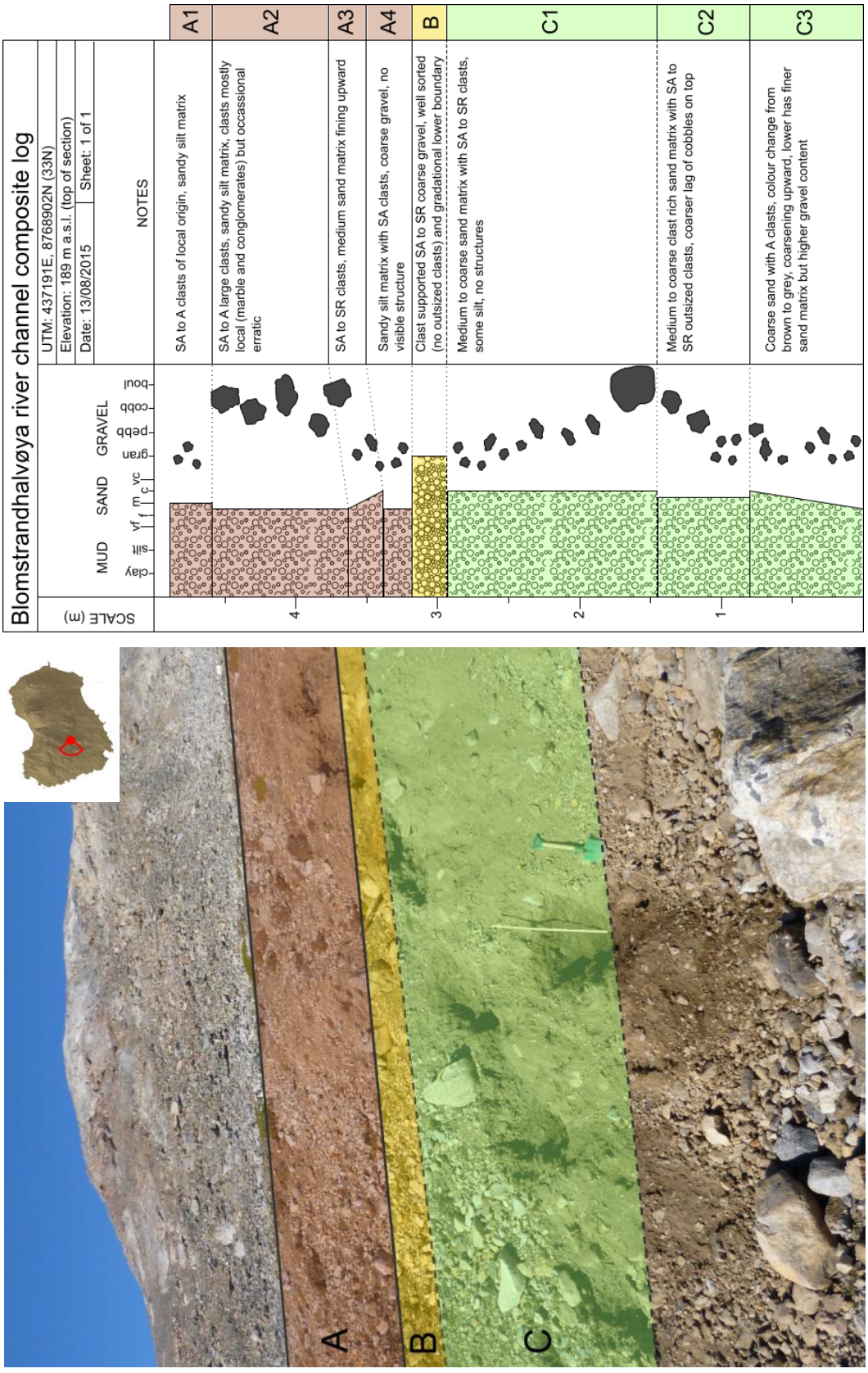

Figure 4.17: Sediment section in the upper reach of the Londonelva catchment, with excavated sections and composite log (Photo: O. Grant 33N 437200 8768900 facing west, shovel and metre rule for scale).

4.2 Exposure dating transects

As described previously, samples for exposure dating were retrieved from three transects covering lateral and vertical dimensions. The western transect on Blomstrandhalvøya (BLOM) consists of twelve samples ranging from 49 m to 367 m a.s.l., with boulders sampled along the exposed weathered bedrock ridges of the Londonelva catchment (Figure 4.30, Appendix A). The eastern transect on Blomstrandhalvøya (GOR) includes the summit of Irgensfjellet at 387 m and down to 131 m a.s.l. with seven boulders sampled on the largely sediment covered slope to Gorilla-Heimen (Figure 1.2, Figure 4.33, Appendix B). A further six samples were taken between 122 m and 360 m a.s.l. from Ossian Sarsfjellet (SARS) at the head of Kongsfjorden, of which two samples were taken from quartz veins in the mica-schist bedrock (Figure 4.36, Appendix C).

4.2.1 BLOM transect sample description

BLOM1401 (33N 437061 8768045, 79 m a.s.l., Figure 4.18a, Figure A.1) – a sub-angular to sub-rounded grey granite boulder measuring 90 cm x 130 cm x 130 cm (height x length x width), perched on marble bedrock with a thin drape of diamicton. Quartz, feldspar and biotite are visible at the surface, which has a roughness not exceeding 2 mm, indicating minimal grain-by-grain weathering. The boulder has minor lichen coverage and little evidence of biologically enhanced chemical weathering. The relatively exposed position of BLOM1401 ensures limited shielding from surrounding topography.

BLOM1402 (33N 437051 8768041, 78 m a.s.l., Figure 4.18a, Figure A.2) – a sub-angular to sub-rounded grey granite boulder situated ca. 10 m from BLOM1401, the boulder measures 100 cm x 155 cm x 120 cm, and is perched on bedrock with a thin drape of diamicton. BLOM1402 has quartz and feldspar grains protruding the surface, giving a roughness around 3 mm, indicating minimal grain-by-grain weathering, while the topographic shielding is the same as BLOM1401.

BLOM1403 (33N 436975 8768247, 100 m a.s.l., Figure 4.18b, Figure A.3) – an angular to sub-angular granitic gneiss boulder rich in biotite and mica, measuring 150 cm x 240 cm x 200 cm perched on bedrock and smaller erratic clasts. The boulder has an undulating surface topography with a maximum roughness of 5 mm, and a near-continuous lichen cover on the flat surface. As BLOM1403 is situated on an exposed slope of <10°, the topographic shielding is low.

Figure 4.18: (a) BLOM1401 and BLOM1402 perched on exposed bedrock with a thin drape of diamicton (Photo: A. Hormes facing southeast, persons for scale), and (b) BLOM1403 perched on bedrock and smaller erratic boulders (Photo: O. Grant facing north, person for scale).

BLOM1405 (33N 437411 8768513, 162 m a.s.l., Figure 4.19a, Figure A.4) – a large sub-angular to sub-rounded fine-grained grey granite boulder measuring 200 cm x 400 cm x 350 cm is perched on bedrock and diamicton. The sediments beneath the boulder may be creeping, but no evidence in the field suggests rotation of the boulder. Biotite is seen at the surface of the boulder, which has a maximum roughness of 2 mm. The slightly irregular sub-angular geometry of BLOM1405 provides some self-shielding, and the local slope provides minor topographic shielding.

BLOM1406 (33N 437428 8768182, 104 m a.s.l., Figure 4.19b, Figure A.5) – a sub-angular to rounded grey granite boulder measuring 160 cm x 290 cm x 200 cm is perched on bedrock and diamicton. The surface has a maximum roughness of 2 mm, with some feldspar and quartz grains protruding but no mica visible at the surface. Lichen growth is restricted to the upper face of the boulder suggesting wind-polishing or snow shielding, and the surrounding topography provides minimal shielding.

BLOM1407 (33N 437387 8768164, 101 m a.s.l., Figure 4.19c, Figure A.6) – a sub-angular to sub-rounded anvil-shaped grey granite boulder measuring 150 cm x 200 cm x 150 cm is perched on bedrock, close to the edge of the ridge demarcating the eastern limit of the Londonelva catchment. Polished quartz grains are visible at the uniform surface, which has a maximum roughness of 2 mm and restricted lichen growth. The surrounding topography provides minimal shielding.

Figure 4.19: (a) BLOM1405 located on bedrock and diamicton (Photo: O. Grant facing east, backpack and rifle for scale), (b) BLOM1406 perched on bedrock and a thin drape of diamicton (Photo: O. Grant facing north, backpack for scale), and (c) The anvil shaped BLOM1407 perched on bedrock ridge overlooking the Londonelva catchment (Photo: O. Grant facing west, backpack and rifle for scale).

BLOM1408 (33N 437290 8768100, 80 m a.s.l., Figure 4.20a, Figure A.7) – a sub-angular to sub-rounded grey granite boulder measuring 200 cm x 200 cm x 150 cm is perched on bedrock. Quartz and feldspar is visible at the surface, but no mica or biotite, the surface roughness does not exceed 2 mm, but extensive lichen growth and abundant guano may suggest increased biologically enhanced chemical weathering. The topography surrounding BLOM1408 provides little shielding.

BLOM1409 (33N 437260 8767890, 49 m a.s.l., Figure 4.20b, Figure A.8) – an angular to sub-rounded granitic gneiss boulder measuring 220 cm x 250 cm x 200 cm, perched on bedrock and a thin drape of diamicton. Larger quartz and feldspar grains can be observed on the surface, which has a maximum roughness of ca. 4 mm and a thin cover of lichen and guano. The topographic shielding of BLOM1409 by the surrounding landscape is small.

BLOM1410 (33N 436975 8769284, 303 m a.s.l., Figure 4.20c, Figure A.9) – a sub-rounded to rounded grey granite boulder measuring 150 cm x 200 cm x 140 cm is perched on bedrock and scree/grus from an adjacent marble outcrop. The upper surface of the boulder has been fairly weathered, leading to a separation of the upper surface from the main boulder body at ca. 0.5 cm depth, which has been re-cemented in places with a secondary precipitate, likely kaolinite derived from feldspar decomposition. The surface is relatively uniform with quartz and feldspar visible, a maximum roughness of 2 mm, and limited lichen cover. The aforementioned adjacent outcrop provides spatially-limited topographic shielding otherwise offset by the exposed location of BLOM1410.

Figure 4.20: (a) BLOM1408 perched on a bedrock shelf (Photo: O. Grant facing east, backpacks for scale), (b) BLOM1409 perched partly on bedrock (Photo: O. Grant facing east, backpacks for scale), and (c) BLOM1410 located on bedrock and grus from adjacent marble outcrop (Photo: O. Grant facing south, person for scale).

BLOM1411 (33N 437472 8769629, 369 m a.s.l., Figure 4.21a, Figure A.10) – a sub-rounded to rounded rhomboidal-shaped grey granite boulder with the dimensions; 120 cm x 175 cm x 150 cm, perched on a bedrock shelf close to the summit of Bratliekollen. Some small cracks are visible on the surface, as are larger quartz and feldspar grains providing a maximum surface roughness of ca. 4 mm. Despite the exposed location of BLOM1411, there is some local shielding from an adjacent larger erratic boulder.

BLOM1412 (33N 437381 8768829, 194 m a.s.l., Figure 4.21b, Figure A.11) – a sub-rounded to rounded grey granite boulder measuring 80 cm x 95 cm x 75 cm is perched on bedrock and talus on a platform formed by a break in slope. It was necessary to remove a man-made cairn from the surface of the boulder, which otherwise shows some wind-polishing, guano and limited lichen cover. Quartz and feldspar grains can be seen protruding the surface but provide a maximum roughness of ca. 3 mm. The proximity of BLOM1412 to the slope results in a relatively high degree of topographic shielding.

BLOM1413 (33N 436935 8769640, 316 m a.s.l., Figure 4.21c, Figure A.12) – a sub-angular to sub-rounded grey granite boulder found distal to a morainal ridge, the boulder measures 170 cm x 220 cm x 200 cm, and is perched on bedrock. The surface of BLOM1413 is fairly weathered, with weaknesses exploited at a depth of ca. 1 cm producing sheets with secondary precipitate cementing the cracks. Quartz and feldspar grains are visible at the surface, which has a maximum roughness of ca. 2 mm and a relatively thick lichen and guano cover. The exposed position of the boulder ensures minimal topographic shielding.

68-BRATLIE (33N 437172, 8769740, 341 m a.s.l., Figure 4.21d) – a large angular to sub-angular quartz-biotite schist boulder, measuring 250 cm x 650 cm x 400 cm, perched on bedrock and diamicton on the westernmost summit of Blomstrandhalvøya. The boulder has minimal lichen cover, but guano is found on the upper surface, while large slabs appear to have spalled off the parent boulder. The 32° inclination toward 260° presents an element of self-shielding despite the boulders exposed position.

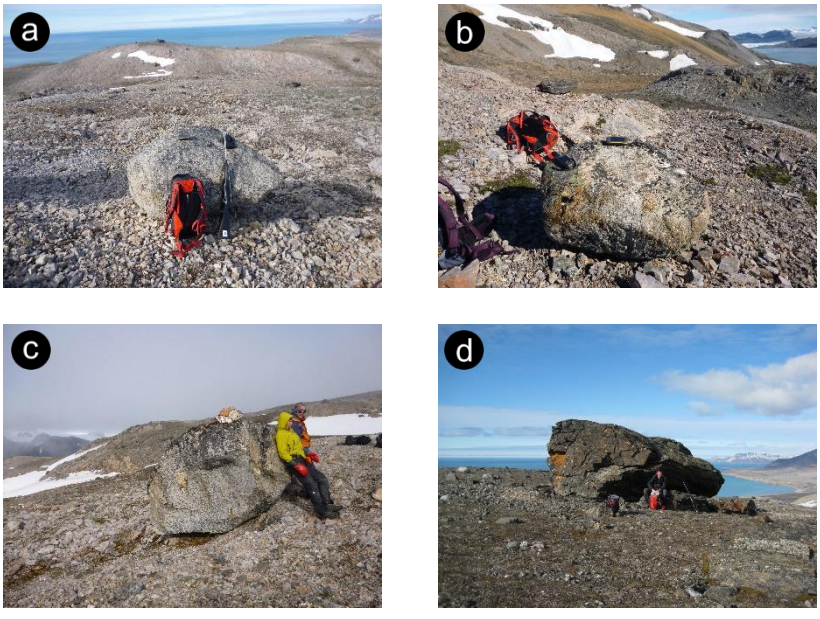

Figure 4.21: (a) BLOM1411 perched on bedrock on the summit of Bratliekollen (Photo: O. Grant facing west, backpack and rifle for scale), (b) BLOM1412 located on a bedrock shelf (Photo: O. Grant facing east, backpack and GPS for scale), (c) BLOM1413 perched on bedrock and found distal to a moraine feature out of frame (Photo: O. Grant facing northwest, persons for scale), and (d) 68-BRATLIE on mixed substrate of bedrock and diamicton, on the westernmost summit of Blomstrandhalvøya (Photo: H. Linge facing west, person for scale).

4.2.2 GOR transect sample description

GOR1401 (33N 439792 8769927, 210 m a.s.l., Figure 4.22a, Figure B.1) – an angular to sub-angular granitic gneiss boulder measuring 120 cm x 270 cm x 180 cm, perched on diamicton on a shallow gradient <5° with no evidence of post-depositional movement. Minimal lichen growth on the surface of the boulder, and minimal weathering, with quartz, feldspar and mica visible at the surface which has a maximum roughness of ca. 2 mm. The surrounding topography provides minimal shielding.

GOR1402 (33N 439924 8769998, 211 m a.s.l., Figure 4.22b, Figure B.2) – a sub-angular to sub-rounded grey granite boulder measuring 50 cm x 100 cm x 90 cm, perched on diamicton close to the edge of the slope. The boulder has a flat upper surface with limited weathering and lichen growth, and the small size of the boulder may mean it has been sediment and/or snow covered in its depositional history. Larger quartz and feldspar grains protrude the surface which has a roughness of ca. 3 mm, while the surrounding landscape provides minor shielding.

GOR1403 (33N 438960 8769240, 288 m a.s.l., Figure 4.22c, Figure B.3) – a sub-rounded to rounded grey granite boulder measuring 100 cm x 220 cm x 100 cm, perched on diamicton at the top of the slope. The boulder has a man-made cairn or N.E.C. claim sign on top of its flat surface, which displays minimal weathering or lichen growth, but a relatively high surface roughness up to 7 mm. The exposed position of GOR1403 ensures minimal topographic shielding.

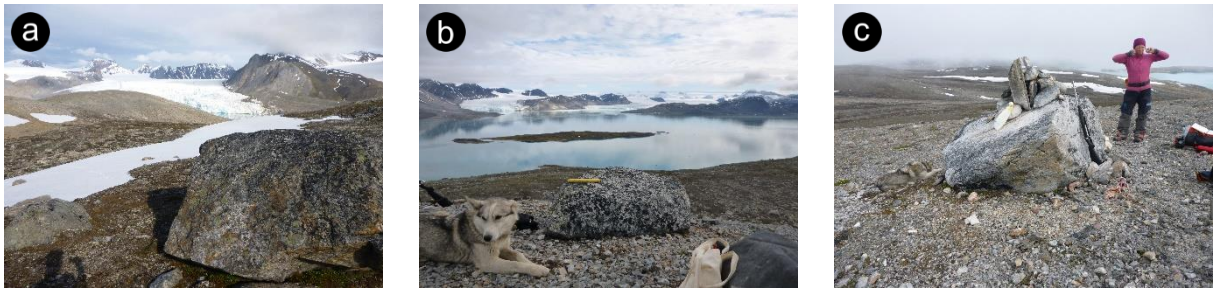

Figure 4.22: (a) GOR1401 perched on diamicton at the top of the slope (Photo: O. Grant facing north), (b) GOR1402 perched on the edge of the slope partly on bedrock (Photo: O. Grant facing east, dog for scale), and (c) GOR1403 with man-made cairn or N.E.C. claim post (Photo: O. Grant facing north, person for scale).

GOR1404 (33N 439306 8769072, 197 m a.s.l., Figure 4.23a, Figure B.4) – a sub-angular to sub-rounded grey granite boulder measuring 95 cm x 200 cm x 160 cm, is perched partly and bedrock and partly within solifluction material close to the edge of a ca. 35° slope. Some of the boulders surface shows enhanced weathering from lichen and guano, with larger quartz and feldspar protruding the surface, of which the sampled area had a surface roughness of ca. 2 mm. Due to the slope-edge position of GOR1404, there is relatively high topographic shielding.

GOR1405 (33N 439413 8768939, 166 m a.s.l., Figure 4.23b, Figure B.5) – a large flat-topped angular to sub-angular fine-grained grey granite boulder, measuring 160 cm x 200 cm x 160 cm, perched on bedrock close to the edge of a ca. 30° slope. The surface is slightly weathered with oxidisation staining and restricted lichen growth, the uniform surface has a maximum roughness of 2 mm. The steep marble cliffs in the vicinity of GOR1405 provide a relatively high degree of topographic shielding.

GOR1406 (33N 439751 8769146, 131 m a.s.l., Figure 4.23c, Figure B.6) – a large sub-angular to sub-rounded grey granite boulder measuring 120 cm x 340 cm x 250 cm, is found within solifluction material from a degraded lateral moraine. Quartz, feldspar, biotite, and mica are visible at the surface, which has a maximum roughness of ca. 3 mm, with some cracks cemented by a secondary precipitate. The local topography has a minor but not negligible influence on the overall shielding of GOR1406.

69-IRGENS (33N 438787 8770531, 382 m a.s.l., Figure 4.23d) – A sub-rounded grey granite boulder measuring 60 cm x 120 cm x 110 cm, located on the summit of Irgensfjellet, its exposed position means no topographic shielding. The boulder surface shows some flaking on the outer edges and possible wind polishing, with limited lichen cover.

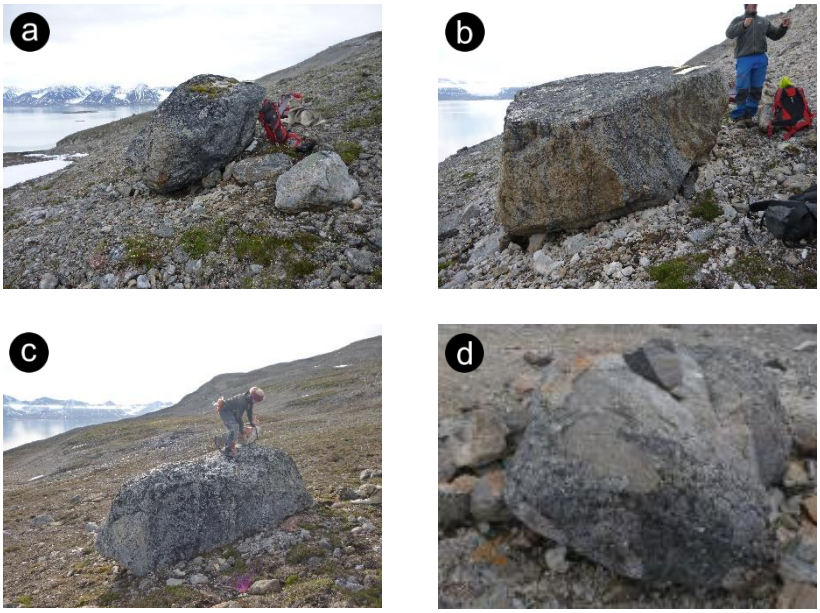

Figure 4.23: (a) GOR1404 perched partly on bedrock with solifluction material on the ca. 35° slope (Photo: O. Grant facing south, backpack for scale), (b) GOR1405 perched partly on bedrock close to a trimline (Photo: O. Grant facing south, person for scale), (c) GOR1406 on diamicton at the edge of a possible degraded moraine (Photo: O. Grant facing southwest, person for scale), and (d) 69-IRGENS perched on bedrock and small erratic blocks on the summit of Irgensfjellet (Photo: O. Grant).

4.2.3 SARS transect sample description

SARS1401 (33N 446124 8765801, 154 m a.s.l., Figure 4.24a, Figure C.1) – a well-rounded to rounded grey granite boulder measuring 60 cm x 90 cm x 70 cm, perched on mica-schist bedrock. Larger quartz and feldspar grains are visible at the surface, which has limited lichen growth, and has a maximum roughness of ca. 3 mm, and the local topography has minimal shielding effect.

SARS1402 (33N 446142 8765785, 167 m a.s.l., Figure 4.24b, Figure C.2) – a sample taken from a protruding quartz vein in mica-schist bedrock, the vein extends up to 50 cm above the surrounding surface, and runs for ca. 5 m. The surface of the sample has small fractures infilled by lichen, and a maximum surface roughness of ca. 4 mm. Surrounding topography has a minor shielding effect.

SARS1404 (33N 445828 8764686, 360 m a.s.l., Figure 4.24c, Figure C.3) – a sub-angular to sub-rounded granitic gneiss boulder perched on fractured mica-schist bedrock close to the summit of Ossian Sarsfjellet. The boulder measures 50 cm x 65 cm x 40 cm, and has some larger quartz grains visible at the surface, which has a roughness <4 mm and limited lichen growth potentially reflecting the exposed position of the boulder, such exposure leads to minimal topographic shielding.

Figure 4.24: (a) SARS1401 rounded grey granite boulder perched on bedrock (Photo: O. Grant facing north, 20 cm ruler for scale), (b) the quartz vein in the mica-schist bedrock where SARS1402 was retrieved (Photo: O. Grant facing north, hammer for scale), and (c) SARS1404 situated close to the summit of Ossian Sarsfjellet (Photo: H. Linge facing west, GPS for scale).

SARS1405 (33N 446428 8766192, 125 m a.s.l., Figure 4.25a, Figure C.4) – a sub-rounded with flat upper surface grey granite boulder measuring 30 cm x 70 cm x 50 cm, and perched on a mica-schist bedrock shelf. Feldspars and quartz grains are visible at the surface of the sample, with some lichen coverage and a maximum surface roughness of ca. 3 mm. The surrounding topography provides minimal shielding.

SARS1406 (33N 446425 8766183, 122 m a.s.l., Figure 4.25b, Figure C.5) – a sample taken from a quartz vein in mica-schist bedrock underlying SARS1405, the blocky nature of the bedrock implies some plucking which must have been precedent or coincident with the deposition of erratics such as SARS1405. The sample was retrieved from polished quartz outcrops, which have limited lichen growth and a smooth surface with a roughness <2 mm. The shielding is identical to SARS1405.

SARS1407 (33N 445952 8765429, 210 m a.s.l., Figure 4.25c, Figure C.6) – a sub-angular biotite-rich grey granite boulder measuring 30 cm x 100 cm x 65 cm, is perched on mica schist bedrock in an exposed location less than 6 m from the slope edge in all directions. The boulder has a slight concave surface geometry with evidence of water pooling, while the boulder also exhibits weathering of mica and feldspars and fairly extensive lichen cover, giving an overall surface roughness of ca. 5 mm. The surrounding topography provides minimal shielding.

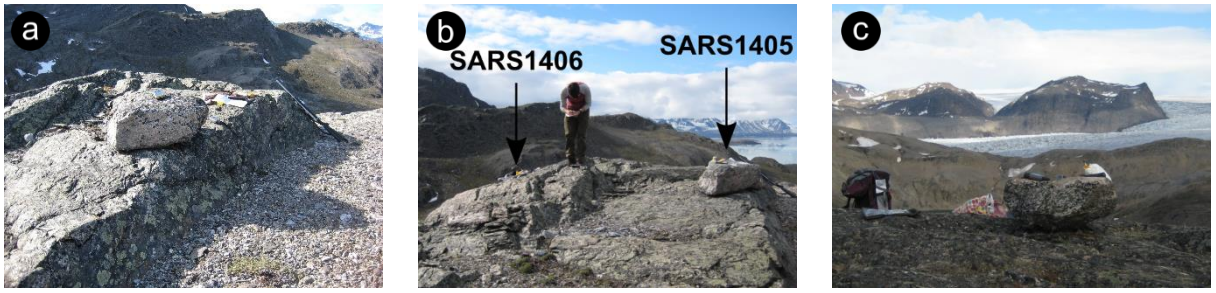

Figure 4.25: (a) SARS1405 perched on a mica-schist bedrock shelf (Photo: H. Linge facing northwest, rifle for scale), (b) bedrock sample SARS1406 is within close proximity to the erratic boulder SARS1405 (Photo: H. Linge facing west, person for scale), and (c) SARS1407 in an exposed location close to the edge of the slope (Photo: H. Linge facing north, backpack for scale).

Table 4.1: Sample information and cosmogenic nuclide data from Blomstrandhalvøya and Ossian Sarsfjellet.

Sample[a]	Latitude (°N)	Longitude (°E)	Elevation (m a.s.l.)	Lithology[b]	Topo-shielding factor[c]	Thickness[d] (cm)	Quartz[e] (g)	^{9}Be carrier[f] (g)	^{10}Be/^{9}Be[g,h] (x10^{-15})	^{10}Be Conc.[i,j] (x10^{4} at g^{-1} SiO_2)	Uncorrected ^{10}Be age[k,l] (ka)	Corrected ^{10}Be age[m] (ka)
BLOM1401	78.968475	12.052400	79	gran.	0.9995	2.95	27.14	0.2404	116.15 ± 3.37	65.56 ± 2.22	13.21 ± 0.68 (0.45)	13.42 ± 0.69 (0.46)
BLOM1402	78.968435	12.051941	78	gran.	0.9995	3.12	25.15	0.2412	123.42 ± 3.82	75.62 ± 2.67	15.28 ± 0.80 (0.54)	15.53 ± 0.81 (0.55)
BLOM1403	78.970244	12.047901	100	gran. gne.	0.9994	2.69	29.76	0.2405	125.89 ± 3.75	65.07 ± 2.21	12.80 ± 0.66 (0.44)	12.99 ± 0.67 (0.44)
BLOM1405	78.972821	12.067663	162	gran.	0.9986	1.67	27.16	0.2413	125.38 ± 3.79	71.22 ± 2.45	12.99 ± 0.67 (0.45)	13.20 ± 0.68 (0.46)
BLOM1406	78.969866	12.069236	104	gran.	0.9993	3.31	24.24	0.2412	101.18 ± 3.08	63.69 ± 2.32	12.53 ± 0.66 (0.46)	12.72 ± 0.67 (0.47)
BLOM1407	78.969687	12.067361	101	gran.	0.9987	2.26	24.20	0.2415	119.97 ± 3.62	76.38 ± 2.65	14.96 ± 0.77 (0.52)	15.20 ± 0.79 (0.53)
BLOM1408	78.969071	12.062976	80	gran.	0.9986	2.47	25.00	0.2422	116.74 ± 3.46	72.08 ± 2.48	14.47 ± 0.75 (0.50)	14.70 ± 0.76 (0.51)
BLOM1409	78.967178	12.062068	49	gran. gne.	0.9991	1.11	25.94	0.2411	103.25 ± 3.27	60.78 ± 2.27	12.49 ± 0.67 (0.47)	12.68 ± 0.68 (0.48)
BLOM1410	78.979523	12.045444	303	gran.	0.9985	2.64	24.86	0.2426	113.41 ± 3.60	70.43 ± 2.58	11.19 ± 0.59 (0.41)	11.35 ± 0.60 (0.42)
BLOM1411	78.982834	12.067892	367	gran.	0.9987	3.32	25.76	0.2413	169.52 ± 5.00	102.70 ± 3.30	15.39 ± 0.77 (0.50)	15.63 ± 0.79 (0.51)
BLOM1412	78.975635	12.065516	194	gran.	0.9915	2.46	25.75	0.2388	130.84 ± 3.73	77.74 ± 2.52	13.91 ± 0.70 (0.45)	14.11 ± 0.71 (0.46)
BLOM1413	78.982690	12.042728	316	gran.	0.9999	2.30	26.85	0.2414	155.05 ± 4.59	89.89 ± 2.94	14.04 ± 0.71 (0.46)	14.26 ± 0.72 (0.47)
68-BRATLIE	78.983692	12.053586	341	qz.-b. sch.	0.9723	4.50	30.42	0.6079	164.10 ± 3.47	81.60 ± 1.72	14.24 ± 0.62 (0.30)	14.46 ± 0.63 (0.31)
GOR1401	78.986526	12.175831	210	gran. gne.	0.9997	2.80	27.25	0.2410	233.10 ± 6.62	134.50 ± 4.05	23.58 ± 1.15 (0.71)	23.99 ± 1.18 (0.73)
GOR1402	78.987218	12.181852	211	gran.	0.9997	1.00	23.24	0.2428	155.96 ± 4.66	105.07 ± 3.45	18.11 ± 0.92 (0.60)	18.41 ± 0.93 (0.61)
GOR1403	78.980015	12.138446	288	gran.	0.9999	2.46	27.36	0.2399	155.99 ± 9.23	89.40 ± 5.47	14.39 ± 1.04 (0.88)	14.61 ± 1.06 (0.90)
GOR1404	78.978663	12.155024	197	gran.	0.9959	2.96	25.41	0.2411	75.67 ± 2.56	45.86 ± 1.86	8.16 ± 0.46 (0.33)	8.28 ± 0.46 (0.34)
GOR1405	78.977519	12.160335	166	gran.	0.9957	3.31	26.25	0.2408	261.09 ± 7.65	157.90 ± 4.80	29.26 ± 1.44 (0.90)	29.80 ± 1.47 (0.92)
GOR1406	78.979519	12.175682	131	gran.	0.9986	3.22	25.07	0.2413	104.06 ± 3.92	64.78 ± 2.69	12.37 ± 0.70 (0.52)	12.56 ± 0.71 (0.52)
69-IRGENS	78.989880	12.127788	382	gran.	1.0000	1.60	20.33	0.2264	120.73 ± 2.34	89.85 ± 1.75	14.30 ± 0.61 (0.28)	14.53 ± 0.63 (0.28)

Sample[a]	Latitude (°N)	Longitude (°E)	Elevation (m a.s.l.)	Lithology[b]	Topo-shielding factor[c]	Thickness[d] (cm)	Quartz[e] (g)	^{9}Be carrier[f] (g)	^{10}Be/^{9}Be[g,h] (x10^{-15})	^{10}Be Conc.[i,j] (x10^{4} at g^{-1} SiO_2)	Uncorrected ^{10}Be age[k,l] (ka)	Corrected ^{10}Be age[m] (ka)
SARS1401	78.952193	12.480793	154	gran.	0.9992	0.33	26.46	0.2405	150.22 ± 4.55	89.16 ± 2.91	16.25 ± 0.82 (0.53)	16.50 ± 0.83 (0.54)
SARS1402	78.952056	12.481666	167	quartz	0.9979	1.31	25.99	0.2415	149.17 ± 4.47	90.51 ± 2.93	16.41 ± 0.82 (0.53)	16.67 ± 0.84 (0.54)
SARS1404	78.942097	12.469229	360	gran.	0.9999	2.63	25.13	0.2415	137.06 ± 4.14	85.83 ± 2.83	12.84 ± 0.65 (0.42)	13.03 ± 0.66 (0.43)
SARS1405	78.955810	12.494206	125	gran.	0.9991	2.42	27.47	0.2410	121.32 ± 3.63	69.14 ± 2.30	13.08 ± 0.66 (0.44)	13.28 ± 0.68 (0.44)
SARS1406	78.955728	12.494084	122	quartz	0.9991	1.27	25.03	0.2416	135.82 ± 4.14	85.42 ± 2.84	16.44 ± 0.84 (0.55)	16.70 ± 0.85 (0.56)
SARS1407	78.948796	12.473513	210	gran.	0.9992	2.83	24.94	0.2288	123.00 ± 4.07	71.41 ± 2.71	12.30 ± 0.66 (0.47)	12.48 ± 0.67 (0.48)

[a] All BLOM, GOR, and SARS samples processed at the Cosmogenic Nuclide Laboratory in Bergen and SUERC, 68-BRATLIE and 69-IRGENS processed at University at Buffalo and measured at Lawrence Livermore National Laboratory

[b] gran. = granite, gran. gne. = granitic gneiss, quartz = quartz vein sample from bedrock, qz.-b. sch. = quartz-biotite schist

[c] Geometric shielding factor calculated from Eq. 1 (Dunne *et al.* 1999)

[d] Sample thickness measured from the surface, with weighted average from Eq. 2 or Eq. 3

[e] Density of 2.65 g cm^{-3} used, with the CRONUS-Earth calculator using an effective attenuation length for spallation in rock of 160 g cm^{-2} (Balco *et al.* 2008)

[f] Be carrier was Scharlau 2453 batch 14569501, with a known ^{9}Be concentration of 998.9 ± 3.6 ppm, 68-BRATLIE and 69-IRGENS used a ^{9}Be carrier with a concentration of 372.5 ppm

[g] Isotope ratios are normalised to NIST SRM 4325, the ^{10}Be standard has a known ^{10}Be/^{9}Be ratio of 3.06 x 10^{-11}

[h] Uncertainties reported at 1σ confidence level

[i] Procedural blanks used to correct for background ^{10}Be; UiB1501 (background ^{10}Be/^{9}Be: 5.28 ± 1.01 x 10^{-15}) & UiB1502 (background ^{10}Be/^{9}Be: 3.50 ± 0.71 x 10^{-15}) used for BLOM1401 to GOR1402, UiB1503 (background ^{10}Be/^{9}Be: 3.25 ± 0.71 x 10^{-15}) used for GOR1403 to SARS1406, and UiB1504 (background ^{10}Be/^{9}Be: 6.37 ± 1.13 x 10^{-15}) used for SARS1407

[j] Uncertainties include error in the blank and counting statistics

[k] ^{10}Be exposure ages were calculated with the CRONUS-Earth calculator version 2.2 (Balco *et al.* 2008), assuming no atmospheric anomaly, zero denudation, and zero temporal shielding (snow, sediment, vegetation, etc.)

[l] Ages are calculated using the Arctic ^{10}Be production rate of 3.96 ± 0.15 atoms g^{-1} a^{-1} (Young *et al.* 2013), with the Lal/Stone scaling (St). Systematic errors in the calculated ages include the ^{10}Be production rate and ^{10}Be decay constant uncertainties. Parenthesis contain only the analytical uncertainty in the nuclide concentration (Balco *et al.* 2008).

[m] A conservative correction factor was applied, comprising; the product of topographic shielding and snow shielding (Table 4.2), sample elevation - 3 m (to account for GPS barometric altitude uncertainty), and an erosion rate of 0.2 mm ka^{-1} after Henriksen *et al.* (2014). No correction was made for historic sea level change.

4.3 Exposure dating sensitivity analysis and correction factor

4.3.1 Snow-shielding

An unknown factor in the production of the ^{10}Be isotope is snow cover, which is spatially and temporally variable, and can result in corrections exceeding 10 % for exposure ages in mountainous or high latitude locations (Schildgen *et al.* 2005). In order to test the possible minimum impact of snow-shielding on the exposure ages from Kongsfjorden, recent (2009–2015) mean monthly snow depth and snow density data minus one standard deviation was used from Ny-Ålesund (Table 4.2) as a proxy for snow cover over the period of exposure. A non-dimensional snow correction value (S_c) is obtained through Eq. 7 (Vermeesch 2007):

$$S_c = \frac{1}{n}\sum_{i=1}^{n} e^{-\frac{\rho_{(i)} z_{(i)}}{\Lambda_0}}$$

Eq. 7

Where; n = number of records (e.g. 12 for months), i = index of summation, $\rho_{(i)}$ = snow density (g cm^{-3}), $z_{(i)}$ = depth of snow (cm), and $\Lambda_{(i)}$ = spallogenic neutron attenuation length (g cm^{-2}) which is given as 164 g cm^{-2} for latitudes exceeding 60° after Lingenfelter (1963) (Gosse & Phillips 2001).

Following Vermeesch (2007), the product of the snow correction value and the topographic shielding value (Eq. 1) was used as the shielding correction for input into the CRONUS-Earth calculator. The snow correction value calculated for the Kongsfjorden samples suggests that the exposure ages are underestimated by at least 1.00 ± 0.03 %, falling within the analytical uncertainty of the method (3.57 ± 0.6 %). The snow correction assumes that simplified minimal modern snow characteristics extrapolated from Ny-Ålesund are representative for the sample localities on Blomstrandhalvøya and Ossian Sarsfjellet for the entirety of exposure, Figure 4.27a gives further possible shielding scenarios based on snow depth and density by calculating differences to uncorrected ages reported in Table 4.1.

Table 4.2: Mean monthly snow depth -1σ ($z_{(i)}$) (Norwegian Meteorological Institute 2016), snow density -1σ ($\rho_{(i)}$) (Jack Kohler, personal communication) for the period 2009–2015 in Ny-Ålesund, with individual snow correction factors ($S_{c(i)}$) and overall snow correction factor (S_c) from Eq. 7.

	Jan	Feb	Mar	Apr	May	Jun	Jul	Aug	Sep	Oct	Nov	Dec
$z_{(i)}$ (cm)	3.73	14.73	17.88	21.71	14.86	0.00	0.00	0.00	0.00	0.58	3.22	0.98
$\rho_{(i)}$ (g cm^{-3})	0.27	0.27	0.27	0.27	0.27	0.00	0.00	0.00	0.27	0.27	0.27	0.27
$S_{c(i)}$	0.99	0.98	0.97	0.96	0.98	1.00	1.00	1.00	1.00	1.00	0.99	1.00
S_c	0.9899											

4.3.2 Elevation uncertainty and sea-level change

Given that the cosmic-ray flux is a function of latitude and altitude (Lal 1991; Stone 2000), the production rate of cosmogenic nuclides is sensitive to atmospheric pressure and subsequently changes in sea level. The exposure ages obtained from Blomstrandhalvøya and Ossian Sarsfjellet are also subject to uncertainty in the GPS barometric altitude measurement (±3 m), however the difference in exposure age created by elevation measurement uncertainty alone is in the order of -0.31 to 0.33 % (Figure 4.27b).

The reconstructed sea level history for Kongsfjorden suggests a Last Glacial Maximum marine limit at 36 m a.s.l. for Blomstrandhalvøya (Figure 2.5 and Figure 4.26) (Lehman & Forman 1992), hitherto the samples in Kongsfjorden would have experienced lower cosmogenic nuclide production via spallation due to the lower cosmic ray flux caused by higher atmospheric pressure when sea level was higher (Stone 2000). The correction factor is problematic given that sea level rapidly fell at the Younger Dryas to Preboreal transition in northwestern Spitsbergen (Forman *et al.* 1987; Forman 1990; Landvik *et al.* 1998; Forman *et al.* 2004), see Figure 4.26. A maximum increase of 3.98 % on uncorrected exposure ages is estimated (Figure 4.27b), however integrating the period of sea level change over the corresponding period of exposure produces a significantly smaller correction, expressly; notable variation in sea level such as at the Younger Dryas to Preboreal transition only affects a short period of a sample's exposure history.

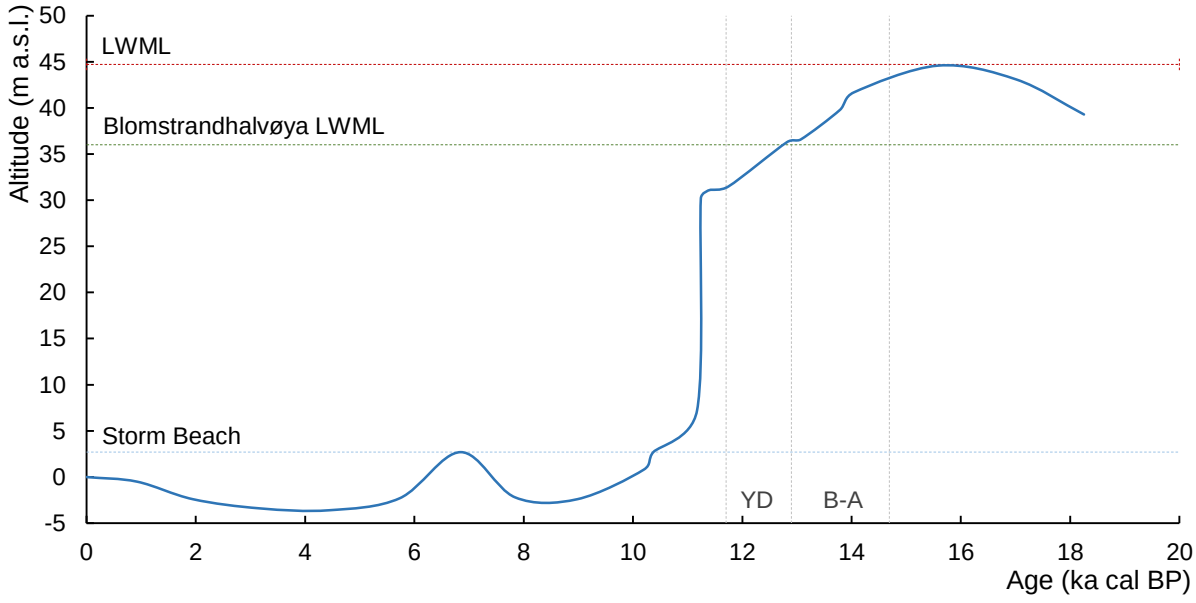

Figure 4.26: Simplified relative sea level curve for Brøggerhalvøya, modified from Forman et al. (1987), and calibrated to calendar years before present (cal BP) using the IntCal13 radiocarbon calibration curve (Reimer et al. 2013). The Late Weichselian Marine Limit (LWML) and Storm Beach elevation are indicated (Forman *et al.* 1987), as is the Late Weichselian Marine Limit for Blomstrandhalvøya (Lehman & Forman 1992). The Younger Dryas (YD) and Bølling-Allerød (B-A) epochs are indicated with grey stippled lines (Rasmussen *et al.* 2006).

4.3.3 Denudation of the sample surface

A large geological uncertainty inherent in the use of cosmogenic nuclide dating is the lack of *a priori* knowledge of the denudation affecting sampled boulders and bedrock (Dunai 2010). As weathering and erosion of samples will remove accumulated cosmogenic nuclides, primarily originating via spallation at or close to the surface, so calculated ages assuming zero erosion since exposure (as in Table 4.1) will be underestimated. A conservative erosion rate of 0.2 mm ka^{-1} as used by Henriksen *et al.* (2014) results in an underestimation of uncorrected ages by ca. 0.25 % (Figure 4.27c).

The Holocene rockwall erosion rate in north west Spitsbergen attributed to biogenic flaking is estimated at a mean of 2.1 mm ka^{-1} (André 1997), a rate which would lead to an underestimation of ca. 2.7 % in the exposure ages obtained from Blomstrandhalvøya and Ossian Sarsfjellet (Figure 4.27c), within analytical uncertainties of the method. Cryogenic processes are responsible for enhanced erosion rates in granite (French & Guglielmin 2000) by increased granular disintegration induced by thermal stress gradients at grain boundaries (Hall & André 2003; Hall *et al.* 2008), subsequently the weathering rate of granite in a polar climate may exceed that typical for arid climates at ca. 6 mm ka^{-1} (Owens & Watson 1979; Ollier 1984), and would give an underestimation exceeding 8.2 %.

It is evident that weathering and removal of material from the surface of sampled boulders and bedrock must be accounted for when calculating the exposure age from the ^{10}Be concentration of a sample. It is necessary to assume a rate of surface denudation when applying corrections to obtained exposure ages. The conservative 0.2 mm ka^{-1} denudation rate used by Henriksen *et al.* (2014) is derived from the depth of measured quartz vein protrusions, and is applicable to samples on Blomstrandhalvøya and Ossian Sarsfjellet given the geographic proximity, time since exposure, and similarity in lithology.

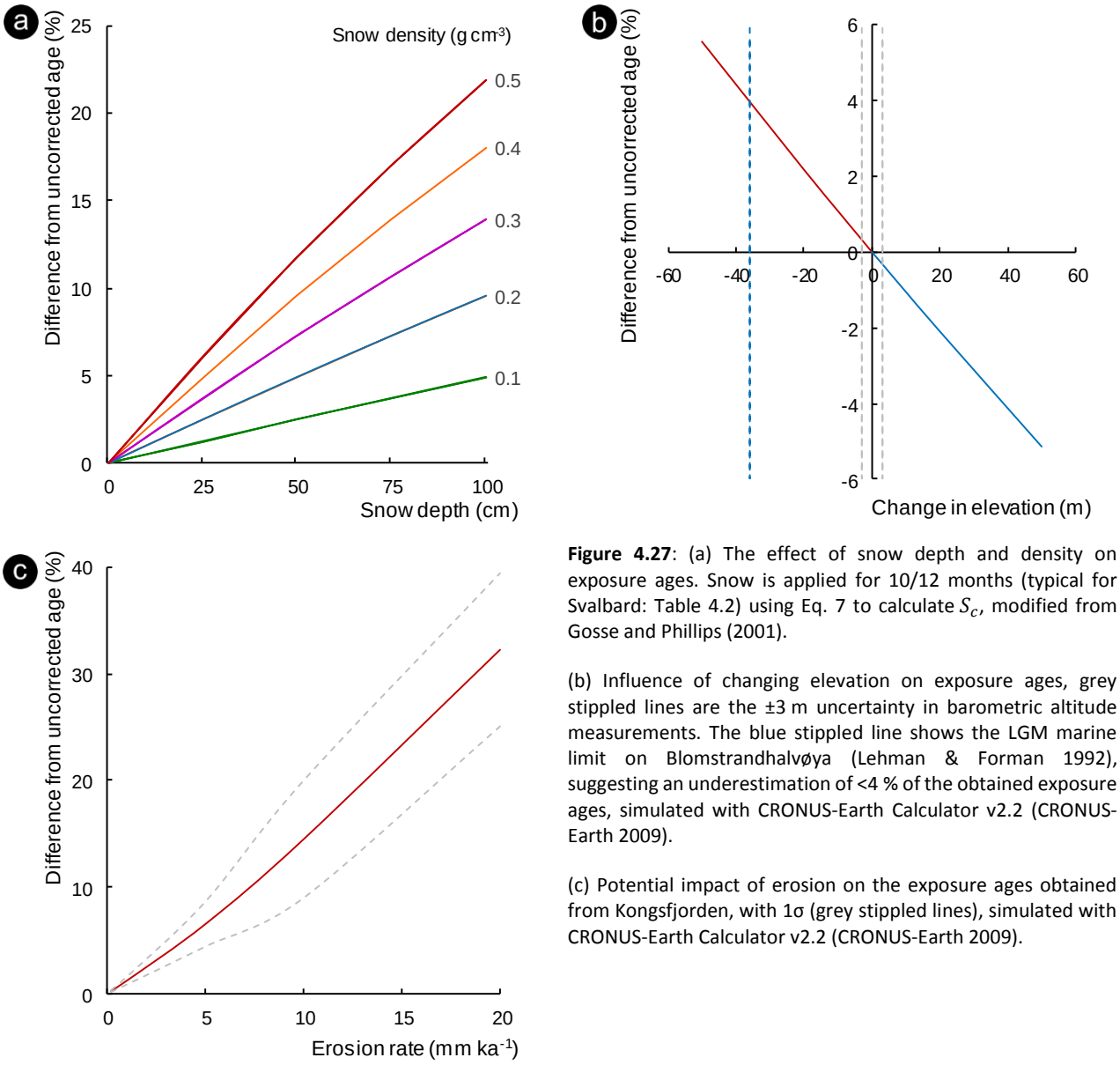

Figure 4.27: (a) The effect of snow depth and density on exposure ages. Snow is applied for 10/12 months (typical for Svalbard: Table 4.2) using Eq. 7 to calculate S_c, modified from Gosse and Phillips (2001).

(b) Influence of changing elevation on exposure ages, grey stippled lines are the ±3 m uncertainty in barometric altitude measurements. The blue stippled line shows the LGM marine limit on Blomstrandhalvøya (Lehman & Forman 1992), suggesting an underestimation of <4 % of the obtained exposure ages, simulated with CRONUS-Earth Calculator v2.2 (CRONUS-Earth 2009).

(c) Potential impact of erosion on the exposure ages obtained from Kongsfjorden, with 1σ (grey stippled lines), simulated with CRONUS-Earth Calculator v2.2 (CRONUS-Earth 2009).

4.4 Exposure age correction

Figure 4.27 highlights the impact of snow shielding, changes in elevation, and denudation of the boulder or bedrock surface on the ^{10}Be concentration of samples. A correction must be applied to obtained exposure ages in order to incorporate these largely unknown factors. In order to quantify a reasonable corrected exposure age, a conservative approach has been taken, which comprises; the product of topographic shielding and snow shielding (without uncertainties, from Table 4.2, after Vermeesch (2007)), the sample elevation -3 m (to account for uncertainty in GPS barometric altitude measurement, given that a higher elevation leads to higher cosmogenic nuclide production (Stone 2000)), and a denudation rate of 0.2 mm ka^{-1} after Henriksen *et al.* (2014). The exposure dates with the conservative correction as in Table 4.1 will be presented and discussed henceforth.

4.5 Exposure age distribution and observed parameters

The quantitative and qualitative observations from the boulders and bedrock sampled on Blomstrandhalvøya and Ossian Sarsfjellet, such as the surface relief attributed to weathering, the physical dimensions of the boulder, degree of lichen cover, and substrate material, may have some systematic relationship to the yielded exposure age. From Table 4.3, it appears that the strongest relationship between external parameters and exposure age is that of substrate.

The exposure age (without uncertainty) for each sample is non-normally distributed, and so a Mann-Whitney test was conducted to assess the statistical significance between the median values for samples on bedrock and samples on sediment or mixed substrate, the P-value of 0.07 is not significant at the 95 % confidence interval. However, the BLOM subset does show a normal distribution, and so an unpaired two-tailed Student's t-test produces a statistically significant relationship between substrate and exposure age (P = 0.003), suggesting the mean age for samples on bedrock (14.8 ka) is significantly older than samples on sediment or mixed substrate (12.8 ka). However this does not account for the analytical uncertainty in the exposure age, which reduces the relationship below the 95 % confidence interval.

Geological observations thus remain key for identifying and interpreting differences in exposure ages, as samples on mixed substrate are generally in stable positions with no evidence of burial or post depositional movement. Other factors, i.e. length of exposure, must account for the yielded exposure ages, and the largest controlling factor should therefore be timing of ice retreat.

Table 4.3: Evaluation of observed parameters versus yielded exposure age. (Y = yes, N = no, B = bedrock, M = mixed, S = sediments, n/a = not available or applicable), analytical uncertainty in exposure age is shown.

Sample	Height (cm)	Surface lichen	Side lichen	Guano	Weathering relief (± mm)	Substrate	Corrected ^{10}Be Age (ka)
BLOM1401	90	Y	N	N	2.0	B	13.42 ± 0.46
BLOM1402	100	Y	N	N	3.0	B	15.53 ± 0.55
BLOM1403	150	Y	Y	N	3.0	M	12.99 ± 0.44
BLOM1405	200	Y	Y	N	2.0	M	13.20 ± 0.46
BLOM1406	160	Y	N	N	2.0	M	12.72 ± 0.47
BLOM1407	150	Y	N	N	2.0	B	15.20 ± 0.53
BLOM1408	200	Y	Y	Y	2.0	B	14.70 ± 0.51
BLOM1409	220	Y	Y	Y	4.0	M	12.68 ± 0.48
BLOM1410	150	N	N	N	2.0	M	11.35 ± 0.42
BLOM1411	120	Y	N	N	4.0	B	15.63 ± 0.51
BLOM1412	80	Y	N	Y	3.0	M	14.11 ± 0.46
BLOM1413	170	Y	N	Y	2.0	B	14.26 ± 0.47
68-BRATLIE	240	Y	N	Y	n/a	M	14.46 ± 0.31

Sample	Height (cm)	Surface lichen	Side lichen	Guano	Weathering relief (± mm)	Substrate	Corrected ^{10}Be Age (ka)
GOR1401	120	Y	N	N	2.0	S	23.99 ± 0.73
GOR1402	50	Y	N	N	3.0	S	18.41 ± 0.61
GOR1403	100	Y	N	N	7.0	S	14.61 ± 0.90
GOR1404	95	Y	Y	Y	2.0	M	8.28 ± 0.34
GOR1405	160	Y	N	N	2.0	B	29.80 ± 0.92
GOR1406	120	Y	Y	N	3.0	S	12.56 ± 0.52
69-IRGENS	60	Y	Y	N	n/a	M	14.53 ± 0.28
SARS1401	60	N	N	N	3.0	B	16.50 ± 0.54
SARS1402	n/a	Y	Y	N	4.0	n/a	16.67 ± 0.54
SARS1404	50	Y	Y	N	4.0	B	13.03 ± 0.43
SARS1405	30	Y	N	N	3.0	B	13.28 ± 0.44
SARS1406	n/a	N	N	N	2.0	n/a	16.70 ± 0.56
SARS1407	30	Y	Y	N	5.0	B	12.48 ± 0.48

4.6 Exposure age data presentation

The following section contains a camel-plot, elevation versus exposure age, and map for each of the BLOM, GOR, and SARS sampling transects. The camel-plot displays each sample with mean and analytical uncertainties as a Gaussian curve, which are then summed as a probability distribution function curve (PDF) to give a normal kernel density estimate. Large distinct peaks in the PDF curve suggests that individual samples are measuring the same entity albeit with inaccuracies, while several small or diffuse peaks suggests discreet exposure ages with little or no overlap (Balco 2011b).

The elevation versus exposure age plot is intended to highlight any relationship between the elevation of the sample and its ^{10}Be exposure age, given the objective to unveil the vertical downwasting of glacial ice in Kongsfjorden. The plots show analytical and systematic uncertainties for each sample, the boundaries between the Bølling-Allerød and Younger Dryas epochs from Rasmussen *et al.* (2006), and the mean exposure age with one standard deviation from the camel-plot.

The location map shows the exposure ages for each transect with analytical uncertainties, and the local Quaternary sediments and landforms. The interpretation of the camel-plots, elevation versus exposure age, and maps is given in the subsequent section.

4.6.1 BLOM transect exposure age results

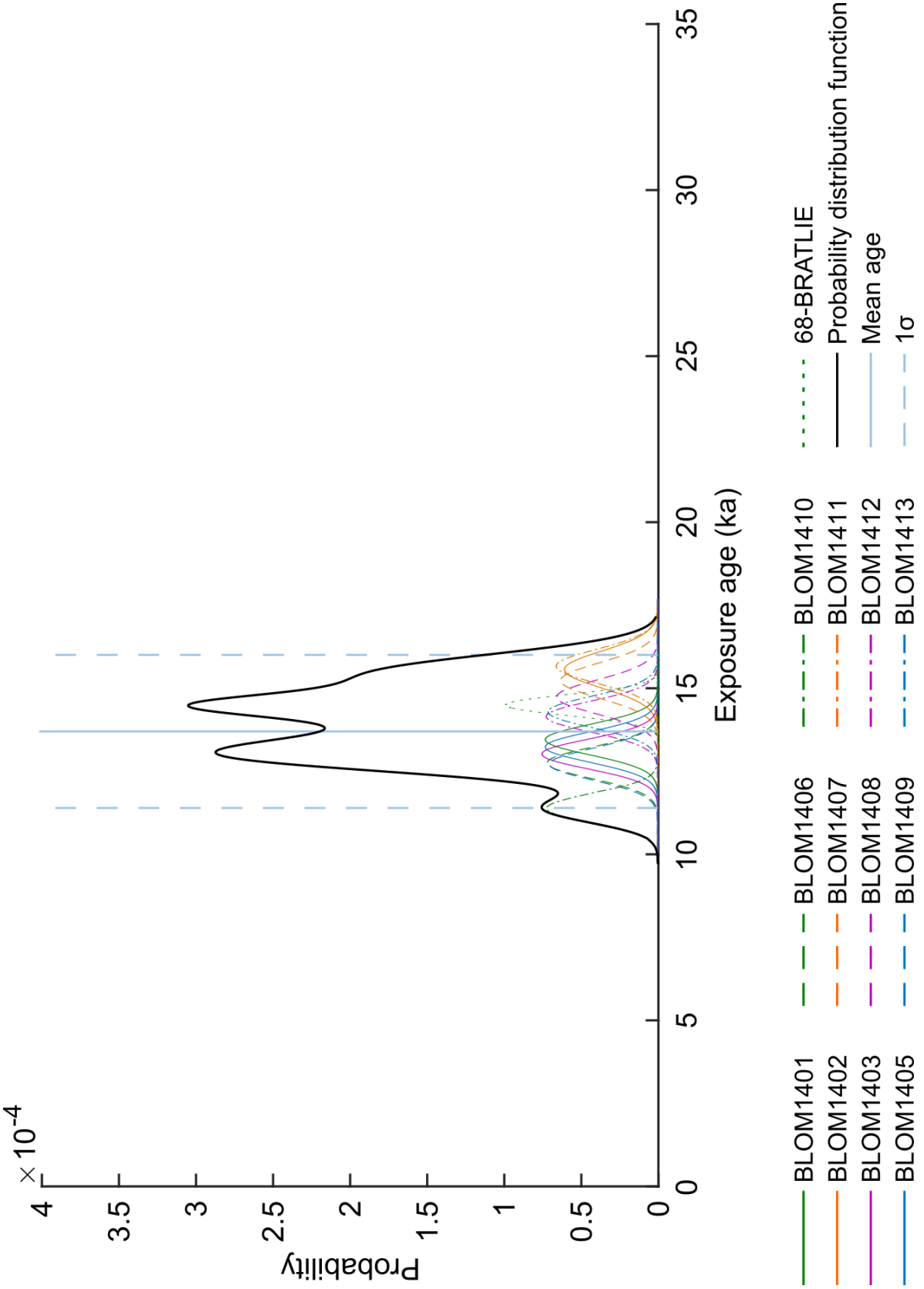

Figure 4.28: Camel-plot showing the normal kernel density estimate of the corrected BLOM transect ^{10}Be exposure ages calculated with the Young *et al.* (2013) Arctic production rate. The mean age (13.7 ka) and one standard deviation (2.3 ka) of the probability distribution function curve (summation of individual Gaussian curves) are plotted, modified from MATLAB source code from Balco (2001).

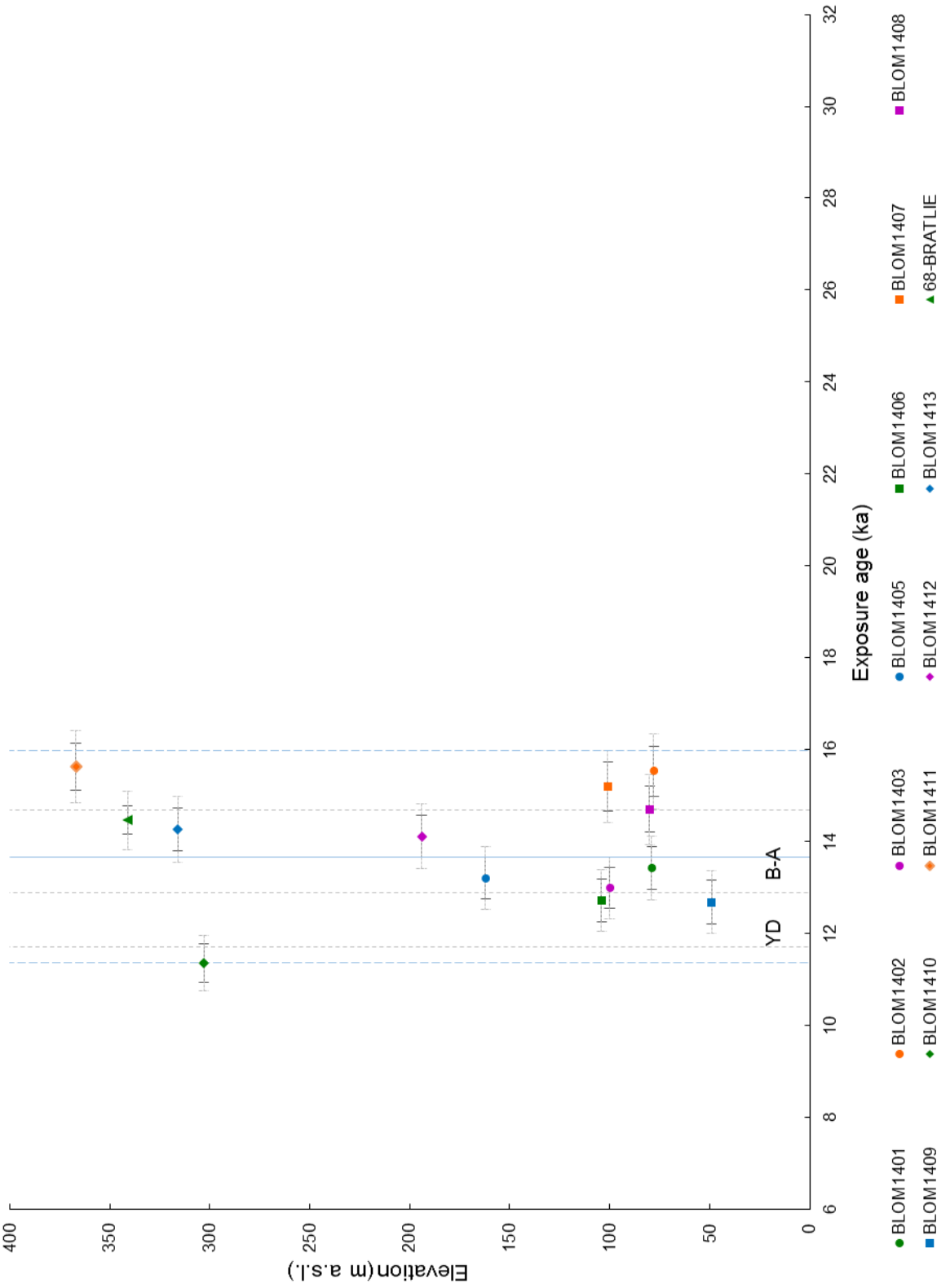

Figure 4.29: Elevation versus exposure age for the BLOM transect, displaying analytical uncertainty (black error bars) and systematic uncertainty (grey error bars) in the 10Be exposure age for each sample, the mean exposure age and 1σ uncertainty are plotted in solid blue and stippled blue lines respectively. The grey stippled lines demark climatic epochs, with the onset of the Bølling-Allerød (B-A) at 14.7 ± 0.2 ka, and the timing of the Younger Dryas (YD) between 12.9 ± 0.1 ka and 11.7 ± 0.1 ka (Rasmussen *et al*. 2006).

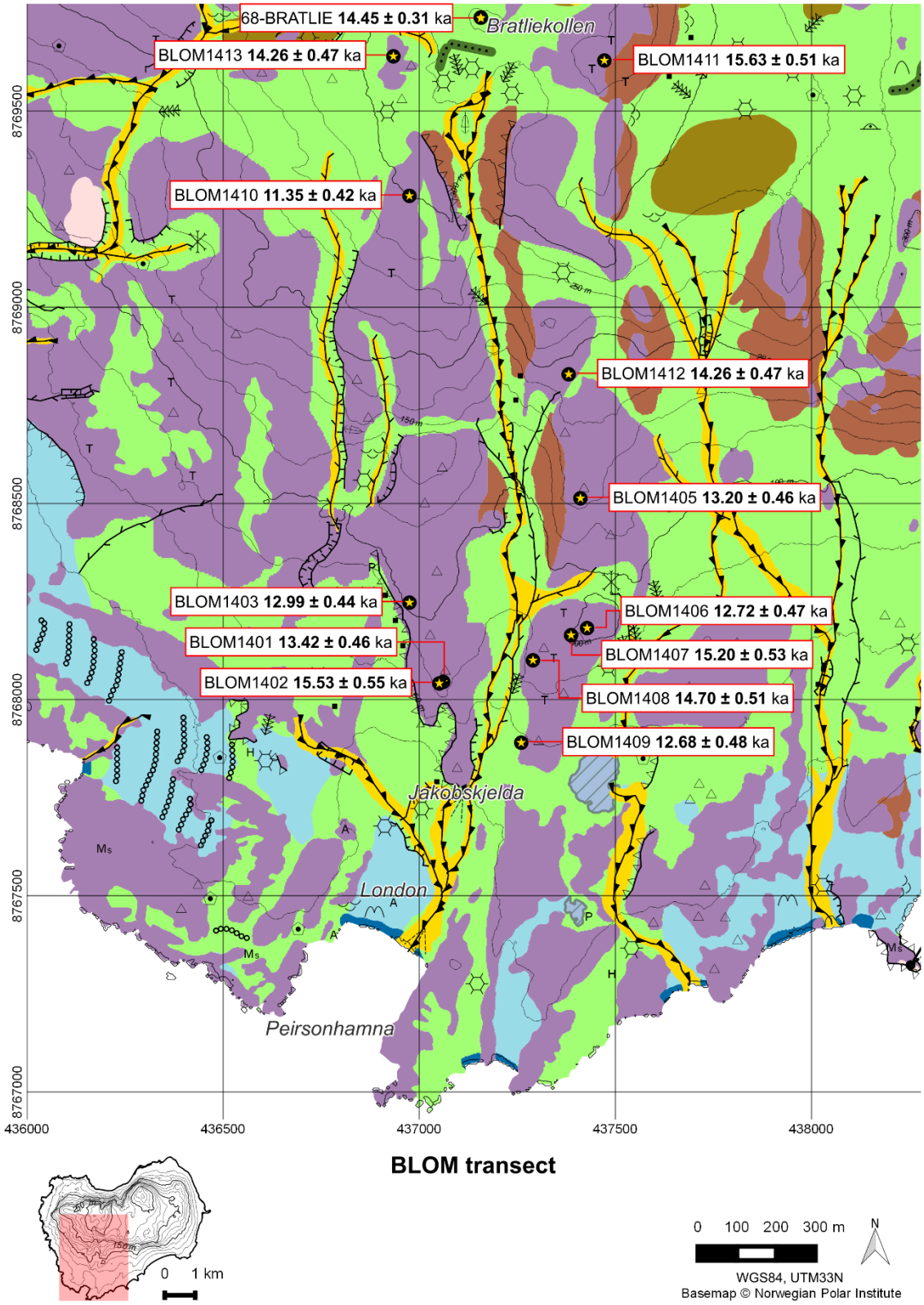

Figure 4.30: Geomorphological map showing the Quaternary landforms and deposits of the BLOM transect on western Blomstrandhalvøya, with the location of corrected ^{10}Be exposure ages (calculated with the Young et al. (2013) Arctic production rate) and analytical uncertainty. For map legend see Figure D.1 (Appendix D), for sample photographs see Appendix A.

4.6.2 GOR transect exposure age results

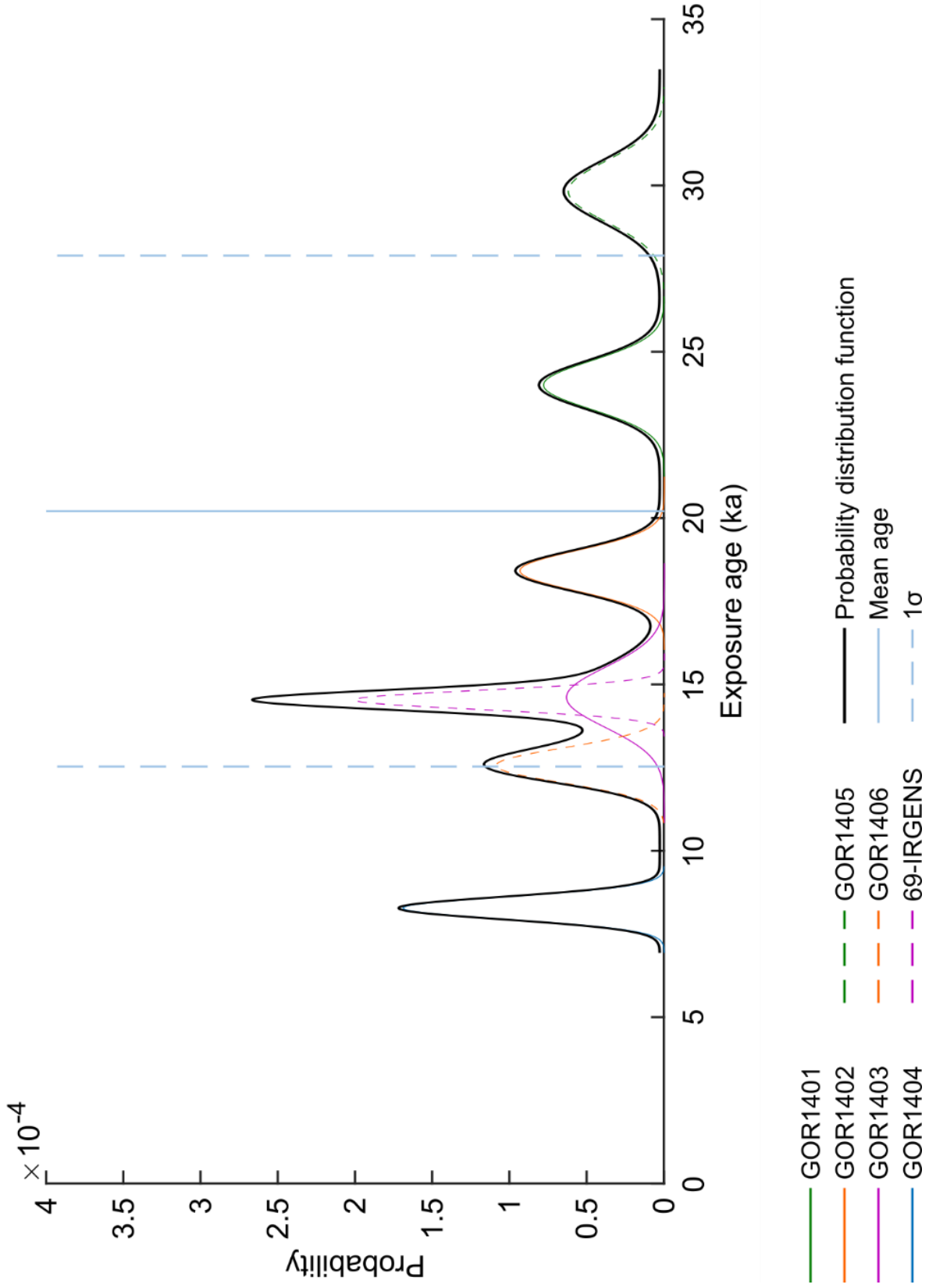

Figure 4.31: Camel-plot showing the normal kernel density estimate of the corrected GOR transect ^{10}Be exposure ages calculated with the Young *et al.* (2013) Arctic production rate. The mean age (20.2 ka) and one standard deviation (7.6 ka) of the probability distribution function curve (summation of individual Gaussian curves) are plotted, modified from MATLAB source code from Balco (2001).

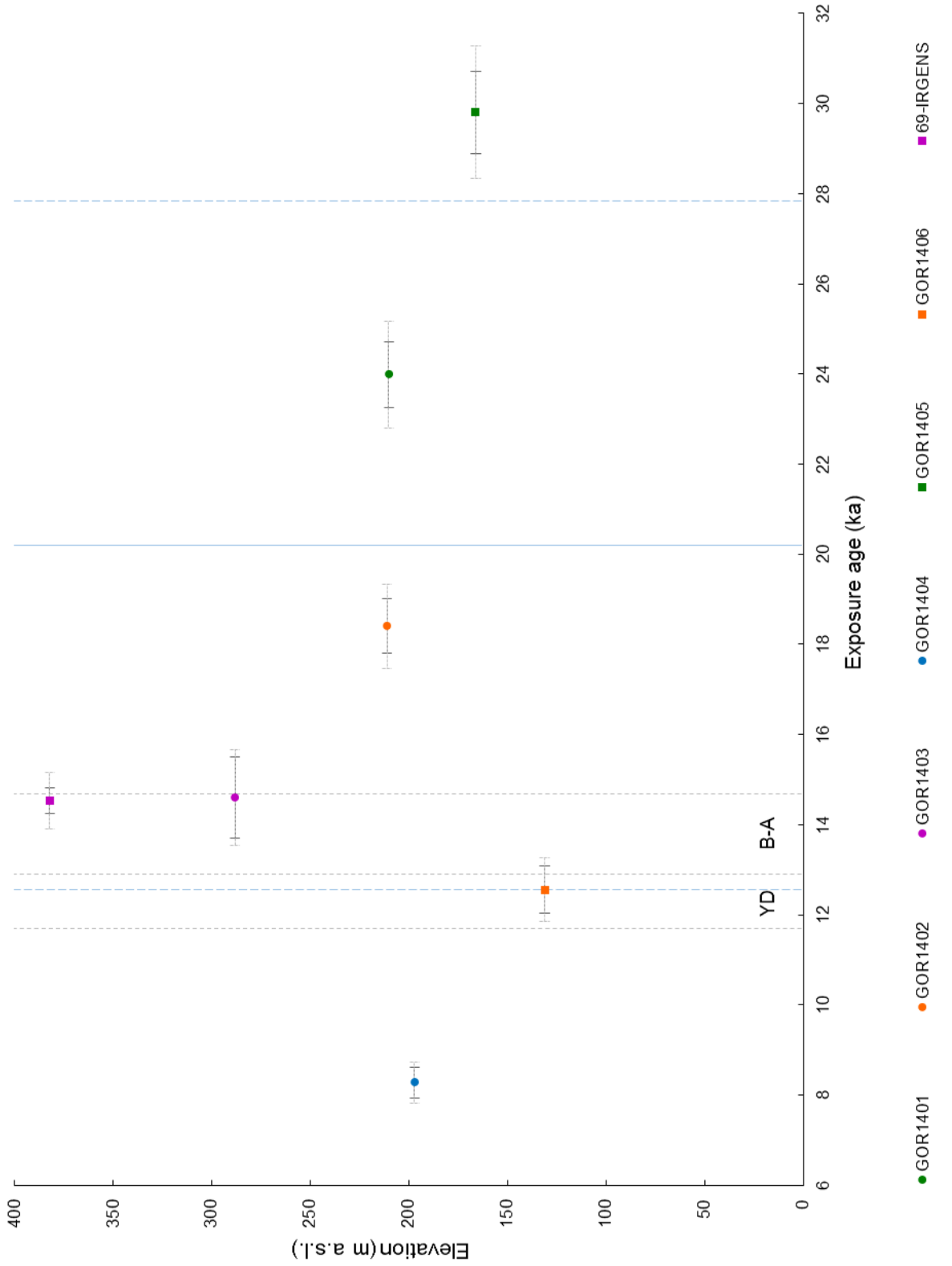

Figure 4.32: Elevation versus exposure age for the GOR transect, displaying analytical uncertainty (black error bars) and systematic uncertainty (grey error bars) in the 10Be exposure age for each sample, the mean exposure age and 1σ uncertainty are plotted in solid blue and stippled blue lines respectively. The grey stippled lines demark climatic epochs, with the onset of the Bølling-Allerød (B-A) at 14.7 ± 0.2 ka, and the timing of the Younger Dryas (YD) between 12.9 ± 0.1 ka and 11.7 ± 0.1 ka (Rasmussen *et al.* 2006).

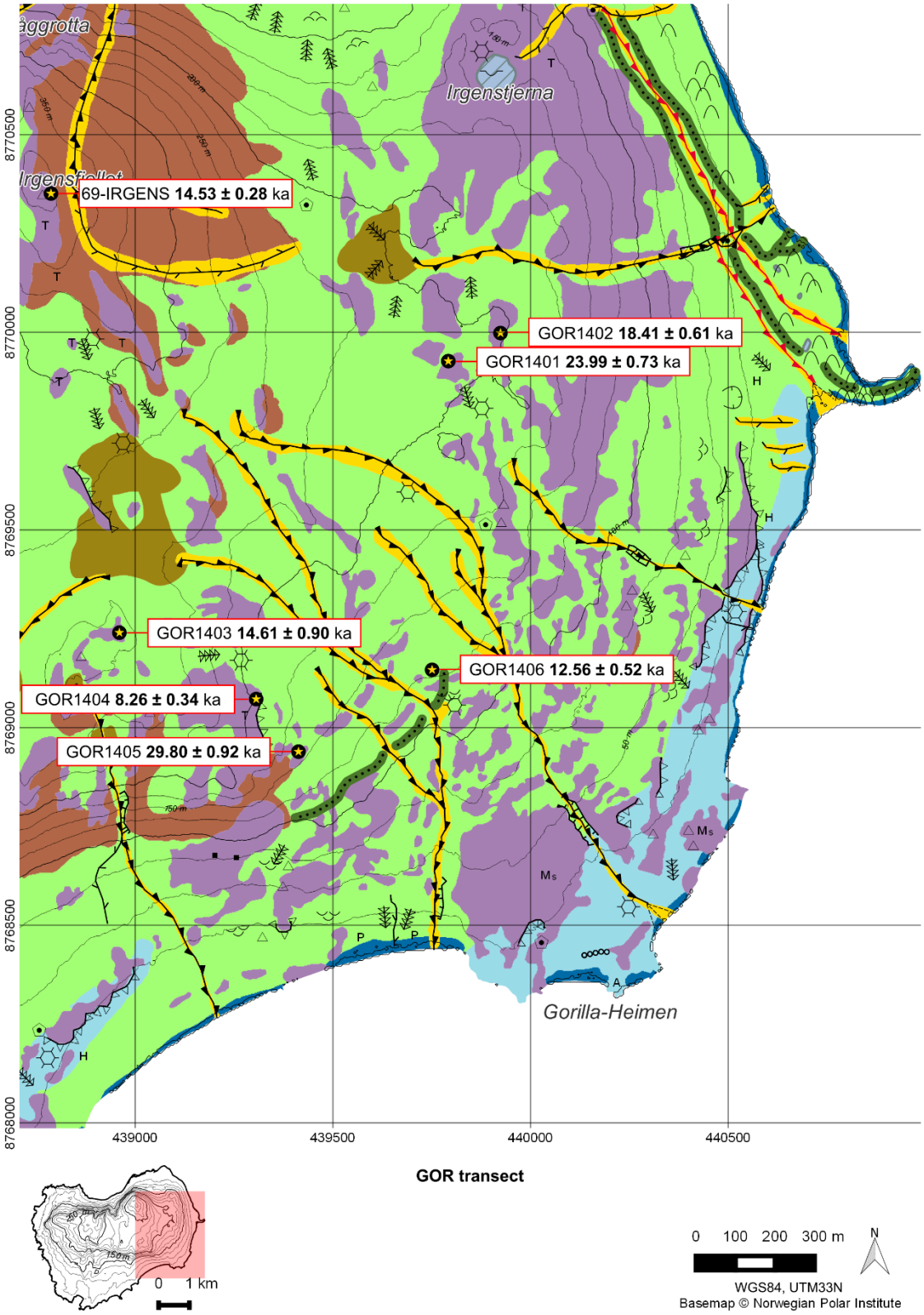

Figure 4.33: Geomorphological map showing the Quaternary landforms and deposits of the GOR transect on eastern Blomstrandhalvøya, with the location of corrected ^{10}Be exposure ages (calculated with the Young et al. (2013) Arctic production rate) and analytical uncertainty. For map legend see Figure D.1 (Appendix D), for sample photographs see Appendix B.

4.6.3 SARS transect exposure age results

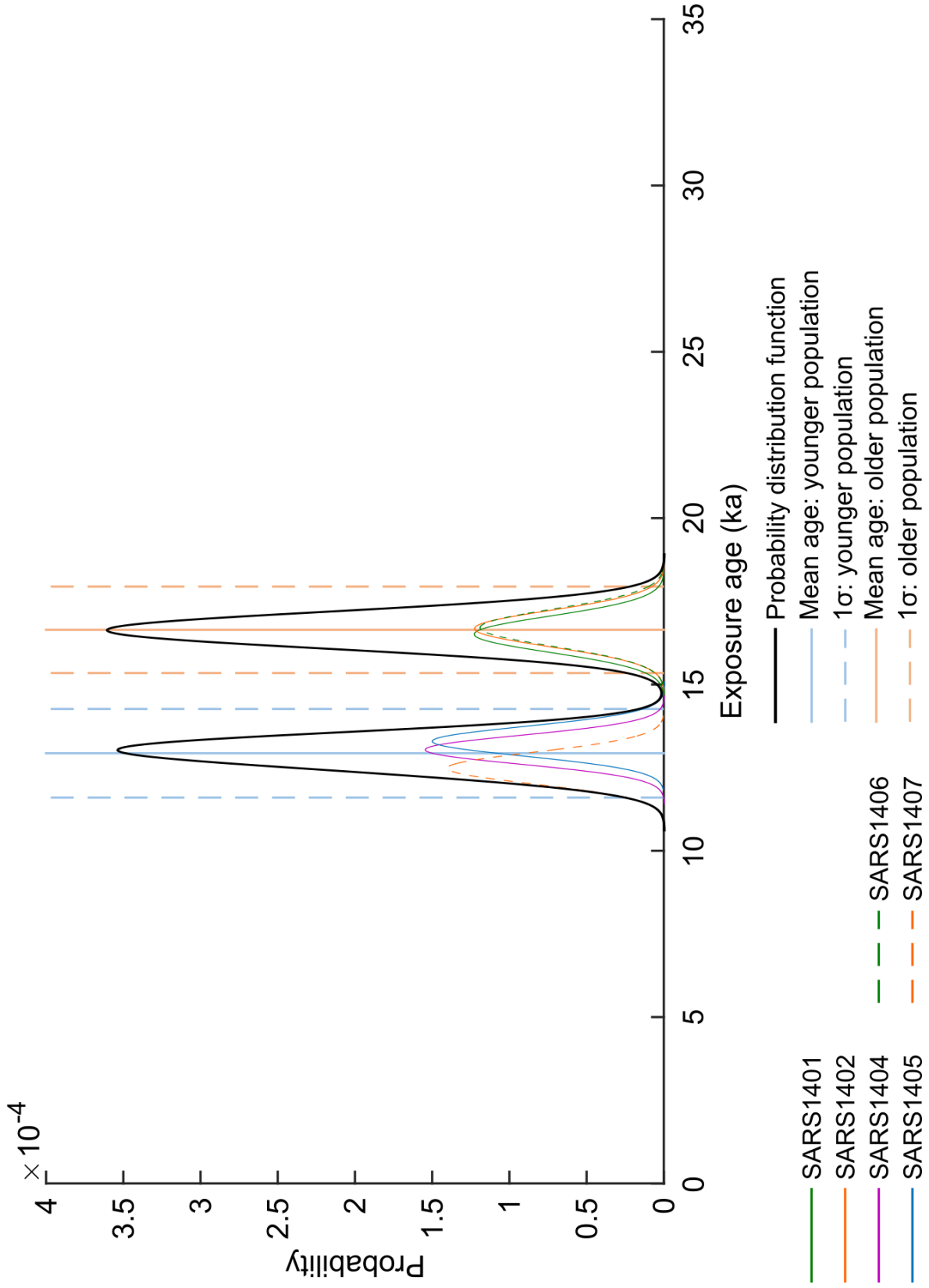

Figure 4.34: Camel-plot showing the normal kernel density estimate of the SARS transect ^{10}Be exposure ages calculated with the Young et al. (2013) Arctic production rate. Two populations are observed from the probability distribution function; the younger with a mean age of 12.8 ± 1.3 ka (blue lines) and an older population with a mean age of 16.6 ± 1.3 ka (brown lines), modified from MATLAB source code from Balco (2001).

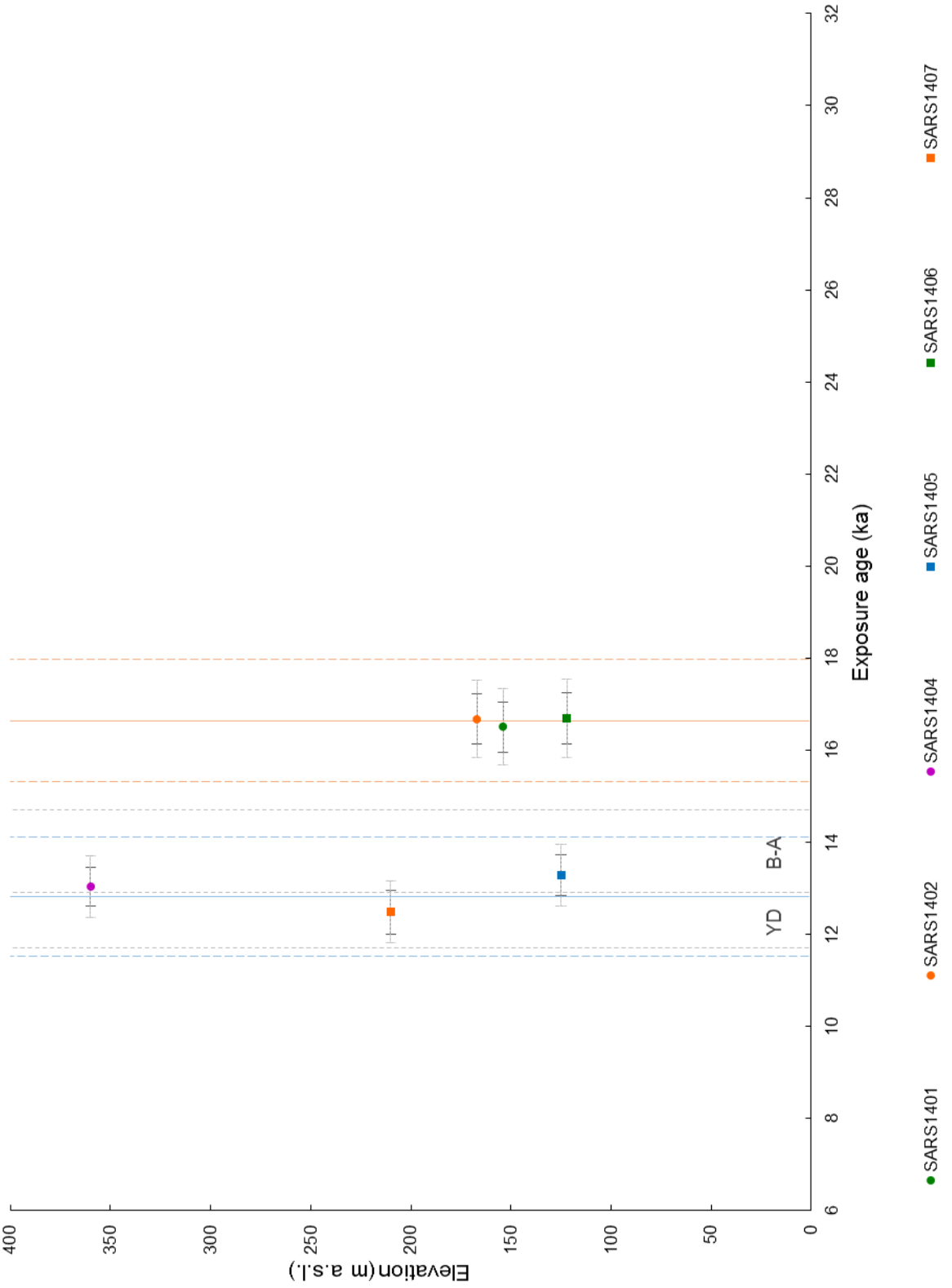

Figure 4.35: Elevation versus exposure age for the SARS transect, displaying analytical uncertainty (black error bars) and systematic uncertainty (grey error bars) in the ^{10}Be exposure age for each sample. The mean exposure age and 1σ uncertainty are plotted in solid blue and stippled blue lines respectively for the younger population, and solid brown and stippled brown lines for the older population. The grey stippled lines demark climatic epochs, with the onset of the Bølling-Allerød (B-A) at 14.7 ± 0.2 ka, and the timing of the Younger Dryas (YD) between 12.9 ± 0.1 ka and 11.7 ± 0.1 ka (Rasmussen *et al*. 2006).

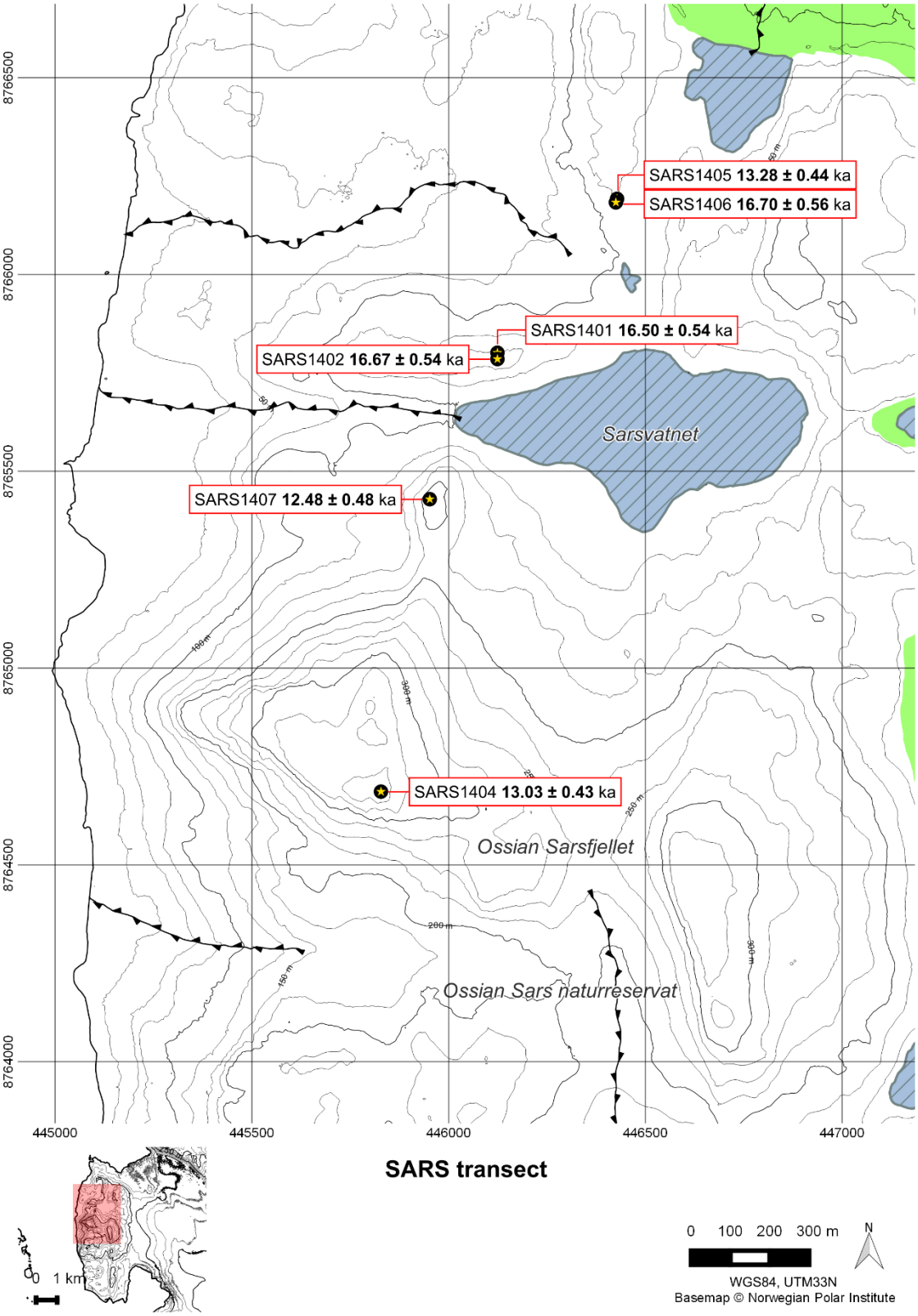

Figure 4.36: Location map of the SARS transect on Ossian Sarsfjellet, with the location of corrected ^{10}Be exposure ages (calculated with the Young et al. (2013) Arctic production rate) and analytical uncertainty. For map legend see Figure D.1 (Appendix D), for sample photographs see Appendix C.

5. Interpretation and discussion

5.1 Interpretation of the BLOM transect

The camel-plot of the exposure ages obtained from the western Blomstrandhalvøya transect (Figure 4.28) shows a spread of ages with a high degree of overlap between samples given their analytical uncertainty, leading to an irregular probability distribution function (PDF) curve. The two peaks of the PDF curve suggests a deglaciation age of the western transect at ca. 13.0 ka, and 14.5 ka, however the mean age obtained from the curve indicates an exposure of 13.7 ± 2.3 ka.

Figure 4.29 shows the highest sample (BLOM1411, 367 m a.s.l.) was the earliest exposed at 15.6 ± 0.5 ka, but no trend between sample elevation and ^{10}Be exposure age exists for the western Blomstrandhalvøya transect, suggesting a complex deglaciation history, with relatively young and old boulders at similar elevations and within close geographic proximity, typified by BLOM1401 (13.4 ± 0.5 ka) and BLOM1402 (15.5 ± 0.6 ka) (Figure 4.30).

The mean age of all BLOM samples (13.7 ± 2.3 ka) straddles the transition from the Bølling-Allerød (B-A) interstadial to the Younger Dryas (YD) stadial at 12.9 ± 0.14 ka (Rasmussen *et al.* 2006). However, a cluster of samples (BLOM1411, BLOM1407, BLOM1408, BLOM1402, and 68-BRATLIE) display an Oldest Dryas to B-A exposure signal with a mean age of 15.2 ± 1.5 ka, and a cluster of samples (BLOM1405, BLOM1506, BLOM1403, BLOM1401, and BLOM1409) give an early YD signal with a mean exposure age of 13.0 ± 1.3 ka. It is suggested therefore that the BLOM transect may reflect at least two episodes of retreat; during the early Bølling interstadial, and at the end of the Allerød interstadial to Younger Dryas transition, and is illustrated by the two peaks in Figure 4.29.

There is limited geomorphological evidence on Blomstrandhalvøya for a re-advance or stillstand during the Older Dryas or early Younger Dryas, however the trimline-degraded moraine complex (Figure 4.7) may represent an early Younger Dryas ice marginal position, with early to mid-Younger Dryas aged samples located below this threshold at ca. 120 m a.s.l. on the west of Blomstrandhalvøya (Figure 5.4). The suppressed Marine Limit on Blomstrandhalvøya (Figure 2.5 and Figure 4.26) is also indication of a Younger Dryas stillstand or re-advance at or proximal to the island (Lehman & Forman 1992). The precision of ^{10}Be exposure dating leads to overlapping uncertainties with such tightly clustered exposure ages, and thus complicates the resolution of different populations, therefore a reliance of geological interpretation is necessary to determine discreet clusters and explain outliers.

BLOM1411 and BLOM1413 show a discrepancy in exposure age of 1.4 ± 0.9 ka, despite their similar elevation and geographic position (Figure 4.30). The minimum difference in ^{10}Be concentration between BLOM1411 and BLOM1413 is 6536 atoms g^{-1} SiO_2, which represents 6.4 % of the ^{10}Be

concentration recorded for BLOM1411 (Table 4.1), a shortfall of 6.4 % in ^{10}Be production via spallation requires a correction factor of 0.9360, which can be feasibly explained by unknown variables such as differing snow shielding and/or denudation rates between the two samples (Figure 4.27).

BLOM1410 appears to be the most obvious outlier from the BLOM transect, giving an exposure age of 11.4 ± 0.4 ka and thus on the Younger Drays to Preboreal transition (Rasmussen *et al.* 2006) despite its relatively high elevation (303 m a.s.l.). The young age of the sample is unlikely to be explained by its physiographic setting (Figure 5.1a), with an adjacent bedrock outcrop providing topographic shielding which would be accounted for in the shielding measurement. However, the outcrop may potentially allow for snow-drift accumulation given its sheltered position. Weathering provides a more likely scenario for the underestimation of the exposure age, as when sampling the boulder, a sheet with a thickness of ca. 0.5 cm separated from the surface (Figure 5.1b) with partial cementing by a precipitate, and so weathering is likely to have removed in-situ produced ^{10}Be atoms at or close to the surface of the boulder (Johnsen *et al.* 2009).

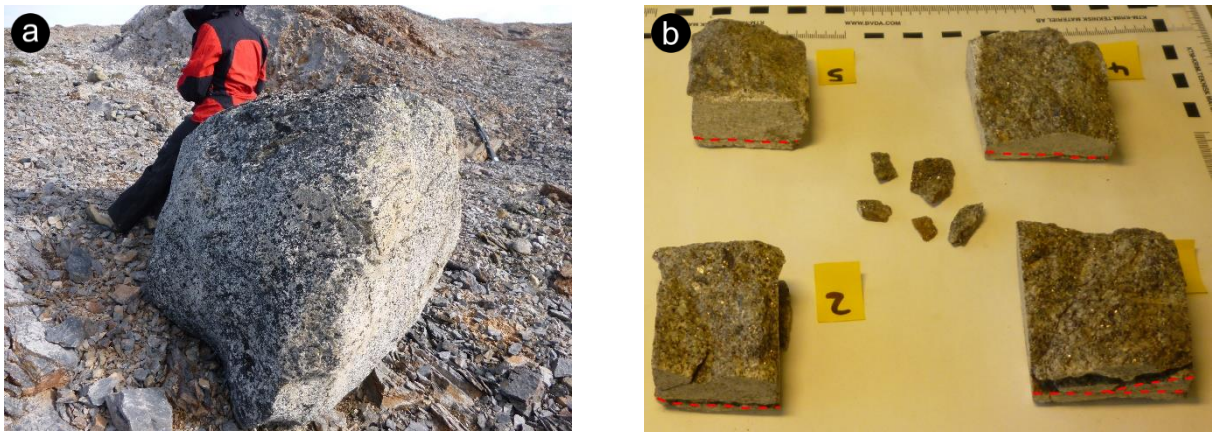

Figure 5.1: (a) BLOM1410 boulder perched on weathered bedrock and grus, situated south of a bedrock outcrop seen immediately behind the boulder (Photo: O. Grant, 33N 436975 8769284 facing north), and (b) the samples retrieved from BLOM1410 showing the weathering horizon (red stippled line) ca. 0.5 cm from the surface of the sample (Photo: O. Grant, samples oriented with underside up).

5.2 Interpretation of the GOR transect

Figure 4.31 shows the wide spread in exposure ages obtained from the eastern transect on Blomstrandhalvøya, ranging from 29.8 ± 0.9 ka to 8.3 ± 0.3 ka with little to no overlap, and thus producing a highly irregular PDF curve. The exposure age from the highest point of Blomstrandhalvøya (69-IRGENS, 382 m a.s.l.) is 14.5 ± 0.3 ka, which corresponds with GOR1403 (288 m a.s.l.) at 14.6 ± 0.9 ka (Figure 4.32), and thus gives an initial exposure of eastern Blomstrandhalvøya ca. 1 ka later than the western transect (BLOM1411), indicating a lateral retreat between 0.84 and 6.55 m a^{-1} of the ice margin on Blomstrandhalvøya at the onset of the Bølling interstadial.

GOR1406 located immediately above the trimline-degraded moraine ridge complex on the south eastern slope of Blomstrandhalvøya (Figure 4.7, Figure 4.33) gives a mid-Younger Dryas exposure age of 12.6 ± 0.5 ka. The YD age of GOR1406 suggests that the trimline and moraine located at ca. 120 m a.s.l. represent an early Younger-Dryas lateral ice marginal position, implying a stillstand or re-advance of the Kongsfjorden Ice Stream during the early YD or late B-A, with Blomstrandhalvøya a nunatak above ca. 120 m a.s.l..

Three exposure ages from the GOR transect produce ages which are outside two standard deviations of the exposure ages from the west of the island and on Ossian Sarsfjellet, and are thus identified as outliers. The samples; GOR1401 (24.0 ± 0.7 ka), GOR1402 (18.4 ± 0.6 ka), and GOR1405 (29.8 ± 0.9 ka) most likely contain an inherited ^{10}Be signal from a previous exposure. The inherited signal implies that glacial abrasion or plucking failed to remove the upper 2–3 m of surface containing the previous spallation induced ^{10}Be exposure signal (Balco 2011a). Alternatively the boulders originate from an earlier glacial advance, were covered and re-exposed or re-worked with minimal erosion during the Last Glacial Maximum (Wilson *et al.* 2013). The relatively high age of the samples consequently has implications as to the glacial transport pathway, erosion mechanism, and depositional conditions of the Kongsfjorden Ice Stream on the stoss slope of Blomstrandhalvøya.

In contrast to the aforementioned too-old ages, GOR1404 provides a seemingly too-young Holocene exposure age of 8.3 ± 0.3 ka (Figure 4.32). The young age of GOR1404 is not feasibly explained by snow, sediment, or topographic shielding effects, nor is there evidence of significant denudation of the boulder surface (Figure 5.2a). It is therefore suggested that GOR1404 has experienced post-depositional movement (Balco 2011a) incurred by down-slope sediment flow on the ca. 28° slope leading to rotation of the boulder, and thus the sampled surface is not the originally exposed face (Figure 5.2b) and has subsequently accumulated less ^{10}Be isotopes given its previous shielded position.

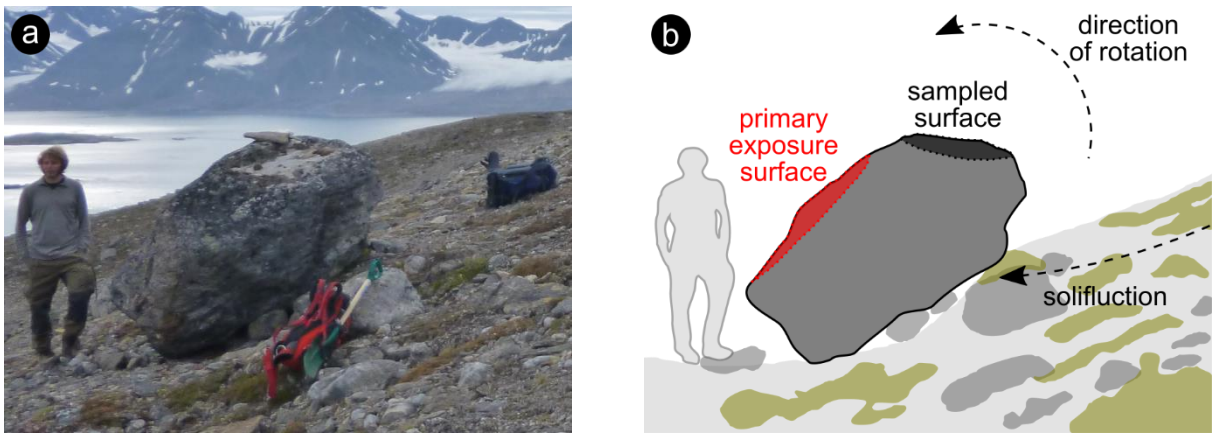

Figure 5.2: (a) GOR1404 located on the south eastern slope of Blomstrandhalvøya (Photo: O. Grant, 33N 439400 8769100 facing south), and (b) sketch to highlight the possible post-depositional movement of the boulder, with the sampled surface not corresponding to the primary exposure surface owing to rotation of the boulder.

The increased thickness and spatial coverage of till on Blomstrandsalen and to the east of Blomstrandhalvøya is a key geomorphic difference when compared to the thin sediment drape on bedrock to the west (Figure D.1, Appendix D). The till may be melt-out till (Boulton 1970), which would infer stagnant ice overlying Blomstrandsalen and the east of Blomstrandhalvøya during deglaciation. A present-day analogue to such a scenario can be observed at the front of Kongsbreen to the east of Ossian Sarsfjellet (Schellenberger *et al.* 2014), where an area of ca. 3 km^2 is covered by debris-rich stagnant ice up to 100 m thick. Stagnant ice would have significance as a geomorphic agent, with sediment gravity flows re-mobilising and re-working saturated glacial sediments (Vivian 1965; Schomacker & Kjær 2008), and may in-part be responsible for the old exposure ages of GOR1401, GOR1402, and GOR1405, while also providing an unknown degree and duration of shielding to sampled boulders.

5.3 Interpretation of the SARS transect

The probability distribution function curve from Figure 4.34 shows two near-equal peaks, with no overlap between the Gaussian curves given the analytical uncertainty. The younger population, comprising; SARS1404, SARS1405, and SARS1407, has a mean age of 12.8 ± 1.3 ka, while the older population comprising; SARS1401, SARS1402, and SARS1406, produces a mean age of 16.6 ± 1.3 ka.

As with the BLOM and GOR transects, no trend exists between elevation and exposure age for the SARS transect (Figure 4.35). The younger population, which are all derived from erratic boulders, gives ages at or close to the Bølling-Allerød to Younger Dryas transition. The 235 m vertical difference between SARS1404 (360 m a.s.l.), and SARS1405 (125 m a.s.l.) suggests rapid draw-down of the Kongsfjorden Ice Stream close to the onset of the Younger Dryas.

The older population consists of two bedrock samples (SARS1402 and SARS1406) and one erratic boulder (SARS1401), the clustering of these samples to ca. 16.6 ± 1.3 ka is not consistent with other exposure ages from Blomstrandhalvøya, and would require a pre-Bølling retreat and re-advance to explain the occurrence of B-A to YD samples at adjacent positions, such as SARS1405 (13.3 ± 0.4 ka), or higher elevations such as SARS1404 (13.0 ± 0.4 ka). It is subsequently suggested that the older exposure ages obtained from Ossian Sarsfjellet bedrock result from some inherited ^{10}Be concentration from a previous exposure (Dunai 2010) similar to other studies (Hormes *et al.* 2011; Landvik *et al.* 2013), and thus implies that glacial erosion was insufficient to remove the ca. 2–3 m of previously exposed surface at the sampling localities (Balco 2011a).

From Figure 4.36 it is evident that the bedrock samples SARS1402 (167 m a.s.l.) and SARS1406 (122 m a.s.l.) are taken from high points relative to the river channels leading from Sarsvatnet, it is

therefore suggested that bedrock topography had some influence on glacier flow velocity, with faster and potentially more abrasive ice in troughs, and less abrasive slower-flowing ice on ridges owing to greater basal sheer stress (Sugden & John 1976; Harbor *et al.* 1988; Benn & Evans 2010). Less abrasive ice may also explain the exposure age of SARS1401 (16.5 ± 0.5 ka), as the boulder is located in a sheltered position adjacent to the bedrock sample SARS1402, and thus allowed for preservation of some previous ^{10}Be concentration. Alternatively, the transport pathway of SARS1401 may be responsible for the higher exposure age compared to other sampled boulders on Ossian Sarsfjellet, as the boulder may have been transported supraglacially or englacially and subsequently experienced reduced abrasion compared to boulders close to the glacier bed (Guillon *et al.* 2015).

5.4 Glacier surface reconstruction

The exposure ages from the Blomstrandhalvøya and Ossian Sarsfjellet transects allow for a lateral and vertical reconstruction of ice surface variability during the deglaciation of Kongsfjorden (Figure 5.4), which is further constrained by published radiocarbon and cosmogenic nuclide dates, and submarine morphology from the fjord (Figure 5.3). The mouth of the fjord was deglaciated at ca. 16.3 ± 0.2 cal ka BP (Landvik *et al.* 2005; Hormes *et al.* 2013; Hughes *et al.* 2016), from this point, time slices have been selected based on the clustering of exposure dates.

BLOM1411 and SP08-5012 (Henriksen *et al.* 2014) overlap ca. 15.6 ka, and represent the late Oldest Dryas (Ehlers *et al.* 2011) (Figure 4.29). BLOM1407, BLOM1408, BLOM1412, BLOM1413, 68-BRATLIE, GOR1403, and 69-IRGENS overlap ca. 14.5 ka representing the mid Bølling-Allerød to Older Dryas, with the ice terminus constrained by radiocarbon dates from Site 12 on Brandalpynten (Lehman & Forman 1992). BLOM1401, BLOM1403, BLOM1405, BLOM1406, BLOM1409, GOR1406, SARS1404, SARS1405, and SARS1407 overlap ca. 12.7 ka which corresponds to the early Younger Dryas (Rasmussen *et al.* 2006). The Little Ice Age margin is reconstructed from historical observations of ice front positions and submarine landforms (Liestøl 1988; Streuff *et al.* 2015) as well as trimlines observed above present-day Kongsbreen, and is illustrated in Figure 5.4.

The ice surface gradient has been approximated between exposure dates based on linear best-fit of sample elevation versus position along profile A–A', while the lower (a mean gradient of 7.1 m km^{-1} (n=7)) and upper (a mean gradient of 25.7 m km^{-1} (n=8)) surface profiles derive from Greenlandic outlet glaciers (isbræ) (Thomas *et al.* 2009). The thickness of ice above contemporaneous sea level (Forman *et al.* 1987) is given as 50 m (van der Veen 1996), and the terminal positions are tentatively correlated with the transverse ridges identified by Maclachlan *et al.* (2010), which are bedrock sills

draped with glaciomarine sediments (Matthias Forwick, personal communication) and highlighted in Figure 5.3 and Figure 5.4.

Figure 5.4 is further constrained by a ^{10}Be exposure age from Kongsfjordhallet (SP08-5012 = 15.9 ± 0.7 ka, (Henriksen et al. 2014)), and a radiocarbon date from Site 12 at Brandalpynten (WHG-531 = 14.4 ± 0.3 cal ka BP Lehman and Forman (1992), recalibrated by Henriksen et al. (2014)) for the northern and southern shores of the fjord respectively. The outer margin of Profile A–A' is constrained by a deglacial radiocarbon date of 16.3 ± 0.2 cal ka BP from core NP90-9-PC3 (Landvik et al. 2005; Hormes et al. 2013; Hughes et al. 2016). The Little Ice Age ice surface (blue dot-dash line) is reconstructed from interpolation between the 1869 Kongsbreen moraine (Liestøl 1988; Streuff et al. 2015) and trimlines observed on Stemmeknausane and Snøsporven (Norwegian Polar Institute 1999).

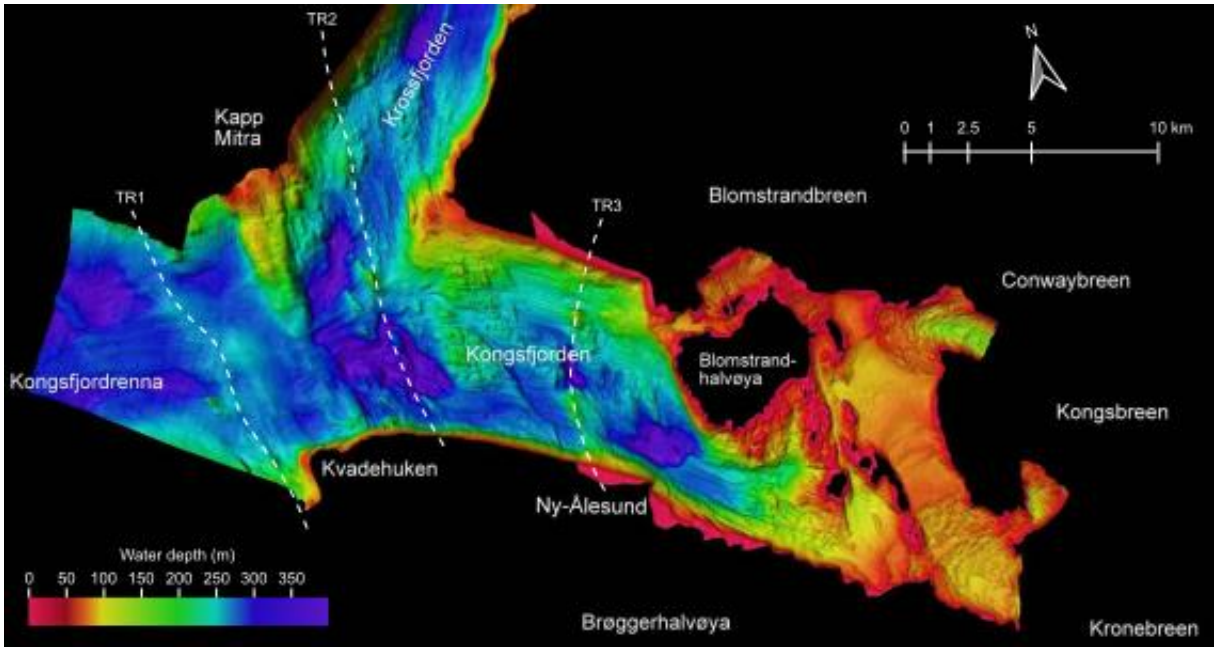

Figure 5.3: Detailed (5 x 5 m grid) bathymetry of Kongsfjorden-Krossfjorden and Kongsfjordrenna, modified from Kuipers (2013) and Dallmann *et al*. (2015). TR1–3 represent the transverse ridges identified by Maclachlan *et al*. (2010) and are potential pinning points during glacier retreat.

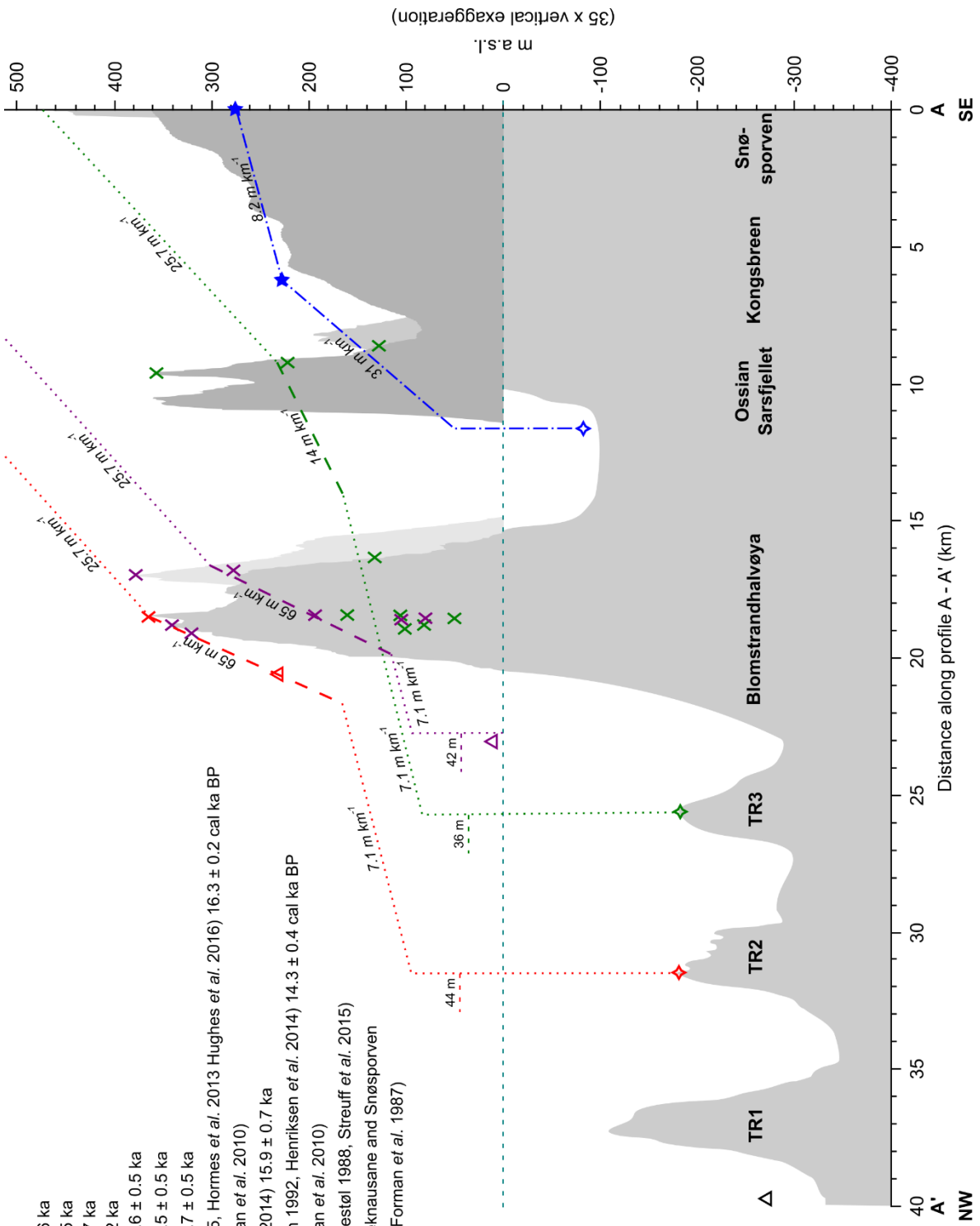
Legend
Estimated ice surface ca. 15.6 ka
Estimated ice surface ca. 14.5 ka
Estimated ice surface ca. 12.7 ka
Estimated ice surface ca. 0.02 ka
Exposure age overlapping 15.6 ± 0.5 ka
Exposure age overlapping 14.5 ± 0.5 ka
Exposure age overlapping 12.7 ± 0.5 ka
WHG-941 (Landvik et al. 2005, Hormes et al. 2013 Hughes et al. 2016) 16.3 ± 0.2 cal ka BP
Transverse ridge 2 (Maclachlan et al. 2010)
SP08-5012 (Henriksen et al. 2014) 15.9 ± 0.7 ka
WHG-531 (Lehman & Forman 1992, Henriksen et al. 2014) 14.3 ± 0.4 cal ka BP
Transverse ridge 3 (Maclachlan et al. 2010)
1869 Kongsbreen moraine (Liestøl 1988, Streuff et al. 2015)
Trimline elevation on Stemmeknausane and Snøsporven
Contemporaneous sea level (Forman et al. 1987)
Ice surface gradient
44 m
7.1 m km-1
m a.s.l.
(35 x vertical exaggeration)
500
400
300
200
100
0
-100
-200
-300
-400
0
5
10
15
20
25
30
35
40
A
A'
SE
NW
Distance along profile A - A' (km)
TR1
TR2
TR3
Blomstrandhalvøya
Ossian Sarsfjellet
Kongsbreen
Snø-sporven
65 m km-1
25.7 m km-1
14 m km-1
31 m km-1
8.2 m km-1
7.1 m km-1
42 m
36 m
44 m

Figure 5.4: Illustration of possible ice surfaces along profile A–A' (for location see Figure 1.1) in Kongsfjorden following the LGM, with thick stippled lines representing the linear best-fit between exposure ages which overlap; 15.6 ± 0.5 ka (red, n=2), 14.5 ± 0.5 ka (purple, n=8), and 12.7 ± 0.5 ka (green, n=8). The dotted lines represent extrapolated glacier surface elevation profiles from Greenlandic outlet glaciers (Thomas *et al*. 2009), grounding lines are extrapolated from the location of transverse ridges (TR1–3) in Kongsfjorden (Maclachlan *et al*. 2010), with the elevation of the calving front given as 50 m (van der Veen 1996) above the indicated contemporaneous sea level (Forman *et al.* 1987).

5.5 Kongsfjorden deglacial ice configuration

At ca. 15.6 ka, the western summit of Blomstrandhalvøya was likely ice free, as was the foot of Knølen above Kongsfjordhallet at 230 m a.s.l. (Henriksen *et al.* 2014), which provides a relatively steep surface gradient of ca. 65 m km^{-1} over the topographic pinning point provided by Blomstrandhalvøya, albeit in-line with the outlet-glacier gradient proposed by Henriksen *et al.* (2014). The ice frontal position has been tentatively correlated to Transverse Ridge 2 (Maclachlan *et al.* 2010) which is coincident with the Kongsfjorden moraine described and dated to 16.6 ± 0.8 ka by Henriksen *et al.* (2014), thus Transverse Ridge 2 is a possible pinning point, and the outer limit for an ice margin at ca. 15.6 ka.

The lower gradient of 7.1 m km^{-1} is calculated from the surface profile of the marine-terminal calving reaches of Greenlandic Isbræ (n=7) (Thomas *et al.* 2009) which is consistent with the Storstrømmen outlet glacier (4.8 to 10.9 m km^{-1}) (Funder *et al.* 1998) as well as the inactive Kamb Ice Stream and inter-ice stream ridges (5 m km^{-1}) (Rose 1979; Shabtaie *et al.* 1987). The upper extrapolated gradient of 25.7 m km^{-1} is calculated from upstream grounded portions of Greenlandic Isbræ (n=8) (Thomas *et al.* 2009), which is consistent with Daugaard-Jensen Gletscher (25.3 m km^{-1}) (Funder *et al.* 1998), Jakobshavn Isbræ (18 m km^{-1}) (Truffer & Echelmeyer 2003), and Late Weichselian ice-sheet profiles in northwest Spitsbergen (23 m km^{-1}) (Gjermundsen *et al.* 2013). Such a surface gradient would leave Irgensfjellet covered and ensure that Ossian Sarsfjellet remained under relatively thin non-erosive ice at this time, further supporting the interpretation of inherited ages for the older samples (with a mean age of 16.6 ± 1.3 ka) obtained from the SARS transect (Figure 4.34).

By ca. 14.5 ka, the summit of Irgensfjellet was ice free, showing a continued retreat of the Kongsfjorden Ice Stream from the Oldest Dryas to Older Dryas. The exposure ages overlapping 14.5 ka from the BLOM and GOR transects provide a surface gradient as equally steep as at ca. 15.6 ka, with the ice terminus constrained at 14.3 ± 0.4 cal ka BP by radiocarbon dated ice-proximal benthic foraminifera in the stratigraphy at Site 12 on Brandalpynten (Lehman & Forman 1992; Henriksen *et al.* 2014).

At ca. 14.5 ka, Ossian Sarsfjellet remained below ice cover, while increasing portions of Blomstrandhalvøya were exposed by the retreating ice margin, with a rate estimated at 2.5 km ka^{-1}. Around this time the Kongsfjordhallet strandflat (Houmark-Nielsen & Funder 1999) also became ice free below 100 m a.s.l., owing to the ^{10}Be exposure ages of 13.3 ± 0.9 ka (Henriksen *et al.* 2014). The

location of an ice margin on Blomstrandhalvøya, as implied by Figure 5.4, is complicated by the lack of any direct geomorphological evidence, it could be inferred that the thin sediment drape on bedrock to the west, and the thicker till cover on Blomstrandsalen and to the east (Figure D.1, Appendix D) may reflect the differential downwasting from west to east on the island around this time.

A cluster (n=4) of exposure ages around 12.7 ka are found below 120 m a.s.l. on western Blomstrandhalvøya, which is consistent with the trimline-moraine complex found to the east of the island (Figure 4.7) which yields the exposure age of 12.6 ± 0.5 ka from GOR1406. Further east, the summit of Ossian Sarsfjellet is likely ice free at this time, giving a significantly shallower surface profile of ca. 14 m km^{-1} for ice in Kongsfjorden compared to previous configurations, closer to that of the minimum gradient of the Kongsfjorden Ice Stream at the Late Weichselian Glacial Maximum (8 m km^{-1}) (Henriksen *et al.* 2014), or present-day Jakobshavn Isbræ (18 m km^{-1}) (Truffer & Echelmeyer 2003).

The grounding position of the Kongsfjorden glacier at ca. 12.7 ka is tentatively drawn to Transverse Ridge 3 (Maclachlan *et al.* 2010), with the lower (7.1 m km^{-1}) and upper (25.7 m km^{-1}) gradients approximated as described previously. A key implication from this inferred grounding position is that the early Younger Dryas glacier terminus extended beyond Site 12 at Brandalpynten, and thus beyond the inferred position of the Older Dryas (ca. 14.5 ka). The stratigraphic section at Site 12 contains no diamict above Unit 6 which is inferred as pre-YD given the ice proximal foraminifera date of 14.3 ± 0.4 cal ka BP from Unit 5 (Lehman & Forman 1992; Henriksen *et al.* 2014), however the stratigraphy from a bedrock-notch close to Solvatnet in Ny-Ålesund suggests later deglaciation, with bird colonisation after ca. 10.7 cal ka BP (Yuan *et al.* 2009), providing a window for YD ice coverage.

The supressed marine limit on Blomstrandhalvøya provides further evidence for a persistent still-stand in inner Kongsfjorden during the YD, reducing isostatic rebound and/or covering lower-elevations with ice (Lehman & Forman 1992). However it is evident that glaciers on Spitsbergen retreated close-to or behind present margins during the early Holocene (Svendsen & Mangerud 1997). 17th Century whaler's maps document an isolated Blomstrandhalvøya (Liestøl 1988), and thus showing the 18th and 19th Century Little Ice Age Advance to be the maximum Holocene extent in Kongsfjorden, although this has been challenged given an abundance of exposure ages clustering around 1.3 ka distal to established LIA moraines in Kongsfjorden and other fjords on Svalbard (Reusche *et al.* 2014; Gislefoss 2015; Phillips *et al.* Submitted for review) (Dylan Rood, personal communication).

Another implication of an early YD stillstand or slight advance in Kongsfjorden is the subsequent deposition of erratic boulders within close geographic proximity and elevation to boulders yielding B-A exposure ages on western Blomstrandhalvøya. The physiographic position of the boulders on western Blomstrandhalvøya is typically directly on weathered bedrock with only a thin drape of diamicton

(Figure 4.8b; Figure 4.30), so melt-out deposition from relatively clean ice is inferred (Boulton 1978), the presence of isolated erratic blocks on locally derived grus may be explained by cold-based ice-flow and deposition via surface lowering (Atkins *et al.* 2002). Cold-based ice on Blomstrandhalvøya during the early Younger Dryas could be explained by its marginal position to the outlet glacier, and thus differing thermal regime and erosion to the main flow-line, with cold-based ice bounding faster-flowing warm-based ice (Sugden 1977, 1978; Briner *et al.* 2006).

Bathymetric evidence shows retreat moraines starting offshore from Ny-London (Maclachlan *et al.* 2010; Kuipers 2013; Streuff *et al.* 2015) which suggests episodic retreat of a grounded ice mass, where Blomstrandhalvøya acted as a topographic pinning point stabilising the ice margin during retreat (Benn & Evans 2010). Given the lack of dates within the fjord east of Blomstrandhalvøya, it is assumed that this retreat continued through the late Younger Dryas and Preboreal, close to the present margins (Liestøl 1988).

The most recent moraine features observed in the bathymetry represent 19th and 20th Century advances of the outlet glaciers in Kongsfjorden (Streuff *et al.* 2015), with the Kongsbreen, Kronebreen, Conwaybreen, Kongsvegen, and Blomstrandbreen calving margins extending up to 5 km further into the fjord in 1869 compared to 2015. The freshness of trimlines east of Ossian Sarsfjellet, and corresponding terminal moraines in the bathymetry, allow for an interpolation of the Little Ice Age surface profile which is approximated at 31 m km^{-1} (Figure 5.4), in line with the present outlet glaciers (ca. 45 m km^{-1} for Kongsbreen), while the upper gradient is shallower at ca. 8.2 m km^{-1} following the observed dip in the trimlines.

The proposed course of deglaciation in Kongsfjorden is illustrated in Figure 5.5, which was constructed from a GIS model, with the glacier surface built as a triangular irregular network (TIN) based on interpolation of known and extrapolated points from the surface profiles of Figure 5.4, and from Henriksen *et al.* (2014) for ca. 16.6 ka. The contemporaneous sea level is also shown, which was produced by masking the digital terrain model (DTM) of Kongsfjorden (Norwegian Polar Institute 2014) by the calibrated (Reimer *et al.* 2013) published sea level for Brøggerhalvøya (Forman *et al.* 1987). The glacier outline for each time slice was then taken as the intersection between the TIN and DTM, with the exception of ca. 0.02 ka which was produced by tracing the Little Ice Age trimlines and moraines. The resulting time-slice reconstruction shows the thinning and subsequent retreat of the ice body in Kongsfjorden, which shows increasing topographic bounding and emergence of nunataks.

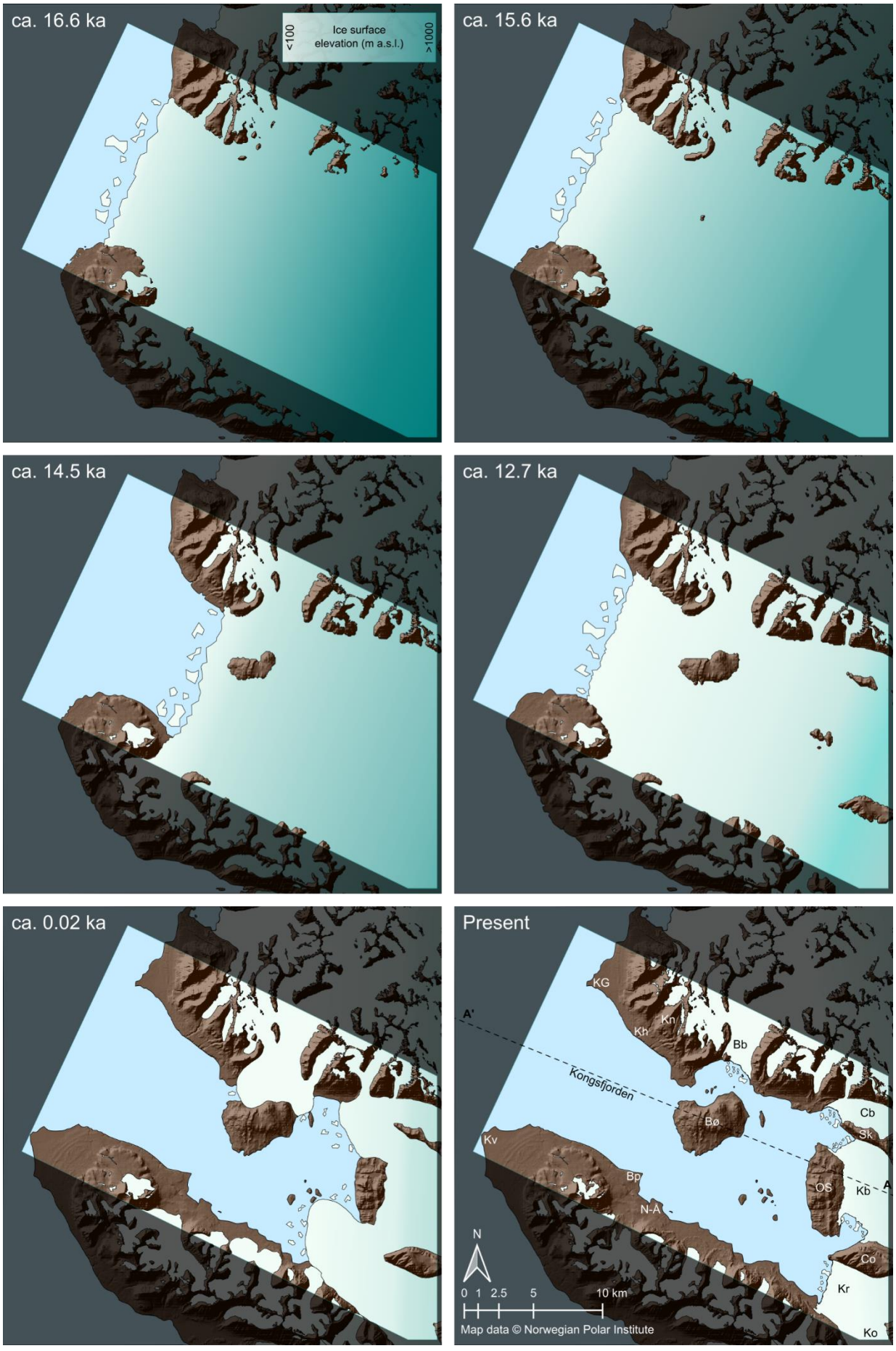
ca. 16.6 ka
Ice surface elevation (m a.s.l.)
<100
>1000
ca. 15.6 ka
ca. 14.5 ka
ca. 12.7 ka
ca. 0.02 ka
Present
KG
Kn
Kh
Bb
A'
Kongsfjorden
Bø
Cb
Sk
Kv
Bp
OS
Kb
A
N-A
N
Co
Kr
Ko
0 1 2.5 5 10 km
Map data © Norwegian Polar Institute

Figure 5.5: Illustrated time-slice reconstruction of the deglaciation of Kongsfjorden, based on ice surface profiles from Figure 5.4, the contemporaneous sea level for each time slice is shown (16.6 ka = 45 m, 15.6 ka = 44 m, 14.5 ka = 42 m, and 12.7 ka = 36 m) (Forman *et al.* 1987), with the proposed ice margin position and suggested elevation above present sea level. The present ice margins are shown for Kongsfjorden (Norwegian Polar Institute 2014) with outlet glaciers labelled (Bb = Blomstrandbreen, Cb = Conwaybreen, Kb = Kongsbreen, Ko = Kongsvegen, and Kr = Kronebreen), along with notable landmarks (Bø = Blomstrandhalvøya, Bp = Brandalpynten, Co = Colletthøgda, Kh = Kongsfjordhallet, KG = Kapp Guissez, Kn = Knølen, Kv = Kvadehuken, N-Å = Ny-Ålesund, OS = Ossian Sarsfjellet, and Sk = Stemmeknausane), profile line A–A' is also shown and can be seen in Figure 1.1c.

5.6 The chronology of glacier retreat in Kongsfjorden

The exposure ages obtained from Blomstrandhalvøya and Ossian Sarsfjellet suggest a stepped deglaciation of Kongsfjorden following the Late Weichselian Glacial Maximum. The chronology of the deglaciation of the fjord is outlined in this section, within the context of previous work in the Kongsfjorden and western Spitsbergen area.

5.6.1 Pre-Bølling – shelf-edge glaciation and retreat

The outer shelf west of Kongsfjorden was deglaciated prior to ca. 16.3 cal ka BP (Landvik *et al.* 2005; Hormes *et al.* 2013; Hughes *et al.* 2016), in line with the ice retreat from the shelf edge west of Isfjorden, occurring prior to ca. 16.5 cal ka BP (Elverhøi *et al.* 1995; Svendsen *et al.* 1996). Jessen *et al.* (2010) concluded that deglaciation from the western Svalbard shelf began up to 3 ka earlier than the suggested ca. 17.7 cal ka BP (Jones & Keigwin 1988; Elverhøi *et al.* 1995; Siegert & Dowdeswell 1995a, b; Landvik *et al.* 1998), with ice rafted debris peaks recorded around 20.5 cal ka BP on the shelf-edge west of Bellsund and outside of Storfjordrenna (Cadman 1996; Rasmussen *et al.* 2007), this early-onset deglaciation is attributed to reduced glacial accumulation due to starvation of moisture by extensive sea ice and low atmospheric temperatures (Gildor & Tziperman 2001; Jessen *et al.* 2010).

Svendsen *et al.* (1996) suggest that the initiation of pre-Bølling retreat from the shelf-edge was triggered by rising global sea levels, given the limited evidence for a warming Norwegian Sea (Lowe & NASP Members 1995). However, Ślubowska *et al.* (2005) found evidence of Atlantic water masses along the western and northern Svalbard shelf from ca. 17.5 ka onwards, leading to reduction in sea ice based on *I. norcrossi/helenae* benthic foraminifera abundance (Ślubowska *et al.* 2005; Ślubowska-Woldengen *et al.* 2007).

The style of deglaciation from the shelf-edge appears to fit an episodic retreat mode (Dowdeswell *et al.* 2008), with grounding zone wedges and transverse ridges overprinting mega-scale glacial lineations in the bathymetry of Kongsfjorden and Kongsfjordrenna (Figure 1.4, Figure 2.4, and Figure 5.3) (Ottesen *et al.* 2007; Maclachlan *et al.* 2010; Kuipers 2013; Dallmann *et al.* 2015; Streuff *et al.* 2015), with superimposed retreat moraines only found in the inner fjord.

5.6.2 Bølling-Allerød – drivers of retreat

The tributary ice-stream (Rignot *et al.* 2011; Landvik *et al.* 2013) in Kongsfjorden had receded from an isbræ-type ice stream (Truffer & Echelmeyer 2003) to an outlet-glacier or ephemeral ice stream (Kleman *et al.* 2007) at the mouth of Kongsfjorden by around 16.6 ka (Henriksen *et al.* 2014; Landvik *et al.* 2014), and continued to retreat to at least ca. 14.5 ka. This is in contrast to the deglaciation of Isfjorden, which experienced an Older Dryas readvance with ice lobes extending onto the inner shelf at ca. 14.7 cal ka BP (Svendsen *et al.* 1996), and is not represented by the Kongsfjorden Moraine which is shown to be a retreat feature (Landvik *et al.* 2005).

The timing of the retreat to mid-Kongsfjorden and the deglaciation of eastern Blomstrandhalvøya above ca. 300 m a.s.l. (Figure 5.4 and Figure 5.5) is contemporaneous with the Bølling-Allerød interstadial recorded in Greenland ice cores (Alley *et al.* 1993; Rasmussen *et al.* 2006), with this period showing an increased advection of relatively warm Atlantic Water in the bottom waters over the north and west Svalbard shelf (Koç *et al.* 2002; Ślubowska *et al.* 2005; Ślubowska-Woldengen *et al.* 2007), and is likely to have entered Kongsfjorden, accelerating glacial retreat with a peak in IRD recorded between 15.7–14.7 cal ka BP (Jessen *et al.* 2010). The early-Bølling timing of deglaciation at the fjord-mouths along the west of Spitsbergen appears to be a regional trend with other fjords on the west coast of Spitsbergen experiencing deglaciation (Mangerud *et al.* 1987), with Atlantic Waters also found over the south western Svalbard shelf (Rasmussen *et al.* 2007).

Lehman and Forman (1992) suggest that Bølling-Allerød Kongsfjorden ice retreat is tied to the northward migration of the Polar Front in the North Atlantic at this time (Ruddiman & Mcintyre 1981), creating sea-ice-free oceans and a subsequent atmospheric warming in the northern Norwegian Sea region, partially ice-free oceans are indicated by the increase in planktonic foraminifera during the Bølling-Allerød (Ślubowska *et al.* 2005). Rising atmospheric temperatures during the Bølling interstadial are also suggested as a driver for deglaciation by Hormes *et al.* (2013), and may have acted in combination with a perturbation in sea level owing to the meltwater plumes dated to 14.8 ± 0.2 and 14.3 ± 0.3 cal ka BP (Jessen *et al.* 2010). An alternative source for abrupt sea level rise around 14.5 ka is the onset of deglaciation of the Western Antarctic ice sheet (Clark *et al.* 2009). Winsborrow *et al.* (2012) suggest that grounding line bathymetry (the depth and slope of grounding line) has the strongest control on ice stream behaviour on the millennial timescale of deglaciation, with sea level rise causing a grounding line retreat (Jamieson *et al.* 2014).

The combination of atmospheric warming, warm water advection, and potential eustatic rise led to the collapse of Ice Shelves on the west of Spitsbergen, with a subsequent debuttressing and enhanced ablation of outlet glaciers such as that in Kongsfjorden during the Bølling interstadial (Hormes *et al.*

2013), leading to the continued lateral retreat, and the exposure of eastern Blomstrandhalvøya above ca. 280 m a.s.l. (Figure 4.31, Figure 4.33, and Figure 5.5).

5.6.3 Younger Dryas – stillstand or readvance

Lehman and Forman (1992) suggested a stillstand or slight readvance of the Kongsfjorden outlet glacier during the Younger Dryas, lasting until ca. 11.6 cal ka BP, based primarily on the supressed Late Weichselian marine limit observed on Blomstrandhalvøya. The 20 m difference in observed and expected marine limit (Figure 2.5 and Figure 4.26) implies a reduced glacioisostatic uplift, and thus an incomplete unloading, which is also observed contemporaneously further south in Isfjorden (Svendsen *et al.* 1996), with a trace of a possible readvance in Billefjorden around 11 cal ka BP denominating the Billefjorden Stage (Boulton 1979), and further corroborated with boulders on Reuschhalvøya and Krossfjorden yielding exposure ages of 11.7 ± 0.8 ka and 12.3 ± 0.9 ka respectively (Hormes *et al.* 2013).

It is suggested that a stagnation in retreat or possible readvance on the west coast of Spitsbergen during the Younger Dryas was a result of ice cap stabilisation or growth over central-eastern Spitsbergen (Boulton 1979; Forman *et al.* 1987; Landvik *et al.* 1987; Lehman & Forman 1992), with continued accumulation on eastern Spitsbergen ice caps (Svendsen *et al.* 1996), precipitation was predominantly from the southeast (Jonsson 1982; Lehman & Forman 1992), while ablation dominated to the west with reduced precipitation. The persistence of the Polar Front over the northern Svalbard shelf during the Younger Dryas (Ślubowska *et al.* 2005) may indicate a weakened Western Spitsbergen Current (Figure 2.3) (Hald *et al.* 2004) and thus a thicker sea ice cover and starved precipitation from the west, combined with increased insolation this caused the retreat of local and cirque glaciers (Mangerud & Svendsen 1990; Mangerud & Landvik 2007; Reusche *et al.* 2014; Patton *et al.* 2015) and the thinning of outlet glaciers.

By contrast, Henriksen *et al.* (2014) suggest that valley glaciers in Kongsfjorden, such as Olssønbreen, advanced between ca. 12.1 and 9.2 ka, in line with other Younger Dryas and early Holocene glacial advances on western Spitsbergen (Lønne 2005; Forwick & Vorren 2009; Landvik *et al.* 2014). The driver for such terrestrial local ice-flow advance (Landvik *et al.* 2013; Landvik *et al.* 2014) may have been climatic (Patton *et al.* 2015), leading to a multi- decadal advance (Lønne 2005).

Fjord glaciers experienced a stillstand or advance resulting from reduced calving or seasonal ablation owing to lower summer temperatures (Forwick & Vorren 2009), and the exposure dates obtained from Blomstrandhalvøya and Ossian Sarsfjellet indicate a shallower ice gradient at ca. 12.7 ka compared to the early Bølling and Pre-Bølling gradients, suggesting dynamic thinning as opposed to lateral retreat

as the main mechanism of ice loss in Kongsfjorden during the Younger Dryas. The conflicting evidence for Younger Dryas glacial activity on Svalbard highlights the time-transgressive heterogeneity in the response of ice sheet margins during deglaciation (Patton *et al.* 2015), largely controlled by fjord or inter-fjord physiography (Landvik *et al.* 2013; Landvik *et al.* 2014), complexities incurred upstream by ice-stream flow and velocity switching (Dowdeswell *et al.* 2006; Nygård *et al.* 2007), and also variable timing of response to drivers between local glaciers and outlet glaciers.

5.6.4 Preboreal to Holocene – periglacial landscape development

It is likely that the remnant outlet glacier from the Younger Dryas stillstand or readvance retreated rapidly at the Younger Dryas to Preboreal transition, close to present-day margins given the radiocarbon date of 10.7 ± 0.2 cal ka BP from Ossian Sarsfjellet (Forman 1990; Lehman & Forman 1992). This pattern of rapid Preboreal retreat caused by increased calving is observed in fjords along the west coast of Spitsbergen (Mangerud & Svendsen 1990; Svendsen *et al.* 1996; Svendsen & Mangerud 1997; Baeten *et al.* 2010; Skirbekk *et al.* 2010), with increased influence of Atlantic Water between ca. 11.5–10.6 cal ka BP recorded in marine fauna in Kongsfjorden (Skirbekk *et al.* 2010).

Blomstrandhalvøya was most likely completely ice free by the Preboreal to Holocene transition, allowing for the development of periglacial landforms as continuous permafrost aggraded to depths exceeding 150 m in a near-shore setting (Liestøl 1977; Humlum 2005) although some permafrost may have survived below the Late Weichselian ice sheet (Kleman 1994; Humlum *et al.* 2003).

One of the most striking periglacial landforms observed on Blomstrandhalvøya is the talus-derived rock glacier on the northern slope with the foot at ca. 30 m a.s.l. (Figure 4.14), which has topo-climatic and geomorphic significance, indicating a persistent dry climate with cool summers through the Holocene (Humlum 1998), although it may be an isolated landform owing to its northern aspect. The approximate volume of rock-glacier debris (ca. 325,000 m^3 assuming 40 % porosity after Humlum (2000)) and headwall surface area (97,500 m^2) indicates a rockwall retreat of ca. 3.3 m, with a mean rate of ca. 290 mm ka^{-1} during the Preboreal and Holocene, two orders of magnitude greater than the rockwall retreat induced by biogenic flaking (André 1997), and thus implying an increased rockfall rate under recently deglaciated terrain, enhanced by prevailing periglacial conditions.

The abundance of patterned ground and stone stripes on Blomstrandhalvøya (Herz & Andreas 1966a) also shows continued glacier-free conditions from the end of the Younger Dryas, allowing cryoturbation and frost-creep processes in the permafrost active-layer to rework till deposits (Van Vliet-Lanoë 1988, 1995). The deceleration in falling relative sea-level from ca. 11.2 cal ka BP (Figure 4.26) (Forman *et al.* 1987) produced the flight of beach ridges and strandlines particularly prominent

on the south west of Blomstrandhalvøya, beaches up to ca. 3 m a.s.l. were likely overprinted by the Talavera Transgression culminating at ca. 6.8 ka (Forman *et al.* 1987; Forman 1990), synchronous with the Tapes Transgression in western Norway (Svendsen & Mangerud 1987).

5.6.5 The Little Ice Age – Holocene glacial maximum

The onset of Neoglaciation in western Spitsbergen is suggested from 3.5 cal ka BP (Baranowski 1977), however the maximum glacial extent in the Holocene in Kongsfjorden is the Little Ice Age (LIA), demarked by fresh trimlines and terminal moraines (Mellor 1957; Liestøl 1969), the LIA is also seen as the most significant Holocene glacial advance in western Spitsbergen (Mangerud & Svendsen 1990; Svendsen *et al.* 1996; Mangerud & Landvik 2007), with the maximum ice front position for Kongsbreen recorded at 1869 (Liestøl 1988; Streuff *et al.* 2015). On Blomstrandhalvøya, the lateral and end-moraine complex observed to the north and east of the island (Figure D.1, Appendix D) represent the LIA advance from Blomstrandbreen, with glacial ice bridging Nordvågen until 1992 when Blomstrandhalvøya became an island (Svendsen *et al.* 2002; Ziaja & Ostafin 2014).

The initiation of the LIA advance was asynchronous around the North Atlantic (Grove 2001), but shows a time-transgressive onset on a transect from Norway to Svalbard (Gjerde *et al.* Submitted for review). The climatic deterioration has been attributed to; volcanic eruptions (Porter 1981), summer temperature anomalies (Briffa *et al.* 1998), changing solar irradiance (Crowley 2000), and reduced meridional overturning circulation in the North Atlantic (Bianchi & McCave 1999), while a recent study suggests mild conditions in the Little Ice Age over Svalbard, with increased winter precipitation tied to the increased heat transport of the West Spitsbergen Current from ca. 1600 (D'Andrea *et al.* 2012). It is evident that similar 'Little Ice Age'-type climatic events have occurred throughout the Holocene (Matthews & Briffa 2005), however any traces of previous Holocene glacial advances initiated by such climatic forcing have largely been erased by the 18th and 19th Century advance in Kongsfjorden.

5.7 Geomorphic implications

The central position of Blomstrandhalvøya in Kongsfjorden may have geomorphic significance, as the island is essentially a large roche moutonnée (Sugden & John 1976; Lauritzen 2006; Benn & Evans 2010) providing a topographic barrier to along-fjord glacier flow. The resulting reduction in normal pressure on the lee side of Blomstrandhalvøya during glacial overriding may have generated conditions for cold-based ice to develop over Kongsfjordhallet to the northwest during the Late Weichselian and earlier glaciations, thus preserving the early Pleistocene till (≥1 Ma), and providing an explanation for

the lack of Middle and Late Weichselian till (Houmark-Nielsen & Funder 1999). Cold-based or dynamically less active ice has been proposed as the mechanism by which raised beaches and other delicate landforms on Brøggerhalvøya, Kongsfjordhallet, and Prins Karls Forland have survived Late Weichselian glaciation (Landvik *et al.* 1998; Landvik *et al.* 2005; Ottesen *et al.* 2007; Landvik *et al.* 2013; Henriksen *et al.* 2014), with the climatic amelioration during deglaciation being too short-lived to influence the basal thermal regime (Sollid & Sørbel 1988).

It is thus suggested that the lateral moraines traced along Kongsfjordhallet up to ca. 300 m a.s.l. (Lehman & Forman 1992; Houmark-Nielsen & Funder 1999; Landvik *et al.* 2005; Peterson 2008; Henriksen *et al.* 2014) represent an ice marginal position during recession from the Late Weichselian Glacial Maximum, and has been dated by Henriksen *et al.* (2014) to ca. 16.6 ± 0.8 ka. At this time the glacial ice covering Kongsfjordhallet switched from cold-based to periodically more active ice (Landvik *et al.* 2013), depositing the lateral moraine ridges on Kongsfjordhallet and building the Kongsfjorden Moraine in the mouth of the fjord.

5.8 Comparing local and regional deglaciation

This reconstruction of the deglaciation of Kongsfjorden following the Late Weichselian Glacial Maximum (Figure 5.4 and Figure 5.5) may be compared to other reconstructions local to Kongsfjorden and northwest Spitsbergen, and also to the wider regional context of the Svalbard-Barents Sea Ice Sheet.

5.8.1 Kongsfjorden and Krossfjorden

The general pattern of deglaciation in northwest Spitsbergen fjords during the Late Glacial was presented by Sexton *et al.* (1992) based on sedimentological analysis from Krossfjorden. The retreat signature was summarised as; (1) deposition of basal till or glaciomarine sediments during or just after the Late Weichselian glacial maximum, (2) Ice retreat to at least the present position by ca. 10.2 cal ka BP, (3) subaqueous fans deposited in front of tidewater glaciers at or close to present margins for a period up to ca. 10 ka, (4) LIA advance up to 3 km beyond present margins, deforming subaqueous fans and depositing submarine terminal moraines and basal till, (5) tidewater glaciers retreated from their LIA extent towards present margins from the end of the 19th Century (Sexton *et al.* 1992). The deglaciation of Kongsfjorden presented in this study substantially builds on this conceptual model, given the timing of retreat to present margins and the maximum Holocene advance represented by the LIA, however the model does not reflect the temporal and spatial variability during

retreat, such as a Younger Dryas stillstand or readvance, for which there is dated geomorphic and bathymetric evidence presented in the wider succeeding literature and in this study.

It is evident that Kongsfjorden was glaciated up to at least 450 m a.s.l. during the Late Weichselian, with the preservation of the autochthonous blockfield above ca. 500 m a.s.l. on Knølen either representing a nunatak or thermal boundary in the ice sheet (Henriksen *et al.* 2014). The Kongsfjorden ice stream slowed and stabilised between 16.5 ± 0.3 and 15.2 ± 0.5 cal ka BP, when the Kongsfjordhallet lateral moraines and the 'Kongsfjorden Moraine' were deposited (Henriksen *et al.* 2014), marking the starting point for this study given the early exposure dates of 15.6 ± 0.5 ka from the summit of western Blomstrandhalvøya.

The Kongsfjorden ice stream at ca. 16.6 ± 0.9 ka reflected a surface gradient equivalent to Greenlandic topographically constrained outlet glaciers or isbræ (Henriksen *et al.* 2014) which is also suggested in this study for later ice surfaces, however Henriksen *et al.* (2014) suggest a dynamic thinning without marginal retreat from ca. 16.6 ka, in line with other studies on the ice cap dynamics in northwest Spitsbergen (Gjermundsen *et al.* 2013; Hormes *et al.* 2013). This study suggests that between ca. 15.6 and 14.5 ka, the ice surface gradient remained much the same while lateral retreat occurred, and thus ablation via calving was possibly the key mechanism for mass loss during the Bølling interstadial, this is indicated by the increased IRD flux between 15.2 ± 0.5 and 14.5 ± 0.3 cal ka BP in the Kongsfjorden trough (Landvik *et al.* 2005).

Contemporary to the work of Sexton *et al.* (1992) in Krossfjorden, Lehman and Forman (1992) focused on reconstructing the deglaciation of Kongsfjorden from terrestrial observations, and proposed a two-step deglaciation, with a fjord-mouth to inner-basin deglaciation between 15.6 and 14.0 cal ka BP, and an inner-basin to present-margin retreat between 11.6 and 10.8 cal ka BP (Lehman & Forman 1992). This two-step deglaciation provided a window for Younger Dryas stabilisation or readvance, further corroborated by the supressed marine limit on Blomstrandhalvøya (Lehman & Forman 1992), and further highlighted by the presence of a YD dated trimline-moraine complex and erratic boulders on Blomstrandhalvøya from this study. The YD ice marginal positions proposed by Lehman and Forman (1992) are not fully consistent with the ice surface gradient proposed in Figure 5.4 which suggests an ice frontal position beyond Brandalpynten, however there is no sedimentological evidence of Site 12 being overridden after ca. 14.4 ± 0.3 cal ka BP (Lehman & Forman 1992), although this may represent clean cold-based ice cover during the Younger Dryas, as on Blomstrandhalvøya discussed below.

Evidence for a YD stillstand or readvance in Kongsfjorden is presented by Skirbekk *et al.* (2010), with late YD conditions shown to be cold, harsh and ice-proximal close to the fjord mouth over core site NP05-11-21. Basin fills and subglacial channels delivering sediments were observed in the fjord

bathymetry, and an accumulation rate of up to 30 cm a^{-1} was suggested for basins in mid-Kongsfjorden (Howe *et al.* 2003), a marine to terrestrial difference in sediment delivery is thus presented, given the thin till drape over western Blomstrandhalvøya compared to the >30 m thick basin fills in the fjord. It is therefore likely that Younger Dryas sediment delivery was primarily through subglacial meltwater channels, as observed in front of present-day Kronebreen and Kongsvegen (10 cm a^{-1}) (Elverhøi *et al.* 1980), while relatively clean ice melted out on Blomstrandhalvøya, producing the till veneer and abundant erratics but lacking observable moraines.

Henriksen *et al.* (2014) do not rule out the possibility of a YD stillstand or readvance of the Kongsfjorden outlet glacier, and provide evidence for late YD to early Holocene advance of cirque glaciers in the fjord, which would thus suggest a lowering of the equilibrium line altitude (ELA) of such glaciers. Present ELA of cirques in northwest Spitsbergen is around 260 m a.s.l. and has been reconstructed to below 200 m a.s.l. during the LIA (Røthe *et al.* 2015), it is therefore conceivable that Blomstrandsalen, at around 280 m a.s.l., could have contained a small plateau glacier (either a re-activation of stagnant ice or a re-nucleation) at one or multiple periods during the Holocene given the suggested reoccurrence of LIA-type climatic conditions (Matthews & Briffa 2005). Such a plateau glacier could explain the medial moraine (Figure 4.6), the lateral and end moraine to the west (Figure 4.5), and the abundance of active and abandoned fluvial channels draining radially from Blomstrandsalen (Figure D.1, Appendix D).

Overall, the pattern of deglaciation reconstructed in this study from ca. 15.6 ka in Kongsfjorden builds on the conceptual model of Sexton *et al.* (1992), while remaining consistent with the stepwise deglaciation suggested by Lehman and Forman (1992) and Henriksen *et al.* (2014). The style of deglaciation during the Bølling interstadial appears to be calving-dominant over dynamic thinning given the suggested ice margin retreat, and the Younger Dryas stabilisation or readvance is consistent with Lehman and Forman (1992) and Skirbekk *et al.* (2010) but with a shallower gradient and therefore a dynamic thinning rather than calving-dominated retreat. Further, Blomstrandhalvøya (and therefore most of Kongsfjorden) above ca. 200 m a.s.l. may have been susceptible to LIA-type climatic deteriorations during the Holocene.

5.8.2 Northwest Spitsbergen

The fjord sea floor morphology in Woodfjorden (ca. 55 km northwest of Kongsfjorden) and its tributaries (Bockfjorden and Liefdefjorden) shows evidence of northward ice streaming during the Late Weichselian, with a subsequent stepwise deglaciation (Hansen 2014). As with Kongsfjorden (Howe *et al.* 2003; Maclachlan *et al.* 2010; Streuff *et al.* 2015), grounding zone wedges, transverse ridges, and

recessional moraines indicate punctuated ice retreat in Woodfjorden (Dowdeswell *et al.* 2008; Hansen 2014), with rapid deglaciation of the outer fjord and slower retreat in the mid- and inner-fjord.

The timing of retreat from the mouth of Woodfjorden differs from that of Kongsfjorden, with Reinsdyrflya becoming ice-free between 14.8 ± 1.0 and 13.4 ± 1.0 ka (Hormes *et al.* 2013), compared to the mouth of Kongsfjorden at ca. 16.6 ka (Landvik *et al.* 2005; Henriksen *et al.* 2014), inner Kongsfjorden was subject to deglaciation during the Bølling interstadial from this study, whereas mid-Krossfjorden was ice-free slightly later (ca. 13.7 ± 1.0 ka) (Gjermundsen *et al.* 2013; Landvik *et al.* 2013).

An asynchronous Late Weichselian retreat in the fjords of northwest Spitsbergen is therefore suggested, similar to that of the northwest Fennoscandian Ice Sheet over Finnmark (Stokes *et al.* 2014), thus implying a fjord-geometry/topographic control on deglaciation, with deep-narrow or wide-shallow fjords with topographic pinning points deglaciating slower than deep-wide fjords without pinning points under the same climatic or oceanic forcing (Hansen 2014). Alternatively, Reinsdyrflya may have been an inter-ice stream area (Ottesen & Dowdeswell 2009; Landvik *et al.* 2013; Hansen 2014) under cold-based ice given the preservation of pre-Late Weichselian raised beaches (Salvigsen & Österholm 1982; Gjermundsen *et al.* 2013), and thus may have deglaciated later than the Woodfjorden trough.

A key similarity between Woodfjorden and Kongsfjorden is the reduced IRD flux during the Younger Dryas, with a reduction in IRD seen between ca. 12.8 and 12.1 cal ka BP in Woodfjorden (Hansen 2014) and a low IRD flux in Kongsfjorden prior to ca. 11.5 cal ka BP (Skirbekk *et al.* 2010), however as with Kongsfjorden, there is little geomorphic, sedimentary or bathymetric evidence for a Younger Dryas ice marginal position beside some faint grounding zones and basin-fills (Howe *et al.* 2003; Hansen 2014). The final stage of Late Weichselian deglaciation in Kongsfjorden and Woodfjorden appears near-synchronous, with IRD peaks at ca. 10.8 cal ka BP in Kongsfjorden (Skirbekk *et al.* 2010) and ca. 10 cal ka BP in Woodfjorden (Hansen 2014), thus fulfilling the conceptual model of Sexton *et al.* (1992) with ice margins at or behind present positions by ca. 10.2 ka.

In contrast to the fast flowing ice streams in Kongsfjorden-Krossfjorden and Woodfjorden, the islands of Amsterdamøya and Danskøya in northwesternmost Svalbard (ca. 90 km northeast of Kongsfjorden) provide evidence for a restricted glaciation during the Late Weichselian (Landvik *et al.* 2003). The plateaus above ca. 300 m a.s.l. have remained ice-free for >80 ka, while the fjords, troughs, straits and coastal lowlands were glaciated during the last glacial, giving a deglaciation age between 18 and 15 ka based on ^{10}Be exposure dating (Landvik *et al.* 2003) in line with the shelf-edge to fjord-mouth

deglaciation in western and northern Spitsbergen (Svendsen *et al.* 1996; Landvik *et al.* 2005; Jessen *et al.* 2010).

The exposure dating on Amsterdamøya and Danskøya provided the first geological evidence of nunataks throughout the Late Weichselian in northwest Spitsbergen (Landvik *et al.* 2003), however the evidence does not corroborate the restricted-ice conditions postulated by authors observing pre-Late Weichselian landforms on Brøggerhalvøya, Kongsfjordhallet, and Prins Karls Forland (Forman & Miller 1984; Miller *et al.* 1989; Andersson *et al.* 1999; Houmark-Nielsen & Funder 1999), given the likelihood of preservation beneath cold-based or periodically active ice (Landvik *et al.* 2013; Landvik *et al.* 2014).

The 20 to 40 m km^{-1} Late Weichselian ice gradient extrapolated from Amsterdamøya and Danskøya (Landvik *et al.* 2003) could provide scope for nunataks further inland during the last glacial maximum, with peaks above ca. 950 m in the Kongsfjorden-Krossfjorden area potentially ice free, in keeping with the >900 m ice depth suggested for Krossfjorden during the Late Weichselian (Gjermundsen *et al.* 2013).

5.8.3 Western Spitsbergen

The deglaciation of Isfjorden (ca. 90 km south of Kongsfjorden) was also suggested to have occurred stepwise by Elverhøi *et al.* (1995) and Svendsen *et al.* (1996), the authors proposed an Older Dryas readvance in Isfjorden at ca. 14.7 cal ka BP beyond the fjord-mouth (Figure 5.6), related to a reduced Atlantic Water inflow (Lehman & Keigwin 1992), and tentatively correlated this advance with the deposition of the 'Kongsfjorden Moraine' (Lehman & Forman 1992), however this has since been shown as a pre-Bølling retreat moraine (Henriksen *et al.* 2014) and no evidence for an Older Dryas advance is found in Kongsfjorden. Forwick and Vorren (2009) suggest that tidewater outlet glaciers were present in Isfjorden during the Allerød and into the Younger Dryas, mirroring but lagging the retreat pattern in Kongsfjorden where the ice stream stabilised close to the fjord mouth by ca. 16.6 ka (Figure 5.5) (Henriksen *et al.* 2014).

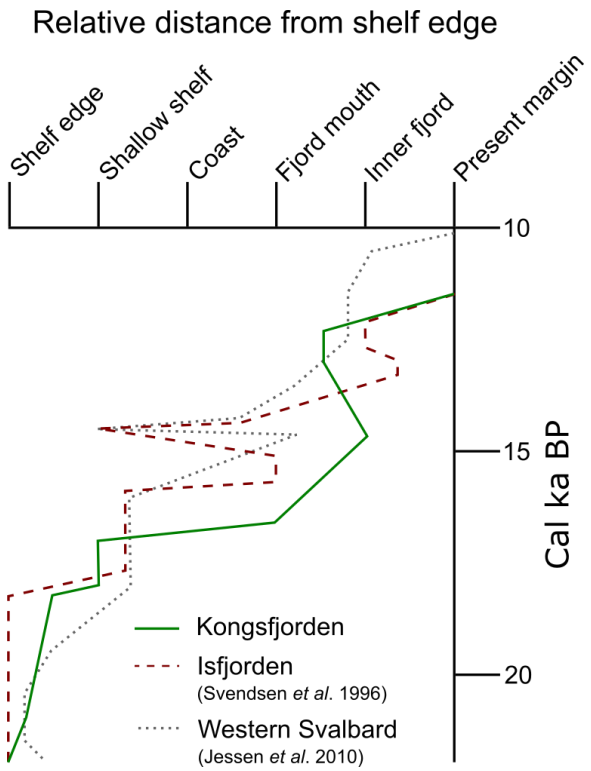

Figure 5.6: Simplified relative time-distance diagram for the ice margin retreat since the Late Weichselian Glacial Maximum, with the relative curve for Kongsfjorden constructed from; Lehman and Forman (1992); Landvik *et al*. (2005); Jessen *et al*. (2010); Henriksen *et al*. (2014), and this study. Isfjorden was recalibrated via IntCal13 (Reimer *et al*. 2013) and modified from Svendsen *et al*. (1996), and the Western Svalbard curve is modified from the compilation of Jessen *et al*. (2010).

Supressed glacioisostatic uplift recorded in Isfjorden and western Spitsbergen fjords suggested a Younger Dryas stabilisation or growth of an ice sheet over central/eastern Svalbard (Forman *et al.* 1987; Landvik *et al.* 1987; Lehman & Forman 1992), and Svendsen *et al.* (1996) suggest a YD advance in Isfjorden prior to ca. 11.6 cal ka BP (Figure 5.6), corroborating the advance in Billefjorden proposed by Boulton (1979), and reflected in the ice-proximal sedimentary facies in mid-Isfjorden between ca. 12.7 and 11.2 cal ka BP (Forwick & Vorren 2009). A parallel can therefore be drawn between Kongsfjorden and Isfjorden regarding a Younger Dryas stillstand or readvance and the onset of final deglaciation, with Isfjorden (ca. 11.2 cal ka BP) (Forwick & Vorren 2009) deglaciating near-synchronously with Kongsfjorden (ca. 10.8 cal ka BP) (Skirbekk *et al.* 2010).

Ca. 150 km south of Kongsfjorden, a Younger Dryas ice marginal position is proposed at the mouth of Van Mijenfjorden close to the pinning point of Akseløya (Mangerud *et al.* 1992; Svendsen *et al.* 1996), while in Hornsund (ca. 230 km south of Kongsfjorden), Treskelen ridge in the mid-fjord was deglaciated at 12.6 ± 0.7 ka (Gislefoss 2015), The YD deglaciation age may indicate that Hornsund was beyond the influence of a YD stillstand or readvance caused by ice sheet stabilisation over central/eastern Svalbard, given the straightforward isostatic uplift isobases from the fjord (Birkenmajer 1960) and the consistent chronology of raised beaches (Lindner *et al.* 1991).

Overall, the deglaciation of Kongsfjorden is generally consistent with the stepwise deglaciation observed along northern and western Spitsbergen following the Late Weichselian Glacial maximum (Figure 5.6). Major differences appear to be the timing of retreat to the fjord-mouth, the possibility of an Older Dryas advance, and the extent of a Younger Dryas readvance. However key similarities exist between the major fjord systems of Kongsfjorden-Krossfjorden, Woodfjorden, and Isfjorden, which all provide traces of a Younger Dryas stillstand or readvance, and all show rapid Younger Dryas to Preboreal retreat, with the LIA most likely representing the Holocene glacial maximum.

5.8.4 Svalbard-Barents Sea Ice Sheet and Eurasian Ice Sheet

Mangerud *et al.* (1992) postulated that the Svalbard-Barents Sea Ice Sheet was configured of two separate ice masses, with (1) the largely marine-based Barents Sea Ice Sheet located east of the mountains of Spitsbergen, and (2) local glaciers and ice domes on Spitsbergen. The two components would have been contiguous during the <10 ka period of maximum Late Weichselian glaciation (Landvik *et al.* 1998; Mangerud *et al.* 1998), however the local ice domes may have grown and decayed out of phase with the marine-based Barents Sea Ice Sheet (Mangerud *et al.* 1992). It is therefore important to consider the deglaciation of Kongsfjorden foremost in terms of the local ice domes and glaciers over Spitsbergen, as the dynamic behaviour in the fjords on the west may not be representative of the marine-based portion to the east.

The outer coast of Isfjorden, western Spitsbergen, was ice free by ca. 15 cal ka BP (Mangerud *et al.* 1992), which is slightly later than the outer coast of Kongsfjorden (ice free by ca. 16.6 ka (Henriksen *et al.* 2014; Hughes *et al.* 2016)) (Figure 5.7) synchronous with the end of the Late Weichselian Glacial Maximum of the Fennoscandian Ice Sheet and the onset of retreat from the Barents/Kara Sea in Arctic Russia (Svendsen *et al.* 2004). A peak in IRD flux is recorded along the western Svalbard slope between ca. 15.7 and 14.7 cal ka BP linked to increased iceberg calving (Jessen *et al.* 2010), suggesting the break-up of ice streams and their conversion to tidewater outlet glaciers, and consistent with the continued Bølling retreat in Kongsfjorden via calving. The early Bølling interstadial (ca. 14.7 to 14.4 cal ka BP) is represented by thick laminated sediments on the continental slope, which have been interpreted as rapid sedimentation derived from turbid meltwater during the retreat of the Svalbard-Barents Sea Ice Sheet (Elverhøi *et al.* 1995; Svendsen *et al.* 1996; Rasmussen *et al.* 2007), and may be linked to a single outburst flood event during the Bølling (Jessen *et al.* 2010).

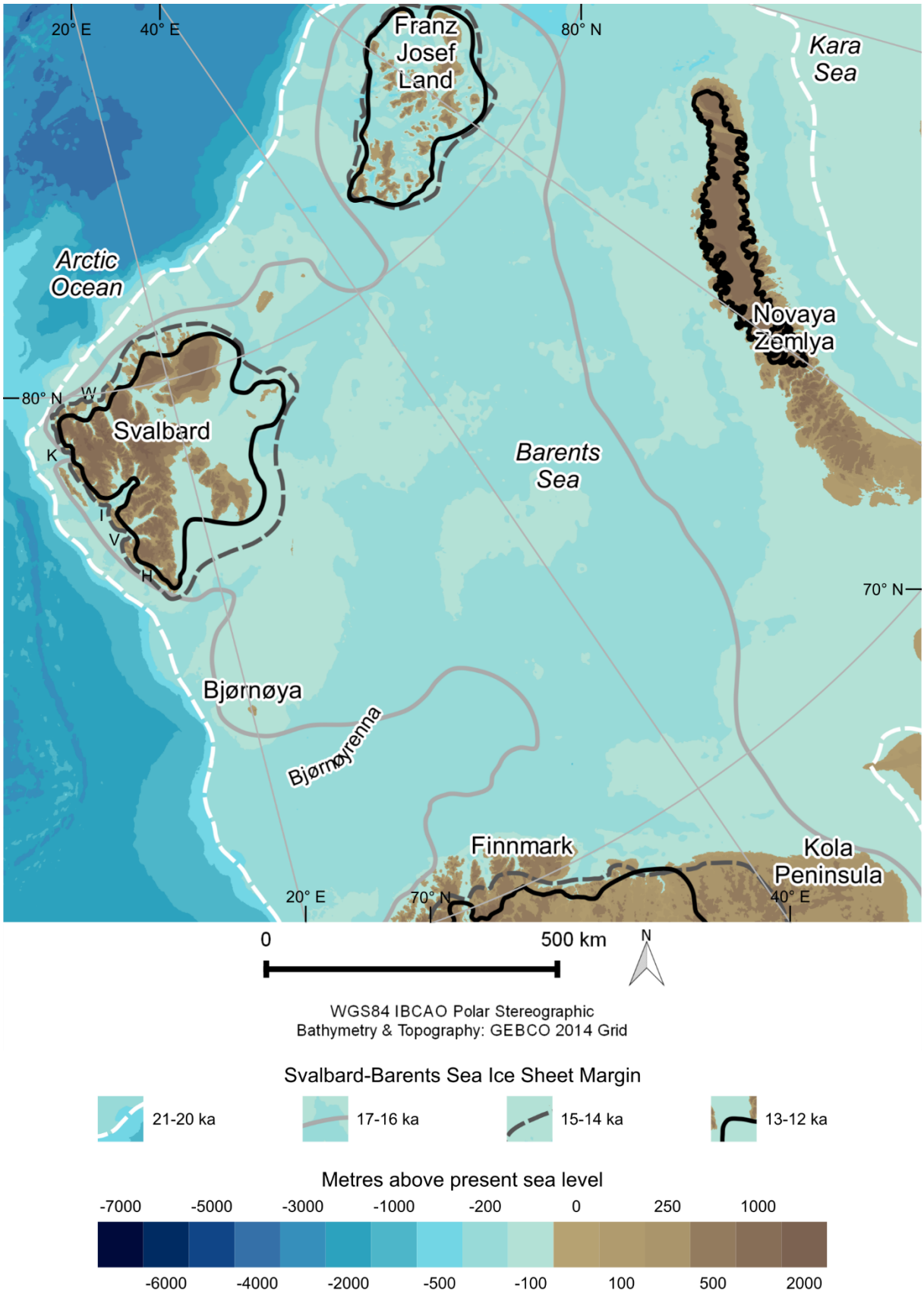
20° E
40° E
80° N
Franz Josef Land
Kara Sea
Arctic Ocean
Novaya Zemlya
80° N
W
Svalbard
K
I
V
H
Barents Sea
70° N
Bjørnøya
Bjørnøyrenna
Finnmark
Kola Peninsula
20° E
70° N
40° E
0
500 km
N
WGS84 IBCAO Polar Stereographic
Bathymetry & Topography: GEBCO 2014 Grid
Svalbard-Barents Sea Ice Sheet Margin
21-20 ka
17-16 ka
15-14 ka
13-12 ka
Metres above present sea level
-7000
-5000
-3000
-1000
-200
0
250
1000
-6000
-4000
-2000
-500
-100
100
500
2000

Figure 5.7: Reconstructed ice sheet margins of the Svalbard-Barents Sea Ice Sheet at four time slices (21–20, 17–16, 15–14, and 13–12 ka) modified from the most credible ice margins from Hughes *et al.* (2016), redrawn at Kongsfjorden according to the time-distance diagram (Figure 5.6). Bathymetry and topography is derived from the GEBCO 2014 30 second grid (GEBCO 2014), and western Spitsbergen fjords are labelled (W = Woodfjorden, K = Kongsfjorden, I = Isfjorden, V = Van Mijenfjorden, and H = Hornsund).

The possibility of stable or growing ice caps over central Spitsbergen during the Younger Dryas indicates precipitation feeding the YD ice sheet on Svalbard from the south and east, and therefore a largely ice-free Barents Sea (Svendsen *et al.* 1996), which is possible given the initiation of marine-based Barents Sea Ice Sheet disintegration from ca. 18.4 cal ka BP (Jones & Keigwin 1988; Winsborrow *et al.* 2010) and illustrated in Figure 5.7, as the southwestern Barents Sea is largely ice-free by 16 ka.

The final phase of Late Weichselian deglaciation appears synchronous across the entire Svalbard archipelago, with the heads of fjords ice free at ca. 11.6 cal ka BP (Mangerud *et al.* 1992; Svendsen *et al.* 1996) which is substantiated by the rapid isostatic uplift experienced at this time (Forman 1990), and suggests a near instantaneous disappearance of a significant ice mass over eastern Svalbard and the Barents Sea at the Preboreal transition (Mangerud *et al.* 1992; Svendsen *et al.* 1992), possibly tied to the maximum tilt of the 41 ka obliquity cycle, with high latitudes receiving high summer insolation (Mangerud & Svendsen 1992; Mangerud *et al.* 1996; Mangerud *et al.* 1998).

The deglaciation of the marine-based Barents Sea Ice Sheet has been reconstructed by Winsborrow *et al.* (2010), and divided into five stages and is illustrated in Figure 5.7. (1) at ca. 19 cal ka BP the Late Weichselian maximum Svalbard-Barents Sea Ice Sheet occupied the entire Barents Sea shelf, with dynamics controlled by the Bjørnøyrenna Ice Stream, initiation of retreat was caused by rising global eustatic sea level of 10 to 15 m (Clark *et al.* 2004; Peltier & Fairbanks 2006). (2) at ca. 17 cal ka BP deglaciation was occurring along the western continental shelf and the southern Barents Sea margin, with enhanced calving in the Bjørnøyrenna trough. (3) at ca. 16 cal ka BP the terminus of the Bjørnøyrenna Ice Stream retreated rapidly but was periodically grounded, the main ice volume was shifting east as the southwest Barents Sea was largely ice-free. (4) at ca. 15 cal ka BP the western margins had retreated onshore, as seen along the west coast of Spitsbergen, mass loss was primarily through thinning via melting rather than calving, ice streams activated in the eastern sector of the Barents Sea, draining ice to the southwest. (5) at ca. 12.5 to 12 cal ka BP the southern margin had retreated onshore, with the Barents Sea ice-free and local ice caps retreated slowly (Winsborrow *et al.* 2010).

The model of marine-based deglaciation is consistent with the isostatic uplift record (Landvik *et al.* 1998), as well as the Mangerud *et al.* (1992) prediction of asynchronous dynamic behaviour between the two Svalbard-Barents Sea Ice Sheet components. The dynamic behaviour of the Kongsfjorden Ice

Stream presented in this study from ca. 15.6 ka would have been independent of the marine-based portion of the Svalbard-Barents Sea Ice Sheet, and thus can explain differences between north/western Spitsbergen and the Barents Sea, such as the possible Younger Dryas stillstand in Kongsfjorden and other west Spitsbergen fjords, which is not present in the Barents Sea given that it was likely deglaciated during the Bølling-Allerød (Winsborrow *et al.* 2010; Hughes *et al.* 2016) (Figure 5.7), although a lack of constraining dates from the inner Barents Sea shelf confounds the timing of marine-based deglaciation (Landvik *et al.* 1998; Landvik *et al.* 2005; Klitgaard Kristensen *et al.* 2013).

The complex multi-dome polythermal configuration of the Late Weichselian ice sheet over Svalbard consisted of localised ice-domes discharging as fast-flowing warm-based ice streams in fjords and lowlands, and slow flowing cold-based inter-ice stream areas (Landvik *et al.* 2005; Ottesen & Dowdeswell 2009; Alexanderson *et al.* 2011; Hormes *et al.* 2011; Ingólfsson & Landvik 2013; Landvik *et al.* 2013; Landvik *et al.* 2014). Gjermundsen *et al.* (2013) and Hormes *et al.* (2013) suggest a local ice dome over northwest Spitsbergen extended up to 300 m above the mountain peaks, draining radially as ice streams (Gjermundsen *et al.* 2013), with flow from the east into the Kongsfjorden channel. The dynamic behaviour of the local ice dome is reconstructed from ^{10}Be exposure dates, and suggests an early thinning 25 to 20 ka, prior to retreat from the shelf-edge (Jessen *et al.* 2010) and contemporaneous with Heinrich event H2, but most likely driven by thinning caused by aridification (Hormes *et al.* 2013), followed by marginal retreat between 18 and 15 ka (Gjermundsen *et al.* 2013), consistent with onshore retreat in Kongsfjorden.

Hormes *et al.* (2013) recognise several (n=12) deglaciation dates overlapping Heinrich event H1 at ca. 16.8 ka, suggesting thinning and early on-shore retreat at the coast in northwest Spitsbergen, with; Auriviliusfjellet in Smeerenburgfjorden and Flakstor in inner Krossfjorden ice-free at ca. 16.8 ± 0.8 ka, a boulder on Danskøya ice-free at 16.2 ± 0.8 ka (Landvik *et al.* 2003), Northern Prins Karls Forland ice-free at 16.9 ± 0.8 ka (Landvik *et al.* 2013), and later shown by the average exposure age of the lateral moraine on Kongsfjordhallet at 16.6 ± 0.8 ka (Henriksen *et al.* 2014).

The H1 Heinrich event thinning and margin-retreat was then followed by a rapid Bølling retreat in the fjords, with a conservative estimate of 20 cm ka^{-1} contribution to global sea-level rise from the northwest portion of the Barents Sea Ice Sheet between 15 and 14 ka (Hormes *et al.* 2013), with this study showing calving losses in Kongsfjorden through the Bølling (Figure 5.5). Marginal areas continued to deglaciate during the Younger Dryas chronozone including; Prins Karls Forland, Gråhuken, the lowlands of Nordaustlandet, and parts of eastern Svalbard (Hormes *et al.* 2013) (Figure 5.7). Barentsøya and Edgeøya were ice-free by ca. 12.1 ± 0.8 cal ka BP (Landvik *et al.* 1992), thus highlighting the spatially restricted Younger Dryas ice sheet over central-eastern Spitsbergen (Hughes *et al.* 2016).

The present-day glacier coverage on the Svalbard archipelago was attained when Wahlenbergfjorden and Rijpdalen on Nordaustlandet were deglaciated at 10.8 ± 0.2 and 9.8 ± 0.3 cal ka BP respectively (Blake 2006; Hormes *et al.* 2013).

5.9 Further research

In order to validate the proposed deglaciation of Kongsfjorden, particularly the ice surface gradients and marginal positions in Figure 5.4 and Figure 5.5, it is necessary to conduct further investigation into the terrestrial and marine archives. A suitable method for constraining the possible ice surface gradients and Younger Dryas thinning would be to sample transects on potential nunataks, such as Stemmeknausane and Snøsporven, for surface exposure dating of erratic boulders. Further, a dual-nuclide approach such as ^{10}Be and ^{26}Al, or ^{10}Be and ^{14}C, from the same samples can provide valuable inheritance signals and therefore potential erosion rate differences (Ivy-Ochs & Briner 2014) which could reveal the spatial heterogeneity of subglacial thermal conditions, and possibly help constrain the timing and duration of peak Ice Stream discharge in Kongsfjorden.

An enduring enigma in western Spitsbergen is the extent of the Younger Dryas within the fjord systems, this study provides a first possible dated Younger Dryas glacial landform in western Spitsbergen in the trimline-degraded moraine complex on Blomstrandhalvøya (Figure 4.7), but given the limited preservation potential of terrestrial glacial landforms on Svalbard (Lukas *et al.* 2005), it is necessary to look in the marine archive for traces of the Younger Dryas. Sediment cores from mid- and inner-Kongsfjorden should be retrieved, aiming to locate till units which may correlate to a Younger Dryas stillstand or advance. The transverse ridges proposed by Maclachlan *et al.* (2010) appear more likely to be bedrock outcrops than moraine ridges, but still provide potential pinning-points for glacial retreat, and thus obtaining minimum dates of the glacial sediments on the ridges may provide a deglaciation chronology within the fjord and a constraint on Younger Dryas ice margin position.

Analysis of already collected data could be conducted as a pilot study in the Kongsfjorden area. During the field campaign of July–August 2014 led by Dr Anne Hormes of the University of Gothenburg, preliminary studies were conducted on Sarsvatnet on Ossian Sarsfjellet (Figure 4.36), a ca. 0.2 km^2 lake with a maximum depth of ca. 20 m and a base level at 100 m a.s.l.. A crude (ca. 20 x 20 m grid) bathymetric map was produced, soil and water samples taken, and short-cores obtained and extruded which showed variable depositional conditions in the lake. In September 2014, a team led by Professor Jostein Bakke of the University of Bergen obtained long-cores from Sarsvatnet, but they have yet to be analysed in detail, they may hold key information pertaining to the timing of deglaciation of the head

of the fjord, climatic and environmental development, and any glacial oscillations through the Holocene given the inflow of meltwater from Kongsbreen and input from threshold lakes.

The largest lake in the southwest corner of Blomstrandhalvøya, Øvretjørna (Figure 1.2) (Dallmann *et al.* 2015), can also be considered as a potential target for sediment coring, given its base level at 38 m, just above the ca. 36 m marine limit on the Island (Figure 2.5) (Lehman & Forman 1992) the sediment archive should reveal the isolation of the lake, and may also show exposure following the Younger Dryas, as well as the Holocene environmental and climatic development in the fjord. The present-day high organic input into the lake (primarily as bird guano) may hold key paleoenvironmental and paleoclimatic signals as alkenone paleothermometers (D'Andrea *et al.* 2012).

The sediment section within the Londonelva catchment which was excavated and logged (Figure 4.17) may also be revisited and expanded, provenance and fabric studies can reveal the nature of the diamict units, aiding the distinction between glacial till and locally derived talus, and thus resolve the unanswered question surrounding the possibility of Unit A representing a Younger Dryas till. If age constrain can be obtained via e.g. radiocarbon dating, then it may also be possible to identify the minimum age for the lower diamicton (Unit C) and maximum age for the upper diamicton (Unit A) to provide a greater understanding of the deglaciation of Blomstrandhalvøya, and link the stratigraphy to Site 12 at Brandalpynten and the sediment sections at Kongsfjordhallet. Raised marine deposits, such as those to the north and the southeast of the island may yield useful sediment sections for constraining the sea level history for inner Kongsfjorden.

The medial (Figure 4.6), lateral and end moraines (Figure 4.5) observed on or close to Blomstrandsalen may justify further investigation. Lithostratigraphic logging, fabric analysis and provenance studies can reveal the nature of the landforms, while exposure dating of erratic boulders on the landforms can determine the timing of stabilisation and ice retreat. This would elucidate the possibility of a plateau glacier or a remnant ice mass on Blomstrandhalvøya, providing evidence for glacial activity through the Holocene. The trimline-moraine complex on the southeast of the island (Figure 4.7) should be sampled further for surface exposure dating, with the objective of validating its age as Younger Dryas and provide unequivocal evidence for a Younger Dryas ice marginal position of the Kongsfjorden outlet glacier.

The rock glacier on the northwest of Blomstrandhalvøya (Figure 4.14a) entails further investigation given its potential paleoclimatic significance owing to its dependence on a narrow range in precipitation and temperature (Humlum 1998). Surface exposure dating will provide the timing and therefore rate of accumulation of the feature which is currently undetermined. Its isolated occurrence

may also be a function of aspect (north facing), physiographic setting (distal to neoglacial limits) and geology (source from a graphitic quartz-carbonate schist outcrop).

The abundant cave systems on Blomstrandhalvøya are a potentially rich archive for glacial and interglacial climatic and environmental signatures, with small speleothems collected from Sørvåggrotta and Kronegrotta yielding Kapp Ekholm interstadial ages via Uranium-series dating (Lauritzen 2006). The $\delta^{18}O$ signal from speleothems can indicate the water source feeding their growth (Ruddiman 2008), and thus may reflect the interglacial or interstadial meteoric input versus glacial or stadial meltwater input, and therefore the timing and duration of subglacial conditions during the Late Weichselian. The caves may also contain glacially transported material, which would allow for provenance studies, and the timing of deposition via burial dating, given the differential decay of cosmogenic nuclides once no longer exposed (Dunai 2010). If older glacial sediments are preserved in caves, burial dating may reveal a high resolution timing of pre-Late Weichselian glaciations.

6. Conclusions

The results, interpretation, and discussion from this study are summarised as follows:

- The western Blomstrandhalvøya sampling transect (BLOM) reveals the onset of deglaciation from ca. 15.6 ± 0.5 ka, however there appears to be at least two populations of exposure ages which are not possible to distinguish with the precision of the single isotope exposure dating method. An Oldest Dryas to Bølling-Allerød cluster providing a deglaciation age of 15.2 ± 1.5 ka, and an early Younger Dryas cluster at 13.0 ± 1.3 ka.
- The eastern Blomstrandhalvøya sampling transect (GOR) provides a wide spread in exposure ages, with too-old and too-young ages present, however the summit yields a Bølling-Allerød exposure age at 14.5 ± 0.3 ka. The trimline-moraine complex produces a mid-Younger Drays age of 12.6 ± 0.5 ka and may be the first direct dated evidence for a terrestrial Younger Dryas ice margin on Svalbard.
- The Ossian Sarsfjellet sampling transect (SARS) produces two distinct populations of exposure ages, with the bedrock providing 16.6 ± 1.3 ka owing to inheritance, while the boulders provide a Younger Dryas deglaciation age of 12.8 ± 1.3 ka.
- The deglaciation of the outer fjord is constrained by a radiocarbon date from a marine core and exposure dating from erratic boulders between ca. 16.6 and 16.3 ka, synchronous with Heinrich event H1 (Landvik *et al.* 2005; Henriksen *et al.* 2014), and is significantly earlier than neighbouring fjords in western Spitsbergen.
- A stepwise deglaciation following the Late Weichselian Glacial Maximum is proposed which significantly builds upon previous conceptual models for fjord deglaciation (Lehman & Forman 1992; Sexton *et al.* 1992). At ca. 15.6 ka, the Kongsfjorden paleo-ice stream was an outlet glacier, and continued to retreat laterally through the Bølling-Allerød, where a clustering (n=8) of exposure dates and published radiocarbon dates constrain the ice marginal position and relatively steep surface profile around ca. 14.5 ka. The Early Bølling-Allerød retreat is linked to warm Atlantic Water advection as bottom waters along the western Svalbard shelf, with the northward migration of the Polar Front (Ruddiman & Mcintyre 1981) leading to sea ice-free oceans and a rising atmospheric temperature, calving was enhanced by sea-level perturbations such as Melt Water Pulse 1a (Hormes *et al.* 2013). No Older Dryas advance is identified in Kongsfjorden, and is therefore a key difference to neighbouring fjords (Jessen *et al.* 2010).
- A cluster of exposure ages (n=9) delimit the Younger Dryas in Kongsfjorden, with a stillstand or slight readvance of the Kongsfjorden outlet glacier, but with a shallower gradient indicating dynamic thinning of the ice sheet, with geomorphic observations suggesting a variable basal

thermal regime during the Younger Dryas. The Younger Dryas ice marginal position proposed in this study is consistent with the supressed marine limit previously observed in the area (Lehman & Forman 1992) albeit in contrast to local and cirque glacier retreat (Mangerud & Landvik 2007), and suggests a stabilisation or growth of an ice cap over central-eastern Svalbard, resulting from a persistent Polar Front to the north (Ślubowska *et al.* 2005), a weakened West Spitsbergen Current (Hald *et al.* 2004), and a source area for precipitation from the deglaciated Barents Sea to the southeast. The Younger Dryas stillstand or readvance and Preboreal retreat is a key similarity to Isfjorden (Svendsen *et al.* 1996).

- Deglaciation occurred asynchronously between the marine-based Barents Sea Ice Sheet and the land-based Svalbard Ice Caps, with a local ice dome over northwest Spitsbergen the likely source for ice-flow through Kongsfjorden, the early thinning of which is synchronous with the onset of shelf-edge and later on-shore retreat west of Kongsfjorden (Gjermundsen *et al.* 2013; Hormes *et al.* 2013).
- A rapid Preboreal retreat is inferred, and is linked to the rapid isostatic uplift over eastern Svalbard at this time (Landvik *et al.* 1998).
- Quaternary geological mapping reveals a periglacial landscape development on Blomstrandhalvøya following the Preboreal retreat. A persistently dry and cool climate is inferred from the rock glacier and abundant patterned ground features, while rapid sea level regression has left faint traces in the landscape.
- The Little Ice Age represents the Holocene glacial maximum in Kongsfjorden, with Blomstrandhalvøya a potential host for a plateau glacier if the ELA fell ca. 100 m.
- Further research in the Kongsfjorden area or northwest Spitsbergen fjords should aim to identify Younger Dryas ice marginal positions with greater certainty.

Overall the findings from this thesis project and discussion from the wider literature show the deglaciation of Kongsfjorden was a punctuated stepwise process, with strong evidence for a Younger Dryas stillstand or readvance, and therefore not a rapid collapse or unrelenting retreat from the Late Weichselian Glacial Maximum. The Oldest Dryas through Bølling-Allerød retreat was calving dominant, while the Younger Dryas through Preboreal retreat was ablation dominant.

The nature of deglaciation in Kongsfjorden suggests a dynamic ice sheet behaviour during deglaciation, with changing thermal and flow regimes of outlet glaciers, and stabilisation of ice caps linked to climatic and oceanographic forcing.

7. References

Alexanderson, H., Landvik, J. Y. & Ryen, H. T. 2011: Chronology and styles of glaciation in an inter-fjord setting, northwestern Svalbard. *Boreas 40*, 175–197.

Alexanderson, H., Backman, J., Cronin, T. M., Funder, S., Ingólfsson, Ó., Jakobsson, M., Landvik, J. Y., Löwemark, L., Mangerud, J., März, C., Möller, P., O'Regan, M. & Spielhagen, R. F. 2014: An Arctic perspective on dating Mid-Late Pleistocene environmental history. *Quaternary Science Reviews 92*, 9–31.

Alley, R. B., Blankenship, D. D., Rooney, S. T. & Bentley, C. R. 1989: Sedimentation beneath ice shelves — the view from ice stream B. *Marine Geology 85*, 101–120.

Alley, R. B., Meese, D. A., Shuman, C. A., Gow, A. J., Taylor, K. C., Grootes, P. M., White, J. W. C., Ram, M., Waddington, E. D., Mayewski, P. A. & Zielinski, G. A. 1993: Abrupt Increase in Greenland Snow Accumulation at the End of the Younger Dryas Event. *Nature 362*, 527–529.

Andersen, E. S., Dokken, T. M., Elverhøi, A., Solheim, A. & Fossen, I. 1996: Late Quaternary sedimentation and glacial history of the western Svalbard continental margin. *Marine Geology 133*, 123–156.

Andersson, T., Forman, S. L., Ingólfsson, Ó. & Manley, W. F. 1999: Late Quaternary environmental history of central Prins Karls Forland, western Svalbard. *Boreas 28*, 292–307.

Andersson, T., Forman, S. L., Ingólfsson, Ó. & Manley, W. F. 2000: Stratigraphic and Morphologic Constraints on the Weichselian Glacial History of Northern Prins Karls Forland, Western Svalbard. *Geografiska Annaler: Series A, Physical Geography 82*, 455–470.

André, M. F. 1997: Holocene rockwall retreat in Svalbard: a triple-rate evolution. *Earth Surface Processes and Landforms 22*, 423–440.

Atkins, C. B., Barrett, P. J. & Hicock, S. R. 2002: Cold glaciers erode and deposit: Evidence from Allan Hills, Antarctica. *Geology 30*, 659–662.

Baeten, N. J., Forwick, M., Vogt, C. & Vorren, T. O. 2010: Late Weichselian and Holocene sedimentary environments and glacial activity in Billefjorden, Svalbard. *Geological Society, London, Special Publications 344*, 207–223.

Balco, G. 2001: *Camelplot MATLAB script*. http://depts.washington.edu/cosmolab/pubs/gb_pubs/camelplot.m. Date accessed: 7 May 2016.

Balco, G. 2006: *Converting Al and Be isotope ratio measurements to nuclide concentrations in quartz*. http://hess.ess.washington.edu/math/docs/common/ams_data_reduction/. Date accessed: 28 October 2015.

Balco, G., Stone, J. O., Lifton, N. A. & Dunai, T. J. 2008: A complete and easily accessible means of calculating surface exposure ages or erosion rates from (10)Be and (26)Al measurements. *Quaternary Geochronology 3*, 174–195.

Balco, G. 2011a: Contributions and unrealized potential contributions of cosmogenic-nuclide exposure dating to glacier chronology, 1990–2010. *Quaternary Science Reviews 30*, 3–27.

Balco, G. 2011b: *What is a camel diagram anyway?* https://cosmognosis.wordpress.com/2011/07/25/what-is-a-camel-diagram-anyway/. Date accessed: 10 May 2016.

Ballantyne, C. K. & Matthews, J. A. 1982: The Development of Sorted Circles on Recently Deglaciated Terrain, Jotunheimen, Norway. *Arctic and Alpine Research 14*, 341–354.

Ballantyne, C. K. 2002: Paraglacial geomorphology. *Quaternary Science Reviews 21*, 1935–2017.

Baranowski, S. 1977: Subpolar glaciers of Spitsbergen seen against the climate of this region. *Acta Universitatis Wratislaviensis 410*, 1–94.

Barr, S., Newman, D. & Nesteroff, G. 2012: *Ernest Mansfield (1862-1924) : "Gold - or I'm a Dutchman"*. 192 pp. Akademika, Trondheim.

Batchelor, C. L. & Dowdeswell, J. A. 2014: The physiography of High Arctic cross-shelf troughs. *Quaternary Science Reviews 92*, 68–96.

Benn, D. I. & Evans, D. J. A. 2010: *Glaciers and Glaciation*. 802 pp. Hodder Education, London.

Bergh, S. G., Maher, H. D. & Braathen, A. 2000: Tertiary divergent thrust directions from partitioned transpression, Brøggerhalvøya, Spitsbergen. *Norsk Geologisk Tidsskrift 80*, 63–81.

Bianchi, G. G. & McCave, I. N. 1999: Holocene periodicity in North Atlantic climate and deep-ocean flow south of Iceland. *Nature 397*, 515–517.

Bierman, P. R., Caffee, M. W., Davis, P. T., Marsella, K., Pavich, M., Colgan, P., Mickelson, D. & Larsen, J. 2002: Rates and timing of earth surface processes from in situ-produced cosmogenic Be-10. *Beryllium: Mineralogy, Petrology, and Geochemistry 50*, 147–205.

Birkenmajer, K. 1960: Raised marine features of the Hornsund area, Vestspitsbergen. *Studia Geologica Polonica 5*, 3–95.

Blake, W. 2006: Occurrence of the Mytilus edulis complex on Nordaustlandet, Svalbard: radiocarbon ages and climatic implications. *Polar Research 25*, 123–137.

Blomstrand, C. W. 1864: Geognostiska iakttagelser under en resa till Spetsbergen år 1861 af C. W. Blomstrand. *Kongliga Svenska Vetenskaps-Akademiens Handlingar 4*, 1–48.

Bogen, J. & Bønsnes, T. E. 2003: Erosion and sediment transport in High Arctic rivers, Svalbard. *Polar Research 22*, 175–189.

Boulton, G. S. 1970: On the deposition of subglacial and melt-out tills at the margins of certain Svalbard glaciers. *Journal of Glaciology 9*, 231–245.

Boulton, G. S. 1978: Boulder Shapes and Grain-Size Distributions of Debris as Indicators of Transport Paths through a Glacier and Till Genesis. *Sedimentology 25*, 773–799.

Boulton, G. S. 1979: Glacial history of the Spitsbergen archipelago and the problem of a Barents Shelf ice sheet. *Boreas 8*, 31–57.

Boulton, G. S., Baldwin, C. T., Peacock, J. D., McCabe, A. M., Miller, G., Jarvis, J., Horsefield, B., Worsley, P., Eyles, N., Chroston, P. N., Day, T. E., Gibbard, P., Hare, P. E. & von Brunn, V. 1982: A glacio-isostatic facies model and amino acid stratigraphy for late Quaternary events in Spitsbergen and the Arctic. *Nature 298*, 437–441.

Boulton, G. S. 1990: Sedimentary and sea level changes during glacial cycles and their control on glacimarine facies architecture. *Geological Society, London, Special Publications 53*, 15–52.

Briffa, K. R., Jones, P. D., Schweingruber, F. H. & Osborn, T. J. 1998: Influence of volcanic eruptions on Northern Hemisphere summer temperature over the past 600 years. *Nature 393*, 450–455.

Briner, J. P., Miller, G. H., Davis, P. T. & Finkel, R. C. 2006: Cosmogenic radionuclides from fiord landscapes support differential erosion by overriding ice sheets. *Geological Society of America Bulletin 118*, 406–420.

Brown, N. E., Hallet, B. & Booth, D. B. 1987: Rapid soft bed sliding of the Puget glacial lobe. *Journal of Geophysical Research: Solid Earth (1978–2012) 92*, 8985–8997.

Buggisch, W., Piepjohn, K., Thiedig, F. & von Gosen, W. 1994: A Middle Carboniferous Conodont Fauna from Blomstrandhalvøya (NW-Spitsbergen): Implications on the Age of Post-Devonian Karstification and the Svalbardian Deformation. *Polarforschung 62*, 83–90.

Cadman, V. 1996: *Glacimarine sedimentation and environments during the Late Weichselian and Holocene in the Bellsund Through and van Keulenfjorden, Svalbard.* Ph.D. thesis, University of Cambridge,

Child, D., Elliott, G., Mifsud, C., Smith, A. M. & Fink, D. 2000: Sample processing for earth science studies at ANTARES. *Nuclear Instruments and Methods in Physics Research Section B: Beam Interactions with Materials and Atoms 172*, 856–860.

Christl, M., Wieler, R. & Finkel, R. C. 2014: Measuring one atom in a million billion with mass spectrometry. *Elements 10*, 341–346.

Christoffersen, P., Piotrowski, J. A. & Larsen, N. K. 2005: Basal processes beneath an Arctic glacier and their geomorphic imprint after a surge, Elisebreen, Svalbard. *Quaternary Research 64*, 125–137.

Clark, P. U., McCabe, A. M., Mix, A. C. & Weaver, A. J. 2004: Rapid Rise of Sea Level 19,000 Years Ago and Its Global Implications. *Science 304*, 1141–1144.

Clark, P. U., Dyke, A. S., Shakun, J. D., Carlson, A. E., Clark, J., Wohlfarth, B., Mitrovica, J. X., Hostetler, S. W. & McCabe, A. M. 2009: The Last Glacial Maximum. *Science 325*, 710–714.

Cottier, F., Tverberg, V., Inall, M., Svendsen, H., Nilsen, F. & Griffiths, C. 2005: Water mass modification in an Arctic fjord through cross-shelf exchange: The seasonal hydrography of Kongsfjorden, Svalbard. *Journal of Geophysical Research: Oceans 110*, 1–18.

CRONUS-Earth 2009: *CRONUS-Earth online calculators*. http://hess.ess.washington.edu/math/. Date accessed: 29 October 2015.

Crowley, T. J. 2000: Causes of Climate Change Over the Past 1000 Years. *Science 289*, 270–277.

D'Andrea, W. J., Vaillencourt, D. A., Balascio, N. L., Werner, A., Roof, S. R., Retelle, M. & Bradley, R. S. 2012: Mild Little Ice Age and unprecedented recent warmth in an 1800 year lake sediment record from Svalbard. *Geology 40*, 1007–1010.

Dallmann, W. K. 2012: *Geological map Svalbard 1:100 000, sheet B7G Tre Kroner*`. Tromsø: Norsk Polarinstitutt.

Dallmann, W. K., Forwick, M., Hormes, A., Christiansen, H., Jernas, P. E., Laberg, J. S., Salvigsen, O. & Vorren, T. O. 2015: Quaternary geology and geomorphology. *In* Dallmann, W. K. (ed.): *Geoscience Atlas of Svalbard*, 292 pp. Norwegian Polar Institute, Tromsø.

Denton, G. H. & Hughes, T. J. 1981: *The last great ice sheets*. 484 pp. Wiley-Blackwell, New Jersey.

Dowdeswell, J. A., Ottesen, D. & Rise, L. 2006: Flow switching and large-scale deposition by ice streams draining former ice sheets. *Geology 34*, 313–316.

Dowdeswell, J. A., Ottesen, D., Evans, J., Cofaigh, C. Ó. & Anderson, J. B. 2008: Submarine glacial landforms and rates of ice-stream collapse. *Geology 36*, 819–822.

Dowdeswell, J. A., Hogan, K. A., Evans, J., Noormets, R., Ó Cofaigh, C. & Ottesen, D. 2010: Past ice-sheet flow east of Svalbard inferred from streamlined subglacial landforms. *Geology 38*, 163–166.

Dunai, T. J. 2010: *Cosmogenic Nuclides: Principles, concepts and applications in the Earth surface sciences*. 187 pp. Cambridge University Press, Cambridge.

Dunai, T. J. & Lifton, N. A. 2014: The Nuts and Bolts of Cosmogenic Nuclide Production. *Elements 10*, 347–350.

Dunne, J., Elmore, D. & Muzikar, P. 1999: Scaling factors for the rates of production of cosmogenic nuclides for geometric shielding and attenuation at depth on sloped surfaces. *Geomorphology 27*, 3–11.

Dyke, A. S. 1993: Landscapes of cold-centred Late Wisconsinan ice caps, Arctic Canada. *Progress in Physical Geography 17*, 223–247.

Ehlers, J., Gibbard, P. L. & Hughes, P. D. 2011: *Quaternary Glaciations - Extent and Chronology: A Closer Look*. 1108 pp. Elsevier, Amsterdam.

Elverhøi, A., Liestøl, O. & Nagy, J. 1980: Glacial erosion, sedimentation and microfauna in the inner part of Kongsfjorden, Spitsbergen. *Norsk Polarinstitutt Skrifter 172*, 33–58.

Elverhøi, A., Lønne, Ø. & Seland, R. 1983: Glaciomarine sedimentation in a modern fjord environment, Spitsbergen. *Polar Research 1*, 127–150.

Elverhøi, A., Fjeldskaar, W., Solheim, A., Nyland-Berg, M. & Russwurm, L. 1993: The Barents Sea Ice Sheet—a model of its growth and decay during the last ice maximum. *Quaternary Science Reviews 12*, 863–873.

Elverhøi, A., Andersen, E. S., Dokken, T., Hebbeln, D., Spielhagen, R., Svendsen, J. I., Sorflaten, M., Rornes, A., Hald, M. & Forsberg, C. F. 1995: The growth and decay of the late weichselian ice sheet in western Svalbard and adjacent areas based on provenance studies of marine sediments. *Quaternary Research 44*, 303–316.

Eppes, M. C. & Griffing, D. 2010: Granular disintegration of marble in nature: A thermal-mechanical origin for a grus and corestone landscape. *Geomorphology 117*, 170–180.

Etzelmüller, B. & Sollid, J. L. 1991: The role of weathering and pedological processes for the development of sorted circles on Kvadehuksletta, Svalbard-a short report. *Polar Research 9*, 181–191.

Evans, D. J. A. & Rea, B. R. 1999: Geomorphology and sedimentology of surging glaciers: a land-systems approach. *Annals of Glaciology 28*, 75–82.

Evans, D. J. A., Phillips, E. R., Hiemstra, J. F. & Auton, C. A. 2006: Subglacial till: Formation, sedimentary characteristics and classification. *Earth-Science Reviews 78*, 115–176.

Eyles, N. & Rogerson, R. J. 1978: A framework for the investigation of medial moraine formation: Austerdalsbreen, Norway, and Berendon Glacier, British Columbia, Canada. *Journal of Glaciology 20*, 99–113.

Eyles, N., Sladen, J. A. & Gilro, S. 1982: A depositional model for stratigraphic complexes and facies superimposition in lodgement tills. *Boreas 11*, 317–333.

Farnsworth, W. R., Ingólfsson, Ó., Retelle, M. & Schomacker, A. 2016: Over 400 previously undocumented Svalbard surge-type glaciers identified. *Geomorphology 264*, 52–60.

Forman, S. L. & Miller, G. H. 1984: Time-Dependent Soil Morphologies and Pedogenic Processes on Raised Beaches, Bröggerhalvöya, Spitsbergen, Svalbard Archipelago. *Arctic and Alpine Research 16*, 381–394.

Forman, S. L., Mann, D. H. & Miller, G. H. 1987: Late Weichselian and Holocene relative sea-level history of Bröggerhalvöya, Spitsbergen. *Quaternary Research 27*, 41–50.

Forman, S. L. 1989: Late Weichselian glaciation and deglaciation of Forlandsundet area, western Spitsbergen, Svalbard. *Boreas 18*, 51–60.

Forman, S. L. 1990: Postglacial Relative Sea-Level History of Northwestern Spitsbergen, Svalbard. *Geological Society of America Bulletin 102*, 1580–1590.

Forman, S. L., Lubinski, D. J., Ingólfsson, Ó., Zeeberg, J. J., Snyder, J. A., Siegert, M. J. & Matishov, G. G. 2004: A review of postglacial emergence on Svalbard, Franz Josef Land and Novaya Zemlya, northern Eurasia. *Quaternary Science Reviews 23*, 1391–1434.

Forwick, M. & Vorren, T. O. 2009: Late Weichselian and Holocene sedimentary environments and ice rafting in Isfjorden, Spitsbergen. *Palaeogeography, Palaeoclimatology, Palaeoecology 280*, 258–274.

Frauenfelder, R., Haeberli, W. & Hoelzle, M. 2003: Rockglacier occurrence and related terrain parameters in a study area of the Eastern Swiss Alps. *Proceedings 8th International Conference on Permafrost. Swets and Zeitlinger, Lisse*, 253–258 pp.

Freeman, S., Bishop, P., Bryant, C., Cook, G., Fallick, A., Harkness, D., Metcalfe, S., Scott, M., Scott, R. & Summerfield, M. 2004: A new environmental sciences AMS laboratory in Scotland. *Nuclear Instruments and Methods in Physics Research Section B: Beam Interactions with Materials and Atoms 223–224*, 31–34.

French, H. M. & Guglielmin, M. 2000: Cryogenic Weathering of Granite, Northern Victoria Land, Antarctica. *Permafrost and Periglacial Processes 11*, 305–314.

Friend, P. F. & Moody-Stuart, M. 1972: Sedimentation of the Wood Bay Formation (Devonian) of Spitsbergen: regional analysis of a late orogenic basin. *Norsk Polarinstitutt Skrifter 157*, 1–80.

Funder, S., Hjort, C., Landvik, J. Y., Nam, S. I., Reeh, N. & Stein, R. 1998: History of a stable ice margin East Greenland during the Middle and Upper Pleistocene. *Quaternary Science Reviews 17*, 77–123.

GEBCO 2014: *GEBCO_2014 Grid — a global 30 arc-second interval grid*. http://www.gebco.net/data_and_products/gridded_bathymetry_data/. Date accessed: 18 April 2016.

Gee, D. G. & Hjelle, A. 1966: On the crystalline rocks of northwest Spitsbergen. *Norsk Polarinstitutt Årbok 1964*, 31–45.

Gerland, S. & Hall, R. 2006: Variability of fast-ice thickness in Spitsbergen fjords. *Annals of Glaciology 44*, 231–239.

Gildor, H. & Tziperman, E. 2001: A sea ice climate switch mechanism for the 100-kyr glacial cycles. *Journal of Geophysical Research-Oceans 106*, 9117–9133.

Ginés, A., Knez, M., Slabe, T. & Dreybrodt, W. 2009: *Karst Rock Features: Karren sculpturing*. 561 pp. Založoba ZRC, Ljubljana.

Gislefoss, L. 2015: *Deglaciation and late Holocene glacier re-advances in Hornsund, Svalbard, based on ^{10}Be surface exposure ages from erratic boulders.* M.Sc Thesis, University of Bergen, 113 pp.

Gjelsvik, T. 1974: A new occurrence of Devonian rocks in Spitsbergen. *Norsk Polarinstitutt Årbok 1972*, 23–28.

Gjerde, M., Bakke, J., D'Andrea, W. J., Balascio, N. S., Bradley, R. S., Vasskog, K., Ólafsdóttir, S., Røthe, T. O., Perren, B. B. & Hormes, A. Submitted for review: Late Glacial and Holocene multi-proxy environmental reconstruction from Lake Hakluytvatnet, Amsterdamøya Island, Svalbard (79°N). *Quaternary Science Reviews*, 1–38.

Gjermundsen, E. F., Briner, J. P., Akçar, N., Salvigsen, O., Kubik, P., Gantert, N. & Hormes, A. 2013: Late Weichselian local ice dome configuration and chronology in Northwestern Svalbard: early thinning, late retreat. *Quaternary Science Reviews 72*, 112–127.

Gjermundsen, E. F., Briner, J. P., Akçar, N., Foros, J., Kubik, P. W., Salvigsen, O. & Hormes, A. 2015: Minimal erosion of Arctic alpine topography during late Quaternary glaciation. *Nature Geosci 8*, 789–792.

Goldthwait, R. P. 1976: Frost sorted patterned ground: A review. *Quaternary Research 6*, 27–35.

Gosse, J. C. & Phillips, F. M. 2001: Terrestrial in situ cosmogenic nuclides: theory and application. *Quaternary Science Reviews 20*, 1475–1560.

Grosswald, M. G. 1980: Late Weichselian ice sheet of Northern Eurasia. *Quaternary Research 13*, 1–32.

Grove, J. M. 2001: The Initiation of the "Little Ice Age" in Regions Round the North Atlantic. *In* Ogilvie, A. E. J. & Jónsson, T. (eds.): *The Iceberg in the Mist: Northern Research in pursuit of a "Little Ice Age"*, 53–82 pp. Springer Netherlands, Dordrecht.

Guillon, H., Mugnier, J.-L., Buoncristiani, J.-F., Carcaillet, J., Godon, C., Prud'homme, C., van der Beek, P. & Vassallo, R. 2015: Improved discrimination of subglacial and periglacial erosion using 10Be concentration measurements in subglacial and supraglacial sediment load of the Bossons glacier (Mont Blanc massif, France). *Earth Surface Processes and Landforms 40*, 1202–1215.

Hagerup, H. 1912: 26/08/1912. *Tidens Tegn.* Oslo.

Hald, M., Ebbesen, H., Forwick, M., Godtliebsen, F., Khomenko, L., Korsun, S., Ringstad Olsen, L. & Vorren, T. O. 2004: Holocene paleoceanography and glacial history of the West Spitsbergen area, Euro-Arctic margin. *Quaternary Science Reviews 23*, 2075–2088.

Hall, K. & André, M.-F. 2003: Rock thermal data at the grain scale: applicability to granular disintegration in cold environments. *Earth Surface Processes and Landforms 28*, 823–836.

Hall, K., Guglielmin, M. & Strini, A. 2008: Weathering of granite in Antarctica: II. Thermal stress at the grain scale. *Earth Surface Processes and Landforms 33*, 475–493.

Hansen, T. 2014: *Late Weichselian and Holocene sedimentary processes and glacier dynamics in Woodfjorden, Bockfjorden and Liefdefjorden, North Spitsbergen.* M.Sc. Thesis, University of Tromsø, 162 pp.

Harbor, J. M., Hallet, B. & Raymond, C. F. 1988: A numerical model of landform development by glacial erosion. *Nature 333*, 347–349.

Henriksen, M., Alexanderson, H., Landvik, J. Y., Linge, H. & Peterson, G. 2014: Dynamics and retreat of the Late Weichselian Kongsfjorden ice stream, NW Svalbard. *Quaternary Science Reviews 92*, 235–245.

Herber, L. J. 1969: Separation of feldspar and quartz by flotation. *The American Mineralogist 54*, 1212–1215.

Herz, K. & Andreas, G. 1966a: Untersuchungen zur Morphologie der periglazialen Auftauschicht im Kongsfjordgebiet (Westspitzbergen). *Petersmanns Mittellungen 110*, 190–198.

Herz, K. & Andreas, G. 1966b: Untersuchungen zur Ökologie der periglazialen Auftauschicht im Kongsfjordgebiet (Westspitzbergen). *Petersmanns Mittellungen 110*, 260–274.

Heyman, J., Stroeven, A. P., Harbor, J. M. & Caffee, M. W. 2011: Too young or too old: Evaluating cosmogenic exposure dating based on an analysis of compiled boulder exposure ages. *Earth and Planetary Science Letters 302*, 71–80.

Hindmarsh, R. C. A. 1996: Sliding of till over bedrock: scratching, polishing, comminution and kinematic-wave theory. *Annals of Glaciology 22*, 41–47.

Hjelle, A. 1979: Aspects of the geology of northwest Spitsbergen. *Norsk Polarinstitutt Skrifter 167*, 37–62.

Hjelle, A., Piepjohn, K., Saalmann, K., Salvigsen, O., Thiedig, F. & Dallmann, W. K. 1999: *Geological map Svalbard 1:100 000 Spitsbergen, sheet A7G Kongsfjorden*. Tromsø: Norsk Polarinstitutt.

Hoel, A. 1966: *Svalbard : Svalbards historie 1596-1965 : 1*. 487 pp. S. Kildahls boktrykkeri, Oslo.

Hogan, K. A., Dowdeswell, J. A., Noormets, R., Evans, J. & Ó Cofaigh, C. 2010: Evidence for full-glacial flow and retreat of the Late Weichselian Ice Sheet from the waters around Kong Karls Land, eastern Svalbard. *Quaternary Science Reviews 29*, 3563–3582.

Hormes, A., Akçar, N. & Kubik, P. W. 2011: Cosmogenic radionuclide dating indicates ice-sheet configuration during MIS 2 on Nordaustlandet, Svalbard. *Boreas 40*, 636–649.

Hormes, A., Gjermundsen, E. F. & Rasmussen, T. L. 2013: From mountain top to the deep sea - Deglaciation in 4D of the northwestern Barents Sea ice sheet. *Quaternary Science Reviews 75*, 78–99.

Houmark-Nielsen, M. & Funder, S. 1999: Pleistocene stratigraphy of Kongsfjordhallet, Spitsbergen, Svalbard. *Polar Research 18*, 39–50.

Howe, J. A., Moreton, S. G., Morri, C. & Morris, P. 2003: Multibeam bathymetry and the depositional environments of Kongsfjorden and Krossfjorden, western Spitsbergen, Svalbard. *Polar Research 22*, 301–316.

Howell, D., Siegert, M. J. & Dowdeswell, J. A. 2000: Modelling the influence of glacial isostasy on Late Weichselian ice-sheet growth in the Barents Sea. *Journal of Quaternary Science 15*, 475–486.

Hughes, A. L. C., Gyllencreutz, R., Lohne, Ø. S., Mangerud, J. & Svendsen, J. I. 2016: The last Eurasian ice sheets–a chronological database and time-slice reconstruction, DATED-1. *Boreas 45*, 1–45.

Hughes, T. J. 1987: The Marine Ice Transgression Hypothesis. *Geografiska Annaler. Series A, Physical Geography 69*, 237–250.

Humlum, O. 1982a: Rock glacier types on Disko, Central West Greenland. *Geografisk Tidsskrift-Danish Journal of Geography 82*, 59–66.

Humlum, O. 1982b: Rock Glaciers in Northern Spitsbergen: A Discussion. *The Journal of Geology 90*, 214–217.

Humlum, O. 1998: The climatic significance of rock glaciers. *Permafrost and Periglacial Processes 9*, 375–395.

Humlum, O. 2000: The geomorphic significance of rock glaciers: estimates of rock glacier debris volumes and headwall recession rates in West Greenland. *Geomorphology 35*, 41–67.

Humlum, O. 2002: Modelling late 20th-century precipitation in Nordenskiold Land, Svalbard, by geomorphic means. *Norsk Geografisk Tidsskrift-Norwegian Journal of Geography 56*, 96–103.

Humlum, O., Instanes, A. & Sollid, J. L. 2003: Permafrost in Svalbard: a review of research history, climatic background and engineering challenges. *Polar Research 22*, 191–215.

Humlum, O. 2005: Holocene permafrost aggradation in Svalbard. *Geological Society, London, Special Publications 242*, 119–129.

Hunt, A. L., Larsen, J., Bierman, P. R. & Petrucci, G. A. 2008: Investigation of factors that affect the sensitivity of accelerator mass spectrometry for cosmogenic Be-10 and Al-26 isotope analysis. *Analytical Chemistry 80*, 1656–1663.

ICEBOUND 2010: *Icebound – An important contribution to improving today's climate models*. Hormes, A. & Gjermundsen, E. F. Project overview poster. http://icebound.no/.

Ingólfsson, Ó. & Landvik, J. Y. 2013: The Svalbard-Barents Sea ice-sheet - Historical, current and future perspectives. *Quaternary Science Reviews 64*, 33–60.

Isachsen, G. 1912: *The Hydrographic Observations of the Isachsen Spitsbergen Expedition 1909-1910*. 36 pp. Dybwad, Christiania.

Isachsen, G. & Hoel, A. 1913: *Exploration du Nord-Ouest du Spitsberg entreprise sous les auspices de S. A. S. le Prince de Monaco par la Mission Isachsen*. 150 pp. Imprimerie de Monaco, Monaco.

Ivy-Ochs, S. & Kober, F. 2008: Surface exposure dating with cosmogenic nuclides. *Eiszeitalter und Gegenwart 57*, 179–209.

Ivy-Ochs, S. & Briner, J. P. 2014: Dating Disappearing Ice With Cosmogenic Nuclides. *Elements 10*, 351–356.

Ivy Ochs, S. D. 1996: *The dating of rock surfaces using in situ produced 10 Be, 26 Al and 36 Cl, with examples from Antarctica and the Swiss Alps.* Ph.D. Thesis, Swiss Federal Institute of Technology Zürich, 197 pp.

Jamieson, S. S. R., Vieli, A., Ó Cofaigh, C., Stokes, C. R., Livingstone, S. J. & Hillenbrand, C.-D. 2014: Understanding controls on rapid ice-stream retreat during the last deglaciation of Marguerite Bay, Antarctica, using a numerical model. *Journal of Geophysical Research: Earth Surface 119*, 247–263.

Jessen, S. P., Rasmussen, T. L., Nielsen, T. & Solheim, A. 2010: A new Late Weichselian and Holocene marine chronology for the western Svalbard slope 30,000–0 cal years BP. *Quaternary Science Reviews 29*, 1301–1312.

Johnsen, T. F., Alexanderson, H., Fabel, D. & Freeman, S. P. H. T. 2009: New 10Be cosmogenic ages from the Vimmerby Moraine confirm the timing of Scandinavian Ice Sheet deglaciation in southern Sweden. *Geografiska Annaler: Series A, Physical Geography 91*, 113–120.

Jones, G. A. & Keigwin, L. D. 1988: Evidence from Fram Strait (78[deg] N) for early deglaciation. *Nature 336*, 56–59.

Jonsson, S. 1982: On the Present Glaciation of Storøya, Svalbard. *Geografiska Annaler. Series A, Physical Geography 64*, 53–79.

Kempe, M. 1989: *Geologische Kartierung der östlichen Blomstrandhalvøya und tektonische Untersuchungen an Gesteinen der östlichen Blomstrandhalvøya, NW-Spitzbergen, Svalbard, Norwegen.* MSc Thesis, Westfälische Wilhelms-Universität Münster, 168 pp.

Kempe, M., Niehoff, U., Piepjohn, K. & Thiedig, F. 1997: Kaledonische und svalbardische Entwicklung im Grundgebirge auf der Blomstrandhalvøya, NW-Spitsbergen. *Münstersche Forschungen zur Geologie und Paläontologie 82*, 121–128.

Killingtveit, Å., Pettersson, L.-E. & Sand, K. 2003: Water balance investigations in Svalbard. *Polar Research 22*, 161–174.

Kleman, J. 1994: Preservation of landforms under ice sheets and ice caps. *Geomorphology 9*, 19–32.

Kleman, J., Hättestrand, C., Stroeven, A. P., Jansson, K. N., De Angelis, H. & Borgström, I. 2007: Reconstruction of Palaeo-Ice Sheets - Inversion of their Glacial Geomorphological Record. *In* Knight, P. G. (ed.): *Glacier Science and Environmental Change*, 192–198 pp. Blackwell Publishing, Oxford.

Klitgaard Kristensen, D., Rasmussen, T. L. & Koç, N. 2013: Palaeoceanographic changes in the northern Barents Sea during the last 16 000 years – new constraints on the last deglaciation of the Svalbard–Barents Sea Ice Sheet. *Boreas 42*, 798–813.

Koç, N., Klitgaard-Kristensen, D., Hasle, K., Forsberg, C. F. & Solheim, A. 2002: Late glacial palaeoceanography of Hinlopen Strait, northern Svalbard. *Polar Research 21*, 307–314.

Kohl, C. P. & Nishiizumi, K. 1992: Chemical isolation of quartz for measurement of in-situ-produced cosmogenic nuclides. *Geochimica et Cosmochimica Acta 56*, 3583–3587.

Kohler, J., James, T. D., Murray, T., Nuth, C., Brandt, O., Barrand, N. E., Aas, H. F. & Luckman, A. 2007: Acceleration in thinning rate on western Svalbard glaciers. *Geophysical Research Letters 34*, 1–5.

Kokelj, S. V., Tunnicliffe, J., Lacelle, D., Lantz, T. C. & Fraser, R. H. 2015: Retrogressive thaw slumps: From slope process to the landscape sensitivity of northwestern Canada. *GeoQuebec 2015 Conference.* Quebec City, Quebec, Canada.

Krawczyk, W. E. & Pettersson, L. E. 2007: Chemical denudation rates and carbon dioxide drawdown in an ice-free polar karst catchment: Londonelva, Svalbard. *Permafrost and Periglacial Processes 18*, 337–350.

Kruse, F. 2014: *Frozen Assets: British mining, exploration, and geopolitics on Spitsbergen, 1904-53*. 480 pp. Barkhuis, Groningen.

Kuipers, B. 2013: *Si det med farger*. http://labs.kartverket.no/gjoer-mer-med-farger/. Date accessed: 2 May 2016.

Kvasov, D. D. 1978: The Barents ice sheet as a relay regulator of glacial-interglacial alternation. *Quaternary Research 9*, 288–299.

Lal, D. 1991: Cosmic ray labeling of erosion surfaces: in situ nuclide production rates and erosion models. *Earth and Planetary Science Letters 104*, 424–439.

Lambeck, K. 1996: Limits on the areal extent of the Barents Sea ice sheet in Late Weichselian time. *Global and Planetary Change 12*, 41–51.

Landvik, J. Y., Mangerud, J. & Salvigsen, O. 1987: The Late Weichselian and Holocene shoreline displacement on the west-central coast of Svalbard. *Polar Research 5*, 29–44.

Landvik, J. Y., Hansen, A., Kelly, M., Salvigsen, O., Slettemark, Ø. & Stubdrup, O. P. 1992: The last deglaciation and glacimarine/marine sedimentation on Barentsøya and Edgeøya, eastern Svalbard. *Lundqua Report 35*, 61–83.

Landvik, J. Y., Bondevik, S., Elverhoi, A., Fjeldskaar, W., Mangerud, J., Salvigsen, O., Siegert, M. J., Svendsen, J. I. & Vorren, T. O. 1998: The last glacial maximum of Svalbard and the Barents Sea area: Ice sheet extent and configuration. *Quaternary Science Reviews 17*, 43–75.

Landvik, J. Y., Brook, E. J., Gualtieri, L., Raisbeck, G., Salvigsen, O. & Yiou, F. 2003: Northwest Svalbard during the last glaciation: Ice-free areas existed. *Geology 31*, 905–908.

Landvik, J. Y., Ingólfsson, Ó., Mienert, J., Lehman, S. J., Solheim, A., Elverhøi, A. & Ottesen, D. 2005: Rethinking Late Weichselian ice-sheet dynamics in coastal NW Svalbard. *Boreas 34*, 7–24.

Landvik, J. Y., Brook, E. J., Gualtieri, L., Linge, H., Raisbeck, G., Salvigsen, O. & Yiou, F. 2013: 10Be exposure age constraints on the Late Weichselian ice-sheet geometry and dynamics in inter-ice-stream areas, western Svalbard. *Boreas 42*, 43–56.

Landvik, J. Y., Alexanderson, H., Henriksen, M. & Ingólfsson, Ó. 2014: Landscape imprints of changing glacial regimes during ice-sheet build-up and decay: a conceptual model from Svalbard. *Quaternary Science Reviews 92*, 258–268.

Lauritzen, S.-E. 2006: Caves and speleogenesis at Blomstrandsøya, Kongsfjord, W. Spitsbergen. *International Journal of Speleology 35*, 37–58.

Lehman, S. J. & Forman, S. J. 1987: Glacier extent and sea level variation during the Late Weichselian on northwest Spitsbergen. *Polar Research 5*, 271–272.

Lehman, S. J. & Forman, S. L. 1992: Late Weichselian glacier retreat in Kongsfjorden, west Spitsbergen, Svalbard. *Quaternary Research 37*, 139–154.

Lehman, S. J. & Keigwin, L. D. 1992: Deep circulation revisited. *Nature 358*, 197–198.

Liestøl, O. 1969: Glacier surges in West Spitsbergen. *Canadian Journal of Earth Sciences 6*, 895–897.

Liestøl, O. 1977: Pingos, springs, and permafrost in Spitsbergen. *Norsk Polarinstitutt Årbok 1977*, 7–29.

Liestøl, O. 1988: The glaciers in the Kongsfjorden area, Spitsbergen. *Norsk Geografisk Tidsskrift-Norwegian Journal of Geography 42*, 231–238.

Lindner, L., Marks, L., Roszczynko, W. & Semil, J. 1991: Age of raised marine beaches of northern Hornsund Region, South Spitsbergen. *Polish Polar Research 12*, 161–182.

Lingenfelter, R. E. 1963: Production of carbon 14 by cosmic-ray neutrons. *Reviews of Geophysics 1*, 35–55.

Lønne, I. 2005: Faint traces of high Arctic glaciations: an early Holocene ice-front fluctuation in Bolterdalen, Svalbard. *Boreas 34*, 308–323.

Lowe, J. J. & NASP Members 1995: Palaeoclimate of the North Atlantic seaboards during the last glacial/interglacial transition. *Quaternary International 28*, 51–61.

Lukas, S., Nicholson, L. I., Ross, F. H. & Humlum, O. 2005: Formation, Meltout Processes and Landscape Alteration of High-Arctic Ice-Cored Moraines—Examples From Nordenskiold Land, Central Spitsbergen. *Polar Geography 29*, 157–187.

MacAyeal, D. R. 1993: Binge/purge oscillations of the Laurentide Ice Sheet as a cause of the North Atlantic's Heinrich events. *Paleoceanography 8*, 775–784.

Maclachlan, S. E., Howe, J. A. & Vardy, M. E. 2010: Morphodynamic evolution of Kongsfjorden-Krossfjorden, Svalbard, during the Late Weichselian and Holocene. *Geological Society, London, Special Publications 344*, 195–205.

Maden, C., Anastasi, P. A. F., Dougans, A., Freeman, S. P. H. T., Kitchen, R., Klody, G., Schnabel, C., Sundquist, M., Vanner, K. & Xu, S. 2007: SUERC AMS ion detection. *Nuclear Instruments and Methods in Physics Research Section B: Beam Interactions with Materials and Atoms 259*, 131–139.

Mangerud, J., Bolstad, M., Elgersma, A., Helliksen, D., Landvik, J. Y., Lycke, A. K., Lønne, I., Salvigsen, O., Sandahl, T. & Sejrup, H. P. 1987: The Late Weichselian glacial maximum in western Svalbard. *Polar Research 5*, 275–278.

Mangerud, J. & Svendsen, J. I. 1990: Deglaciation chronology inferred from marine sediments in a proglacial lake basin, western Spitsbergen, Svalbard. *Boreas 19*, 249–272.

Mangerud, J., Bolstad, M., Elgersma, A., Helliksen, D., Landvik, J. Y., Lønne, I., Lycke, A. K., Salvigsen, O., Sandahl, T. & Svendsen, J. I. 1992: The last glacial maximum on Spitsbergen, Svalbard. *Quaternary Research 38*, 1–31.

Mangerud, J. & Svendsen, J. I. 1992: The last interglacial-glacial period on Spitsbergen, Svalbard. *Quaternary Science Reviews 11*, 633–664.

Mangerud, J., Jansen, E. & Landvik, J. Y. 1996: Late Cenozoic history of the Scandinavian and Barents Sea ice sheets. *Global and Planetary Change 12*, 11–26.

Mangerud, J., Dokken, T., Hebbeln, D., Heggen, B., Ingólfsson, Ó., Landvik, J. Y., Mejdahl, V., Svendsen, J. I. & Vorren, T. O. 1998: Fluctuations of the Svalbard-Barents Sea Ice Sheet the last 150,000 years. *Quaternary Science Reviews 17*, 11–42.

Mangerud, J., Astakhov, V. I., Murray, A. & Svendsen, J. I. 2001: The chronology of a large ice-dammed lake and the Barents–Kara Ice Sheet advances, Northern Russia. *Global and Planetary Change 31*, 321–336.

Mangerud, J. & Landvik, J. Y. 2007: Younger Dryas cirque glaciers in western Spitsbergen: smaller than during the Little Ice Age. *Boreas 36*, 278–285.

Matsubara, A., Saito-Kokubu, Y., Nishizawa, A., Miyake, M., Ishimaru, T. & Umeda, K. 2014: Quaternary Geochronology Using Accelerator Mass Spectrometry (AMS)–Current Status of the AMS System at the TONO Geoscience Center. *In* Mörner, N.-A. (ed.): *Geochronology-Methods and Case Studies*, 3–30 pp. InTech.

Matthews, J. A. & Briffa, K. R. 2005: The 'Little Ice Age': Re-evaluation of an evolving concept. *Geografiska Annaler: Series A, Physical Geography 87*, 17–36.

Mattingsdal, R., Knies, J., Andreassen, K., Fabian, K., Husum, K., Grøsfjeld, K. & De Schepper, S. 2014: A new 6 Myr stratigraphic framework for the Atlantic–Arctic Gateway. *Quaternary Science Reviews 92*, 170–178.

Mellor, M. 1957: Glacier observations in north-west Spitsbergen. *Journal of Glaciology 3(21)*, 61–66.

Miller, G. H. 1982: Quaternary Depositional Episodes, Western Spitsbergen, Norway: Aminostratigraphy and Glacial History. *Arctic and Alpine Research 14*, 321–340.

Miller, G. H., Sejrup, H. P., Lehman, S. J. & Forman, S. L. 1989: Glacial history and marine environmental change during the last interglacial-glacial cycle, western Spitsbergen, Svalbard. *Boreas 18*, 273–296.

Müller, J. & Stein, R. 2014: High-resolution record of late glacial and deglacial sea ice changes in Fram Strait corroborates ice–ocean interactions during abrupt climate shifts. *Earth and Planetary Science Letters 403*, 446–455.

Myers, G. 2013: *Ice-stream dynamics based on provenance studies of erratic boulders on Blomstrandøya*. Term Paper, University Centre in Svalbard, 20 pp.

Myhre, P. I., Corfu, F. & Andresen, A. 2008: Caledonian anatexis of Grenvillian crust: a U/Pb study of Albert I Land, NW Svalbard. *Norwegian Journal of Geology 89*, 173–191.

Niehoff, U. 1989: *Geologische Kartierung der westlichen Blomstrandhalvøya und tektonische Untersuchungen an Gesteinen der westlichen Blomstrandhalvøya, NW-Spitzbergen, Svalbard, Norwegen.* MSc Thesis, Westfälische Wilhelms-Universität Münster, 120 pp.

Nishiizumi, K., Winterer, E. L., Kohl, C. P., Klein, J., Middleton, R., Lal, D. & Arnold, J. R. 1989: Cosmic ray production rates of 10Be and 26Al in quartz from glacially polished rocks. *Journal of Geophysical Research: Solid Earth (1978–2012) 94*, 17907–17915.

Nishiizumi, K., Imamura, M., Caffee, M. W., Southon, J. R., Finkel, R. C. & McAninch, J. 2007: Absolute calibration of 10Be AMS standards. *Nuclear Instruments and Methods in Physics Research Section B: Beam Interactions with Materials and Atoms 258*, 403–413.

Norwegian Geological Survey 2015: *Tegnforklaring: Løsmasser N50/N250*. Trondeim, Norway: Norges Geologiske Undersøkelse. http://www.ngu.no/upload/Aktuelt/Tegnforklaring_LosmasserN50N250.pdf.

Norwegian Meteorological Institute 2016: *eKlima*. http://eklima.met.no/. Date accessed: 7 January 2016.

Norwegian Polar Institute 1999: *Svalbard 1:100.000: Spitsbergen. Map B7: Tre Kroner*. Tromsø, Norway: Norsk polarinstitutt.

Norwegian Polar Institute 2003: *The Place Names of Svalbard*. 537 pp. Norsk Polarinstitutt, Tromsø.

Norwegian Polar Institute 2014: *Terrengmodell Svalbard (S0 Terrengmodell)*. Tromsø, Norway: Norwegian Polar Institute. https://data.npolar.no/dataset/dce53a47-c726-4845-85c3-a65b46fe2fea.

Norwegian Polar Institute 2016: *Tjenesten inneholder Geologiske kart i målestokken 1:750 000. Kartgrunnlaget baserer seg fra Berggrunnskart over Svalbard i 1:750 000*. Tromsø, Norway: Norwegian Polar Institute. http://geodata.npolar.no/ArcGIS/services/inspire2/Geologi_S750/MapServer/WMSServer?request=GetCapabilities&service=WMS.

Nygård, A., Sejrup, H. P., Haflidason, H., Lekens, W. A. H., Clark, C. D. & Bigg, G. R. 2007: Extreme sediment and ice discharge from marine-based ice streams: New evidence from the North Sea. *Geology 35*, 395–398.

Ochs, M. & Ivy-Ochs, S. 1997: The chemical behavior of Be, Al, Fe, Ca and Mg during AMS target preparation from terrestrial silicates modeled with chemical speciation calculations. *Nuclear Instruments and Methods in Physics Research Section B: Beam Interactions with Materials and Atoms 123*, 235–240.

Ohta, Y., Larionov, A. N., Tebenkov, A. M., Lepvrier, C., Maluski, H., Lange, M. & Hellebrandt, B. 2002: Single-zircon Pb-evaporation and 40Ar/39Ar dating of the metamorphic and granitic rocks in north-west Spitsbergen. *Polar Research 21*, 73–89.

Ollier, C. 1984: *Weathering*. 270 pp. Longman, New York.

Orvin, A. K. 1934: Geology of the Kings Bay region, Spitsbergen: with special reference to the coal deposits. *Skrifter om Svalbard og Ishavet 57*, 1–195.

Ottesen, D., Dowdeswell, J. A. & Rise, L. 2005: Submarine landforms and the reconstruction of fast-flowing ice streams within a large Quaternary ice sheet: The 2500-km-long Norwegian-Svalbard margin (57°–80°N). *Geological Society of America Bulletin 117*, 1033–1050.

Ottesen, D., Dowdeswell, J. A., Landvik, J. Y. & Mienert, J. 2007: Dynamics of the Late Weichselian ice sheet on Svalbard inferred from high-resolution sea-floor morphology. *Boreas 36*, 286–306.

Ottesen, D. & Dowdeswell, J. A. 2009: An inter-ice-stream glaciated margin: Submarine landforms and a geomorphic model based on marine-geophysical data from Svalbard. *Geological Society of America Bulletin 121*, 1647–1665.

Owens, L. B. & Watson, J. P. 1979: Landscape reduction by weathering in small Rhodesian watersheds. *Geology 7*, 281–284.

OxCal 2015: *OxCal version 4.2*. https://c14.arch.ox.ac.uk/embed.php?File=oxcal.html. Date accessed: 2 May 2016.

Patton, H., Andreassen, K., Bjarnadóttir, L. R., Dowdeswell, J. A., Winsborrow, M. C. M., Noormets, R., Polyak, L., Auriac, A. & Hubbard, A. 2015: Geophysical constraints on the dynamics and retreat of the Barents Sea ice sheet as a paleobenchmark for models of marine ice sheet deglaciation. *Reviews of Geophysics 53*, 1051–1098.

Paul, M. A. & Evans, H. 1974: Observations on the internal structure and origin of some flutes in glacio-fluvial sediments, Blomstrandbreen, north-west Spitsbergen. *Journal of Glaciology 13*, 393–400.

Peltier, W. R. & Fairbanks, R. G. 2006: Global glacial ice volume and Last Glacial Maximum duration from an extended Barbados sea level record. *Quaternary Science Reviews 25*, 3322–3337.

Peterson, G. 2008: *The development and relative chronology of landforms at Kongsfjordhallet, Spitsbergen.* B.Sc Thesis, Stockholm University, 31 pp.

Phillips, W. P., Briner, J. P., Gislefoss, L., Linge, H., Koffman, T., Fabel, D., Xu, S. & Hormes, A. Submitted for review: Late Holocene glacier activity at inner Hornsund and Scottbreen, Southern Svalbard. 1–27.

Piepjohn, K. 1997: Erläuterungen zur Geologischen Karte 1:150,000 des Woodfjorden-Gebietes (Haakon VII Land, Andrée Land), NW-Spitzbergen, Svalbard. *Münstersche Forschungen zur Geologie und Paläontologie 82*, 15–37.

Porter, S. C. 1981: Recent glacier variations and volcanic eruptions. *Nature 291*, 139–142.

Purdue University Primelab 2007: *Froth Flotation*. http://www.physics.purdue.edu/primelab/MSL/froth_floatation.html. Date accessed: 27 October 2015.

Rasmussen, S. O., Andersen, K. K., Svensson, A. M., Steffensen, J. P., Vinther, B. M., Clausen, H. B., Siggaard-Andersen, M. L., Johnsen, S. J., Larsen, L. B., Dahl-Jensen, D., Bigler, M., Rothlisberger, R., Fischer, H., Goto-Azuma, K., Hansson, M. E. & Ruth, U. 2006: A new Greenland ice core chronology for the last glacial termination. *Journal of Geophysical Research-Atmospheres 111*, D06102.

Rasmussen, T. L., Thomsen, E., Ślubowska, M. A., Jessen, S., Solheim, A. & Koç, N. 2007: Paleoceanographic evolution of the SW Svalbard margin (76°N) since 20,000 14C yr BP. *Quaternary Research 67*, 100–114.

Rebesco, M., Laberg, J. S., Pedrosa, M. T., Camerlenghi, A., Lucchi, R. G., Zgur, F. & Wardell, N. 2014: Onset and growth of Trough-Mouth Fans on the North-Western Barents Sea margin – implications for the evolution of the Barents Sea/Svalbard Ice Sheet. *Quaternary Science Reviews 92*, 227–234.

Reimer, P. J., Bard, E., Bayliss, A., Beck, J. W., Blackwell, P. G., Bronk Ramsey, C., Buck, C. E., Cheng, H., Edwards, R. L., Friedrich, M., Grootes, P. M., Guilderson, T. P., Haflidason, H., Hajdas, I., Hatté, C., Heaton, T. J., Hoffmann, D. L., Hogg, A. G., Hughen, K. A., Kaiser, K. F., Kromer, B., Manning, S. W., Niu, M., Reimer, R. W., Richards, D. A., Scott, E. M., Southon, J. R., Staff, R. A., Turney, C. S. M. & van der Plicht, J. 2013: IntCal13 and Marine13 Radiocarbon Age Calibration Curves 0–50,000 Years cal BP. *Radiocarbon 55*, 1869–1887.

Reusche, M., Winsor, K., Carlson, A. E., Marcott, S. A., Rood, D. H., Novak, A., Roof, S., Retelle, M., Werner, A., Caffee, M. & Clark, P. U. 2014: 10Be surface exposure ages on the late-Pleistocene and Holocene history of Linnébreen on Svalbard. *Quaternary Science Reviews 89*, 5–12.

Rignot, E., Mouginot, J. & Scheuchl, B. 2011: Ice Flow of the Antarctic Ice Sheet. *Science 333*, 1427–1430.

Rose, K. E. 1979: Characteristics of ice flow in Marie Byrd land, Antarctica. *Journal of Glaciology 24*, 63–75.

Røthe, T. O., Bakke, J., Vasskog, K., Gjerde, M., D'Andrea, W. J. & Bradley, R. S. 2015: Arctic Holocene glacier fluctuations reconstructed from lake sediments at Mitrahalvoya, Spitsbergen. *Quaternary Science Reviews 109*, 111–125.

Ruddiman, W. F. & Mcintyre, A. 1981: The North-Atlantic Ocean during the Last Deglaciation. *Palaeogeography Palaeoclimatology Palaeoecology 35*, 145–214.

Ruddiman, W. F. 2008: *Earth's climate: past and future*. 388 pp. W. H. Freeman and Company, New York.

Salvigsen, O. 1977: Radiocarbon datings and the extension of the Weichselian ice-sheet in Svalbard. *Norsk Polarinstitutt Årbok 1976*, 209–224.

Salvigsen, O. 1979: The last deglaciation of Svalbard. *Boreas 8*, 229–231.

Salvigsen, O. & Nydal, R. 1981: The Weichselian glaciation in Svalbard before 15,000 B.P.*. *Boreas 10*, 433–446.

Salvigsen, O. & Österholm, H. 1982: Radiocarbon dated raised beaches and glacial history of the northern coast of Spitsbergen, Svalbard. *Polar Research 1982*, 97–115.

Schellenberger, T., Dunse, T., Kääb, A., Kohler, J. & Reijmer, C. H. 2014: Surface speed and frontal ablation of Kronebreen and Kongsbreen, NW-Svalbard, from SAR offset tracking. *Cryosphere Discuss 8*, 6193–6233.

Schildgen, T. F., Phillips, W. M. & Purves, R. S. 2005: Simulation of snow shielding corrections for cosmogenic nuclide surface exposure studies. *Geomorphology 64*, 67–85.

Schomacker, A. & Kjær, K. H. 2008: Quantification of dead-ice melting in ice-cored moraines at the high-Arctic glacier Holmströmbreen, Svalbard. *Boreas 37*, 211–225.

Schytt, V., Hoppe, G., Blake Jr, W. & Grosswald, M. G. 1968: The extent of the Würm glaciation in the European Arctic. *International Association of Hydrological Sciences 79*, 207–216.

Scoresby, W. 1820: *An account of the Arctic regions with a history and description of the northern whale-fishery*. 674 pp. A. Constable & co., Edinburgh.

Sexton, D. J., Dowdeswell, J. A., Solheim, A. & Elverhøi, A. 1992: Seismic architecture and sedimentation in northwest Spitsbergen fjords. *Marine Geology 103*, 53–68.

Shabtaie, S., Whillans, I. M. & Bentley, C. R. 1987: The morphology of ice streams A, B, and C, west Antarctica, and their environs. *Journal of Geophysical Research: Solid Earth 92*, 8865–8883.

Siegert, M. J. & Dowdeswell, J. A. 1995a: Modelling ice-sheet sensitivity to late weichselian environments in the svalbard-barents sea region. *Journal of Quaternary Science 10*, 33–43.

Siegert, M. J. & Dowdeswell, J. A. 1995b: Numerical Modeling of the Late Weichselian Svalbard-Barents Sea Ice Sheet. *Quaternary Research 43*, 1–13.

Siegert, M. J., Dowdeswell, J. A., Svendsen, J. I. & Elverhoi, A. 2002: The Eurasian Arctic during the last ice age. *American Scientist 90*, 32–39.

Siggerud, T. 1963: On the marble-beds at Blomstrandhalvøya in Kongsfjorden. *Norsk Polarinstitutt Årbok 1962*, 44–49.

Skirbekk, K., Klitgaard Kristensen, D., Rasmussen, T. L., Koç, N. & Forwick, M. 2010: Holocene climate variations at the entrance to a warm Arctic fjord: evidence from Kongsfjorden trough, Svalbard. *Geological Society, London, Special Publications 344*, 289–304.

Sletten, K., Lysså, A. & Lønne, I. 2001: Formation and disintegration of a high-arctic ice-cored moraine complex, Scott Turnerbreen, Svalbard. *Boreas 30*, 272–284.

Ślubowska-Woldengen, M. A., Rasmussen, T. L., Koç, N., Klitgaard-Kristensen, D., Nilsen, F. & Solheim, A. 2007: Advection of Atlantic Water to the western and northern Svalbard shelf since 17,500 cal yr BP. *Quaternary Science Reviews 26*, 463–478.

Ślubowska, M. A., Koç, N., Rasmussen, T. L. & Klitgaard-Kristensen, D. 2005: Changes in the flow of Atlantic water into the Arctic Ocean since the last deglaciation: Evidence from the northern Svalbard continental margin, 80 degrees N. *Paleoceanography 20*, 1–15.

Sollid, J. L. & Sørbel, L. 1988: Influence of temperature conditions in formation of end moraines in Fennoscandia and Svalbard. *Boreas 17*, 553–558.

Stokes, C. R., Corner, G. D., Winsborrow, M. C. M., Husum, K. & Andreassen, K. 2014: Asynchronous response of marine-terminating outlet glaciers during deglaciation of the Fennoscandian Ice Sheet. *Geology 42*, 455–458.

Stone, J. O. 2000: Air pressure and cosmogenic isotope production. *Journal of Geophysical Research-Solid Earth 105*, 23753–23759.

Stone, J. O., Balco, G. A., Sugden, D. E., Caffee, M. W., Sass, L. C., Cowdery, S. G. & Siddoway, C. 2003: Holocene Deglaciation of Marie Byrd Land, West Antarctica. *Science 299*, 99–102.

Streuff, K. 2013: *Landform assemblages in inner Kongsfjorden, Svalbard: Evidence of recent glacial (surge) activity.* M.Sc Thesis, University of Tromsø, 154 pp.

Streuff, K., Forwick, M., Szczuciński, W., Andreassen, K. & Cofaigh, C. Ó. 2015: Submarine landform assemblages and sedimentary processes related to glacier surging in Kongsfjorden, Svalbard. *arktos 1*, 1–19.

Sugden, D. E. & John, B. S. 1976: *Glaciers and Landscape*. 376 pp. Arnold, London.

Sugden, D. E. 1977: Reconstruction of the morphology, dynamics, and thermal characteristics of the Laurentide Ice Sheet at its maximum. *Arctic and Alpine Research 9*, 21–47.

Sugden, D. E. 1978: Glacial erosion by the Laurentide ice sheet. *Journal of Glaciology 20*, 367–391.

Sund, M. & Eiken, T. 2010: Recent surges on Blomstrandbreen, Comfortlessbreen and Nathorstbreen, Svalbard. *Journal of Glaciology 56*, 182–184.

Svendsen, H., Beszczynska-Møller, A., Hagen, J. O., Lefauconnier, B., Tverberg, V., Gerland, S., Ørbøk, J. B., Bischof, K., Papucci, C. & Zajaczkowski, M. 2002: The physical environment of Kongsfjorden–Krossfjorden, an Arctic fjord system in Svalbard. *Polar Research 21*, 133–166.

Svendsen, J. I. & Mangerud, J. 1987: Late Weichselian and holocene sea-level history for a cross-section of western Norway. *Journal of Quaternary Science 2*, 113–132.

Svendsen, J. I., Mangerud, J., Elverhøi, A., Solheim, A. & Schüttenhelm, R. T. E. 1992: The Late Weichselian glacial maximum on western Spitsbergen inferred from offshore sediment cores. *Marine Geology 104*, 1–17.

Svendsen, J. I., Elverhøi, A. & Mangerud, J. 1996: The retreat of the Barents Sea Ice Sheet on the western Svalbard margin. *Boreas 25*, 244–256.

Svendsen, J. I. & Mangerud, J. 1997: Holocene glacial and climatic variations on Spitsbergen, Svalbard. *Holocene 7*, 45–57.

Svendsen, J. I., Alexanderson, H., Astakhov, V. I., Demidov, I., Dowdeswell, J. A., Funder, S., Gataullin, V., Henriksen, M., Hjort, C., Houmark-Nielsen, M., Hubberten, H. W., Ingólfsson, Ó., Jakobsson, M., Kjær, K. H., Larsen, E., Lokrantz, H., Lunkka, J. P., Lysså, A., Mangerud, J., Matiouchkov, A., Murray, A., Möller, P., Niessen, F., Nikolskaya, O., Polyak, L., Saarnisto, M., Siegert, C., Siegert, M. J., Spielhagen, R. F. & Stein, R. 2004: Late Quaternary ice sheet history of northern Eurasia. *Quaternary Science Reviews 23*, 1229–1271.

The Northern Exploration Company 1911: *The Northern Exploration Company, Ltd.* 134 pp. Norwegian Polar Institute, Tromsø.

The Northern Exploration Company 1913: *Marble Island: a short account of the discovery, location & products of the property with practical notes and reports upon the unique variety & value of its marbles*. 84 pp. Norwegian Polar Institute, Tromsø.

The Northern Exploration Company 1914: *Some particulars respecting the company's properties in Spitsbergen, with reports and extracts relating thereto*. 66 pp. Norwegian Polar Institute, Tromsø.

Thiedig, F. 1988: Post-Caledonian thrust structures on Blomstrandhalvøya, Kongsfjorden, NW Spitsbergen. *Norsk Polarinstitutt Rapportserie 46*, 15–16.

Thiedig, F. & Manby, G. M. 1992: Origins and deformation of post-Caledonian sediments on Blomstrandhalvøya and Lovenøyane, northwest Spitsbergen. *Norsk Geologisk Tidsskrift 72*, 27–33.

Thomas, R., Frederick, E., Krabill, W., Manizade, S. & Martin, C. 2009: Recent changes on Greenland outlet glaciers. *Journal of Glaciology 55*, 147–162.

Troitsky, L., Punning, J.-M., Hütt, G. & Rajamä, R. 1979: Pleistocene glaciation chronology of Spitsbergen. *Boreas 8*, 401–407.

Truffer, M. & Echelmeyer, K. A. 2003: Of isbræ and ice streams. *Annals of Glaciology 36*, 66–72.

van der Veen, C. 1996: Tidewater calving. *Journal of Glaciology 42*, 375–385.

Van Vliet-Lanoë, B. 1988: The significance of cryoturbation phenomena in environmental reconstruction. *Journal of Quaternary Science 3*, 85–96.

Van Vliet-Lanoë, B. 1995: Solifluxion et transferts illuviaux dans les formations périglaciaires litées. Etat de la question/Solifluction and translocation processes in bedded periglacial formations. State of the art. *Géomorphologie: relief, processus, environnement 1*, 85–113.

Vermeesch, P. 2007: CosmoCalc: An Excel add-in for cosmogenic nuclide calculations. *Geochemistry, Geophysics, Geosystems 8*, Q08003.

Vivian, M. R. 1965: Glaces mortes et morphologie glaciaire. *Revue de géographie alpine 53*, 371–401.

Von Blanckenburg, F., Belshaw, N. S. & O'Nions, R. K. 1996: Separation of 9 Be and cosmogenic 10 Be from environmental materials and SIMS isotope dilution analysis. *Chemical Geology 129*, 93–99.

Vorren, T. O., Lebesbye, E., Andreassen, K. & Larsen, K. B. 1989: Glacigenic sediments on a passive continental margin as exemplified by the Barents Sea. *Marine Geology 85*, 251–272.

Warren, W. P. & Ashley, G. M. 1994: Origins of the ice-contact stratified ridges (eskers) of Ireland. *Journal of Sedimentary Research 64*, 433–449.

Wilson, P., Schnabel, C., Wilcken, K. M. & Vincent, P. J. 2013: Surface exposure dating (36Cl and 10Be) of post-Last Glacial Maximum valley moraines, Lake District, northwest England: some issues and implications. *Journal of Quaternary Science 28*, 379–390.

Winsborrow, M. C. M., Andreassen, K., Corner, G. D. & Laberg, J. S. 2010: Deglaciation of a marine-based ice sheet: Late Weichselian palaeo-ice dynamics and retreat in the southern Barents Sea reconstructed from onshore and offshore glacial geomorphology. *Quaternary Science Reviews 29*, 424–442.

Winsborrow, M. C. M., Stokes, C. R. & Andreassen, K. 2012: Ice-stream flow switching during deglaciation of the southwestern Barents Sea. *Geological Society of America Bulletin 124*, 275–290.

Xu, S., Dougans, A. B., Freeman, S. P. H. T., Schnabel, C. & Wilcken, K. M. 2010: Improved 10Be and 26Al-AMS with a 5 MV spectrometer. *Nuclear Instruments and Methods in Physics Research Section B: Beam Interactions with Materials and Atoms 268*, 736–738.

Young, N. E., Schaefer, J. M., Briner, J. P. & Goehring, B. M. 2013: A Be-10 production-rate calibration for the Arctic. *Journal of Quaternary Science 28*, 515–526.

Yuan, L., Sun, L., Long, N., Xie, Z., Wang, Y. & Liu, X. 2009: Seabirds colonized Ny-Ålesund, Svalbard, Arctic ~9,400 years ago. *Polar Biology 33*, 683–691.

Zhang, T., Barry, R. G., Knowles, K., Heginbottom, J. A. & Brown, J. 1999: Statistics and characteristics of permafrost and ground-ice distribution in the Northern Hemisphere. *Polar Geography 23*, 132–154.

Ziaja, W. & Ostafin, K. 2014: Landscape–seascape dynamics in the isthmus between Sørkapp Land and the rest of Spitsbergen: Will a new big Arctic island form? *AMBIO 44*, 332–342.

Appendix A – BLOM samples

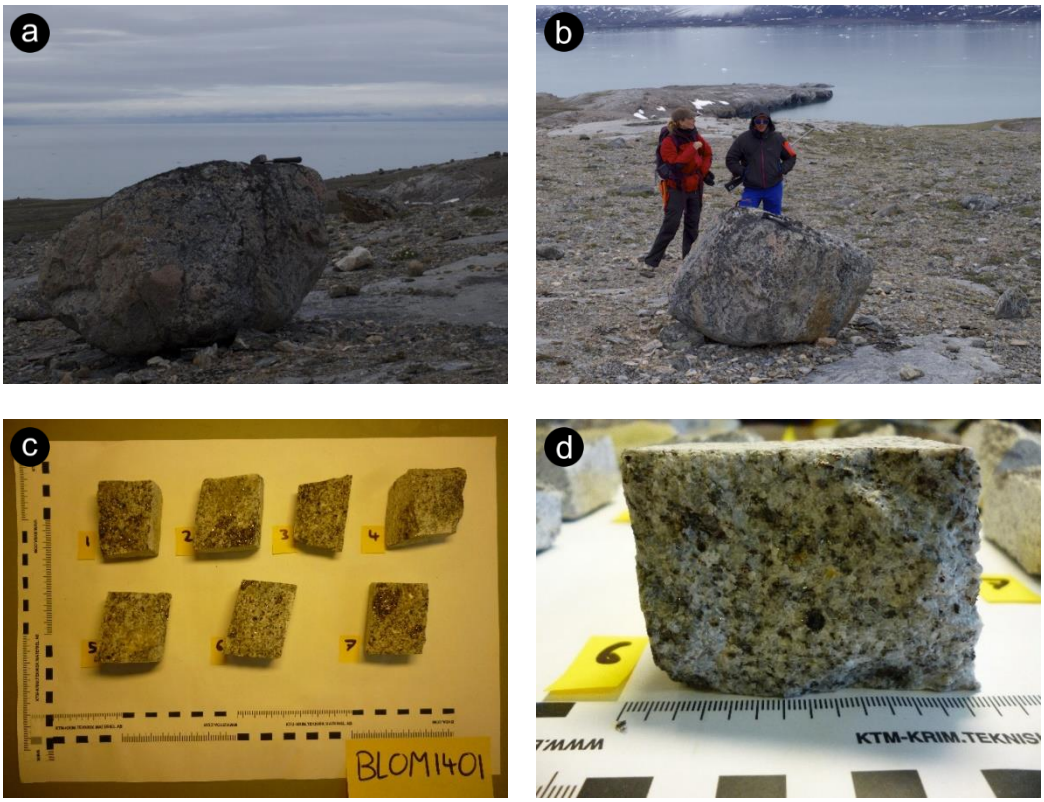

Figure A.1: BLOM1401; (a) facing west, hammer for scale (Photo: A. Hormes), (b) facing south (Photo: A. Hormes), (c) sample pieces (Photo: O. Grant), and (d) close-up showing granite lithology (Photo: O. Grant).

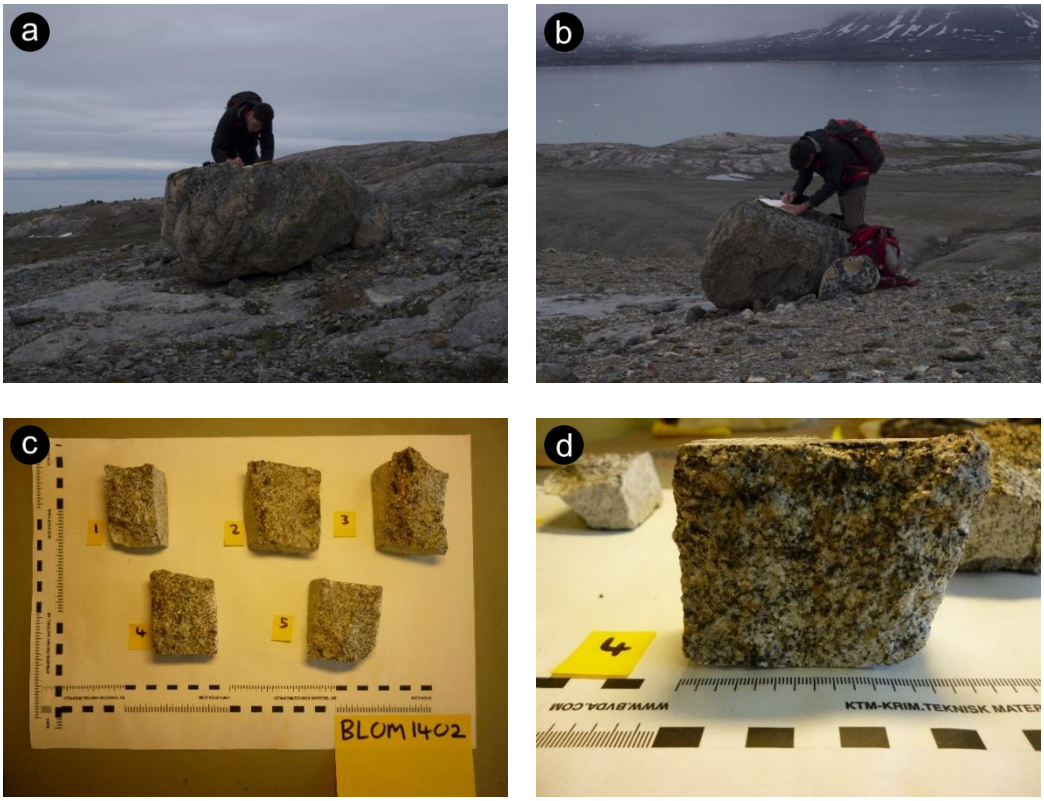

Figure A.2: BLOM1402; (a) facing west, person for scale (Photo: A. Hormes), (b) facing south (Photo: A. Hormes), (c) sample pieces (Photo: O. Grant), and (d) close-up showing granite lithology (Photo: O. Grant).

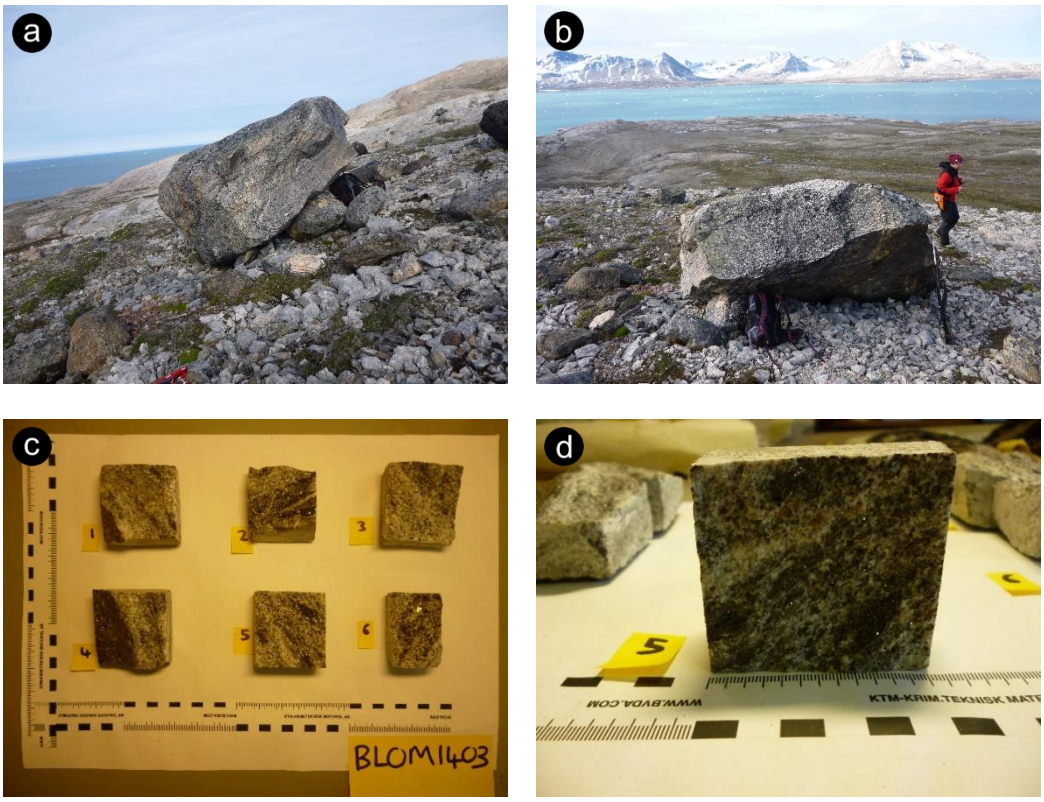

Figure A.3: BLOM1403; (a) facing west, backpack for scale (Photo: O. Grant), (b) facing south (Photo: O. Grant), (c) sample pieces (Photo: O. Grant), and (d) close-up showing granitic gneiss lithology (Photo: O. Grant).

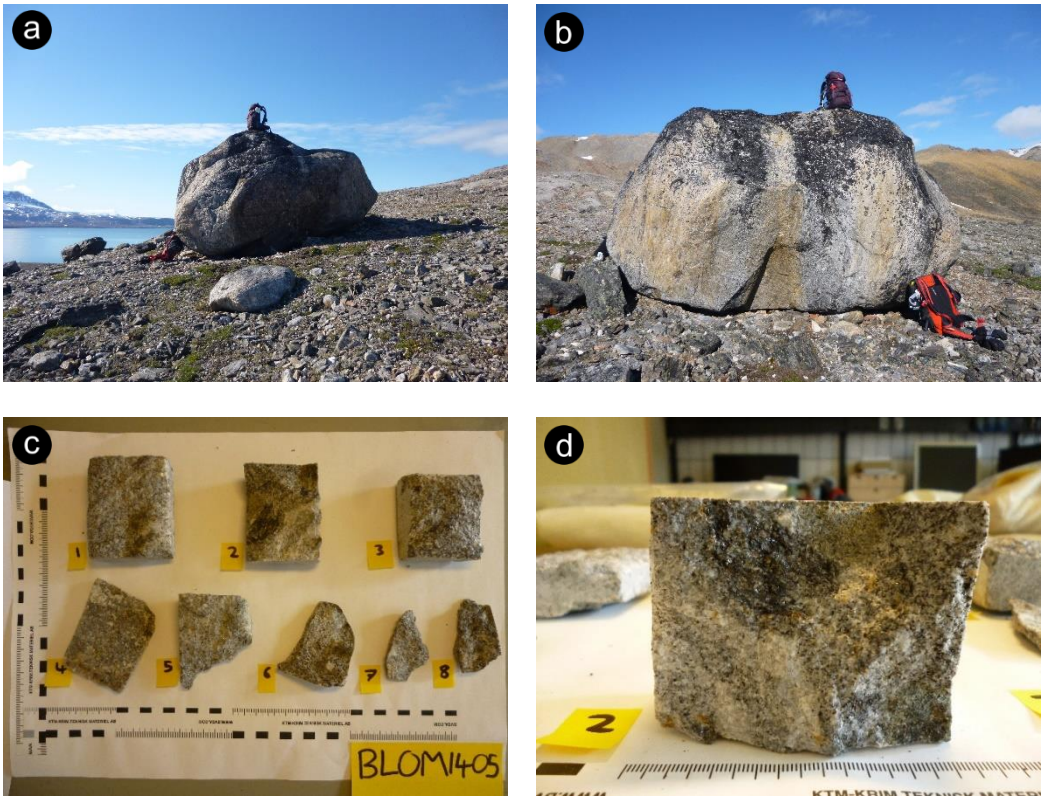

Figure A.4: BLOM1405; (a) facing west, backpack for scale (Photo: O. Grant), (b) facing north (Photo: O. Grant), (c) sample pieces (Photo: O. Grant), and (d) close-up showing granite lithology (Photo: O. Grant).

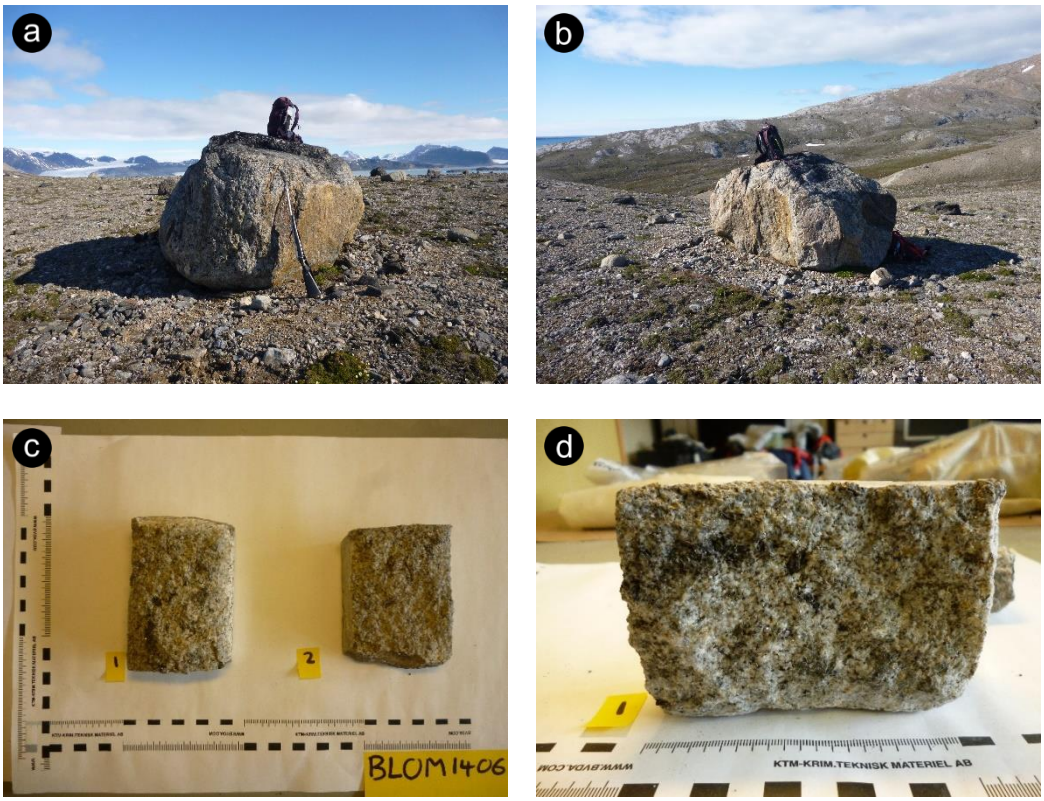

Figure A.5: BLOM1406; (a) facing east, backpack and rifle for scale (Photo: O. Grant), (b) facing west (Photo: O. Grant), (c) sample pieces (Photo: O. Grant), and (d) close-up showing granite lithology (Photo: O. Grant).

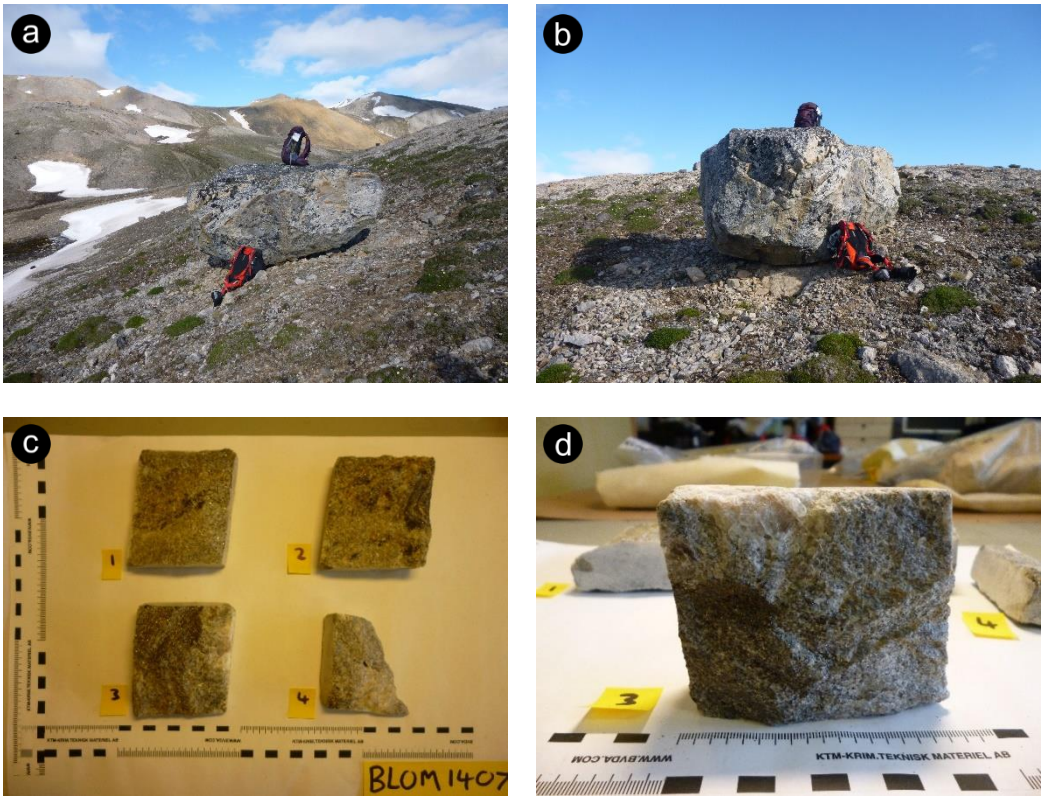

Figure A.6: BLOM1407; (a) facing north, backpack for scale (Photo: O. Grant), (b) facing east (Photo: O. Grant), (c) sample pieces (Photo: O. Grant), and (d) close-up showing granite lithology (Photo: O. Grant).

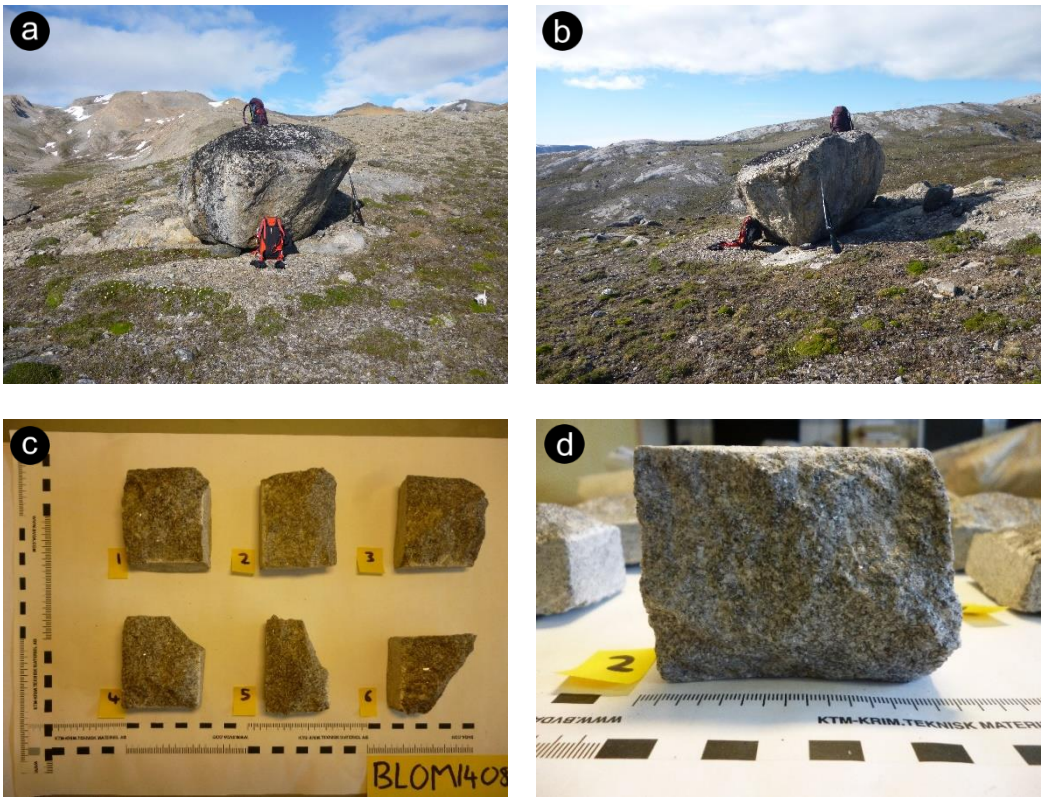

Figure A.7: BLOM1408; (a) facing north, backpack and rifle for scale (Photo: O. Grant), (b) facing west (Photo: O. Grant), (c) sample pieces (Photo: O. Grant), and (d) close-up showing granite lithology (Photo: O. Grant).

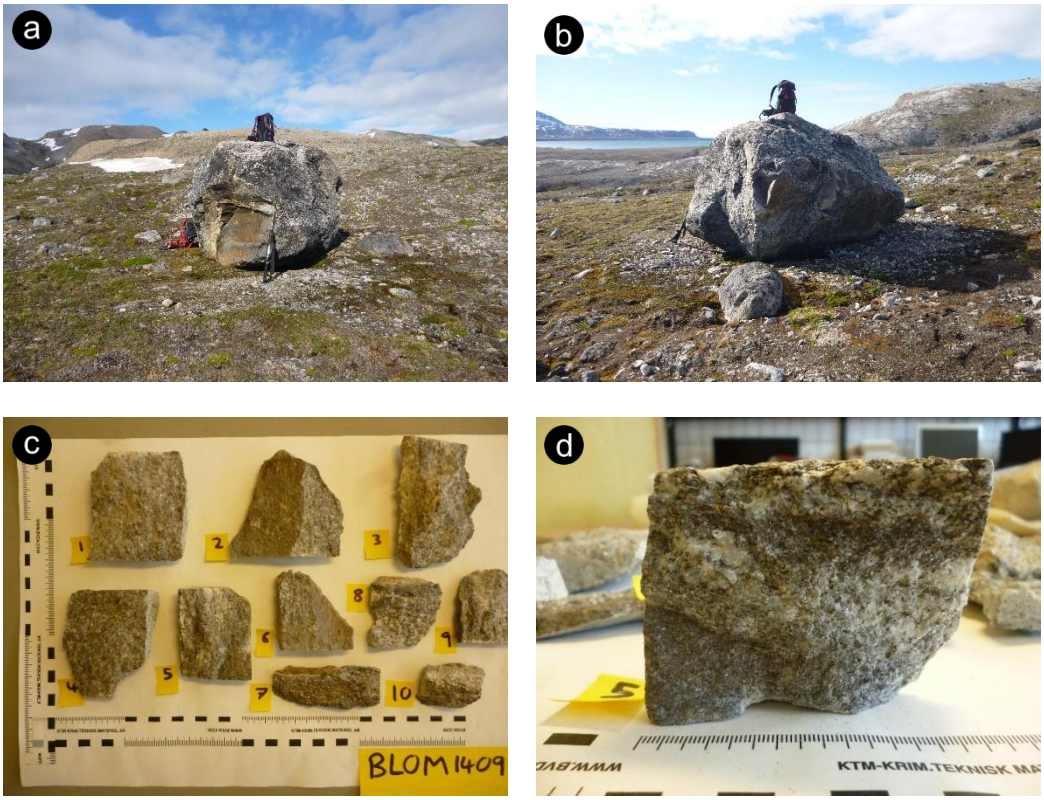

Figure A.8: BLOM1409; (a) facing north, backpack and rifle for scale (Photo: O. Grant), (b) facing west (Photo: O. Grant), (c) sample pieces (Photo: O. Grant), and (d) close-up showing granitic gneiss lithology (Photo: O. Grant).

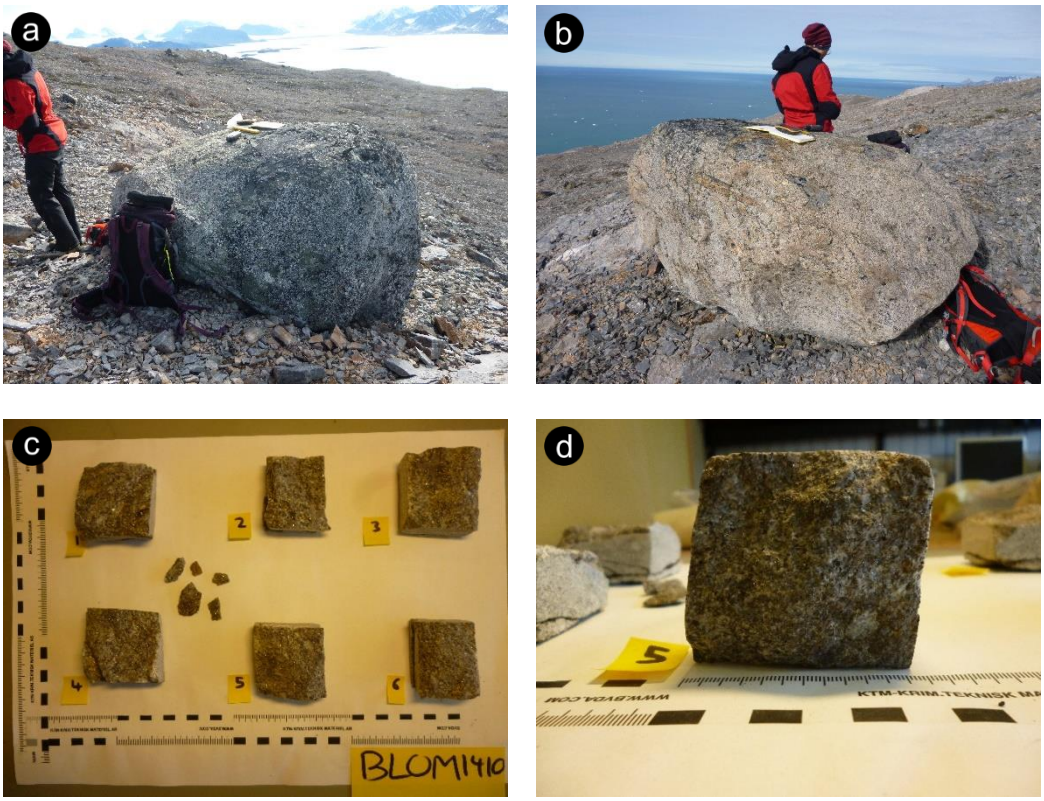

Figure A.9: BLOM1410; (a) facing east, backpack for scale (Photo: O. Grant), (b) facing west (Photo: O. Grant), (c) sample pieces (Photo: O. Grant), and (d) close-up showing granite lithology (Photo: O. Grant).

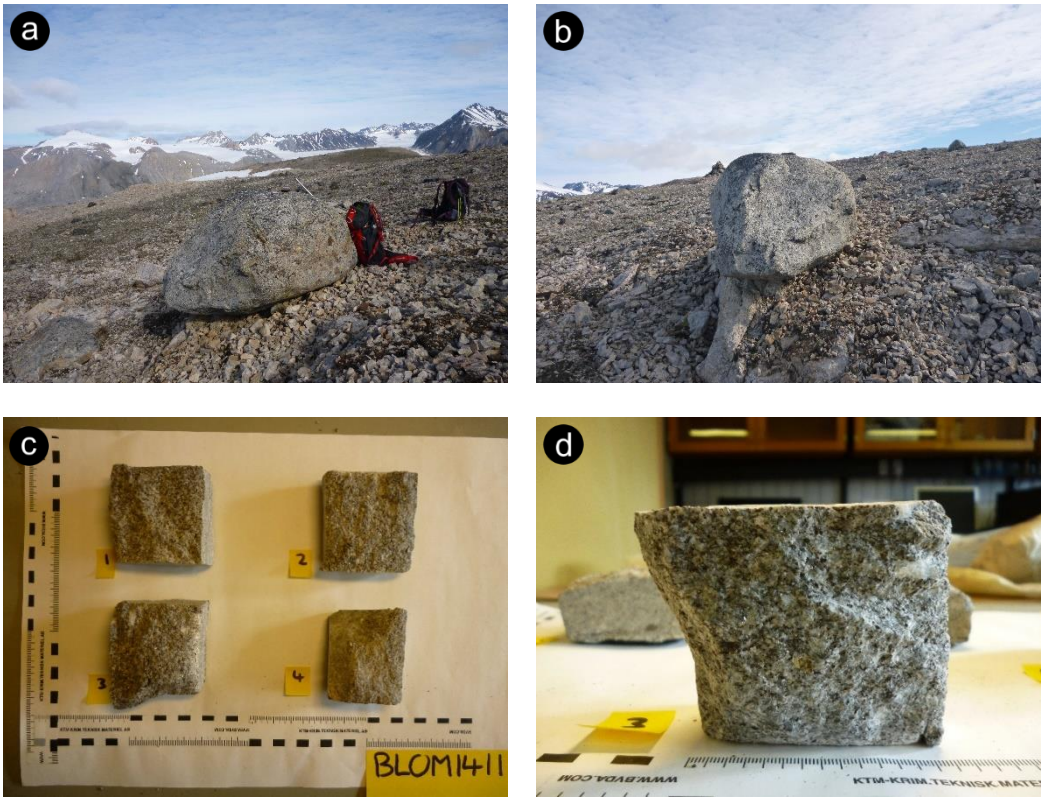

Figure A.10: BLOM1411; (a) facing north, backpack for scale (Photo: O. Grant), (b) facing east (Photo: O. Grant), (c) sample pieces (Photo: O. Grant), and (d) close-up showing granite lithology (Photo: O. Grant).

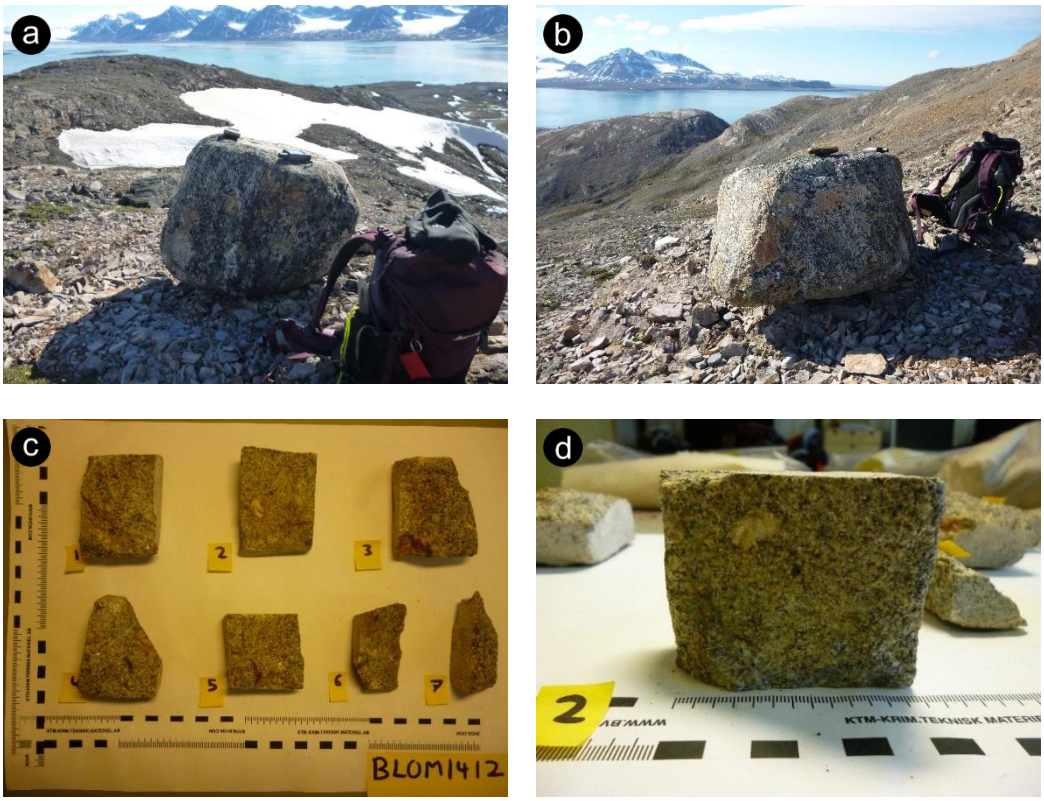

Figure A.11: BLOM1412; (a) facing south, backpack for scale (Photo: O. Grant), (b) facing west (Photo: O. Grant), (c) sample pieces (Photo: O. Grant), and (d) close-up showing granite lithology (Photo: O. Grant).

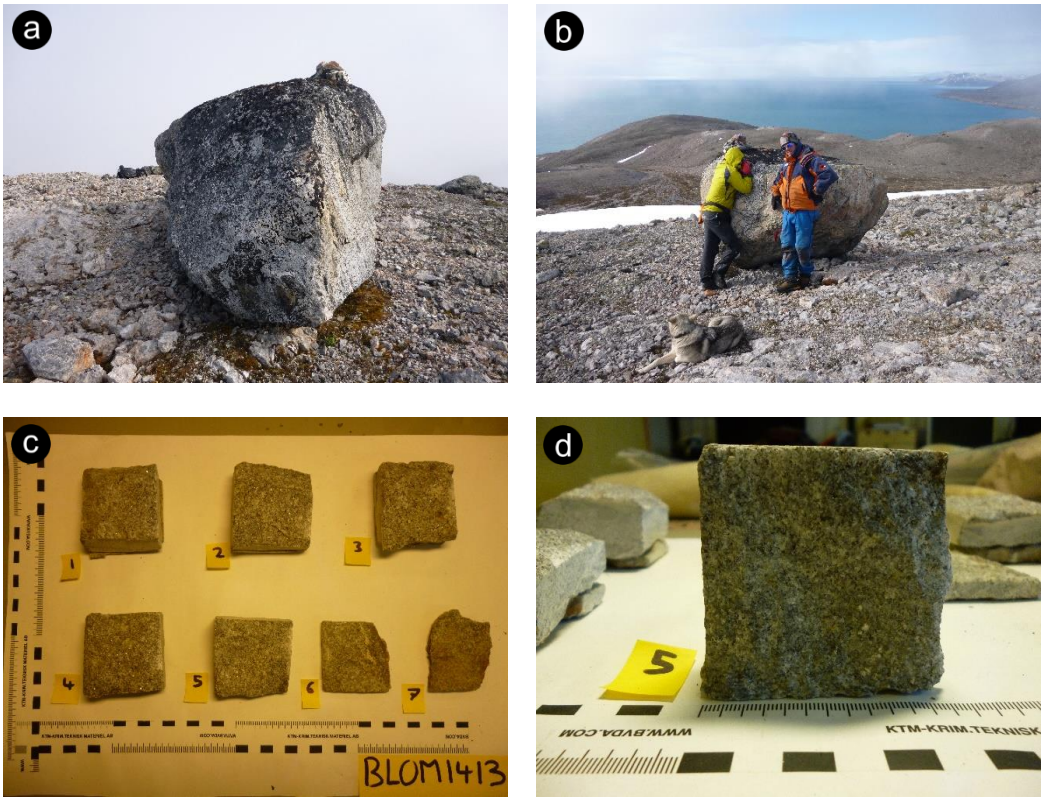

Figure A.12: BLOM1413; (a) facing east (Photo: O. Grant), (b) facing west, persons for scale (Photo: O. Grant), (c) sample pieces (Photo: O. Grant), and (d) close-up showing granite lithology (Photo: O. Grant).

Appendix B – GOR samples

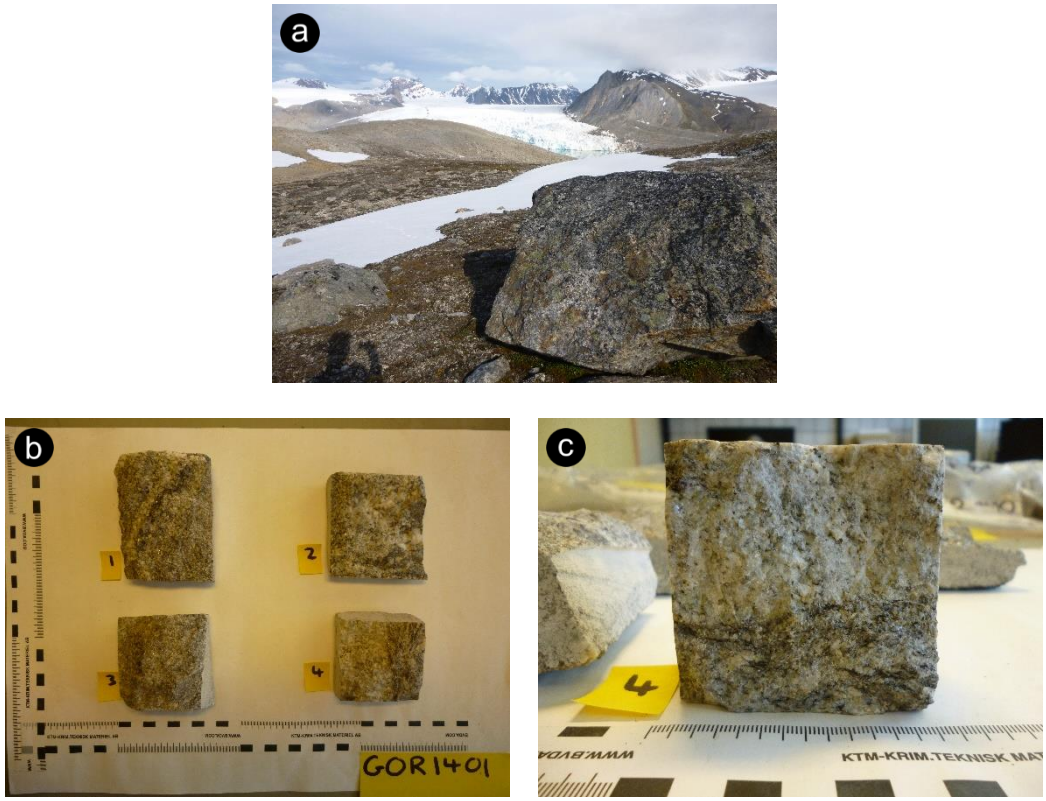

Figure B.1: GOR1401; (a) facing north, ca. 120 cm high (Photo: O. Grant), (b) sample pieces (Photo: O. Grant), and (c) close-up showing granitic gneiss lithology (Photo: O. Grant).

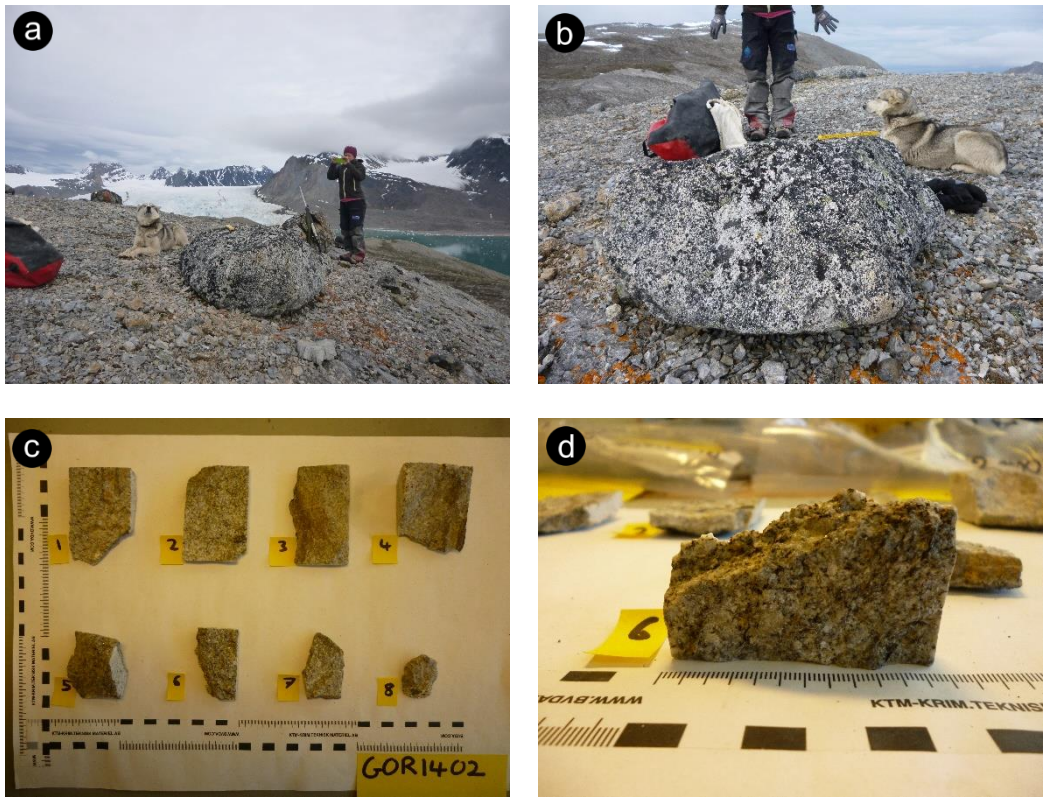

Figure B.2: GOR1402; (a) facing north, backpack and dog for scale (Photo: O. Grant), (b) facing west (Photo: O. Grant), (c) sample pieces (Photo: O. Grant), and (d) close-up showing granite lithology (Photo: O. Grant).

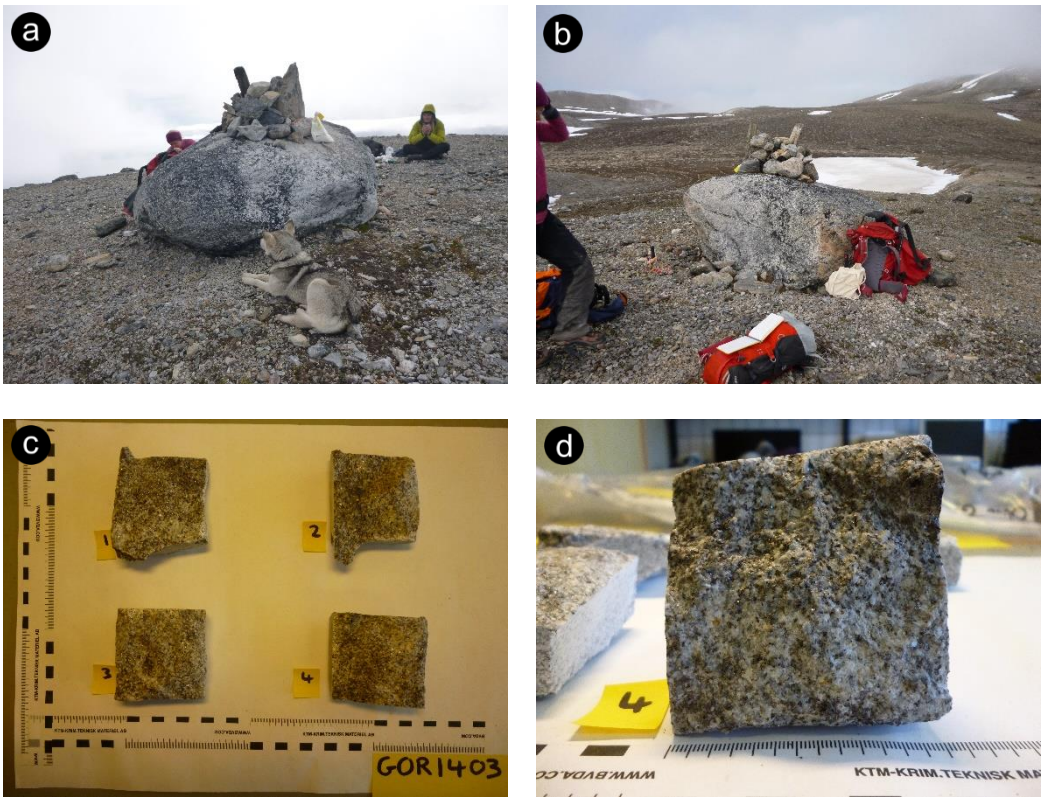

Figure B.3: GOR1403; (a) facing east, persons and dog for scale (Photo: O. Grant), (b) facing west (Photo: O. Grant), (c) sample pieces (Photo: O. Grant), and (d) close-up showing granite lithology (Photo: O. Grant).

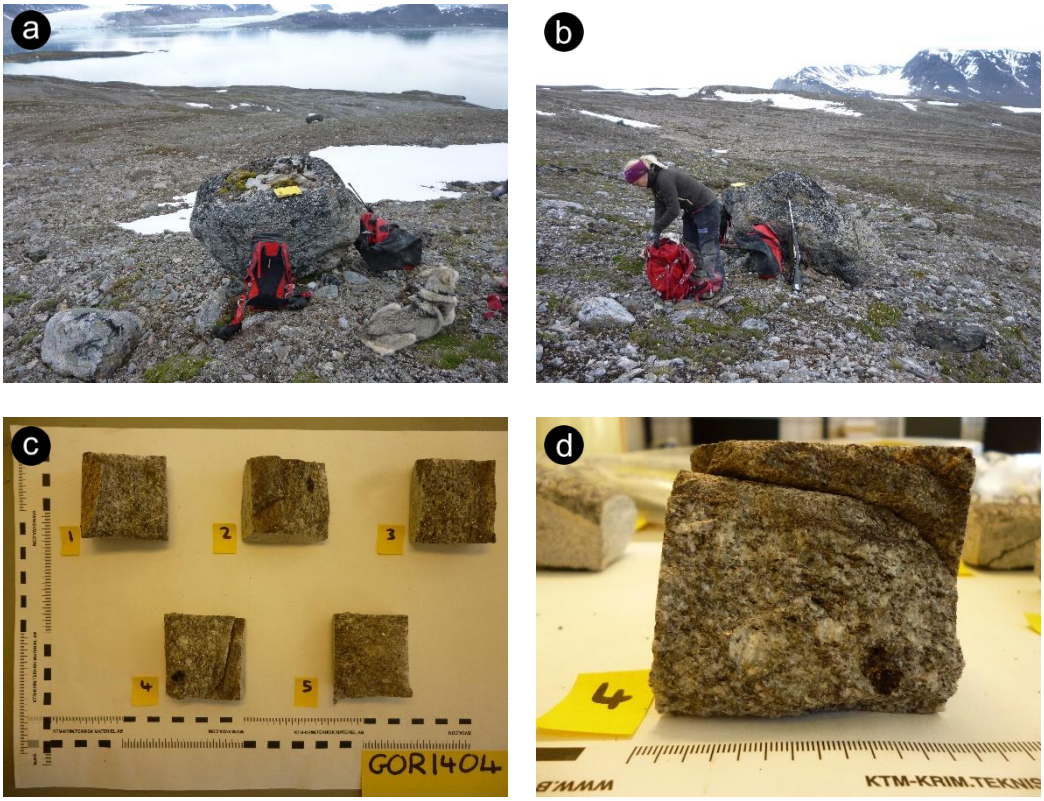

Figure B.4: GOR1404; (a) facing east, backpack and dog for scale (Photo: O. Grant), (b) facing north (Photo: O. Grant), (c) sample pieces (Photo: O. Grant), and (d) close-up showing granite lithology (Photo: O. Grant).

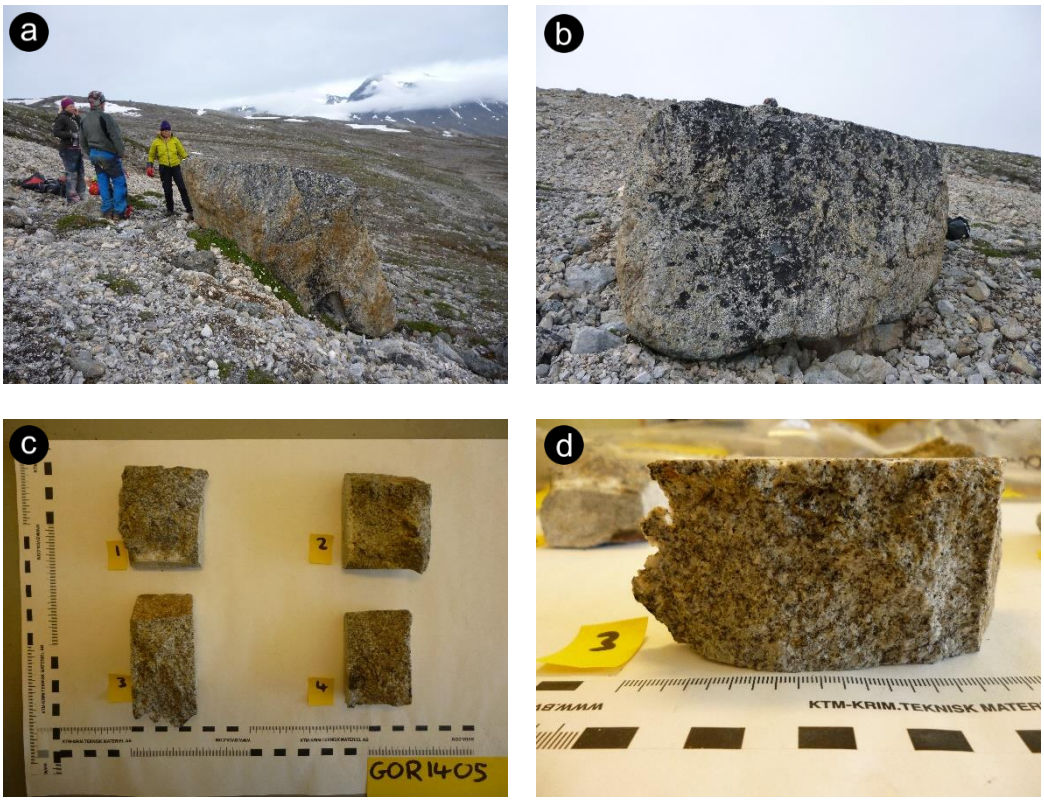

Figure B.5: GOR1405; (a) facing north, persons for scale (Photo: O. Grant), (b) facing west (Photo: O. Grant), (c) sample pieces (Photo: O. Grant), and (d) close-up showing granite lithology (Photo: O. Grant).

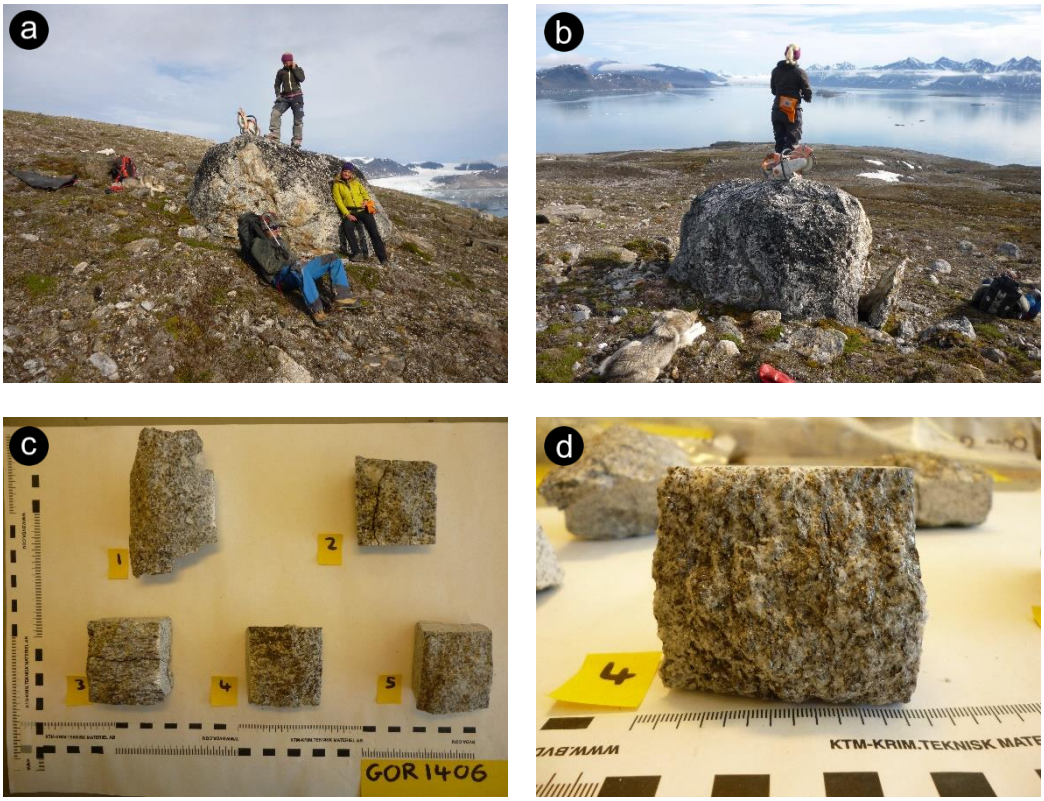

Figure B.6: GOR1406; (a) facing north, persons for scale (Photo: O. Grant), (b) facing east (Photo: O. Grant), (c) sample pieces (Photo: O. Grant), and (d) close-up showing granite lithology (Photo: O. Grant).

Appendix C – SARS samples

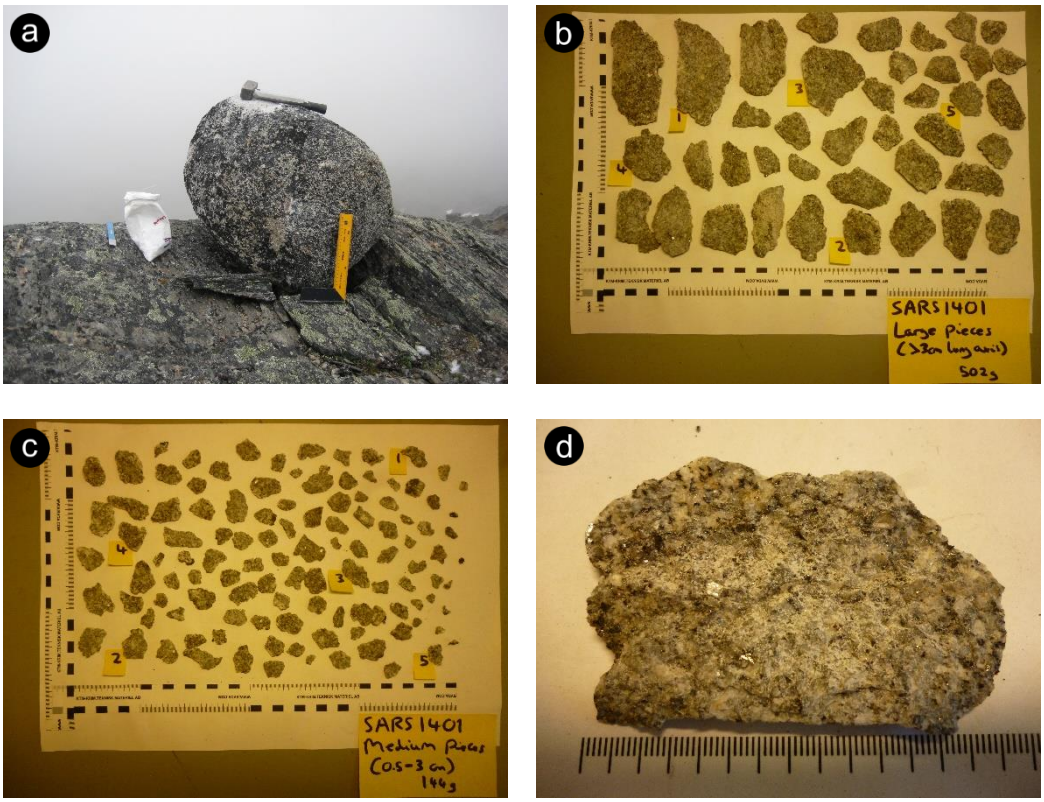

Figure C.1: SARS1401; (a) facing north, hammer for scale (Photo: H. Linge), (b) Large (>3 cm) fraction (Photo: O. Grant), (c) medium (0.5 – 3 cm) fraction (Photo: O. Grant), and (d) close-up showing granite lithology (Photo: O. Grant).

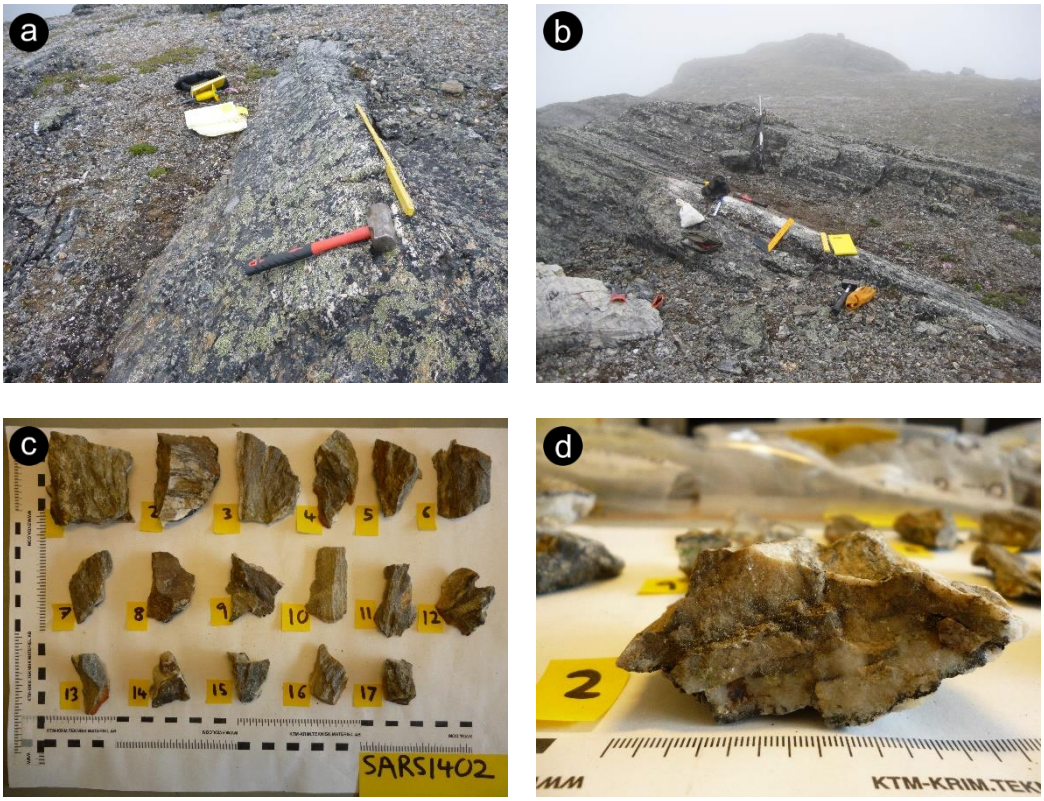

Figure C.2: SARS1402; (a) facing south, hammer and metre rule for scale (Photo: O. Grant), (b) facing east (Photo: H. Linge), (c) sample pieces (Photo: O. Grant), and (d) close-up showing quartz vein from mica schist (Photo: O. Grant).

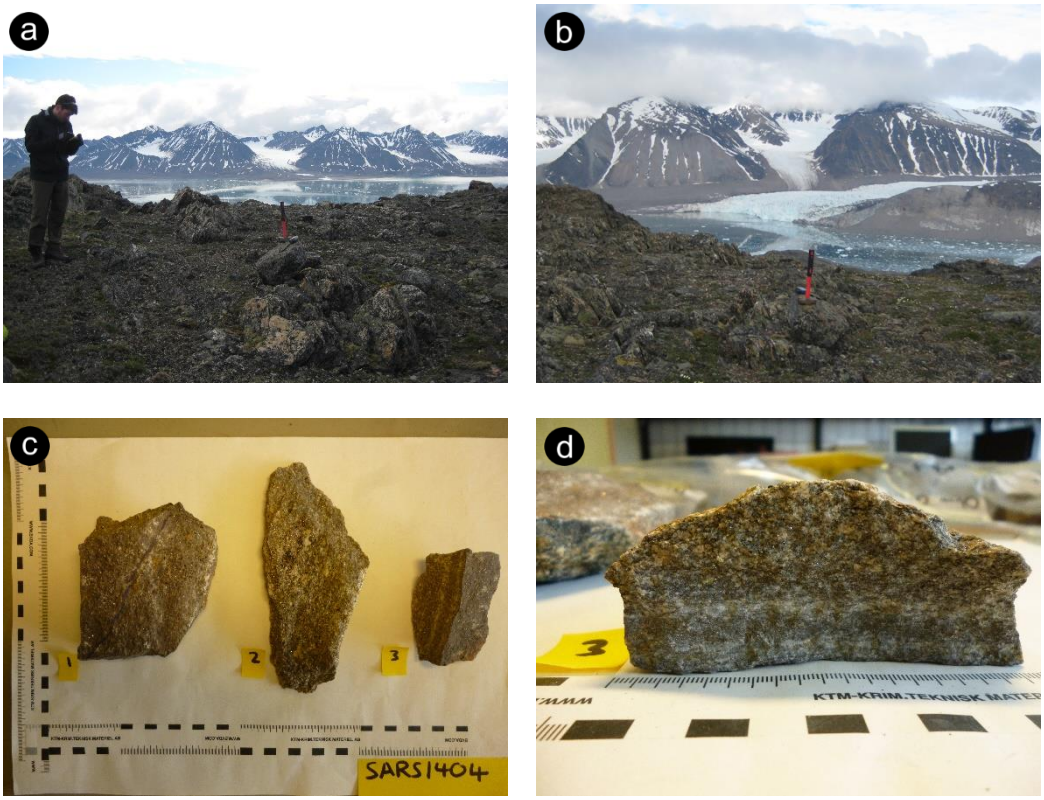

Figure C.3: SARS1404; (a) facing south, hammer and person for scale (Photo: H. Linge), (b) facing north (Photo: H. Linge), (c) sample pieces (Photo: O. Grant), and (d) close-up showing granitic gneiss lithology (Photo: O. Grant).

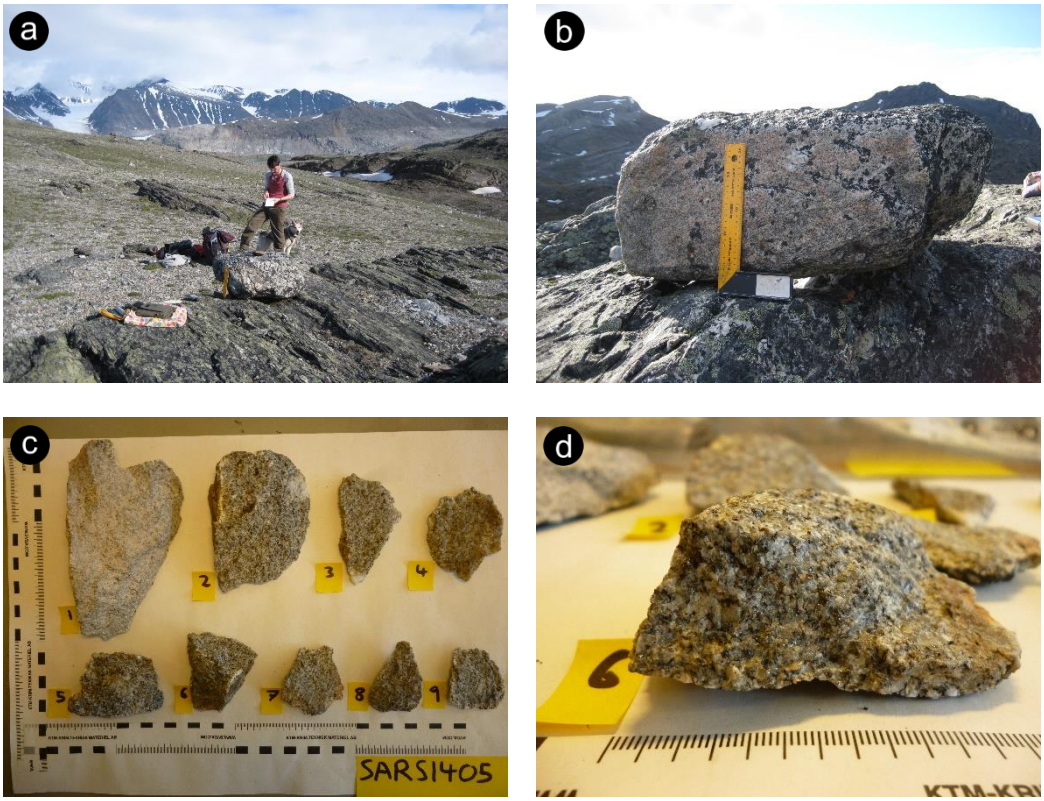

Figure C.4: SARS1405; (a) facing north, person for scale (Photo: H. Linge), (b) facing west (Photo: H. Linge), (c) sample pieces (Photo: O. Grant), and (d) close-up showing granite lithology (Photo: O. Grant).

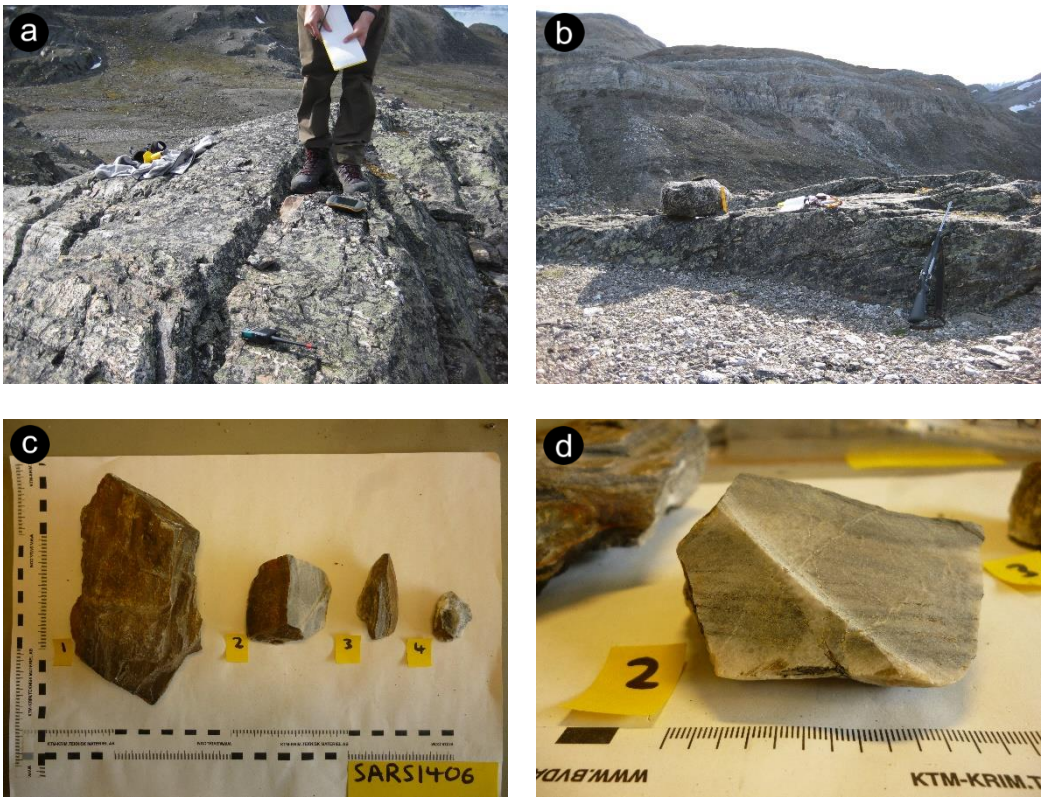

Figure C.5: SARS1406; (a) facing north, person for scale (Photo: H. Linge), (b) facing west (Photo: H. Linge), (c) sample pieces (Photo: O. Grant), and (d) close-up showing quartz vein in mica schist (Photo: O. Grant).

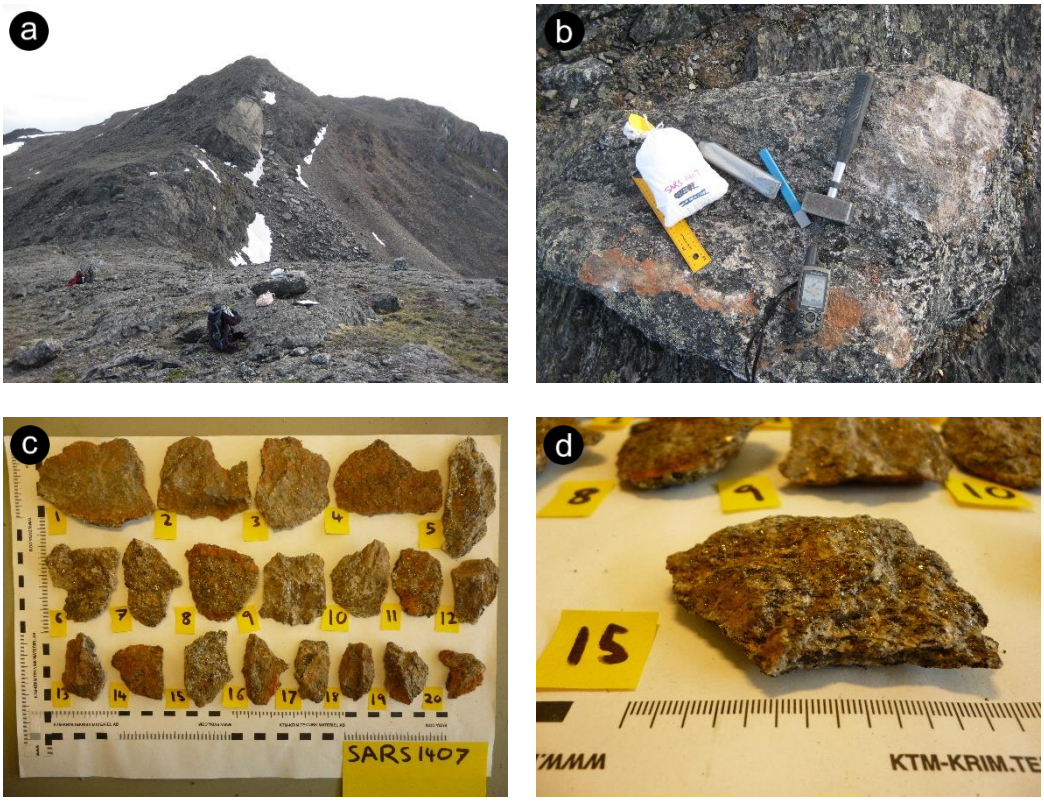

Figure C.6: SARS1407; (a) facing east to summit of Ossian Sarsfjellet, bag for scale (Photo: H. Linge), (b) top of boulder (Photo: H. Linge), (c) sample pieces (Photo: O. Grant), and (d) close-up showing granite lithology with FeO staining (Photo: O. Grant).

Appendix D – Quaternary geological map of Blomstrandhalvøya

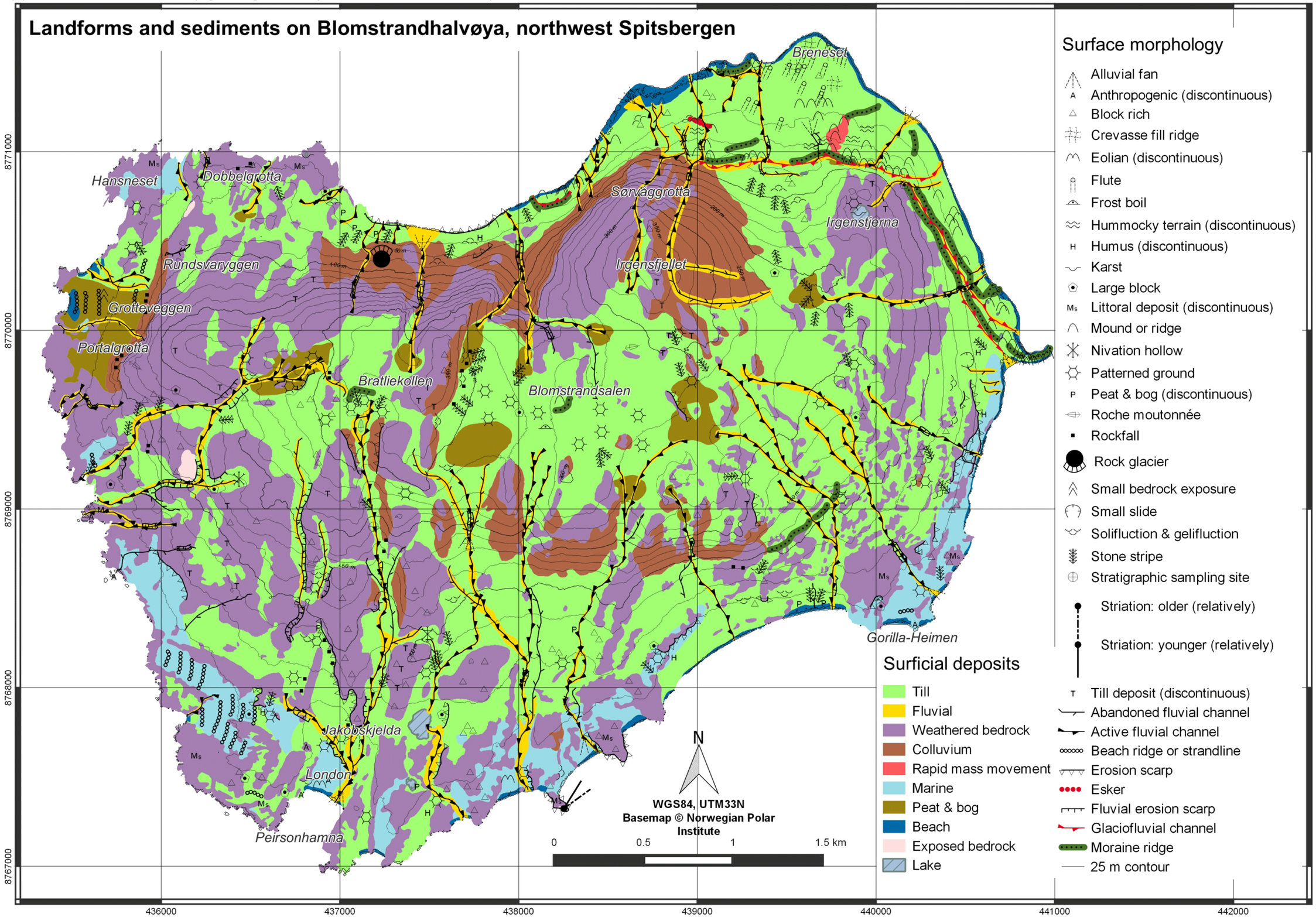

Figure D.1: Map of Quaternary sediment cover and landforms from Blomstrandhalvøya, constructed from field observations, aerial photographs and digital terrain model interpretation, and guided by a draft geomorphological map from Tommaso Piacentini (personal communication) and Herz and Andreas (1966a) (Figure 1.3).